Hydrogen production by steam reforming of biodiesel

August 2014

Gaurav Anil Nahar

Submitted in accordance with the requirements for the degree of

Doctor of Philosophy

The University of Leeds

Energy Research Institute

School of Chemical and Process Engineering

List of Publications

The candidate confirms that the work submitted is his/her own, except where work which has formed part of jointly-authored publications has been included. The contribution of the candidate and the other authors to this work has been explicitly indicated below. The candidate confirms that appropriate credit has been given within the thesis where reference has been made to the work of others. Chapter 3 includes some parts from publications 1 and 3.

1. Nahar G. and V. Dupont, Hydrogen production from simple alkanes and oxygenated hydrocarbons over ceria-zirconia supported catalyst: review. Renewable and sustainable energy reviews, 2014. 32(0): p. 777-796.

   Contribution of Authors: Gaurav Nahar wrote the paper and Valerie Dupont provided advice and edited the paper.

2. Nahar G and V Dupont, Recent advances in hydrogen production via autothermal reforming (ATR) process: a review of patents and research articles. Recent patents on chemical engineering, 2014. 6(1): p. 8-42.

   Contribution of Authors: Gaurav Nahar wrote the paper and Valerie Dupont provided advice and edited the paper.

3. Nahar G and V Dupont, Hydrogen via steam reforming of liquid bio feedstock. Biofuels, 2012.3(2): p.167-191.

   Contribution of Authors: Gaurav Nahar wrote the paper and Valerie Dupont provided advice and edited the paper.

4. Nahar G, V Dupont, M. Twigg and E Dvininov, Feasibility of hydrogen production from steam reforming of biodiesel (FAME) feedstock on Ni-supported catalysts- Submitted to Applied catalysis B.

   Gaurav Nahar-Designed the experimental setup and performed the experiments and wrote the paper.

   Valerie Dupont- editing.

Martyn Twigg- Editing and provided catalyst for the study.

Emiliana Dvininov- Editing and provided catalyst support for the study.

Acknowledgement

I would like to thank all who have been directly or indirectly responsible in completion of this work. All the people have helped and supported me in their own way and I would like to convey my gratitude to all of them.

Firstly I would like to thank “Lord Moraya” and my Guru Dr. Ashok Marathe. This work was completed only as a result of their guidance, direction and blessings. I would like to express my sincere gratitude to my supervisor Dr. Valerie Dupont, for her support guidance, advice and her valuable help and encouragement throughout the course of this research. She was always there when I needed her and always had good ideas and most important she had time to discuss them.

I would like to thank my friends and colleagues namely Dr. Abha Saddawi, Dr. Nikolaos Giannakeas, Zaheer Abbas and Cheng Feng for their help, support, encouragement and valuable discussions which were extremely helpful during the completion of this research.

I would also like to thank Dr. Emiliana Dvininov, MEL Chemical UK for providing the catalyst support essential in completion of this work. The help of all the technical staff at University of Leeds, namely Edmund Woodhouse, Mathew Buckley, Simon Lloyd, Susanne Patel, Tarsem Hunjan is greatly appreciated.

Words are very few to express my appreciation for my parents Anil and Shobha Nahar, and my wife Sharda Nahar, in addition to my sister Pranjal Gohad for their dedication, love, encouragement, patience, persistent confidence in me, which helped me in the successful completion of this undertaking.

Abstract

An experimental set up was designed and commissioned for the steam reforming of biodiesel. The performance of the reactor was evaluated by varying molar steam/carbon ratio in the feed (S/C) , temperature, residence time, catalyst and biodiesel characteristics, at constant input of 1.50×10^{-5} mol of C/s. The effect of temperature was examined in the range of 600-800°C with S/C from 2 to 3. The weight hourly space velocity (a measure of inverse residence time in the reformer) was varied from 3.52 to 2.85 h^{-1}. The experimental results were compared with their chemical equilibrium counterparts in order to determine the efficiency of the processes. The process outputs were measured using a micro-gas chromatograph and material balances were performed to determine the parameters such as H_2 yield, biodiesel and steam conversions, and selectivity to carbon gases such as CO, CO_2, CH_4, C_2H_4, C_2H_6, C_3H_6 and C_3H_8. An elemental carbon balance was performed taking into account the carbon converted to C-containing gases, C deposited on the catalyst and C present in the condensate.

Commercial Ni on alumina supported catalysts and in house prepared Ni catalysts were used for the steam reforming evaluation. Nickel catalysts supported on two different kinds Ce/Zr supports (Zr rich and Ce rich) were formulated in house. The Ce rich catalyst supports were prepared by sol gel synthesis employing tamarind seed polysaccharide as a gelling agent. The Zr support was provided by a commercial manufacturer. The Ni was loaded on the supports by impregnation using nitrate salts. Three kinds of biodiesels i.e. commercial, palm and in house prepared biodiesel were used for hydrogen production. The in house made biodiesel was prepared by acid-base transesterification of waste cooking oil obtained from a local fish and chip shop.

It was found that among the three types of biodiesels tested, commercial biodiesel exhibited higher biodiesel and water conversion resulting in higher H_2 yield. The

highest hydrogen yield and biodiesel conversion was found in the temperature range of 650-700°C with S/C of 3. The optimum residence time to achieve high biodiesel and steam conversion was 3.18 h^{-1}. The selectivity to the main carbon containing gases (CO, CO_2 and CH_4) and to H_2 was very close to its chemical equilibrium value for all the catalysts. The commercial Ni/Al_2O_3 and Zr-rich Ce/Zr supported Ni catalyst were effective for steam reforming and should lower carbon formation as compared to the Ni supported on Ce rich Ce/Zr support. The highest Y_{H2} of 27.8 wt% of biodiesel, i.e. 96% of the chemical equilibrium value, was measured for the Ni/Ce-Zr catalyst using commercial biodiesel. Biodiesel and steam conversions of 96% and 41.3% were responsible for providing such high H_2 yield. The catalyst also exhibited very high H_2 selectivity (99%). Among the carbon CO_2 selectivity was highest 63.6% followed by CO which 33% and finally CH_4 which was a mere 2.1%. Using the catalyst Ni/Ce-Zr, a C balance closure within 2.5% was obtained which corresponded to a carbon deposition of 1.25% of the carbon feed.

H_2 production using autothermal reforming was attempted, i.e. where a source of oxygen, here in the form of air, is introduced in the biodiesel/steam feed to encourage exothermic partial oxidation reactions intended to neutralise the heat demand in the reformer. The experimental set up designed indicated that further optimisation would be required for this process due to large amount of carbon forming at the reactor inlet, in addition to the carbon deposited on the catalyst surface, significantly affecting the process efficiency. Despite this, conditions 12% close to autothermality, as reflected in the ratio of enthalpy balance on the isothermal reactor at 650 °C to the total enthalpy output, were obtained for the condition S/C of 2 for O_2/C of 0.38 and WHSV of 3.23 h^{-1} on the Ni/Ca-Al catalyst, this corresponded to a Y_{H2} that was 69.2 % of the chemical equilibrium value.

Table of Contents

List of Tables

List of Figures

List of Abbreviation

ACR- autothermal Cyclic Reforming

AFC- alkaline fuel cell

ASTM- American Society for Testing and Materials

ATR- autothermal reforming

BET- Brunauer-Emmett-Teller

BJH- Barrett, Joyner and Halenda

BP-British Petroleum

BoP- Balance of plant

CCS- carbon capture and storage

CHP- combined heat and power

CLR- chemical looping steam reforming

CNG- Compressed natural gas

COD-Chemical oxygen demand

COX- Complete oxidation

CSR -Catalytic steam reforming

DME- Dimethyl Ether

EDX- Energy Dispersive X-ray

EEA- European Environmental Agency

EIA- Energy Information Administration

EU- European Union

FAME- fatty acid methyl esters

FCC- fluid catalytic cracking

FFA- Free fatty acids

GC- Gas chromatograph

GCV- Gross calorific value

GHSV- Gas hourly space velocity

LCOE- Levelised cost of electricity

LHSV- Liquid hourly space velocity

IPCC- Intergovernmental Panel on Climate Control

IUPAC- International union of pure and applied chemistry

OECD- Organisation for Economic Co-operation and Development

OPEC- Organization of the Petroleum Exporting Countries

OSC- Oxygen storage capacity

MCFC- Molten carbonate fuel cell

MSW-Municipal solid waste

PAFC- Phosphoric acid fuel cell

PEMFC- Proton exchange membrane fuel cell

PM- Particulate matter

POX- Partial oxidation

P/P_0- relative pressure

PSA- Pressure swing adsorber

R&D- Research and development

S/C- Steam-to-carbon

SEM- Scanning Electron Microscopy analysis

SEM-EDX- Scanning Electron Microscopy- Energy dispersive X-ray

SESR- Sorption enhanced steam reforming

SMR- Steam methane reforming

SOFC- Solid oxide fuel cells

SR- Steam reforming

SRA- Steam reforming of acetic acid

SRE- Steam reforming of ethanol

SSA- Specific surface area

TAG- Triacylglycerol

TC- Temperature controller

TCD- Thermal conductivity detectors

TGA-Thermogravimetric analysis

TGA-FTIR- thermo gravimetric- Fourier transforms infra red spectroscopy

TOC-Total organic carbon

TPO- Temperature programmed oxidation

TSP- Tamarind seed polysaccharide

TWC- Three-way catalysis

VOC- Volatile organic carbon

WBFR- Water-biodiesel molar feed ratio

WGS- Water gas shift reaction

WHSV- Weighted hourly space velocities

XRD- X ray powder diffraction

Nomenclature

Symbol	Full form	Unit
A	Area occupied by an absorbed gas molecule	
B	Full width at half maximum	
Bnl	Billion litres	l
C	Concentration	mol/l
$C_nH_mO_k$	Elemental formula for oxygenated hydrocarbons (biodiesel) where n, m, k are molar number of C,H and O in the compound	
d_c	Diameter of particles	nm
dn/dt	Rate of accumulation of a species	
dn_c/dt	Accumulation of moles of carbon element over the dt period of time	
F	Form factor depending on the meniscus	
K	Dimensionless shape factor (typical values about 0.9)	
LHV_{H2}	Lower heating values of H_2	kJ/mol
LHV_{biod}	Lower heating values of biodiesel	kJ/mol
M	mass	g or kg
$\dot{n}$	Molar flow rate	mol/s
N	Avogadro's number	1/mol
$\dot{n}_{COX}$	Molar flowrate of biodiesel reacted using complete oxidation reaction	mol/s
$\dot{n}_{POX}$	Molar flowrate of biodiesel reacted using partial oxidation reaction	mol/s
$\dot{n}_{CSR}$	Molar flowrate of biodiesel	mol/s

	reacted using complete steam reforming	
$\dot{n}_{out,\ dry}$	Dry gas molar flowrate	mol/s
P	Equilibrium pressures	atm
P_o	Saturation pressures	atm
R	Universal gas constant	m^3atm/mol^{o}K
r_p	Radius of the pore	nm
S_{BET}	BET surface area	m^2/g
Sc	Selectivities for the carbon containing gases	%
$S_{C\text{-}CO}$	Selectivities of CO w.r.t containing gases	%
$S_{H\text{-}H2}$	Selectivities for the H_2	%
$S_{C\text{-}i}$	Selectivities to carbon containing products	%
$S_{H\text{-}i}$	Selectivities to H_2 containing products	%
T	Film thickness	nm
V	Volume	cm^3
$\dot{V}$	Volumetric flowrate	m^3/s
Vm	Molar volume of adsorbate	mol/cm^3
W	Molar mass	kg/mol
X_{biod}	Biodiesel conversion	%
X_{H2O}	Steam conversion	%
$\dot{y}$	Elemental N in biodiesel	%
$Y_{H2,\ eff}$	H_2 yield efficiency	%
Y_{H2}	H_2 yield	wt %
y_i	Mole fraction of i in the dry gas output	
Γ	Surface temperature of the adsorbate at temperature T	^{o}C or K
Θ	Angle of contact equal to 0	^{o}
Λ	Wave length of the X rays	Å
ρ	Density	kg/m^3

Formulas

Symbol	Full form
As	Arsenic
B	Boron
Ba	Barium
Bi	Bismuth
C_2H_5OH	Ethanol
$C_3H_8O_3$	Glycerol
Ca	Calcium
Ce-Zr- 3/1	Zirconia doped ceria with ceria/zirconia ratio with 3:1
Ce-Zr	Zirconia doped ceria
Ce-Al-3/1	Alumina doped ceria with ceria/alumina ratio with 3:1
CeO_2	Cerium oxide
CH_3OH	Methanol
CH_4	Methane
CO	Carbon monoxide
CO_2	Carbon dioxide
Co	Cobalt
Cu	Copper
Cu/Al_2O_3	Copper on alumina
Fe	Iron
Fe/Al_2O_3	Iron on alumina
Ge	Germanium

H_2	Hydrogen
HC	Hydrocarbon
H_2O	Water
Hg	Mercury
K	Potassium
KNO_3	Potassium nitrate
KWh	Kilo Watt hour
Li	Lithium
Mg	Magnesium
MJ/kg	Mega Joule/ Kilo gram
Mn	Manganese
NH_3	Ammonia
Ni-K/Al	Potassium doped 18 wt% NiO doped with 1.67 wt% K_2O supported on Alumina.
NOx	Nitrous oxide
Ni	Nickel
NiO	Nickel oxide
Ni/Ce-Zr	10 wt % Ni supported on pre calcined Ce-Zr mix oxide. The support was provided by MEL Chemicals, UK
Ni-K/Ce-Zr	10 wt % Ni and 2 wt % K supported on pre calcined Ce-Zr mix oxide. The support was provided by MEL Chemicals, UK
Ni-Sn/Ce-Zr	10 wt % Ni and 2 wt % Sn supported on pre calcined Ce-Zr mix oxide. The support was provided by MEL Chemicals, UK
Ni/Ce-Zr-3/1	10wt% Ni supported on zirconium doped ceria with Ce/Zr ratio of 3:1 prepared by sol gel method using TSP
Ni/YSZ	Nickel supported on yttria stabilised zirconia.

O_2	Oxygen
P	Phosphorus
Pb	Lead
S	Sulphur
Sn	Tin
SO_2	Sulphur dioxide
SOx	Sulphur oxide
Zn	Zinc

Introduction

1. Global warming and energy crises

Greenhouse gases such as water vapour and carbon dioxide plays a very vital role in regulating the heat emitted by Earth, in order to keep its surface warm and sustain life. Water vapour causes about 36–70% of global warming; with CO_2 9–26%; CH_4 4–9%; and ozone 3–7% [1]. The absence of GHG's would have resulted in much colder Earth (-6^{o}C) and life would have been completely different. This natural phenomenon helps to raise the temperature of Earth surface by 20^{o}C, which would have maintained the average surface temperature to 14^{o}C [2]. This delicate balance has been disturbed due to human activities, resulting in average temperature rise Earth's climate (global warming).

Figure 1.1 shows the changes in Earth's temperature and its relation to CO_2 emissions since last 1000 years. There is a consensus that increased land and fossil fuel usage has resulted in warming of the world, due to increased CO_2 emissions [3, 4] in the last 200 years. Global temperature are estimated to rise from 1.1 to 6.4^{o}C over 21st century [5] on top of 0.6^{o}C rise observed in the last century [3]. The increased amount of CO_2 due to anthropogenic sources is believed to be one of the main cause of global warming [6]. The Intergovernmental Panel on Climate Control (IPCC) performed a detailed and rigorous study on climate change and reported that global warming is, to a high degree of certainty, caused mainly as a result of human activities after industrial revolution. Since the industrial revolution, atmospheric concentration of CO_2 is reported to have increase by 31% as compared to the values observed prior to it [7]. Fossil fuel fired conventional power plants used for electricity production are considered as the main source of CO_2 emissions in the world. Sector wise distribution of CO_2 emissions is shown in Figure 1.2. The energy sector comprising of power plants and transportation emit 64% of the CO_2 emissions. Fossil fuels such as coal and natural gas are predominantly used in these power plants. The use of liquid fuels is mainly associated with the industrial and

transportation sectors. In some countries having non-uniform power generation and distribution grids, liquid fuels are also used in small scale power generation.

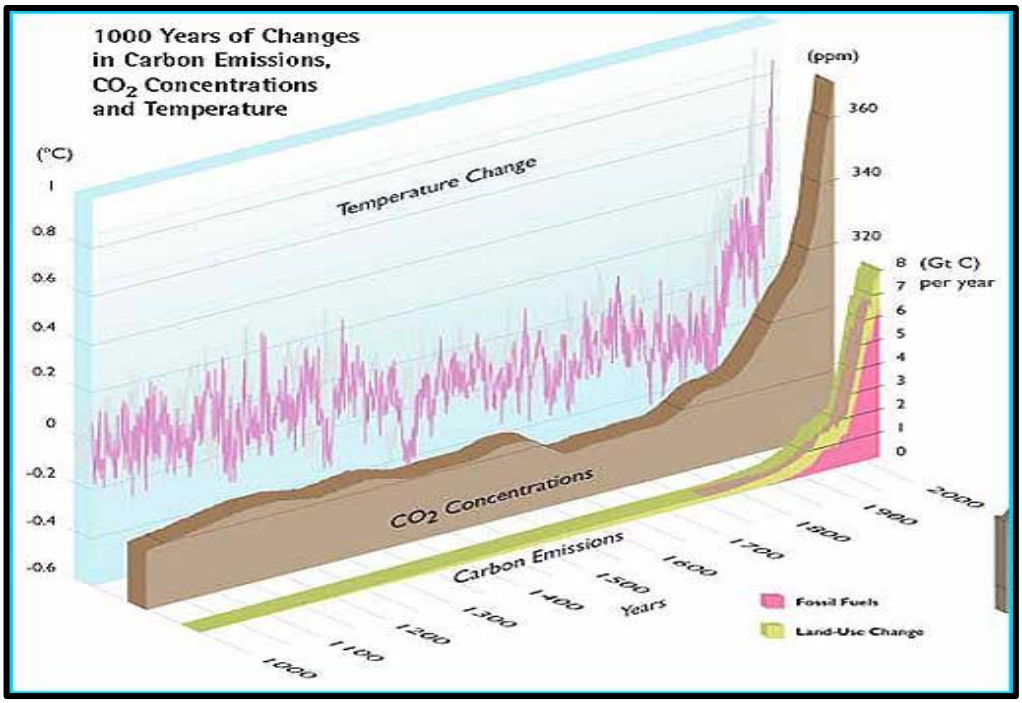

Figure 1.1: CO_2 emissions and temperature changes in last 1000 years [4].

The rise in carbon dioxide emissions is a result of several factors, i.e. increase in world population, increased industrialization and global trade, increased land use and deforestation. The increased population and industrialization of the world has caused enormous increase in energy demand, which could be linked to rise in CO_2 emissions. A 56% rise in world's energy consumption is predicted by the Energy Information Administration (EIA). According to the EIA, energy consumption will rise from 552×10^{15} kJ in 2010 to 664 and 865×10^{15} kJ by 2020 and 2040 respectively. There is a wide variation in energy consumption of OECD and non OECD countries. The variation in the energy consumption is governed by various factors such as economic and population growth. Non OECD countries like China and India are the two fastest growing economies for the last 2 decades growing at a rate of 7.4 and 6% in the first quarter of 2014.

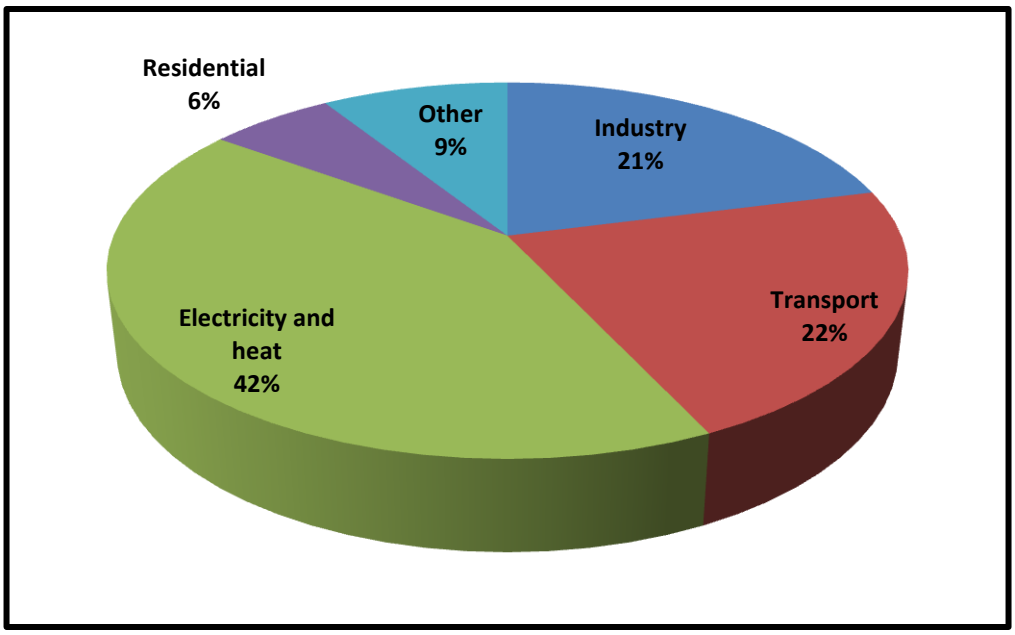

Figure 1.2: Worldwide CO2 emissions, 2011 [8].

The increased economic and population growth in these non OECD countries has resulted in steep rise in energy consumption. On the other hand, OECD countries such as US are matured energy consumers as a result of slower economic growth and negligible or no population growth.

According to the latest statistics released by British Petroleum (BP) in January 2014, global CO_2 emissions are predicted to reach 45×10^{12} tonnes by 2035 (Figure 1.3). In the Figure 1.3, the dotted line represents the emission path required to restrict the global CO_2 concentration to 450 ppm, which would maintain a rise of $2^{o}C$. The IEA predicts that such rise would lead to the catastrophic $6^{o}C$ increase in the atmosphere's global temperature. EIA's prediction matches with BP's and according to them the major contributor to global CO_2 rise will come from non-OECD countries, due to strong economic growth and reliance on fossil fuels [9]. The non OECD share to CO_2 emissions is predicted to exceed OECD's by 127% by 2040. China alone will be responsible for one quarter of the increase in CO_2 emissions (3.6×10^{12} tonnes), which would bring its emissions to 6.7×10^{12} tonnes by 2030 [3]. Regional emissions per capita in China are expected to rise from 3 to 10 tonnes of CO_2 by end of 2035. In India the emissions per

capita are expected to increase from 1 to 3 tonnes of CO_2 by end of 2035. On the other hand per capita emissions in EU and US are expected to decrease by 2035.

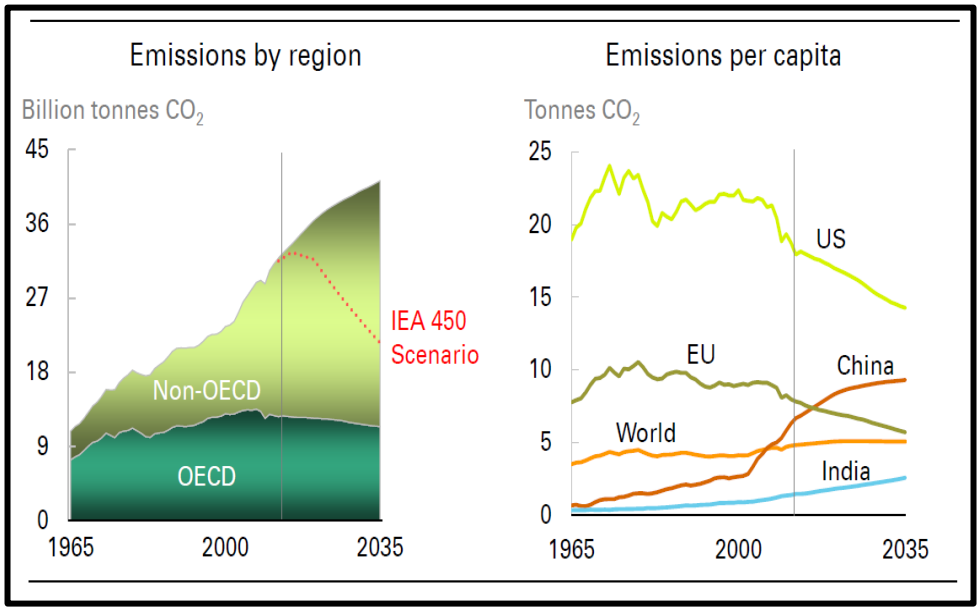

Figure 1.3: Carbon dioxide emissions prediction for 2035 [10].

1.1 Effects of global warming

The increased emissions could cause catastrophic effects on life. Figure 1.4 shows the potential effects of global warming on the environment Climate change will result in, rise in number of very hot days and heat waves, rising sea levels, more frequent intense precipitation events, and also increase in hurricane intensity. Developing countries will be affected more by climate change as compared to developed countries. As climate in many developing countries is already warm as compared to developed countries, increased temperature would result in increased frequency of famines, floods and disease outbreaks.

Increased flood risks by 2080 are reported to affect 80 million people, with 60 likely to be among the poorest parts of South East Asia [3]. Considering Bangladesh, which is situated on the junction of three big rivers of the subcontinent (Ganges, Brahmaputra and

Meghna); as a result of increased temperature, monsoon precipitation has increased resulting in two catastrophic and exceptional floods during the period 1980–1999. The 1998 flood submerged 70% of the country and was reported to affect about 31 million people in 52 out of the 64 districts. An estimated 2.4 million houses were completely or partially destroyed [11]. The frequency of such devastating floods is predicted to increase in the future.

In an opposite scenario, climate change will result in regional scarcity of water and frequent occurrence of famines and droughts. Average seasonal rainfall during the period of 1901 to 2010 over India has reduced by 10% compared to its long period average, resulting in 17% of the years to be drought years [12]. Over 1 billion people are predicted to be affected by fresh water poverty in West Asia and North Africa as a result of global warming by 2030 [13].

The shortage or excess rain will have dire consequences on agriculture dependent countries, by affecting crop yields and food prices. A 3.5°C rise in temperature with 7% precipitation increase is predicted to result in 30-40% yield loss in India resulting in 7-17% revenue loss, by the end of 21st century [14]. As a result of wet or dry conditions, soil moisture content and growing seasons would be affected, reducing the productivity of crops. Increased temperature might be beneficial for some crops but might have adverse effects on others [15]. Plants could grow faster as a result of increased temperature but the higher rate of maturation may alter crop rotation cycles, affecting feasibility and profitability. Faster growth may create smaller plants, because soil may not be able to supply water or nutrients at the required rates, thereby reducing grain, forage, fruit, or fiber production. Similarly pollination of plants would be affected by high temperatures altering the yield, or increasing the risk of failure [16]. The effects on agriculture could lead to severe food shortages and price fluctuations, affecting billions across the globe.

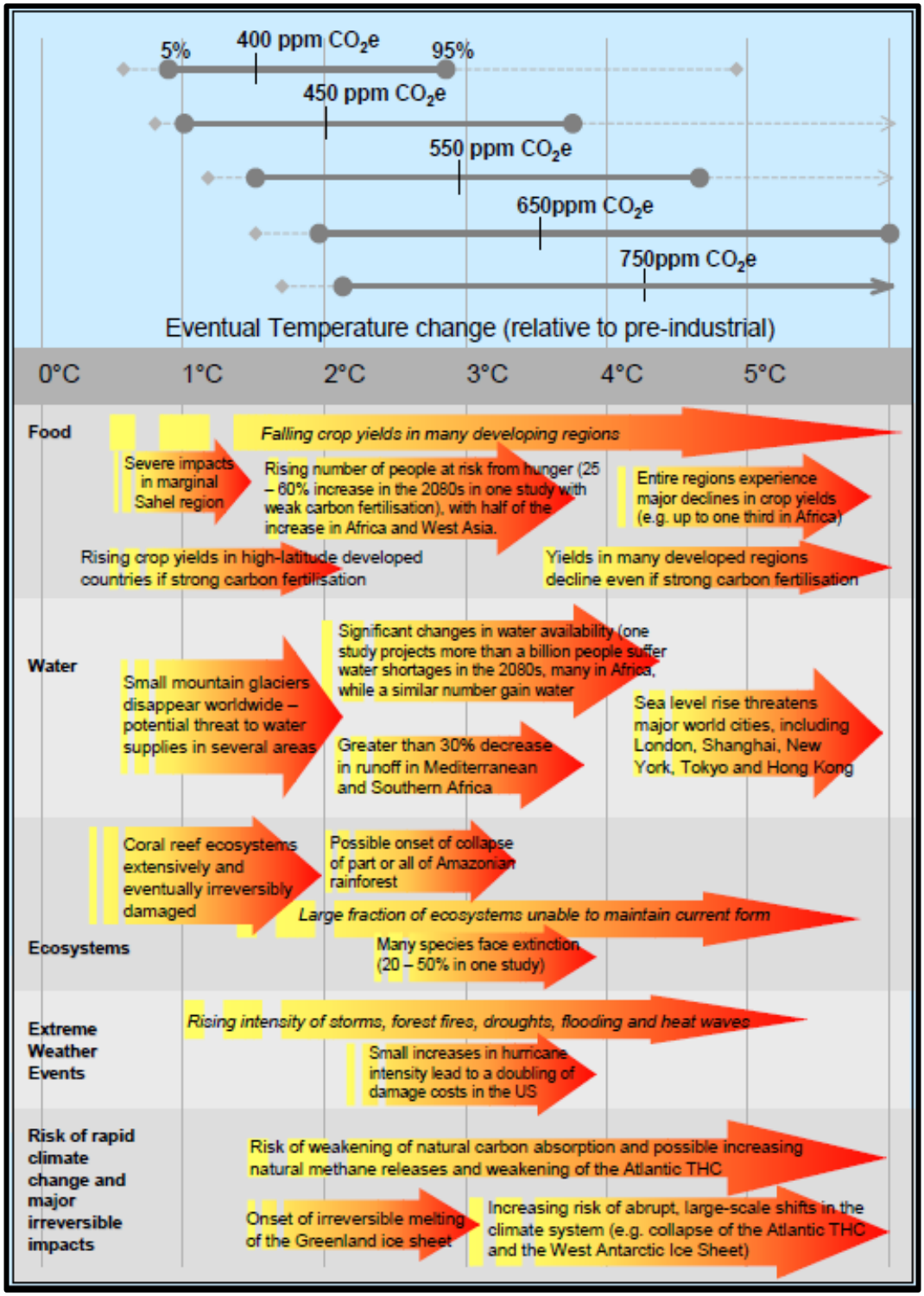

Figure 1.4: Effects of global warming [17].

The bulk of population is concentrated along or near coastal areas of the world. Coastal zones account 60% of the global population with one third of cities that have over 1 million inhabitants [18]. In US, alone 8 million people live in coastal areas [19], while in China 60% of the population reside in coastal provinces [20]. Rising sea level due to climate change would have serious effects on the coastal areas of the world. Sea level is predicted to rise by 20 cm to 2 m by end of 21st century [21]. The magnitude, frequency and duration of flooding during storms will be increased as a result of rise in sea level. Storm surge caused by high winds bring water inland during storms and hurricanes. As a result of elevated sea level these surges can reach farther inland damaging homes and infrastructure. Increased sea level would also submerge low lying coastal areas, drastically affecting populations. Inland intrusion of salt water due to the rising sea level will affect the salinity of coastal fresh water [22]. Coastal wetlands comprise of salt marshes, mangroves and intertidal areas, which are affected by increased sea level. Global wetlands are lost at the rate of 1% every year. These areas have number of important functions such as flood protection, waste assimilation, nursery areas for fisheries and nature conservation. Therefore, wetland loss will ultimately have significant high human cost [23].

Disappearance of Earth's ice cover is one of the outcomes of the global change in surface temperature. The ice cover helps to reflect large part of sun's heat back into space, preventing overheating of the planet. Loss of ice cover will not only affect the temperature around the world, but could result in rising sea level; causing regional flooding, damaged ecosystems and habitats, endangering human and animal life on the planet. Effect of climate change on ice melts around the globe is listed in the Table 1.1.

East Antarctic, West Antarctic, and Greenland ice sheets combined contain approximately 70 m of sea-level equivalence. They have serious potential to affect global climate by altering the ocean circulating patterns. The increased volume of water due to the ice melts will significantly affect global sea level [24]. Large amount of fresh water could be dumped into North Atlantic as a result of melting of arctic ice, disrupting the

ocean currents that enable warm Gulf stream in the north [25]. This could affect parts of EU and eastern US.

Shrinkage of the mountain glaciers have already affected 500 million people in Northern India, who rely on the glacial-fed Indus and Ganges rivers for irrigation and drinking. Shrinkage and retreating of glaciers is increasing the size and number of glacial lakes [26]. The melting of the glaciers have increased river run off, reducing the future availability of fresh water. Counting formation, merging, and expansion of glacial lakes to the stage of glacial outburst floods, 32 records of such events have been recorded in Nepal, Tibet Autonomous Region of China and Bhutan [27]. These could affect other parts of the world which rely on glacial fed rivers for the supply of fresh water.

Approximately 3344×10^{9} tons of organic carbon is contained within the permafrost worldwide [28]. Climate change can accelerate the degradation of the organic carbon by permafrost thawing, resulting in substantial amount of CH_4, release in the atmosphere, which will accelerate global warming of the planet.

It can be summarised that climate change would have irreversible changes to our planet. It would not only affect human beings but animal and plant life too. In addition to the obvious pollution issues, current energy production and consumption patterns would have economic and environmental repercussions.

Table 1.1 :Effects of global warming on ice melts around the world [29].

Name	Location	Measured loss
Arctic sea ice	Arctic ocean	Has shrunk by 6 percent since 1978, with a 14% loss of thicker, year-round ice. Has thinned by 40% in less than 30 years.
Greenland ice sheet	Greenland	Ice has thinned by more than a meter a year on its southern and eastern edges since 1993.
Columbia, Glacier	Alaska, United States	Has retreated nearly 13 kilometres since 1982. In 1999, retreat rate increased from 25 to 35 m/day.
Tien Shan Mountains	Central Asia	Twenty-two percent of glacial ice volume has disappeared in the past 40 years.
Antarctic Sea Ice	Southern Ocean	Ice to the west of the Antarctic Peninsula decreased by some 20 % between 1973 and 1993, and continues to decline.
Pine Island Glacier	West Antarctica	Grounding line (where glacier hits ocean and floats) retreated 1.2 km/y between 1992 and 1996. Ice thinned at a rate of 3.5 m/yr.
Dokriani Bamak Glacier	Himalayas, India	Retreated by 20 meters in 1998, compared with an average retreat of 16.5 m over the previous 5 years.

1.2 Energy from fossil fuels

The majority of world's energy requirement is fulfilled by means of burning non-renewable fossil fuels such as coal, oil and natural gas. Burning of these fossil fuels has created serious environmental degradation and ecological disturbance (caused by climate change and global warming). Global energy generation scenario is shown in Figure 1.5. Fossil fuel resources usage comprises of 87% of the total energy consumed today, while other sources of energy i.e. hydro, nuclear and renewable sources of energy comprise the rest 13%.

Coal accounts for the 28% of world's energy consumption. Coal is the primary means of generating power in most of the countries. World coal consumption increases on an average by 1.3 and 1.9% per year from 2010 to 2100 in OECD and non OECD countries respectively. Since 2000 to 2010 world coal consumption has increased by 59% mainly due to increased energy demand, by flourishing Chinese economy. In China, coal supplies 74% of the total energy usage [30]. Based on projections, China would consume 57% of the world's coal consumption by 2025.

Although major coal usage in China is associated with power generation, a substantial amount is also used in the production of pig iron and crude steel. In 2012, 717 and 658 million tonnes of crude steel and pig iron were produced [31]. These amounts of steel and pig iron manufacture would consume huge amount of the coal mined in China.

In addition to China and US, India is currently the third largest consumer of coal in the world. The power sector was the largest consumer of coal in India. In 2010 about 68% of the country coal produced was used in power generation, while the rest was used in industrial sector in production of iron and steel, and cement production [32].

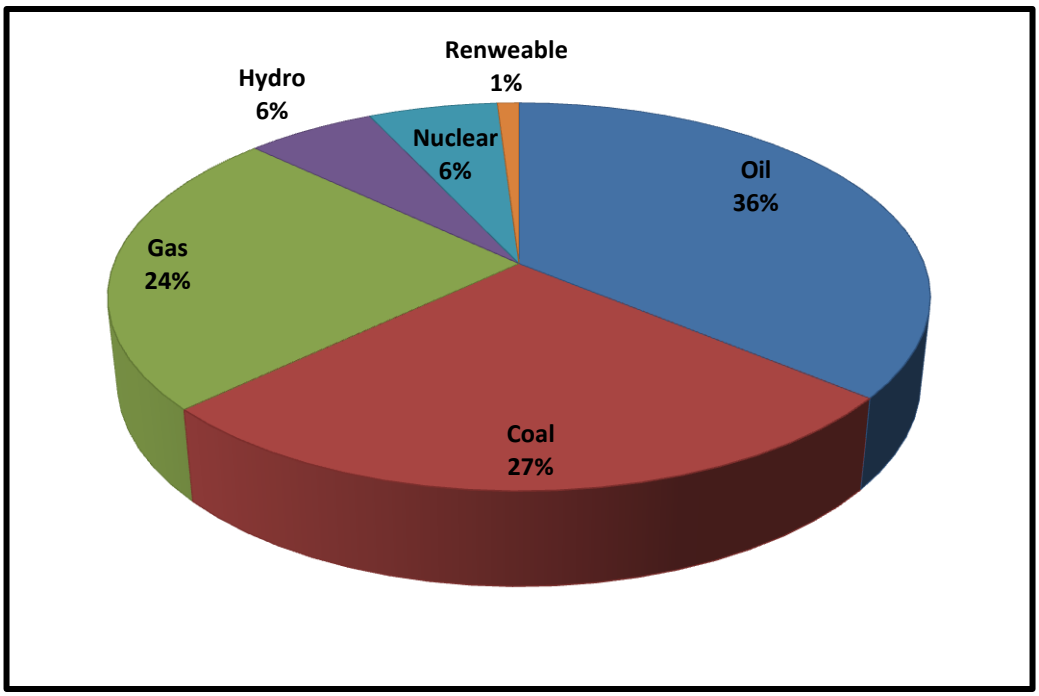

Figure 1.5: Global energy scenario[33].

In order to meet the growing demand of steel and cement to support growth, the Indian government plans to expand its steel production and cement production capacities. In 2012 approximately 78 million tonnes of steel was produced in India. An expansion from estimated 72.5 million tonnes in March 2014 to 304 million by 2020 has been planned [32, 34]. Likewise, India plans to double cement production capacity by 2020, increasing from 330 to 550 million tonnes [35]. As a result of these expansions, considerable amount of coal would be utilised. Other countries i.e. Indonesia, Taiwan, Malaysia, Thailand, and Vietnam are the major consumers of coal in non OECD countries in Asia.

Coal usage in OECD countries such as America and Europe is predicted to decline in the near future [32], but many European power generators have started using cheaper coal instead of natural gas [36]. On the other hand, coal usage from countries such as America has declined due to exploitation of shale gas. The affected economic condition in Europe has adversely affected the incentives provided to reduce carbon emissions. According to

Fabio Marchetti, head of government affairs in Brussels for the Italian energy company ENI, power plants operating on natural gas are going to be dismantled by 2015 and replaced by coal fired power plants. Other countries such as Australia, New Zealand, Latin American and African countries will continue to increase the use of coal in the future. The predicted enormous usage of coal in the growing economies such as China and India will be affected by government policies, infrastructure modernisation and development, availability and procurement of coal for power plants etc.

In addition to coal, natural gas is the second major fossil fuel used in power generation. As compared to coal, natural gas is a lot cleaner and is preferred by power companies, as a result of its low carbon intensity and lower capital investments for new plants. The natural gas is the fastest rising fossil fuel in the world. The consumption of natural gas will increase from 3.2×10^{12} in 2010 to 5.2×10^{12} cubic meters in 2040 [37]. Figure 1.7 shows the natural gas consumption in 2012 [38]. In this Figure, non OECD European countries are counted in Eurasia and similarly OECD Asian countries are classed in Asia and Oceania. America was the biggest consumer of natural gas, followed by Asia and Oceania, Eurasia and Europe.

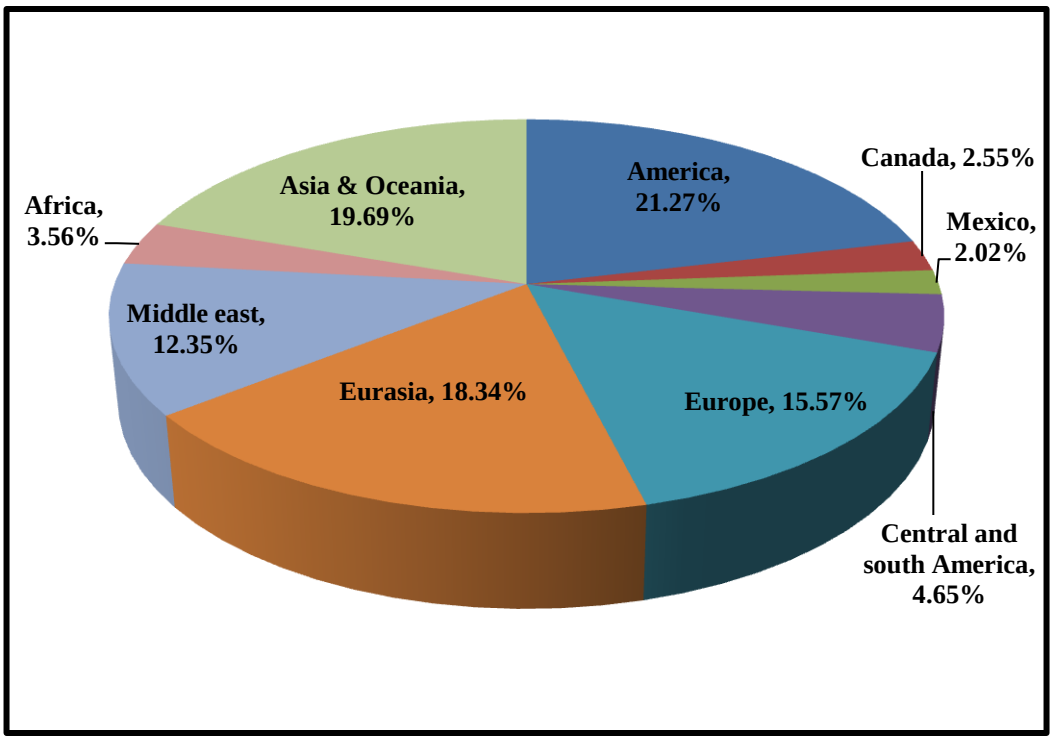

Figure 1.6: Dry natural gas consumption worldwide in 2012.

Natural gas consumption is projected to rise from 0.7 to 0.83×10^{12} and 0.52 to 0.7×10^{12} cubic meters from 2012 to 2040 [37], in America and Europe respectively. Apart from these countries Eurasia will also show an increased demand in natural consumption, increasing from 0.6 to 0.84 trillion cubic meters from 2012 to 2040 [37]. Among all the Eurasian countries Russia was the biggest consumer about 70% in 2012 [38]. The rate of consumption would rise moderately compared to others.

In the Asian countries China and Japan were the major natural gas consumers in 2012, accounting for 21 and 19.5% respectively of the Asian consumption [38]. Recent disasters in Japan have resulted in closures of many nuclear reactors resulting in increased natural gas consumption for power generation. On the other hand, natural gas usage in China will increase to meet the demands of the growing economy and reduce pollution due to heavy coal use. Among all the countries, the highest increase in natural gas consumption will be seen in China. Natural gas consumption will increase from 0.15×10^{12} cubic meters to 0.5×10^{12} cubic meters and decreasing to 0.35 by 2040 [37].

In Middle East, the consumption will increase by 0.3×10^{12} cubic meters from 2012 to 2040 [37, 38]. Like China, natural gas consumption in Africa will increase significantly, increasing from 0.12 to 0.24×10^{12} cubic meters from 2012 to 2040 [37, 38]. Growth in consumption of Central and South American countries would not be significant, increasing from 0.15 in 2012 to 0.17 by 2040 [37, 38]. Among the central and South American countries, Argentina, Brazil and Venezuela were the major consumers of natural gas [38].

Natural gas and coal are the fossil fuels which are associated mainly with power generation. The largest use of fossil fuels is in the transportation sector. America is the largest consumer of liquid fuels in the OECD countries. The slower economic growth along with stagnant or lower population growth would decline the use of liquid fuels in OECD countries. The share of non OECD countries to growth of liquid fuel consumption is largest. More than 70% growth in liquid fuel demand from 2010 to 2040 will be as a result of non OECD countries. Non OECD countries i.e. China and India are the major consumers of liquid fuels in the non OECD countries as result of strong economic growth and population increase. The Chinese consumption of liquid fuels is twice that of India's and will supersede America's consumption by 2035 [39]. In addition to China and India, increase in population and per capita income growth in the Middle East will also influence the consumption of liquid fuels. The higher consumption of liquids in the chemical sector will play a role in the consumption of liquids [39].

EIA has developed two scenarios to predict crude oil's price up to 2040 (Figure 1.8). Low oil prices case was formulated assuming low oil prices and liquid fuel demand, taking into account cheaper non OPEC liquid fuel supply. On the other hand, high price considers higher economic world economic growth and use of less abundant and costlier non OPEC liquid fuel supply. These cases took into account the following factors for predicting the prices.

1. The economics of petroleum liquids supply from non-OPEC countries

2. OPEC investment and production decisions
3. The economics of other non-petroleum liquids supply
4. World demand for petroleum and other liquids

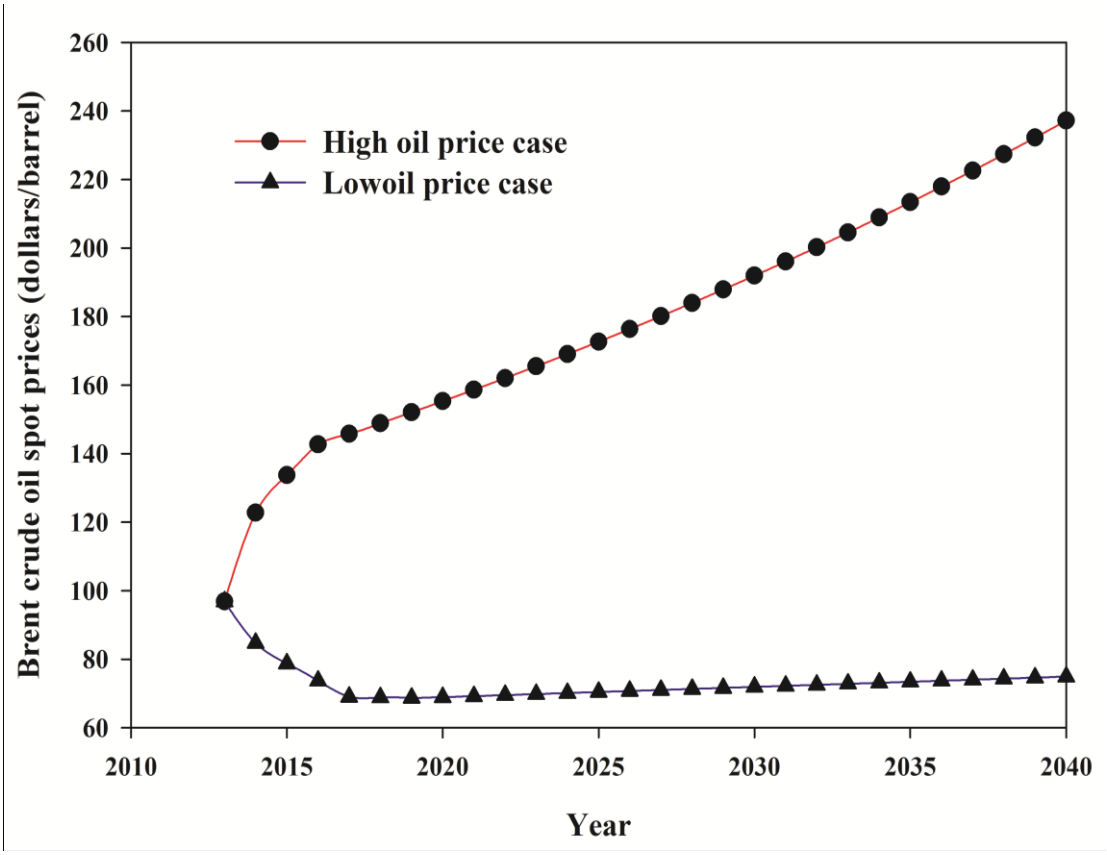

Figure 1.7: Predicted world oil prices in dollars per barrel [39].

As per the high oil price scenario, the price of crude oil is predicted to increase from 96$/barrel in 2013 to 237$/barrel in 2040. This can be reflected in increased consumption by growing economies of China and India. The scarcity of oil reserves in these countries makes them heavily reliant on oil imports from OPEC countries [40]. The Indian crude oil consumption is estimated to double from 2012 to 2040. EIA estimates that Chinese consumption will exhibit highest growth in demand from 2010 to 2040 (10 million barrels/ day) [39, 41]. India would be the second largest consumer predicting a growth of 5 million barrels/day from 2010 to 2040 [40, 42]. At the current rate of oil consumption,

based on conservative estimates, crude oil production in non OPEC countries is estimated to peak from 2020 and will decline after that.

It is can be summarised that fossil fuels are being consumed at much higher rates than being produced especially crude oil. It is estimated that world crude oil reserves will vanish at the rate of 4 billion tons a year, and at the rate of current consumption crude oil reserves will be exhausted by 2050 [43]. Although coal reserves are predicted to be available up to 2081 [44], usage of coal associated with power generation is a highly polluting affair and results in high level of CO_2 production. It is also a source of other highly toxic pollutants such as Hg, trace metals and nitrogen and sulphur oxides etc. Similarly coal production and processing has severe direct and indirect environmental effects. These reasons have promoted reduction of coal usage for power generation in many countries [45]. The increased natural gas production could be useful in filling the gap but these would only provide some breathing space up till 2060 [43]. Consequently a global energy crisis has forced the world in search of alternative energy sources.

1.3 Renewable and alternative energy

Energy crises and climate change has resulted in the exploration of various alternative energy sources. Renewable energy technologies make use of various natural phenomena to generate usable energy. Solar, wind, flowing water (hydro), plant growth (biomass), gravitational force (tidal) and geothermal are used to produce energy. These energy resources have a gained potential and could easily dominate the equivalent fossil energy resources. Despite many challenges, R&D in this field has progressed in the last few decades. Some of these resources are governed by factors such as accessibility, intermittent nature, and regional variations giving rise to technical and economical along with institutional challenges.

1.3.1 Solar energy

Solar energy can be applied on large scale in the countries with abundant sunshine for most of the part of the year. Presence of cloudy skies in countries such as UK restricts the use due to lower efficiency. It also requires large amount of land for capturing energy and the energy produced has to be stored for future use requiring large scale infrastructure. The cost of the cells used in the collectors is expensive. The energy produced has to be used in the same location where generated, restricting its distribution.

1.3.2 Wind

Generation location is also an important factor in case of wind energy. The areas having sufficient wind strength to rotate the wind turbine are less, which restrict their application to hilly and coastal areas of any countries. Countries with large flat ground and smaller coastline cannot make large use of wind energy. Power quality is affected by speed fluctuations due to air movement as a result of several climatological phenomena. The

intermittent power generation may lead to imbalance power demand, leading to adverse voltage variations [46]. Wind mill may also adversely affect wildlife and are known to be quite noisy, which again impairs their installations near residential areas.

1.3.3 Tidal

They can only be located in the countries with large coastline and availability of suitable generating sites. Like wind energy, tidal power generation will be affected by climatological factors such as high and low tide. Power could be generated only during high tide which accounts only for certain part of the day. This means, these forms of energy have to be associated with some form of energy storage installation for successful applications. Tidal energy output is patchy and variable, increase in variable generation increases the cyclic operation of the tidal generators, which would increase in wear and tear on the machines shortening of the life span of the units [47]. Substantial upfront investment is required for the construction of tidal energy infrastructure [48]. Recent research has shown that harnessing tidal energy may also affect residual and transitional oceanic currents over vast distances, indirectly affecting sediment transport rates, pollutant dispersion and nutrient concentrations, thus affecting marine environment [49].

1.3.4 Geothermal

Like solar, tidal and wind energy, geothermal energy is also restricted on the basis of site location. As this form of energy is not widely used, it lacks the availability of infrastructure and staff for the installation of these plants. It also has high initial cost of installation affecting the cost of power produced. The location of the sites can also affect the construction and exploitation of the energy source. Toxic and harmful gases can be released from geothermal sites. Lastly energy generated cannot be transported due to the location of the sites.

1.3.5 Biomass

Biomass as a renewable energy source, is derived from biological material obtained from living organism i.e. plants or plant derived materials. The European Commission specified that there are large varieties of biomass available such as by-products, agricultural, forestry residue, related industries, as well as the non-fossil, biodegradable parts of industry and municipal solid waste (MSW) [50]. Biomass and biomass energy systems are suggested to become one of the important contributors to sustainable energy systems and sustainable development in developed as well as developing countries in near future [51]. Table 1.2 shows biomass resources categorised based on their origin.

Biomass can be the most suitable form of renewable energy source among the various renewable sources due to its various advantages. Biomass can be produced abundantly in most part of the world. Continuous supply can be assured based on constant production. It is important to note that the annual production may vary, depending on the type of biomass grown. It is relatively cheaper to produce and some types of the biomass obtained as by-products are almost free. According to the European Environmental Agency (EEA), 13% of the total energy consumption by 2020, would be provided by biomass [52].

Biomass can also be directly used in the existing power generating infrastructure. Specially grown energy crops and other kinds of biomass can be co-fired with coal to generate electricity. The net energy available from biomass combustion ranges from about 8 MJ/kg for green wood, to 20 MJ/kg for dry plant matter to 55 MJ/kg for CH_4, as compared to 27 MJ/kg for coal [53]. Biomass contains fewer amounts of sulphur and nitrogen in comparison to coal, which in turns reduces the formation of toxic and GHG such as SO_2 and NOx.

Table 1.2: Biomass resources categorised base on their origin [54].

Categories	Source	Representative material
Productive	Terrestrial	
	Carbohydrate	Sugar cane, corn, sweet sorghum
	Starch	Maize, cassava and sweet potato
	Cellulose	Tropical grasses, poplar and sycamore
	Hydrocarbon	Eucalyptus, green coral
	Grease	Sunflower, rapeseed, palm and other oil producing plants
Unused biomass	Aquatic	
	Fresh water	Water hyacinth
	Ocean	Large Kelp
	Micro-organisms	Green algae and photosynthetic bacteria
	Agriculture, forestry and fishery residues	Wheat straw, rice straw and husk Vegetable and processing residues
	Animal husbandry	Animal manure
		Farm residues
	Forestry	Secondary forest
		Woodland remnants
		Crippled materials in plants
	Waste	
	Fisheries	Jettisoned and dead fish
	Municipal waste	Municipal pulp sludge and sewage
	Garbage	Family garbage

In addition to this, biomass contains less amount of ash and higher amount of volatile matter and fixed carbon in comparison to coal. As result biomass can be ignited and gasified or oxidised easily [55]. It also contains oxygen which is non-existent in coal. These properties result in effective combustion of biomass compared to coal. But the higher content of oxygen also reduces the calorific value of biomass. The cost of electricity generated using biomass is often competitive with fossil fuel based power. Figure 1.9 shows the cost effectiveness of electricity generated from various renewable sources. In this Figure, large coloured bars represent the typical levelised cost of electricity (LCOE) range by technology and the coloured horizontal lines the weighted average LCOE by country/region if enough individual project data are available. In the case of biomass, electricity can be produced very cheaply, with prices ranging from USD 0.06/kWh and 0.02/kWh in OCED and developing countries respectively. But the cost will depend on onsite availability of low cost biomass feedstocks.

The use of biomass could augment and complement the current shortage of fossil fuel. It will also help reduce atmospheric concentration of CO_2, as CO_2 produced from biomass can be counter balanced by the amount absorbed during its growth. Cultivation and burning of *Miscanthus* (an energy crop) was predicted to reduce 9% of the total European carbon emissions in 1990 [56]. The use of waste biomass will also help mitigate the CH_4 generated from decaying organic matter. By making use of the sugar cane bagasse for electricity production, more than 100 % reduction in GHG emissions compared to gasoline/diesel, was reported with sugar cane ethanol [57].

Biomass can be converted from one form to another. For e.g. agricultural residue such as wheat straw or rice straw can be converted to biogas a mixture of (CH_4 and CO_2). This in turn could help reduce landfills and increase availability of land for other uses. Likewise liquid fuels such as biodiesel and bio ethanol can also be produced from sugar containing biomass [58, 59] by fermentation processes. Next generation biofuels such as butanol can also be produced from these biomass sources [60]. Complex fuels such as bio-oil can also be generated by pyrolysis of biomass [61].

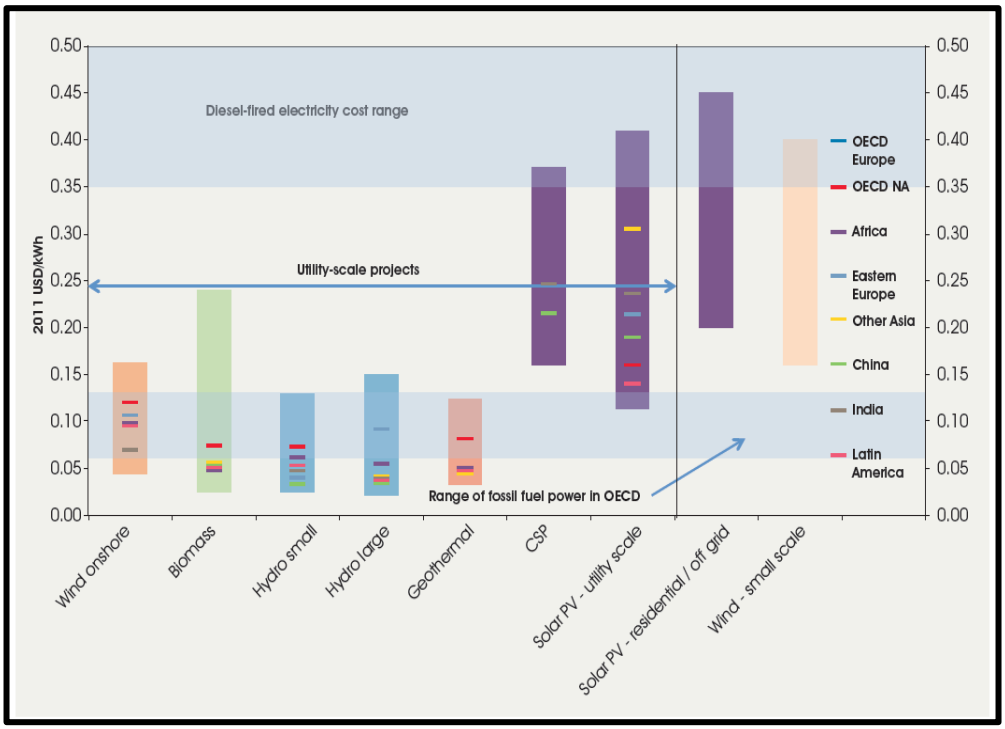

Figure 1.8: LCOE and weighted averages for renewable generation technologies, 2012 [62].

Use of non-food based biomass known as energy crops, can help utilise unused land. Energy crops can be grown in arid or highly erosive land, preventing the utilisation of fertile land allocated for food production [55, 63]. Switch grass is one of the herbaceous perennial energy crops which can be utilised in power generation. This kind of crops offer variety of advantages such as sustainable agriculture as a result of crop diversification, reduction in soil erosion [64] and lastly they also help in improving quality of water [65]. Non-food oil crops such as jatropha, tobacco, karanja, rice bran, rubber seed, and Mahua along with many others can be used in production of oil which could be converted to biofuel [43]. The bio residue left behind after oil extraction could be used as animal feed or could be used for the generation of biogas [66, 67].

The wide variety of biomass available can meet the requirements of the different conversion processes such as combustion, gasification, pyrolysis, fermentation or mechanical extraction of oils. Fuel wood, forestry residues, bagasse and MSW can be directly used in conventional power plants for generating electricity via combustion. Wood is also preferred for pyrolysis and gasification processes for the production of liquid (bio oil) and gaseous fuels (bio syn gas). Energy crops such as switch grass are mainly grown with the intention of utilisation in ethanol production via fermentation for blending with gasoline. Sugar cane is also grown for ethanol production using the same processes. Soya bean, rapeseed corn, palm and canola are grown for oil extraction for production of biodiesel. Agricultural residues, municipal solid waste (MSW), and animal waste are preferred feedstocks for anaerobic digestion to produce biogas.

In addition to the above advantages, biomass will play an important role in rural development by developing an integrated sustainable and flexible system of food, energy and employment, mainly in developing countries such as India. In rural India, fire wood and chips have been the main source of energy for cooking [68]. To promote biomass use in other aspects of day-to-day life, several projects were implemented for utilisation of biomass for energy production [69]. For e.g. animal dung was used for generating biogas a clean fuel for domestic and water heating in Tunkur district, Karnataka, India. Production of non-edible oils such as Pongamia seed oil was collected and used for generating power for illumination and pumping drinking and irrigation water in Kaggenahalli and surrounding villages, Karnataka, India. Biogas generation and utilisation for electricity production for pumping drinking water were implemented in few villages in the Hassan district, Karnataka, India. A Biomass gasifier running on wood chips for generating electricity for pumping household water was installed in the Tunkur district. Use of biogas as a cooking fuel is very popular in rural China and 4.54×10^5 household-sized biogas digesters, 5 medium and large scale biogas projects were installed in the Gansu province of China alone, with 87% of the facilities operational and well maintained up till 2012 [70]. These programs have helped improve the energy independence of the rural population and improved the quality of life in these parts of the world.

Price and availability of renewable resources would be an important factor in selections of the source. Global application of certain forms of renewable energy is restricted due specific requirements. Renewable energy sources such as wind, tidal, geothermal are often located in remote locations which hamper their ability to transfer the energy from the generation to the utilisation locations. Also, the energy generation from sources such as wind, solar and tidal are governed by metrological conditions resulting in intermittent power production. Considering only on availability basis, biomass is far abundant anywhere in the world than other sources. One can say that the power generated using wind, tidal or solar is free, but the infrastructure cost is higher. Cost of biomass is relatively very cheap and is almost free. Biomass can be used in the existing power generation infrastructure, giving it an advantage over others.

Biomass energy can be converted from one form to another and it is easily adapted to end use application. For example, solid biomass can be adopted for power generation, or can be converted to gases which can also be used for power generation or can be fed to gas grids for domestic applications. Liquid biofuels such as ethanol, butanol and biodiesel are produced from biomass and are used as transportation fuels. It can be concluded, that biomass is a versatile renewable energy source with significant potential for securing independence from a fossil based economy.

1.4 Hydrogen energy and fuel cells

As seen above, the energy demand of the world is going to increase. The highest requirement of energy demand would be in the form of electricity. Generation of clean and sustainable power is the major concern for today's world, as the current methods of power generation i.e. combustion of fossil fuels is unsustainable and highly polluting. H_2 as an energy carrier has been widely researched over the world for power generation and propulsion applications. \

1.4.1 Fuel cells

One of the widely studied methods of utilisation of H_2 is fuel cells [71, 72]. Technically, fuel cells can be described as electrochemical energy conversion devices that convert H_2 and O_2 into H_2O and in the process produce electricity [73]. Their mode of operation is similar to that of a battery. Unlike a battery, a fuel cell does not store energy and instead converts chemical energy to electrical energy, without an intermediate conversion steps into heat and then mechanical power, which is required in combustion technologies [74]. Construction of a polymer electrolyte fuel cell is shown in Figure 1.10.

A fuel cell consists of an anode, cathode and an electrolyte. The electrolyte is in intimate contact with the porous anode and cathode. Fuel which is H_2 or a mixture of H_2 rich gas is introduced at the anode surface, and oxidant is fed at cathode. They react electrochemically in the three-phase-boundary region established at the gas-electrolyte-electrode interface. In a proton exchange membrane fuel cell (PEMFC), H_2 gas splits at the anode to form two positively charged protons by releasing two negative electrons, the protons travels to the cathode through the electrolyte and react with oxygen to form water, and completing the circuit.

There are 5 basic types of fuel cells under investigations, classified on the basis of the type of electrolyte used. Table 1.3 and 1.4 summarises the construction and operation parameters of different types of fuel cells.

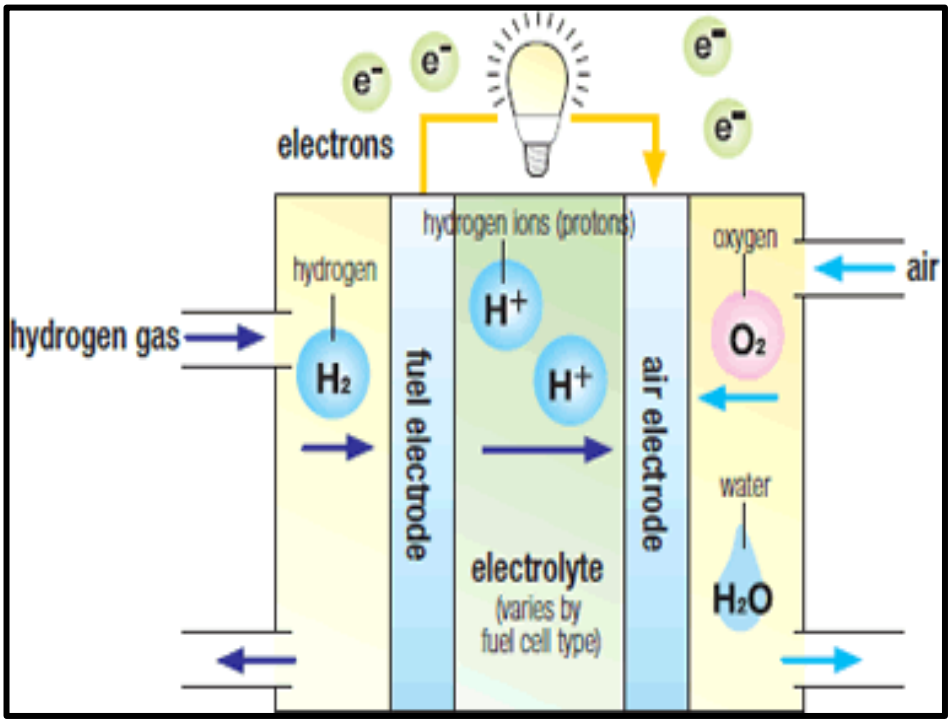

Figure 1.9: Schematic representation of a polymer electrolyte membrane fuel cell [75].

Efficiency exhibited by fuel cells is twice that observed in internal combustion engines and turbines, making them one of the promising energy conversion devices [76]. They can be used in association with other devices such as turbines further increasing their efficiency up to ~70% [77]. PEMFC and solid oxide fuel cells (SOFC) are the two most promising fuel cells. The PEMFC has a polymer based electrolyte such Nafion which provides excellent resistance to gas crossover. The PEMFC's low operating temperature allows rapid start-up and, with the absence of corrosive cell constituents, the use of the exotic materials required in other fuel cell types, both in stack construction and in the BoP (Balance of plant) is not required [72]. Another advantage compared to alkaline fuel cell (AFC), molten carbonate fuel cell (MCFC) and phosphoric acid fuel cell (PAFC)

includes significantly reduced corrosion problems due to the limited operating temperature and the use of a solid electrolyte.

The other big advantage of PEMFC over other fuel cells is its size, weight and compact nature, making it ideal in the cases where size is key parameter for the application. The high power density of these fuel cells makes them ideal for applications in laptops, automotive power, computers and mobile phones. In recent years some of the major drawbacks such as life of the fuel cell and cost of the power generated have been resolved, but further cost improvements are necessary in order to compete with the commercialised internal combustion technologies [78]. One of the key aspects of PEMFC, which need addressing, is its tolerance to impurities in fuel and oxidant, as these affect the performance and expedite degradation. PEMFC fuel cells are extremely vulnerable to CO in the fuel, which poisons the platinum catalysts.

On the other hand, SOFC's are versatile fuel cells with high electrical efficiency of 55% [79]. As a result of their high operating temperatures, SOFCs can be effectively combined with other new energy technologies such as micro turbines to enable the development of electricity generation products with ~70% efficiency [77]. They can also be used in combined heat and power systems (CHP) to provide electricity and heat for applications in cold areas of the world. SOFCs are made from commonly available ceramic materials and have no moving parts or corrosive liquid electrolytes. Therefore they should lead to highly reliable electricity generation systems which require low maintenance [71, 79-81]. The manufacturing process for SOFCs is based on well-known equipment that is widely available and well proven in the manufacture of electronic ceramic components. SOFCs do not require expensive catalysts for their operation, and they can operate directly on CH_4 or natural gas, which avoids expensive and difficult fuel reforming to generate pure H_2.

Table 1.3: Construction and operation summary of various fuel cells [82].

FC	PEMFC	AFC	PAFC	MCFC	SOFC
Electrolyte	Hydrated Polymeric Ion Exchange Membranes.	Mobilized or immobilised KOH in asbestos matrix.	Immobilised liquid H_3PO_4 in SiC.	Immobilised liquid molten carbonate in $LiAlO_2$	Ceramics
Electrodes	Carbon	Transition metals	Carbon	Nickel and Nickel Oxide	Perovskite and perovskite / metal cermet
Catalyst	Platinum	Platinum	Platinum	Electrode Material	Electrode Material
Interconnect	Carbon or Metal	Metal	Graphite	Stainless steel or Nickel	Nickel, ceramic, or steel
Operating Temp	40 – 80°C	65°C – 220 °C	205°C	650°C	600-1000°C
Charge Carrier	H^+	OH^-	H^+	$CO3^=$	$O^=$
External reformer use	Yes	Yes	Yes	No, for some fuels	No, for some fuels and cell designs
External shift conversion	Yes, plus purification to remove CO traces	Yes, plus purification to remove CO& CO_2	Yes	No	No
Prime cell components	Carbon Based	Carbon based	Graphite based	Stainless Based	Ceramic
Water management	Evaporative	Evaporative	Evaporative	Gaseous Product	Gaseous Product
Product heat management	Process Gas + Liquid Cooling Medium	Process Gas + Electrolyte Circulation	Process Gas + Electrolyte Circulation	Internal Reforming + Process Gas	Internal Reforming + Process Gas

Where, FC- fuel cell, PEMFC- Polymer electrolyte membrane fuel cell, AFC- Alkaline fuel cell, PAFC- Phosphoric acid fuel cell, MCFC- Molten carbonates fuel cell, Temp- Temperature and SOFC- Solid oxide fuel cell.

Table 1.4: Performance of comparison of various fuel cells [71, 83].

FC	PMFC	AFC	PAFC	MCFC	SOFC
SO	1-250 KW	10-100 KW	50KW-1MW	1KW-1MW	1 KW-3MW
Eff Elc	53-58% 25-35%	60%	32-38%	45-47%	35-43%
Appl	BPW, PPW and TP	Military and space	DG,	Electric utility, large DG	MPW, electric utility & large scale DG
Adv	Solid Electrolyte reduces corrosion. quick start	Cathode reactions are faster. Higher performance	Increased tolerance to impurities in H_2. Higher overall efficiency with CHP's	High efficiency, fuel flexibility, can use variety of catalysts, suitable for CHP's.	High efficiency, fuel &catalyst flexibility, solid electrolyte reduces electrolyte management problems, suitable for CHP's hybrid GT cycle
Disadv	Requires expensive catalyst, highly sensitive to impurities in fuel, low Temp waste heat not suitable for CHP's	Expensive removal of CO_2 from air & fuel is required to prevent electrolyte degradation.	Requires expensive catalyst, low current &power produced, large size & weight.	Temp speeds corrosion & break down of cell components, complex electrolyte mgmt & slow start up.	Temp speeds corrosion & break down of cell components, slow start up & brittleness of ceramic electrolyte with cycling.

Where, Adv- Advantages, Appl- Applications, BPW- Backup power CHP- Combined heat and power, DG- Distributed generation, Disadv- Disadvantages, Eff- Efficiency, Elc-Electrical, FC- Fuel cell, PPW- Portable power, Temp- Temperature, TP- Transportation and SO- System output.

The high operation temperature of the SOFC also has its drawbacks. There are thermal expansion mismatches among materials, and sealing between cells is difficult in the flat plate configurations. The high operating temperature places severe constraints on materials selection and results in difficult fabrication processes. However, the commercialisation of SOFCs has not been fully demonstrated due to its initial cost of fabrication, degradation in reliability and durability during its prolonged operation. All these problems have originated from the high temperature operation of the SOFCs, which is higher than 900°C. Recent R&D has tended to focus on reduced-temperature SOFCs because of their cost advantages (since they use low cost metallic interconnect plates) and their thermal cycle abilities [84].

1.4.2 Hydrogen energy road map

Figure 1.11 shows the European H_2 energy road map for 2050. The road map is a program for bridging the technological gaps in different areas of H_2 energy which includes production, storage, transportation and delivery, applications, safety. Following are the key challenges which need to be tackled for successful implementation of H_2 economy.

- Reducing cost of production to conventional fuels such as gasoline.
- Generation of renewable and sustainable CO_2 free H_2.
- Construction of efficient, reliable and nationally linked H_2 delivery and refuelling infrastructure.
- Development of feasible H_2 storage for automotive and stationary applications.
- Considerable decrease in cost and significant increase in life of fuel cells**.**

The use and handling of pure H_2 for fuel cell application is risky, due to the formation of explosive mixtures of H_2 and air which can cause serious damage especially during

accidents. Further H_2 has to be liquefied and stored at high pressures which also introduce another risk factor. H_2 is a fuel that has a high gravimetric energy density but also a low volumetric energy density, in both gaseous and liquid states. As a result to store same energy content, larger tanks are required for H_2 as compared to other fuels. Tank size has been a problem for car integration. This storage technique requires a high amount of energy and is therefore a source of considerable environmental impact. New storage methods such as metal hydrides are being explored; they are currently limited by the weight of the system. According to US department of Energy, both cryogenic and high-pressure H_2 storage options can meet the mid-term targets [85]. Safer, efficient, compact systems, with low weights are needed for automotive as well as stationary applications. Along with fuelling stations, H_2 delivery and distribution network (including H_2 pipelines) will need to be developed for the successful implementation of a H_2 economy to replace the current fossil fuel based economy.

Currently most of the H_2 produced comes from fossil fuels such as natural gas, oil and coal. The processes are energy intensive and consume large amount of energy producing CO_2 as a by-product. H_2 production technologies from fossil fuels (steam reforming, partial oxidation, and gasification) are mature and widely used, although some of them need to be optimised for large-scale production from the point of view of energy efficiency, environmental impact, safety and above all, costs. The release of CO_2 can be managed by use of carbon capture and storage (CCS), which involves storing of CO_2 in depleted natural gas and oil wells or in geological formations. However the CCS technology is not commercial proven yet and there are too many unknowns. These technologies need to be connected to the production infrastructure in order to reduce the environmental impacts. New processes such as electrolysis, photo-electrolysis, high-temperature decomposition and photo-biological water splitting are being evaluated. Production of H_2 and pure carbon via high temperature pyrolysis of hydrocarbons, biomass and municipal sewage waste are also under investigations. Fossil fuel generated H_2 would be the primary source of H_2 up to 2020 [85]. The new technologies which are in development stages could become available during the transitory phase. H_2 based on

renewable resources will become commercially viable in the long run and will replace the fossil generated H_2 (natural gas or coal).

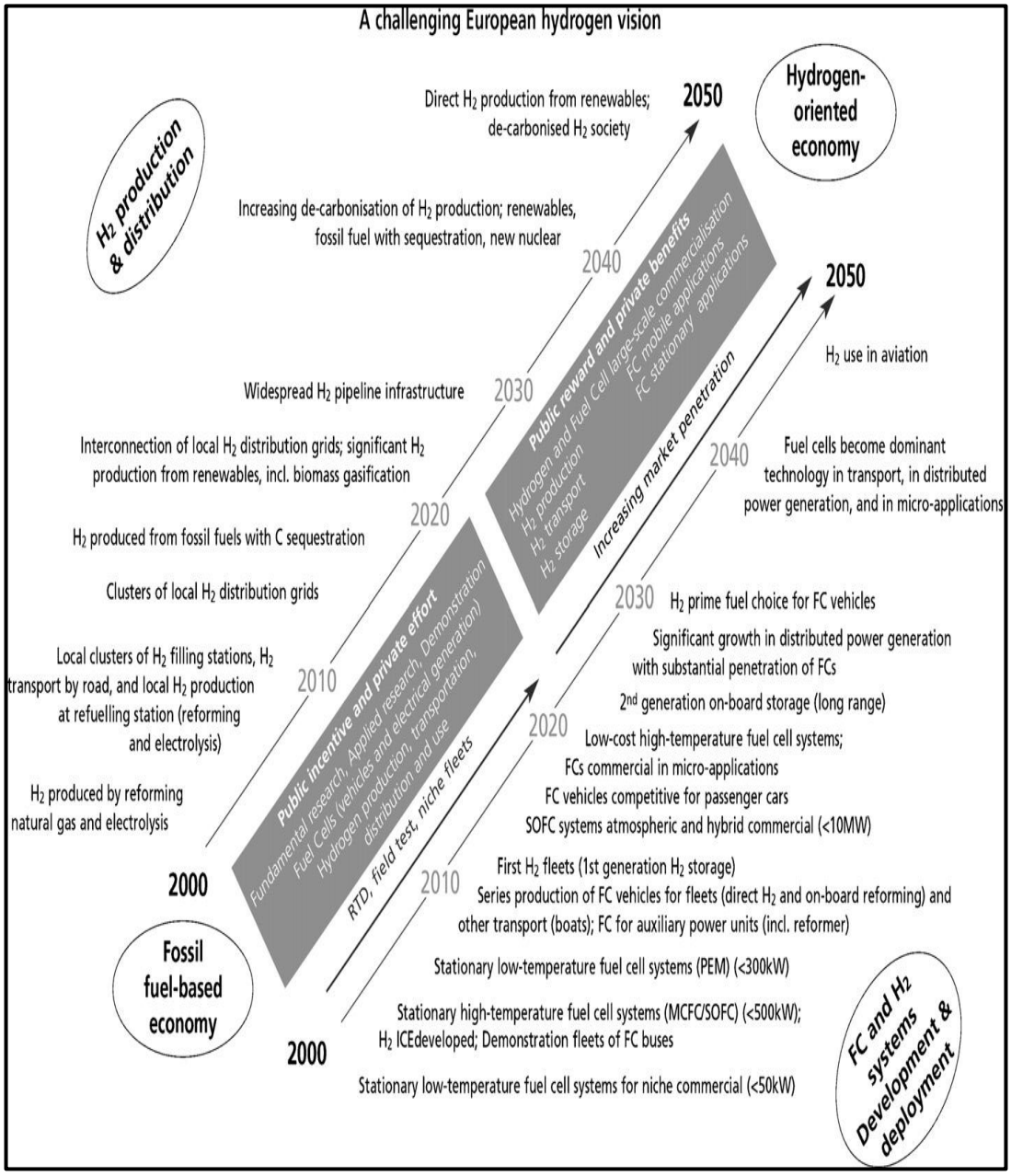

Figure 1.10: European H_2 energy road map [85].

1.4.3 Hydrogen properties and safety

The element H_2 is abundantly available in the nature and is a building block of the universe. Following are some of the advantages of H_2 gas as a fuel.

- H_2 is the lightest element occurring in nature, the H_2 molecule contains a large amount of energy in its chemical bond.
- Combustion of H_2 generates pure water and no harmful greenhouse gases such as CO_2.
- It can be generated from both renewable (solar, wind, geothermal and biomass) and non-renewable sources (coal, natural gas and nuclear).
- H_2 gas is nontoxic, which cannot be said in case of other fuels such as gasoline or coal. Table 1.5 shows some properties of H_2 gas in comparison to other fuels**.**

Properties of H_2 are crucial in determining its usage in the H_2 economy. The boiling point of H_2 is -252.7°C. Being in gaseous form no energy can be lost in vaporisation, if it is utilised in internal combustion engines. Lowest specific heat among the fuels, suggest comparatively less amount of energy would be required if preheating operations are involved in the power generation processes. Heat of combustion for H_2 was highest compared to other fuels, and is clean only producing H_2O. One might assume that H_2 would be a dangerous fuel compared to conventional ones such as gasoline. It can be seen that gasoline and alcohols such as ethanol would ignite quicker than H_2. H_2 is stable and coexists harmlessly with free oxygen (O_2) until an input of energy drives the exothermic reaction that forms H_2O [86]. It is much lighter than other fuels as a result of its low density, dispersing very quickly, which could prevent formation of explosive mixtures in ventilated areas. It also has very low radiative energy in comparison to CH_4 and as a result, at fixed distance away from H_2 fires, temperature will be lower indicating cooler region as compared to that at the centre [87]. Nevertheless care must be taken while handling and using H_2.

Table 1.5: Properties of H_2 and some other fossil fuels [72].

Properties	H_2	CH_4	NH_3	CH_3OH	C_2H_5OH	Gasoline
Molecular weight kg/kmol	2.01	16.04	17.03	32.04	46.07	114.2
Freezing point (°C)	-259.2	-182.5	-77.7	-98.8	-114.1	-56.8
Boiling point (°C)	-252.7	-161.5	-33.4	64.7	78.3	125.7
Enthalpy of combustion at 25°C (MJ/kg)	141.80	55.50	22.5	22.7	29.7	47.30
Heat of vaporisation (kJ/kg)	445.6	510	1371	1129	839.3	368.1
Liquid density (kg/m^3)	77	425	674	786	789	702
Specific heat at STP ($kJ\ kg^{-1}\ K^{-1}$)	14..3	2.22	2.2	2.56	2.72	2.22
Flammability limit in air (%)	4-77	4-16	5-28	6-36	4-10	1-6
Autoignition temperature (°C)	571	632	651	464	423	220

2. Use of vegetable oil as diesel fuel

This section examines the use of edible and non-edible vegetable oils and their blends as a diesel engine fuel.

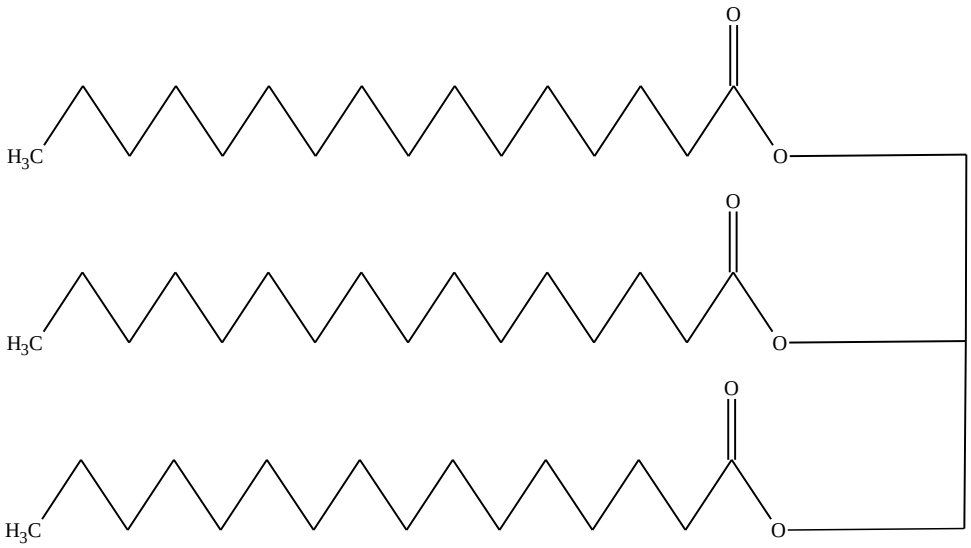

Figure 2.1: Molecular structure of triglyceride molecule.

Figure 2.1 shows a molecular structure of triglyceride molecule. A triglyceride (TG) is also known as a triacylglycerol (TAG), or triacylglyceride. It is an ester derived using a glycerol backbone ($C_3H_8O_3$) and three fatty acids. The free fatty acids can be saturated or unsaturated types. In saturated free fatty acids, H atoms are bonded with C atoms in all the available places, while unsaturated free fatty acids have smaller amount of H atoms as a result of (C=C) double bonds reducing the position where H atoms can bond with C atoms. Other C hydrogen bonds such as =CH-CH=, -CH_2-CH_2- exist in unsaturated free fatty acids. Depending on the source of the triglycerides, animal or vegetable the fatty acid composition vary accordingly as shown in Table 2.1.

The use of vegetable oil as fuel is known to man since end of 18th century. Peanut oil was used for the first time in Augsburg, Germany on August 10, 1893 by Rudolf Diesel to power a 10 feet iron cylinder with a flywheel at its base [88]. In the year 1900 Rudolph Diesel won the highest prize at the world fair held in Paris for his Diesel Engine running on peanut oil. In the 1920s diesel engine manufacturers modified their engines to run on petroleum diesel rather than vegetable oil due to the lower viscosity of the former as well as higher availability and cheaper cost.

Vegetable oil received importance as an emergency fuel during World War II. Countries such as Brazil curtailed the export of cotton seed oil in order to substitute petroleum based diesel [89]. China produced kerosene and gasoline by cracking of Tung oil to be used as fuel [90]. Similarly use of vegetable oil as a substitute diesel fuel was investigated in India during World War II, but it suffered the same fate when the scarcity of the cheaper diesel fuel decreased [89]. Similar attempts to explore the utilization of vegetable oil as diesel fuel were made by Argentina, France, Italy, Japan and Portugal during World War II. Rising prices of petroleum fuels and fuel shortage during the war in United States of America led to investigation of cotton seed and corn oil and its diesel blends to be used as diesel fuel (Ohio State University, (Columbus, USA) [89]. The history of investigation of vegetable oil and other origin oils such as fish oil, cotton seed oil and tallow as diesel fuel has been clearly described in "The Biodiesel Handbook" [90]. According to the authors, in most of the investigations reported, environmental concern was not the primary objective, since no emission studies were conducted. The major focus of the research was investigation of these oils as diesel fuel substitute. Similarly the effects of use of these oils on the life and long term performance were not documented. Jones and Peterson [91] documented literature on use of unmodified vegetable oil as a diesel fuel extender from 1942 to 2000. The authors concluded that short term evaluations of substitution of diesel with any percentage of vegetable oil were successful, but long term evaluations of blends with higher amount of vegetable oil in the blends led to engine damage or created maintenance problems.

2.1 Demerits of vegetable oil as fuel

In recent years energy security and environmental concerns have become a driving force to promote the utilization of vegetable oil- based diesel fuels. As mentioned above raw vegetable and other oils have been shown to work as a fuel for diesel engines since historic times, they exhibit various disadvantages. Raw or refined vegetable oil, or recycled greases have significantly different composition and their properties making them acceptable for use in modern diesel engines. Raw vegetable oil and fats have higher viscosity, and lower volatility fats have been shown to cause problems in a number of areas [92]. Higher viscosity and lower volatility have shown to reduce the brake thermal efficiency of vegetable oil fuelled engine compared to diesel engine resulting in higher HC and CO emissions [93, 94]. The other draw backs are listed below

- piston ring sticking
- injector and combustion chamber deposits.
- fuel system deposits.
- reduced power
- reduced fuel economy and increased exhaust emissions.

Use of unprocessed oils or fats as neat fuels or blending stock lead to excessive fuel condensation and corresponding dilution of the engine's lubricating oil that may result in sludge formation [95]. Any or all of these conditions may result in reduced engine life, increased maintenance costs, or catastrophic engine failure. The significantly higher viscosity of raw vegetable oils (27 - 54 mm^2/s) compared to petroleum diesel fuel (2.6 mm^2/s) has shown to alter fuel injector spray patterns and spray duration, adds stress on fuel injection systems, and results in incomplete combustion and high dilution of the engine lubricating oil [96]. Changes in the fuel injector spray patterns, duration, etc. results in poor engine performance and high emissions levels, caused by ineffective combustion processes. Fuel dilution of engine lubricating oil increases as a result of incomplete combustion leading to sludge development [97, 98]. Nwafor et al. [99, 100] reported that low cetane number of vegetable oil resulted in knocking in diesel engine at

low load and cylinder temperature. Undesirable deposits on pistons, piston rings, fuel injectors, valves occur as result of polymerization of glycerides in raw vegetable oils and animal fats during the combustion processes [95, 101, 102]. Table 2.2 summaries the effects of vegetable oil utilization in a diesel engine. It can be clearly seen that non modified or raw vegetable oil seriously affect the performance of diesel engine in both long and short term use.

Table 2.1: Fatty acid composition (wt %) observed in edible, non-edible oils and animal fat [103-105].

	Fatty acid (wt %)												
	C8:0	**C10:0**	**C12:0**	**C14:0**	**C16:0**	**C18:0**	**C18:1**	**C18:2**	**C18:3**	**C20:0**	**C22:0**	**C22:1**	**C24:0**
Name													
Beef tallow	0	0.1	0.1	3.3	25.2	19.2	48.9	2.7	0.5	-	-	-	-
Butter fat	5.5	3	3.6	11.6	33.4	11.4	27.8	3.1	0.6				
Canola	0	0	0	0.1	3.9	3.1	60.2	21.1	11.1	0.5			
Coconut	8.3	6	46.7	18.3	9.2	2.9	6.9	1.7					
Corn					9.9	3.1	29.1	56.8	1.1				
Cotton seed				0.8	22.9	3.1	18.5	54.2	0.5				
Grape seed					8	4	15	73					
H.O safflower				0.34	5.46	1.75	79.36	12.86		0.23			
Jatropha					14.6	6.8	38.6	36	0.2	0.2	3.6		
Karanja					11.65	7.50	57.32	16.64			1.35	4.45	1.09
Lard		0.1	0.1	1.4	25.5	15.8	47.1	8.9	1.1				
Linseed					4.92	2.41	19.7	18.03	54.94				
Mahua			0.14		21.36	18.97	38.98	19.47	0.16				
Neem				0.26	15	20.6	43.9	17.9	0.4	1.6	0.3		0.3
Olive							19.7	18.03	54				
Palm	0.1	0.1	0.9	1.3	43.9	4.9	39	9.5	0.5				
Rapeseed					2.7	2.8	21.9	13.1	8.6	50.9			
Soybean			0.1	10.3		4.7	22.5	54.1	8.3				
Sunola					3	4.4	88.2	4.3	0.1				

Table 2.2: Long term and short term problems associated with use of vegetable oil as a diesel engine fuel [95].

Sr No	Problem	Nature	Probable cause
1	Cold weather starting	Short term	High viscosity, low flash point and low cetane number
2	Plugging and gumming of filter, lines and injectors	Short term	Natural gums (phosphatides) in vegetable oil. Ash.
3	Engine Knocking	Short term	Very low cetane of some oils. Improper injection timing.
4	Coking of injectors and C deposits on piston and head of engine	Long term	High viscosity of vegetable oil, incomplete combustion of fuel. Poor combustion at part load.
5	Excessive engine wear	Long term	Possibly free fatty acids in vegetable oil. Dilution of engine lubricating oil due to blow-by of vegetable oil.
6	Failure of engine lubricating oil due to polymerization	Long term	Collection of poly-unsaturated vegetable oil blow-by in crank-case to the point where polymerization occurs.

3. Biodiesel: An alternative diesel fuel

As discussed in the previous chapter, the use of vegetable oil as diesel fuel is restricted by the viscosity of the oil or its blends. Several attempts to lower the viscosity by increasing the temperature of the vegetable oil [99] or its blends have been investigated widely [106-109]. Some of the investigations reported negative effect of the preheating of the oils. According to Agarwal and Rajamanoharan [107] preheated and cold Karanja oil showed similar CO emissions, smoke opacity and hydrocarbon emissions. Blends with concentration of 50 (v/v) % could be used directly with or without preheating, but CO, hydrocarbon and smoke emissions were shown to be higher for these blends, questioning their use as blends.

A different approach to reduce the viscosity of the vegetable oil for use in diesel engine was proposed in 1937 by G. Chavanne [110] from the University of Brussels who patented a process called transesterification of vegetable oil. The inventor used ethanol (C_2H_5OH) in order to separate the fatty acids from the glycerol backbone by replacing it with shorter chain linear alcohols. The term biodiesel was used for the first time then to define the products obtained from the process. Biodiesel i.e. fatty acid methyl esters (FAME) are defined as monoalkyl esters of fatty acids.

In 1977, the first patent for industrial process of biodiesel manufacture was applied by Expedito Parente, a Brazilian scientist, with research on biodiesel production from sunflower oil commencing in 1979 [89, 111]. The first pilot plant was established by Gaskoks in 1987, with first manufacturing plant in 1989. Since then several industrial scale biodiesel manufacturing plants were established worldwide depending on the type of oil feedstock, with soybean in America, canola in Canada, rapeseed oil in Europe and UK and palm oil in Malaysia.

In recent years, energy security and environmental concerns have become a driving force in promoting the utilization of vegetable oil based diesel fuels. Laws and policies have been passed in various countries e.g. The Clean Air Act Amendments of 1990, United States and the Energy Policy Act of 1992. United States requires the use of alternative fuels for regulated truck and bus fleets [112]. Similarly Amendments to Energy Policy Act in 1998 provided credits for biodiesel use (also in blends with conventional diesel fuel). Likewise a directive was passed by European Union (EU) known as "Biofuels Directive" in the year 2003 to promote the use of biofuels to replace 5.75% of all the fossil fuel usage (petrol and diesel) by 2010. The energy taxation directive, 2003 allowed the EU state to offer tax exemption for use of biofuels in order to reduce the difference in cost between the fossil and biofuels [112]. Similarly the EU Climate and Energy Package adopted in 2008 also known as "Climate and Energy Package or 20-20-20 targets" was intended to replace 10% of consumption of petrol and diesel by bio fuels by 2020 [112]. According to Diop et al.[57], world production of biodiesel will increase from 21750 thousand tonnes per year in 2011 to 39150 thousand tonnes by 2020 (Figure 3.1) assuming continuous and adequate supply. The EU would remain the largest producer of biodiesel, followed by United States, Argentina, Malaysia and Indonesia. Table 3.1 shows biodiesel production in EU in thousand tonnes from 2009-2011. It can be seen that Germany was the largest producer followed by France, Spain and Italy.

Table 3.1: EU biodiesel production from 2009-2011. Units: thousand tonnes [113].

Year	2009	2010	2011
Germany	2539	2861	2800
France	1959	1910	1559
Spain	859	925	604
Italy	737	706	479
Belgium	416	435	472
Poland	332	370	370
Netherlands	323	368	363
Austria	310	289	287
Portugal	250	289	226
Finland	233	288	225
Denmark/Sweden	220	246	225
Czech Republic	164	181	218
Hungary	137	149	154
UK	133	145	150
Slovakia	101	88	103
Lithuania	98	85	101
Romania	77	70	79
Latvia	44	43	78
Greece	29	33	56
Bulgaria	25	30	26
Ireland	24	28	26
Slovenia	17	22	6
Cyprus	9	6	0
Estonia	9	3	0
Malta	1	0	0
Luxemburg	0	0	0
Total	9046	9570	8607

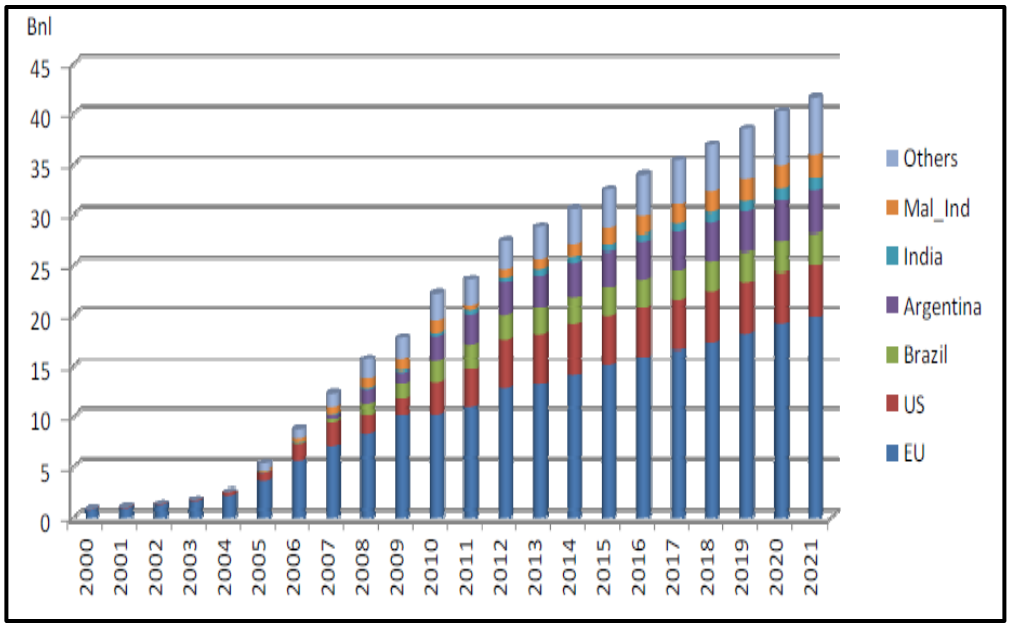

Figure 3.1: Global biodiesel projection by 2020 [57].

3.1 Advantages of biodiesel

The advantages of using biodiesel as a diesel engine fuel are listed below [114-116].

1. Provides a domestic and renewable energy supply.
2. Bio-diesel does not affect GHG emissions, due to balance as a result of balance between the amount of CO_2 emissions and the amount of CO_2 absorbed by the vegetable oil plants.
3. Biodiesel usage in diesel engine improves engine efficiency.
4. Biodiesel can be directly used in diesel engines without any modifications.
5. The physical properties of biodiesel are much closer to diesel compared to vegetable oil. The viscosity of the biodiesel is much lower than vegetable oil and comparable to diesel. Biodiesel higher cetane number compared to diesel or vegetable oil (Table 3.3).

6. Biodiesel can act as a lubricant and helps in preventing premature engine wear and failure. All diesel engine use fuel injection pumps and fuel injectors. These consists moving parts, which undergo wear and corrosion due to metal-to-metal contact as a result of lower lubricity of diesel fuel. Higher lubricity of biodiesel reduces wears and prolongs engine life.
7. Hydrocarbon fuels typically form a layer of deposits on the inside of tanks, hoses, etc. Bio-diesel blends loosen these deposits. It also reduces carbon deposits on injectors.
8. Bio-diesel contains no sulphur hence does not produce toxic sulphur dioxide.
9. It does not require new infrastructure of refuelling stations.
10. Biodiesel is safe to store, due to its high flash point.
11. The emissions of polyaromatic hydrocarbons and nitro-polyaromatic hydrocarbon compounds are substantially lower with bio-diesel compared to conventional diesel fuel [111].
12. It can be used with heavy duty applications. It can work in conjunction with any new vehicle program (i.e. CNG, new and existing vehicles).
13. When ethyl esters are used as fuel the advantage of totally recyclable CO_2 cycle is obtained since C_2H_5OH can be completely of vegetable origin.
14. Biodiesel results in lower soot and PM formation.

Tables 3.2 and 3.3 summarise few physical properties of biodiesel i.e. methyl esters of the various edible and non-edible vegetable oils respectively. As seen in the tables the calorific values of methyl esters i.e. biodiesel are comparable to those of vegetable oil and diesel. The viscosity and cetane number of methyl esters is higher than their respective oils but have much lower viscosity. Similarly the density of biodiesel i.e. esters is lower than virgin oils but is comparable with that of diesel.

Biodiesel consists of shorter chain compounds compared to vegetable oils. Depending on the type of oil edible or non-edible, the composition of the biodiesel varies accordingly. Table 3.4 shows the chemical structure of common fatty acid methyl esters. The

feedstock nature and composition of the oils used for biodiesel production differs from location to location depending on geographical locations. There are more than 350 varieties of oil-producing crops from canola, peanut, safflower, soybean, sunflower and rapeseed. Non edible oils such as *Calophyllum inophyllum*, *Moringa oleifera*, *Sterculia foetida*, *Madhuca indica* (*Mahua*), *Croton megalocarpus and Pongamia pinnata* have become popular worldwide as a result reduce food competition and biodiesel cost reduction. It is very important for biodiesel feedstock to be as cheap as possible in order to reduce the cost of biodiesel production, in order to compare with relatively cheaper diesel. Typical composition of various oils based on edible, non-edible oils and animal fat are included in Table 2.1.

Table 3.2: Physical properties of edible vegetable oils [105, 117, 118].

Fuel	Calorific vale (kJ/kg)	Density (kg/m^3)	Viscosity (mm^2/s)	Cetane number
Olive oil	37,000(lower)	925	32	39
Olive oil methyl ester	37,200(lower)	888	4.70	61
Peanut oil	39,900	888	22.72	41.8
Peanut oil methyl ester	40,100	848.5	4.42	53.9
Rapeseed oil	37,620	914	39.2	37.6
Rapeseed oil methyl ester	37,625	882.2	4.63	54.1
Soybean oil	37,000	925	33	38
Soybean oil methyl ester	39,760	872	4.29	37
Sunflower oil	39,575	918	58.5	37.1
Sunflower oil methyl ester	40,000	878	4.70	45.5
Safflower oil	39,519	914.4	31.3	41.3
Safflower oil methyl ester	40,155	883.8	4.10	51.8

Table 3.3: Physical properties of non-edible vegetable oil [43, 104, 119].

Fuel	Calorific value (kJ/kg)	Density (kg/m^3)	Viscosity (mm^2/s)	Cetane number
Canola oil	39,360	914	78.2	37.6
Canola oil methyl ester	39,975	881.5	4.40	54.8
Coconut oil	38,680	920.6	28.5	37
Coconut oil methyl ester	38,100	8745	4.07	59
Cotton seed oil	39,648	912	50.1	48.1
Cotton seed oil methyl ester	40,580	874	4.70	45.5
Corn oil	39,500	915	46.3	37.6
Corn oil methyl ester	40,190	882.2	4.32	52.5
Diesel	43,350	815	4.3	47
Jatropha oil	39,584	910	38	42.5
Jatropha oil methyl ester	39,594	884	4.12	57
Soybean oil	39,623	914	65.4	38.0
Line seed oil	39,307	894.5	26	34.5
Line seed oil methyl ester	40,759	890	4.3	48
Mahua oil	30,248	918	16.9	45
Mahua oil methyl ester	35,880	874.5	5.06	56.09
Neem oil	35,125	928	30.0	47
Neem oil methyl ester	39,960	876.2	4.72	54.2

Table 3.4: Chemical structures of common methyl esters.

Name of methyl ester	Chemical name	CAS number	Structure	Chemical formula
Caprylic	Decanoic	111-11-5	9:0	$C_9H_{18}O_2$
Capric	Octanoic	110-42-9	11:0	$C_{11}H_{22}O_2$
Lauric	Dodecanoic	29972-79-0	13:0	$C_{13}H_{26}O_2$
Myristic	Tetradecanoic	124-10-7	15:0	$C_{15}H_{30}O_2$
Palmitic	Hexadecanoic	112-39-0	17:0	$C_{17}H_{34}O_2$
Palmitoleic	9-Hexadecenoic	1120-25-8	17:1	$C_{17}H_{32}O_2$
Stearic	Octadecanoic	112-61-8	19:0	$C_{19}H_{38}O_2$
Oleic	cis-9-Octadecenoic	112-62-9	19:1	$C_{19}H_{36}O_2$
Linoleic	cis-9,cis-12-Octadecadienoic	68605-14-1	19:2	$C_{19}H_{34}O_2$
Linolenic	cis-9,cis-12,cis-15-Octadecatrienic 18.3	112-63-0	19:3	$C_{19}H_{32}O_2$
Arachidic	Eicosanoic	1120-28-1	21:0	$C_{21}H_{42}O_2$
Gadoleic	9-Eicosenoic	29204-02	21:1	$C_{21}H_{40}O_2$
Erucic	13-Docosenoic	1120-34-9	23:1	$C_{23}H_{44}O_2$
Lignoceric	Tetracosanoic	2442-49-1	25:0	$C_{25}H_{50}O_2$

3.1.1 Carbon monoxide emissions

Unlike vegetable oil use of biodiesel or its blends in diesel engine has a positive effect on reduction of (CO) emissions. Reasons for CO emission reduction arising from substitution of biodiesel with conventional biodiesel were given by Lapuerta et al. [115]

- The oxygen content of the fuel enhances a complete combustion of the fuel, thus lowering CO emissions.
- The increased cetane number of biodiesel blends lowers the probability of fuel-rich zones formation, which is usually related to CO emissions, as a result of incomplete combustion of fuel. Higher cetane and oxygen content of the fuels lowers CO formation.
- Advanced injection and combustion when using biodiesel may also justify the lower CO emission with this fuel.

3.1.2 Hydrocarbon emissions

One of the main advantages of using biodiesel or its blends over pure vegetable oils is reduction of hydrocarbon emissions. Significant reductions in hydrocarbon emissions were reported by several authors Dhar and Agarwal [120], Dhar et al. [121] , Jindal et al.[122], Kalligeros et al. [123], Misra and Murthy[124], Shi et al [125]. and Sahoo et al [109]. Dhar and Agarwal [120, 121] reported that hydrocarbon emissions from Karanja biodiesel-diesel blends at lower engine loads were higher, but the amount of emissions decreased with increasing engine load. At lower engine loads the emissions from the higher biodiesel blends were comparable to diesel. Following reasons were provided for reduction in hydrocarbons at lower and higher engine loads.

The reduction in hydrocarbons by the use of biodiesel-diesel blends as compared to diesel at lower engine loads was shown to be the result of the following factors.

1. Reduction in over-mixing at lower engine loads due to poor biodiesel volatility.
2. Reduction in stoichiometric air requirement owing to oxygen from biodiesel, which enhances diffusion combustion and also increases heat release/gas temperature as compared to pure diesel.

At higher engine loads, hydrocarbon emissions are caused by deficiency of oxygen in fuel rich zones, presence of oxygen from biodiesel molecules helps in reduction of emissions. Reductions in hydrocarbon emissions were shown to vary with biodiesel concentration, with lower biodiesel showing highest change in the emissions. Reductions from (7 to 56%) and (4 to 33%) were observed 10 and 20% Neem biodiesel-diesel blends [121].

3.1.3 Particulate Matter emissions

One of the important advantages of biodiesel is reduction in particulate matter (PM) emissions, responsible for serious health effects such as asthma, lung cancer and serious

respiratory disorders. This section examines the effects of biodiesel on PM reduction and various factors affecting the emissions will be assessed. According to Kumar et al. [105] higher cetane number of biodiesel resulting in shorter ignition delay and longer combustion duration were responsible in lowering PM emissions. Another reason for reduction in PM was provided by Lapuerta et al. [126], increase in oxygen content of biodiesel promoted oxidation of local fuel rich zones, reducing PM emissions. According to Agarwal et al. [127] fuels having higher oxygen content (30-40%) due to the presence of biodiesel were shown to produce drastic decrease in PM emissions. Reduction in PM emissions particularly soot was not merely by replacement of diesel but can be due to discouragement of soot formation or promotion of soot oxidation. Further pyrolytic reactions in fuel rich regions in the cylinder are suppressed and oxidation reactions due to the oxygen content from biodiesel are promoted reducing soot formation. In essence the excess oxygen (from fuel) is supplied for the combustion reaction in contrast to the oxygen from air, which has no hand to play for the excess oxygen.

The reasons for reduction of PM were compiled by Lapuerta et al. [115] are as follows.

1. Oxygen content of the biodiesel promoting more complete combustion of the fuel even in fuel rich regions of the combustion chamber. The oxidation promotion of the formed soot due to the oxygen content of the fuel.
2. The lowering the stoichiometric air requirement in the case of biodiesel combustion reduces the probability of fuel-rich region formation in the non-uniform fuel/air mixture, thus affecting soot formation.
3. Absence of soot forming aromatics in biodiesel fuels compared to diesel.
4. Formation of oxidation susceptible soot particles with use of biodiesel in comparison to diesel soot particles.
5. Absence of sulphur content of biodiesel prevents the formation of sulphates which is significantly higher in diesel PM. Similarly it prevents the adsorption of hydrocarbons on the soot surface by preventing the scrubbing effect activation of sulphur. This effect is known to increase PM emissions.

6. Lower probability of soot and tar production from difficult to vaporize heavy hydrocarbon being absent as a result of lower final boiling point, despite its higher average distillation temperature.

Summarising, biodiesel is a renewable fuel and has significant advantages as diesel fuel substitute. These advantages are discussed in detail in section 3.1. Apart from them the biggest benefit of biodiesel usage is reduction in emissions of CO, hydrocarbons, particulate matter and smoke. The disadvantage of biodiesel is increased NO_x formation. Absence of sulphur in biodiesel eliminates the emissions of sulphur dioxide with 100% biodiesel usage while it reduces them with use of biodiesel-diesel blends. The reduction of these emissions is a result of molecular oxygen of the fuel, resulting in complete combustion of the fuel even in fuel rich zones formed in the engine. The fuel rich zones are known to result in incomplete combustion increasing CO emissions from the engine. Similarly the molecular oxygen are shown to reduce soot formation considerably thus affecting particulate matter emissions drastically. This was also thought to be the reason for reduction in smoke and hydrocarbon formation.

3.1.4 Effect of biodiesel type on engine emissions

The reduction of emissions is dependent on biodiesel composition which affects combustion processes. Biodiesel obtained from various sources such as vegetable or animal sources, depending on the climatic conditions and geography of the region in which the oil bearing plants are grown. The animal sources of triglyceride will depend on the nature of livestock reared in the region for meat production. The source of oil or animal fat used for biodiesel production hence will vary according to the source of raw material. Higher amount of unsaturated components such as linoleic (C18:2) and linolenic (C18:3) fatty acid esters in biodiesel lower the cetane number resulting in inefficient combustion [105, 128]. On the other hand increase in saturated fatty acid methyl esters such as palmitic (C16:0) and stearic acid (C18:0) improve cetane number and combustion of biodiesel. Level of unsaturation is the most important parameter that

determines the cetane number of the biodiesel, presence of long chain saturated ester is sufficient to provide high cetane number [129]. As biodiesel is made of C, H, O, the ratio of C/H may vary depending the degree of unsaturation in the source of triglyceride used to produce biodiesel. The oxygen content of biodiesel varies between 10-12 wt%, affecting the calorific value of the fuel. Calorific value of biodiesel increases with the chain length. Increasing chain length of compounds had insignificant effect on the NO_x and PM exhaust emissions, while significant effect was exerted on HC and CO emissions, the latter being reduced with decreasing chain length [130]. Increase in unsaturation was shown to increase NO_x emissions. Increase in the double bonds within fatty acid methyl ester, increased PM emissions. Unsaturated fatty acid methyl ester were shown to produce soot forming precursors such as ethylene and ethyne by thermal decomposition [131]. The composition of biodiesel (saturated or unsaturated) also affect other properties such as viscosity and density which are responsible to affect combustion processes directly by affecting fuel atomization in the combustion chamber in turn affecting the emissions. It also affects cold flow properties, oxidation stability which in turn affects the quality of biodiesel. Further type of engine used in the investigation is a very important factor that would influence the performance of biodiesel or its blends.

In addition to the chemical composition of biodiesel, factors such as blend concentration, engine parameters such as load, speed, exhaust temperature, engine duty, engine tuning, and type of diesel affect the emissions. Also type of instruments and techniques used to study the performance of biodiesel and its diesel blends significantly affect the results obtained. The main question of food or fuel would still persist with use of edible oil crops for biodiesel production. Use of non-edible oils, animal fat or other sources of oil such as algae could be influential to solve the dilemma by providing cheaper source of feedstock for biodiesel production.

3.2 Hydrogen production from biodiesel

Biodiesel is produced by transesterification of vegetable oil or animal fat using methanol (CH_3OH) or ethanol (C_2H_5OH) over an alkali catalyst. The schematic of chemo- or bio-catalyzed synthesis of biodiesel by methanolysis of triolein (glyceryl trioleate) is shown in Figure 3.2. As seen previously, biodiesel has several advantages in terms of engine operation, performance and emissions over vegetable oil. It is already commercialised as alternative diesel fuel. Furthermore, production of biodiesel will increase from 122 billion litres in 2014 to 180 billion litres in 2021 assuring a steady supply for the future [57]. All these factors have promoted research in H_2 production from biodiesel. Use of biodiesel leads to a CO_2 reduction of 2.2kg for every litre of displaced fossil fuel [111]. Higher volumetric energy density of biodiesel in comparison to other liquid fuels such as ethanol would suggest lower amount of fuel required to generate same amount of energy.

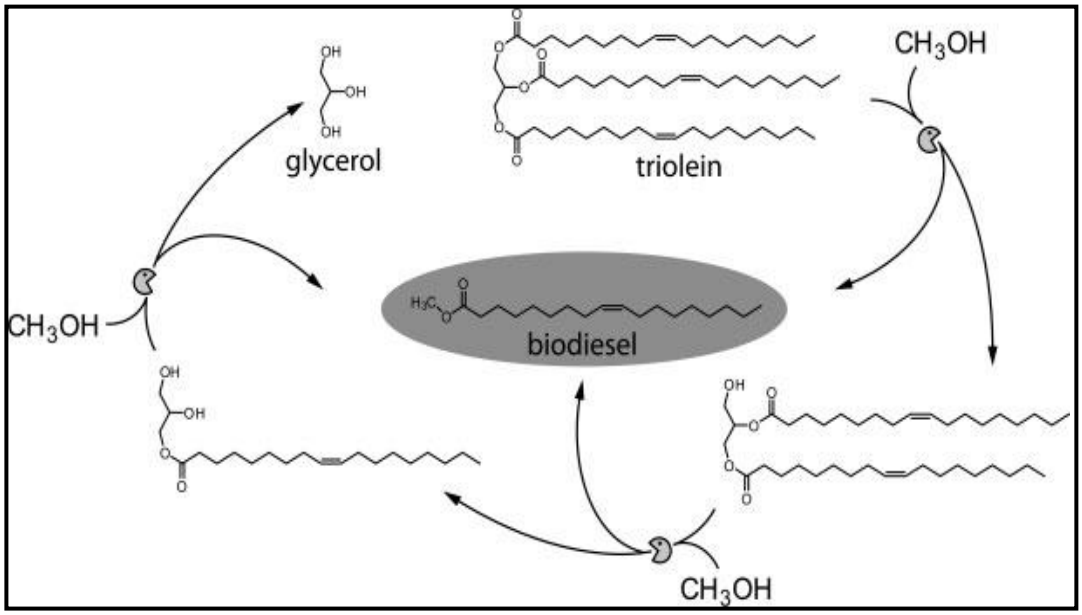

Figure 3.2: Schematic illustration of the chemo- or bio-catalyzed synthesis of biodiesel by methanolysis of triolein (glyceryl trioleate).

Better handling properties of biodiesel (flash point, corrosion test, auto ignition temperature, material of construction of storage tanks and low viscosity) compared to

vegetable oils and diesel could justify the use of biodiesel as a feedstock for H_2 production. Waste cooking oil contains high amount of free fatty acids (FFA), responsible for initiating cracking reactions at the reforming temperatures leading to carbon formation and catalyst deactivation [132]. FFA acids are formed due to hemolytic and hydrolytic reactions which occur in vegetable oil. If triglycerides containing saturated fatty acids are heated at high temperature (180°C) in the absence of oxygen, they produce a series of normal alkanes, alkenes, lower fatty acids, symmetric ketones, oxopropyl esters, CO, and CO_2. The steam produced during food preparation can cause hydrolysis of triglycerides resulting in the formation of FFA, glycerol ($C_3H_8O_3$) and monoglycerides [133]. During the biodiesel production process, most of the FFA content is removed by acid treatment to prevent soap formation and reduction of methyl ester yields. This would help reduce carbon formation from FFA during the H_2 production processes.

Life cycle assessment of biodiesel production using transesterification of waste cooking oil was reported to have a low C footprint, promoting the use of biodiesel as a H_2 carrier [134] as compared to vegetable oorwaste oil. According to Xuan et al [135], as biodiesel consists of shorter C chains in comparison to original oils. As a result it would be easier to convert to H_2 as compared to the original oils. The utilisation of biodiesel for H_2 production or fuel cell usage is relatively new [136-138] and few catalytic investigations have been reported [139, 140]. Direct utilisation of biodiesel formulations in solid oxide fuel cells (SOFC) using Ni/YSZ anodes was reported by Nahar and Kendall [141]. Higher power generation using biodiesel fuelled SOFC over Ni/ScCZ anode was reported by Tuyen et al [142] in comparison to waste cooking oil fuelled SOFC using CeO_2-Rh anodes by Zhou et al [143].

H_2 production via CSR of biodiesel using $NiAl_2O_4/Al_2O_3$-YSZ catalyst was investigated by Abatzoglou et al. [144]. The authors examined the CSR performance at 700°C and S/C of 1.9-2.4. A 100% conversion of biodiesel was reported at GHSV of 5500 cm^3/g_{cat} h which decreased to 88% with increase in gas hourly space velocity (GHSV) to 8700 cm^3/g_{cat} h at constant S/C of 1.9. H_2 production via CSR of biodiesel derived from palm

oil was investigated by Shiratori et al. [140]. A 12 wt% Ni catalyst supported on paper based support was prepared using a dual polyelectrolyte retention system and a subsequent on-paper synthesis. In the synthesis of the catalyst a ceramic fiber suspension containing catalyst powders were mixed with Al sols. This mixture was poured in pulp suspension and hand sheets with grammage of 4 to 5 g/m^2 were prepared. The sheets were pressed at 350 kPa for 5 min and dried at 100°C for 30 min followed by calcination at 350°C for 3 h to remove the organic compounds. The performance of the catalyst was evaluated at S/C of 3.5 at 800 °C and GHSV of 3900 h^{-1}. Catalyst supports containing YSZ and Al fibre in addition to inorganic binders such as Zr or Al sols deactivated after 8 h of operation in a 20 h test. Severe C formation was detected on catalyst containing Al sol as binder. In order to improve the performance bimetallic catalyst containing 4 wt% MgO was prepared and the support was also modified by using different binders such as Ce. The best performance in terms of H_2 composition and conversion was observed over Ni-MgO/ (YSZ+Al) fibre + Ce sol, which exhibited stable performance for about 50 h.

Apart from these few catalytic investigations, conceptual investigations of biodiesel based fuel processor was investigated by Sgroi et al. [145], Specchia et al. [146] and Kraaij et al. [136] who proposed various methods for developing a fuel processor based on biodiesel. Simulations were carried out, and autothermal reforming (ATR) was selected as the best option in developing a fuel processor for the fuel cell. Similarly Martin and Wörner [137] showed that the ATR concept with heat integration was competitive with the SR concept with heat integration in terms of fuel processing efficiency and overall system efficiency. ATR has been reported to increase H_2 yield by increasing $C_3H_8O_3$ conversion [147]. In ATR reaction mode, the heating is done directly by using oxidation reactions. Once the reaction is initiated with effective amount of heat, the reaction is self sustaining from the reaction products. The thermodynamics ATR of biodiesel using Gibbs free minimisation method with water-biodiesel molar feed ratio (WBFR) between 3 to 12, oxygen-biodiesel molar feed ratio (O_XBFR) from 0-4.8 and reaction temperature from 300-800^oC was examined by Nahar [138]. From the results WBFR≥9 and O_XBFR=4.8 are the best conditions to operate the ATR reformer at SOFC

temperature (800 ^{o}C). A 68.80 and 91.66% H_2 and CO yields with 54.14 and 39.2% molar composition respectively was predicted. Increasing WBFR to 12 increased the yield of H_2 to 78.17%. Further the simulations revealed transesterification contributed to increase in H_2 and CH_4 formation. Alkane selectivity decreased with increase in C number while coke formation increased with C number. Alkene and alkane selectivity were found to be lower under ATR as compared to SR conditions.

Although simulations reported ATR to be one of the best option to produce H_2 from biodiesel, successful catalytic investigation were not found in the literature at the time of this review. Ospinal-Jimenez and Colucci [148, 149] carried out ATR of biodiesel and $C_3H_8O_3$ on Pt and Rh based catalysts, with only Pt based catalyst resulting in H_2 production above 500 °C. The experiments were performed using O_2/C of 0.18-0.6 and S/C ratio of 2-6 at 371-571 ^{o}C. A maximum of 25% (g of H_2/g of biodiesel) yield was obtained using an S/C 3.5 and O_2/C ratio of 0.6 at 482^{o}C. The major problem associated with the process was the formation of coke and much less yield of H_2. Heavy organic solvents below 4500 ppm were detected in the condensate. The solvents consisted of hexane, benzene, heptane, toluene, isooctane, o-xylene, m-xylene and p-xylene. In another ATR reforming investigation performed by Lin et al. [139] using S/C of 0.6 and O/C of 1.47 at 900°C, the authors showed that incomplete vaporisation of biodiesel led to higher C formation by self pyrolysis before entering the reformer during ATR of biodiesel. Catalytic partial oxidation (CPO) of biodiesel using Rh/γ-Al_2O_3 and Rh-substituted pyrochlore catalyst was examined by Siefert et al. [150]. CPO experiments were performed at 900 °C with O_2/C of 1.2 and GHSV of 25000 cm^3g^{-1}cat h^{-1} for 100 h. The reformed gas contained 37 mol % H_2, 34 mol % N_2, 23.0 mol % CO, 6 mol % CO_2, 0.038 mol % Ar, 0.09 mol % CH_4, and <0.0001 mol % higher hydrocarbons.

From the literature examined it can be seen that H_2 production from biodiesel is relatively new and only few successful investigations have been reported. SR was shown to be the most effective process among the three i.e. SR, CPO and ATR processes examined. The amount of H_2 produced by SR was highest compared to the other two processes, as would

be expected from the stoichiometry of the reaction, and can be carried out at lower temperatures as compared to CPO and ATR reforming.

3.3 Hydrogen production processes

In 1926, the first CSR plant was built to convert natural gas into a mixture H_2 and CO (synthesis gas) for NH_3 production [151]. Since the SR process was then adopted worldwide to produce H_2 from natural gas, naphtha and heavy oil for utilisation in refineries and NH_3 based fertilisers. In refinery H_2 is used in hydrotreating and hydrocracking process to convert the impure heavier petroleum fractions such as vacuum distillates into clean gasoline or middle distillates [152, 153], where impurities include S, N, Ni and V metals in the crude. H_2 is also the most costly reagent in the manufacture of CH_3OH [154], NH_3 [155] and Fisher Tropsch process [156].

Figure 3.3 shows a schematic of CH_4 steam reforming (SMR) process. The process in performed in a minimum of three main stages i.e. reforming, water gas shift and purification. The first two may consist of more stages, e.g. pre-reforming (the conversion of the higher hydrocarbon gases in the feedstock to CH_4) and primary reforming (CO and H_2 production from CH_4), in NH_3 production, secondary reforming is used too, and then high temperature and low temperature water gas shift. When performing small scale SR for research purposes on unconventional feedstocks such as biodiesel, primary reforming of the received feedstock is the most challenging. In the primary reforming stage the hydrocarbon feedstock is reacted with steam to produce synthesis gas. Here we use CH_4 as an example, as it is the most common SR feedstock which makes SMR currently the single largest producer of H_2 in the world. As CH_4 is a very stable molecule, severe temperature and pressure conditions are required for the reaction. Temperature typically over 800 ^oC and pressure between 15-30 bars is required for converting it to H_2, CO, CO_2 and H_2O by the following reaction (R-3.1). The reaction is performed in tubular reactors

called reformers on Ni based catalyst with H_2O/CH_4 ratio typically between 2 to 5. Alkali metals are used in the catalyst to accelerate coke removal. Excess steam is used to prevent thermal cracking and coke formation. When naphtha is used as the feedstock, conditions are very similar but the catalyst is modified to prevent coking from decomposition of the higher hydrocarbons. The SR reaction is strongly endothermic, and reactor designs in SR industrial plants are typically limited by heat transfer, rather than by reaction kinetics [157].

$$C_mH_n + mH_2O \overset{cat}{\rightleftharpoons} mCO + (m+\frac{n}{2})H_2 \quad \Delta H_{f,298K} > 0 \tag{3.1}$$

The excess steam and CO produced in the reformer are reacted with steam in shift reactors to produce H_2 and CO_2 by R-3.2. The water gas shift reaction (WGS) is performed at two different temperatures i.e. high temperature water gas shift (400-300°C) and low temperature water gas shift (300-200°C). The heat removed while lowering the temperature of the reformate gas to the WGS temperatures is utilised in preheating of the feed or generate steam for the reforming reaction. A chromium based catalyst is used for high temperature WGS in comparison to copper based for to temperature WGS

$$CO + H_2O \overset{cat}{\rightleftharpoons} CO_2 + H_2 \quad \Delta H_{f,298K} = -41.2.\ \text{kJ/mol CO} \tag{3.2}$$

Finally the gas leaving the WGS reactors can be sent to the purification step which most commonly consists of pressure swing adsorber (PSA) although other methods are also used. The PSA process removes trace impurities such as CO, CO_2 N_2, CH_4, and H_2O to deliver high purity H_2. In a different type of purification step the H_2 rich gas leaving the shift reactors is feed to amine scrubbing/stripping columns where most of the CO_2 is removed and the other impurities such as CO is removed in the methanation reaction (reverse R-3.1) and finally H_2 gas leaves the methanator. The choice of the purification method will depend on the end use and the desired purity of H_2.

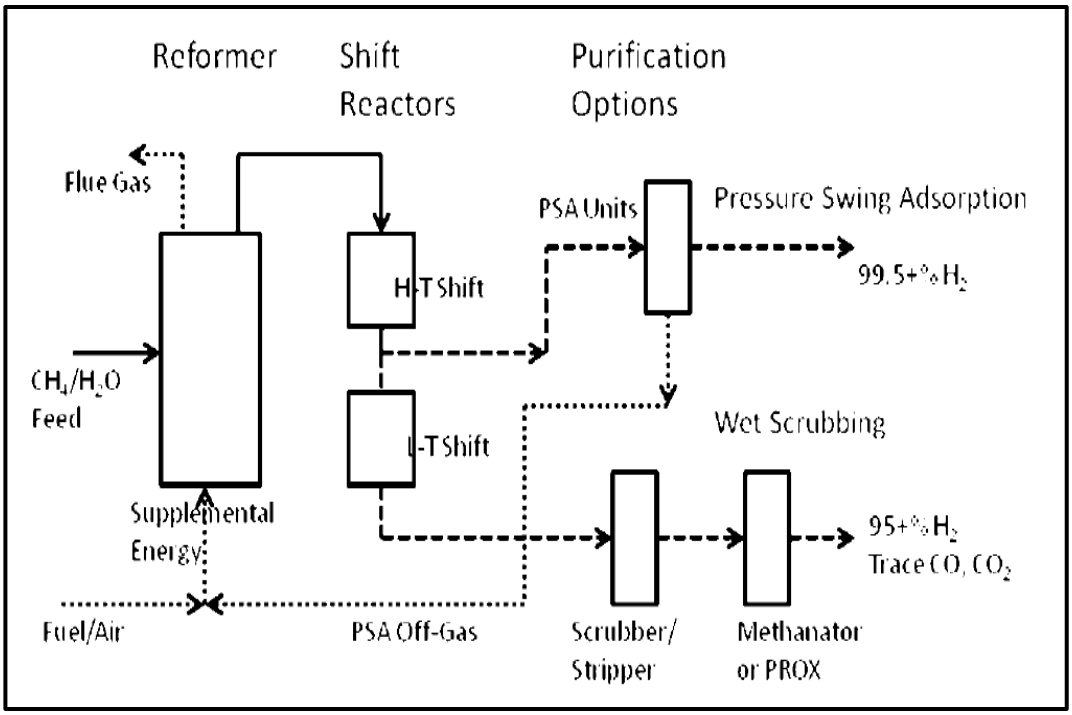

Figure 3.3: Schematic of the SMR process [158].

Although the SR process is highly efficient it has numerous disadvantages. The SR is a highly endothermic reaction and requires burning large amount of fossil fuels to supply the heat required to maintain the reaction. This generates large amount of CO_2 and can cause uneven heating of the reformer tubes leading to hot spots and reduced reformer life. The uneven heating could also result in formation of C leading to catalyst deactivation.

3.3.1 Partial oxidation

As SR is an energy consuming process, extensive work has been done on an alternative process for H_2 production. Partial oxidation (POX) is a process where O_2 is used to react with hydrocarbons to produce H_2 and CO. In POX (R-3.3), using CH_4 as a feedstock, an O_2/CH_4 molar ratio of 0.5 is used to produce H_2/CO of 2. The POX reaction is exothermic, making it desirable as compared to SR. If higher O_2/C is fed, the combustion reaction (R-3.4) occurs, resulting in the formation of CO_2 and H_2O instead of the desired CO and H_2. WGS also occurs in POX producing H_2 and CO_2 from the syngas product via

(R-3.2). POX is faster than SR and requires smaller reactors and, according to [151], higher productivity. The major limitation of POX is carrying out the reaction under flammable and explosive environments. Hot spots can develop, affecting the life of the catalyst [159]. Under oxidation environments, gas phase reactions lead to the formation of C on catalyst surface [160]. The POX systems have high energy consumption and less suitable H_2/N_2-ratios in the produced synthesis gas to be used in NH_3 production and the energy in the PSA purge gas cannot be fully recovered. The application of POX to produce H_2 from alcohols would lead to lower efficiency due to the oxidation of alcohols forming CO_2 and H_2O. Lower conversion and selectivity is reported in POX of alcohols such as CH_3OH on monometallic catalyst [161].

$$C_mH_n + \frac{m}{2}O_2 \longrightarrow mCO + \frac{n}{2}H_2 \quad \Delta H_{f,298K} > 0 \tag{3.3}$$

$$C_mH_n + (m + \frac{n}{4})O_2 \longrightarrow mCO_2 + (\frac{n}{2})H_2O \quad \Delta H_{f,298K} > 0 \tag{3.4}$$

3.3.2 Autothermal reforming

Although SR provides higher efficiency and reformates quality, the reaction is highly endothermic and requires an external heat source to supply the heat for the reaction. ATR is a combination of (SR) and (POX) in a single reactor and is overall a slightly exothermic reaction [157]. Reaction (R-3.5) shows a typical reaction occurring in an ATR reformer.

$$C_mH_n + \frac{m}{2}H_2O + \frac{m}{4}O_2 \rightleftarrows mCO + (\frac{m}{2} + \frac{n}{2})H_2 \quad \Delta H_{f,298K} \text{ -/=0} \tag{3.5}$$

The process was developed by Haldor Topsoe in 1950s [151]. It has been increasingly accepted as the most appropriate processes for the future fuel cell vehicles and is also used in chemical processes [162, 163]. The heat generated by the reaction can be controlled directly by adjusting the proportions of fuel and air/O_2 in the feed. In comparison to SR, POX and ATR processes have the merits of fast start-up times because of the exothermic nature of the oxidation reaction and lower rate of side reactions and

fewer by-products. The main characteristics of ATR are a low energy requirement (due to the complementary SR and POX reactions), low energy consumption, high gas space velocity (GHSV; at least one order of magnitude greater than traditional SR), and a preset H_2/CO ratio regulated by inlet reactant ratios and CO_2 recycling [164]. ATR is considered to be one of the most attractive options for the on-board reforming of complex hydrocarbons such as kerosene and diesel [165, 166]. The ATR reaction is more selective to CO_2 than CO making it compatible with PEMFC's for automotive applications [162, 167].

In spite of all these advantages the technology has not be commercialised yet and further research has to be carried out for successful application. The ATR process produces lower H_2 yield as compared to SR but higher than POX. When using air as the oxidant, the inert N_2 dilutes the products obtained from the reformer. As ATR incorporates POX reaction, both the processes require an expensive and complex oxygen separation unit in order to feed pure oxygen to the reactor in order to prevent product gas dilution with N_2. The use of pure O_2 means formation of explosive environments is possible leading to explosions.

3.3.3 Conclusion

Table 3.5 shows the comparison of various reforming technologies. In all the three processes, SR is quite successful and has been widely used in H_2 production. Highest H_2 yield is obtained in SR as compared to POX and ATR processes. For e.g., maximum H_2 yield from SMR is 4 mol/mol of CH_4 (or 50 wt% of CH_4) with a max purity of 80 vol%, compared to 3 mol/mol (or 37.5 wt%), with a max H_2 purity of 75 vol% from POX of CH_4.

The process has been widely researched for H_2 production from oxygenated hydrocarbon such as DME or CH_3OH which has to be reformed at much lower temperature (>180°) [168, 169] and > 500°C for other hydrocarbons such as C_2H_5OH [170, 171]. Higher and

much more complex oxygenated hydrocarbon such as sunflower oil [172], rapeseed oil [173] and waste cooking oil [174] are also converted to H_2 using SR processes.

In order to improve the thermal efficiency of the SR, new processes such as chemical looping reforming (CLR) and sorption enhanced SR have been developed. The Autothermal Cyclic Reforming (ACR) process was developed by Kumar et al [175], which is operated in three-step cycle that involves SR of fuel on Ni catalyst (reforming), oxidation Ni catalyst (air regeneration) to heat the reactor and the reduction of the catalyst to its original state (fuel regeneration). The process has several advantages as it incorporates SR over ATR and requires less energy compared to conventional SR. It has higher efficiency due to lower internal heat generation by fuel oxidation. High purity H_2 is obtained due to the absence of N_2 in the product gas. The C formed on the catalyst surface is burnt during the regeneration step, generating the heat required for the endothermic SR process. The process is already proved to work with complex hydrocarbons such as waste cooking oil [174].

Table 3.5: Comparison of reforming technologies [176].

Technology	Advantages	Disadvantages
SR	Most extensive industrial application. Oxygen not required. Lowest process temperature. Best H_2/CO ratio for H_2 production.	Highest atmospheric emissions.
POX	Decreased desulfurization requirement No catalyst required. Low CH_4 slip.	Very high processing temperatures. Low H_2/CO ratio. Soot formation/handling adds process complexity. Higher risk of explosion, requires O_2 for undiluted syngas
ATR	Lower process temperature than POX Low CH_4 slip.	Limited commercial experience. Requires O_2 for undiluted syngas.

3.4 Hydrogen production catalysts

Generically a catalyst is defined as a material that has the ability to increase the rate of a chemical reaction without altering its overall Gibbs energy change. The catalyst is not a reactant or product, but is an intermediate that undergoes a cycle. In a heterogeneous catalytic system where the catalyst exits in a different phase than reactants or products, it may form intermediates, but according to definition it should not interfere in a chemical reaction. The most important parameter to be considered during a catalyst selection is the activity of the catalyst. The ability of the catalyst to convert reactants into products is defined as catalyst activity. The second most important parameter to be considered is the selectivity of the catalyst. Selectivity defines the ability of the catalyst to produce desired products over undesired products. In addition to these two factors, 'life' is another most important factor to be considered during catalyst selection. The life of the catalyst is defined as the time for which decent activity and selectivity is maintained.

A SR catalyst must be able to promote the SR reaction and suppress or minimise other side reactions such as C deposition or the methanation reaction. The catalyst should be active for WGS reaction which would help to reduce CO and increase H_2 selectivity. Prior to SR reaction, the catalyst has to be reduced in order to catalyse the reaction between the fuel and steam via SR and WGS reaction. Hence the catalyst should have complete reduction ability in order to exhibit high SR and WGS activity. The catalyst should have sufficient mechanical strength and should be able to withstand high temperature (~800 °C) and pressure for industrial utilisation.

The catalysts used for H_2 can be divided into two types: non-precious metal (typically Ni) and precious metals from Group VIII elements (typically Pt or Rh based). Due to severe mass and heat transfer limitations, conventional steam reformers are limited to an effectiveness factor for the catalyst which is typically less than 5%. The effectiveness factor is the measure of how far the reactant diffuses into a catalyst pellet before reacting. As a result kinetics and catalyst activity are not the limiting factor for conventional steam

reformers, so cheaper Ni catalyst are universally used [176]. The spent Ni catalyst can be recycled and reused easily as compared to noble metals.

3.4.1 Nickel catalysts

Traditionally SMR reforming catalysts are usually deposited on ceramic or metallic monoliths, based on Ni / NiO or cobalt compositions on foams, or other structured inert supports. Depending on the refractory Al_2O_3 or supports such as magnesium Al_2O_3 spinel are promoted with alkali or alkali-earth metals to facilitate C removal [177]. The Ni based catalysts are widely investigated for H_2 production from liquid or gaseous hydrocarbons, oxygenated or not. The applications of Ni based catalysts in SMR process was reviewed by Giannakeas et al. [178]. The author examined use of various formulations for SMR and reported that Ni-Co based catalysts as one of the promising candidate for SMR and chemical looping steam reforming (CLR) of CH_4.

The focus of this section is to review the use of Ni catalyst for CSR of oxygenated hydrocarbons. CSR of four different types of oils rapeseed oil, soybean, corn oil and sunflower oil using commercial Ni catalyst and a hydrotalcite precursor based Ni (HT) catalyst was investigated by Marquevich et al. [173]. The experiments were performed in an isothermal fixed-bed tubular reactor at steam-to-carbon (S/C) ratios of 9, 6, and 3 and temperatures between 500 and 630 °C and high space velocities of 0.76-1.90 mol C/ (gcat h). H_2 productions were from 0.3 to 7.5 mol H_2/ (g_{Ni} h) depending on the operating conditions. The HT catalyst, which was prepared from a hydrotalcite-such as precursor, seemed promising for CSR of vegetable oils because of its very high activity per gram of catalyst. The performance of the catalyst at same temperature and S/C ratio was independent on the type of vegetable oil. The HT catalyst had almost 10 times more catalytic activity than the commercial catalysts [132, 172, 179]. CSR of waste cooking oil using Ni based catalyst supplied by United Catalysts was examined by French and Czernik [180]. At 750 ˚C the highest conversion of 96% was achieved with 70% of the stoichiometric H_2 yield potential for 16 hours of operation.

CLR of waste cooking oil was studied by Pimenidou et al. [174] using a packed bed reactor with a Ni/Al_2O_3 catalyst. The S/C of 4 and temperatures between 600 and 700 ^oC yielded the best results. Six cycles at two weighted hourly space velocities (WHSV of 2.64 and 5.28 h^{-1}) yielded high (>0.74) and low (<0.2) oil conversion respectively. WHSV of 2.64 h^{-1} exhibited conversions close to thermodynamic evaluations. Pimenidou et al. [181] performed sorption enhanced CLR of waste cooking oil with S/C of 4 at 600 °C. Higher fuel and steam conversion were reported in the presence of the sorbent dolomite than without it. Initially, the dolomite carbonation was very high (100%), and 98% H_2 purity was obtained, but the carbonation decreased to around 56% with a H_2 purity of 95% respectively in the following cycles. Reduction of the Ni catalyst occurred along with CSR, WGS and carbonation, with H_2 produced continuously under fuel–steam feeds. Catalyst and CO_2-sorbent regeneration was reported, and a long period of autothermal operation within each cycle was demonstrated.

Ni supported on various supports for CSR of C_2H_5OH (CSRE) has been widely investigated by several research groups. Alberton et al. [182] studied the CSRE over Ni supported Al_2O_3 catalyst at 600 °C and S/C of 1.5. The effect of type of Al_2O_3 on the CSRE was examined. A catalyst supported on α-Al_2O_3 showed lower catalytic activity in comparison with catalyst supported on γ-Al_2O_3 due to lower dispersion of Ni particles. Chen et al. [183] performed CSR of $C_3H_8O_3$ over CRG-LHR Johnson Matthey catalyst containing NiO, Cr_2O_3, MgO and amorphous silica. The experiments were performed in the temperature range 400-600 °C, with S/C of 3 and reactant/inert gas of 1/4. The highest H_2 yield of 88.57% with $C_3H_8O_3$ conversion over >96% were reported at 580 °C with the above conditions. H_2 selectivity was shown to increase with temperature; reaching 100% at ~580 °C.

The process of sorption enhanced steam reforming (SESR) has been investigated with pure $C_3H_8O_3$ and crude $C_3H_8O_3$ as the feedstock. In this process, a high temperature solid

CO_2 sorbent is introduced within the reformer to modify equilibrium conditions through the in situ removal of the CO_2 gas, resulting in higher H_2 yields and purity. Dou et al. [184, 185] reported complete conversion and 68% H_2 purity for crude $C_3H_8O_3$ in comparison with 65 vol% for pure $C_3H_8O_3$ at 600 °C over 18 wt% NiO/Al_2O_3 catalyst with S/C of 3 in CSR of $C_3H_8O_3$ without CO_2 removal. But in the presence of the CO_2-sorbent calcined dolomite the H_2 purity increased to 90 and 94 vol% for crude and pure $C_3H_8O_3$ respectively through the effects of CO_2 in situ capture [183]. Likewise complete conversion and higher H_2 purity of 99% with S/C of 3 with 25%-Ni-15%-Co/ HT type catalyst was reported by He et al [186].

Hu and Lu [187] investigated the CSR of CH_3COOH (CSRA) for H_2 production over 20 wt% transition metals (Ni, Co, Fe or Cu) supported on Al_2O_3 catalyst. Ni/Al_2O_3 and Co/Al_2O_3 were reported to have high activity in comparison with Fe/Al_2O_3 and Cu/Al_2O_3, in SRA, The difference in catalytic activity was attributed to the cracking activity of the metals toward the C–C and C–H bonds of acetic acid. The experiments were carried out in the temperature range of 300-800°C with S/A of 15, liquid hourly space velocity LHSV = 8.3 h^{-1} and 1 atm. The Ni/Al_2O_3 exhibited a more stable activity than the Co/Al_2O_3 catalyst.

It can be seen from above that Ni based catalysts can widely be applied for different H_2 production processes based on CSR. They can be applied for CSR of a variety of simple and complex oxygenated hydrocarbons from C_2H_5OH to vegetable oil. These catalysts can work at various S/C ratio, temperature, Ni loading and residence time successfully. The main disadvantage of using Ni based catalyst is the formation of C on the catalyst surface. Several methods are suggested to minimise C formation. One of the few methods adapted to decrease C formation is the use of bimetallic catalysts or using modified support.

3.4.2 Ceria as catalyst support

CeO_2 based materials have recently received a lot of attention in a wide range of applications. CeO_2 plays an important role in two of the most important commercial catalytic processes: three-way catalysis (TWC) in the automotive industry and fluid catalytic cracking (FCC) [188] in refinery operations. Other applications include diesel soot oxidation [189], oxidation of volatile organic wastes [190] and fuel cell technology [191, 192]. In all these applications the unique features are responsible for making CeO_2 a promising material for use either as a support or as an active catalyst.

The most important property of a CeO_2 based material is its oxygen storage capacity (OSC) by means of redox shift between Ce^{3+} and Ce^{4+} under not only oxidizing but also reduction environments [193]. The OSC ability of CeO_2 helps reduce the formation of C, during H_2 production, CH_4 oxidation, CH_4 decomposition, and ethylene dehydrogenation. Further, Ni supported CeO_2 based catalysts have exhibited self-decoking capability by promoting C gasification reaction by oxygen species supplemented from the lattice oxygen [194]. It is also well known to promote metal activity and dispersion, resulting in investigations of various catalytic formulations for a wide range of reactions.

CeO_2 is widely investigated material as catalyst support for H_2 production from various non oxygenated and oxygenated hydrocarbons. Several investigation involving CSR and ATR of various liquid [192, 195-197] and gaseous hydrocarbons [198-200] using CeO_2 based catalyst have been reported. Similarly H_2 production of oxygenates such as CH_3OH, C_2H_5OH, $C_3H_8O_3$ and propanol using CeO_2 based catalysts have been investigated [170, 171, 201-203]. However, CeO_2 lacks thermal stability and is known to sinter at temperature above 800 ^oC [204], leading to catalyst deactivation [205, 206]. At high temperature the specific surface area of CeO_2 decreases drastically which in turn affects the crucial redox properties i.e. OSC of the material [207]. It was reported that the of rate of O^{-2} depends on the surface area of CeO_2 as a result the reduction in surface area

affects O^{-2} release thus affecting the redox properties of CeO_2. Similarly reduction of surface area reduces the redox sites by affecting the OSC of the material [208]. CeO_2 has weakly bound oxygen species (Frenkel type oxygen defects) in the bulk of the material rather than to the surface, these weakly bound oxygen species undergo fast exchange with the environment and provide OSC. The defects are shown to disappear due to high temperature treatment affecting the OSC of the material [209].

The OSC of pure CeO_2 is unsatisfactory for practical applications. The CeO_2 crystal consists of eight oxygen cations coordinated at a corner of cube, each anion being tetrahedrally coordinated by four cations. This makes its structure more stable and prevents the conversion of Ce^{4+} to Ce^{3+} under reducing conditions. Metal decoration has been observed for metal catalysts supported on reducible oxides [210]. Degradation of catalytic activity is also caused by decreases in metal surface area of the supported catalysts [211].

H_2 production via SR is endothermic and has to be carried out at high temperature i.e. 800 ^oC for CH_4 feedstock or higher, resulting in decrease in surface area by ~ 30% with operation for 10 h [205]. Similarly the increase in the temperature of the CeO_2 supported catalyst in case of exothermic reactions such as PO would result in sintering of the CeO_2 and affecting the activity of the catalyst. Improvement of the thermal properties of CeO_2 and retention of active surface area at high temperature is thus necessary to exploit the redox property of CeO_2 for H_2 production applications via high temperature processes.

Substitution of CeO_2 with metal/metal oxide into the CeO_2 lattice forms composite oxides. It can easily form solid solutions with elements belonging to the transition-metal series. Ionic mobility is modified by replacement of Ce ions by different cations of varying size and/or charge resulting in the formation of a defective fluorite structured solid solution. Transition and non transition metal ions such as Al^{3+}, Si^{4+}, Ti^{4+}, and Zr^{4+} are introduced into the CeO_2 cubic structure [153-157] to counteract these drawbacks.

This modification of CeO_2 lattice confers properties such as resistance to sintering and high catalytic activity according to [207]. Incorporation of Zr increases the specific surface area, OSC, redox property, thermal stability and catalytic activity of CeO_2 for variety of reactions from oxidation to H_2 production [33-35]. The doped support also affects the dispersion of metals. Further addition of Zr to CeO_2 also helps in mitigating the formation of C during various H_2 production processes [212].

The incorporation of Zr^{4+} or Hf^{4+} into the CeO_2 lattice was found to facilitate an increase in the formation of smaller particle sizes. Addition of Zr was found to increase the support metal interactions between the support and the metal. The presence of Zr increased the oxygen mobility in the CeO_2 lattice and the process of vacancy formation was promoted [213-215]. As a result the increased oxygen mobility helps in reducing carbon deposits formed at the metal and support interface and prevent carbon build up on the catalyst surface, keeping the metal surface clean for reforming reactions. Dong et al.[216] and Roh et al.[217] found that mobile oxygen species formed in the Ce-ZrO_2 supported catalyst via a redox cycle enhanced decoking activity resulting higher SMR and ATRM activity. Figure 3.4 shows mechanism of CH_4 conversion in SMR and ATRM using Ni/Ce-ZrO_2 catalyst. Formations of composite layers of material were thought to be the reason for high activity. The composite was made of three different layers with top layer consisting of free Ni species followed by second layer of strongly interacted Ni and Ce–ZrO_2 forming –Ce–Zr–O_x, finally the last layer of Ce–ZrO_2 support. The participation of the lattice oxygen was supplemented by the presence of O_2 molecules.

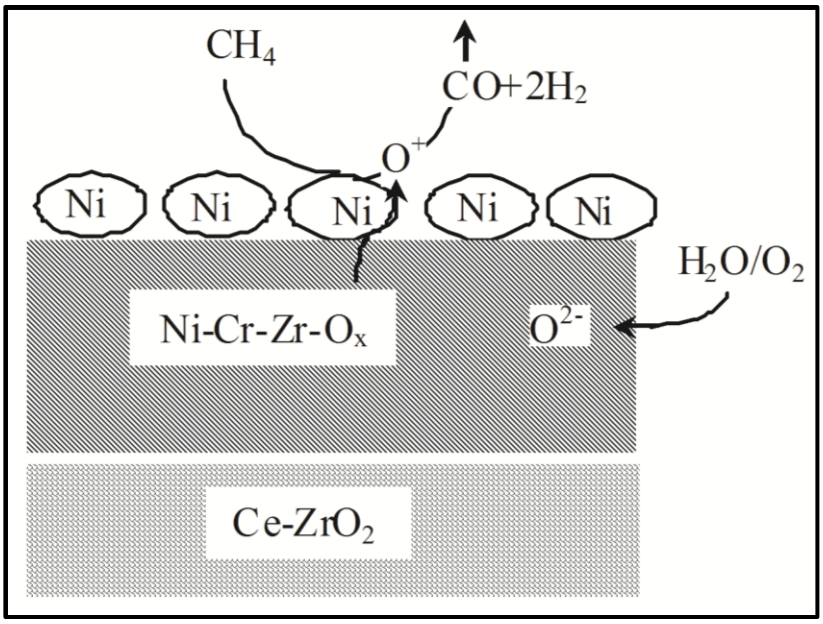

Figure 3.4: Schematics synthesis gas production over Ni/Ce-ZrO_2 catalyst.

In case of Pt supported on Ce-ZrO_2 mixed oxide, Pt sites and the Ce–Pt located at the interface interact, and transfer of electrons from the metal oxide to the noble metal occurs. This results in the lowering of effective activation energy, necessary for the formation of oxygen vacancies, resulting in high oxidation activity [218, 219]. The reduction of the CeO_2 due to addition of Zr is then no longer confined to the surface but extends deep into the bulk [220, 221]. During the reductive treatment transfer of Ce^{4+} to the support surface takes place, resulting in the formation of Ce-rich phase on the surface while the phenomenon is reversed when atmosphere was switched to an oxidative atmosphere [218].

3.4.3 Bimetallic catalyst

In order to overcome the problem of C deposition in H_2 production catalyst and to enhance the catalytic performance, addition of other metals such as Mg, La, Cr, and Co has been widely investigated. The investigation of Ni-Co based catalyst for H_2 from

oxygenated hydrocarbons such as C_2H_5OH, $C_3H_8O_3$, CH_3COOH and gaseous hydrocarbons such as CH_4, biogas was compiled and reviewed by Giannakeas et al. [178]. The author attributed the positive effect of Co addition to the chemical synergism between the Ni and Co metals. Furthermore significantly lower temperature of reduction is needed in comparison with that of the monometallic systems. In a different approach to reduce C formation use of bimetallic catalyst using alkali metals such as K and Sn [222] and Bi [223] to the catalyst have been investigated. Addition of K or Ca to alumina neutralizes acidic sites of Al_2O_3 and reducing the possibility of coke formation suppressing cracking and polymerization reactions [224]. Carbon gasification reaction is enhanced by addition of K and Ca affecting C deposited on the catalyst surface [225]. It also increases the adsorption of steam on the catalyst surface [226] affecting SR reaction. According to Trimm [222] carbide formation is an essential intermediate route to coke formation, formed by interaction of 2p carbon electrons with 3d Ni electrons. Addition of penta-valent p metals (such as Ge, Sn and Pb or As, Sb or Bi) interacts with Ni_3d electrons, thereby reducing the chance of NiC formation in turn affecting carbon formation. Pengpanich et al [227] found addition of Sn to NiO disrupted the active site ensembles responsible for coking. Solubility of carbon in Ni particles responsible for NiC formation is also reduced by addition of Sn to Ni catalyst.

Espinal et al. [228] investigated the use of K to Co hydrotalcite with molar composition (Co: Mg: Al) of 1:2:1 in CSR of bioethanol. Addition of K was responsible for neutralising the number and strength of the acid sites resulting in stable long-term experiments, with very little amount of C formation. The authors reported that formation of ((Co, Mg) O) during the reaction was the active complex formed due to K addition responsible for the high activity of the catalyst. The addition of K to Co/Ce-Zr had a positive effect on the activity of catalyst in ATR of C_2H_5OH. The conversion of C_2H_5OH increased from 46 to 98% with addition of K to the catalyst. The effect of oxidation treatment over CoRhK/Ce-Zr catalyst was also studied by the authors. In comparison to CoK/Ce-Zr catalyst, CoRhK/Ce-Zr catalyst regained its catalytic activity after oxidation and the catalyst produced H_2 at low temperature of 320°C. In CSRA, Iwasa et al. [229]

reported that addition of K to Ni/ Smectite had the best effect among Li, Na, K, and Rh or Cs dopants. The addition of 1 wt% K increased reduction of Ni species incorporated in the smectite, yielding more metallic Ni species than undoped Ni/Smectite sample thus giving high activity for the K-modified Ni/Smectite catalyst. In case of complex hydrocarbons such as kerosene, addition of K to the catalyst increased the conversion of kerosene and H_2 produced Yu et al. [230] Although K addition, increased CH_4 selectivity as a result of reduced CH_4 decomposition, during the CSR reaction.

3.5 Research Rationale

The use of FAME as a diesel engine fuel has been widely investigated due to its many advantages over vegetable oil as a transport fuel. Analysis of the "Well to Wheel" CO_2 emissions of biodiesel have reported a reduction between 50 to 80% in comparison to those of petroleum diesel. The recent boom in H_2 energy technology has resulted in several investigations of H_2 production from various hydrocarbons and oxygenated hydrocarbons such as ethanol, butanol vegetable oil and bio-oil. On the other hand, H_2 production from biodiesel is very new and only few successful investigations have been reported.

There are several advantages of using biodiesel as a H_2 carrier. One of the important advantage of using biodiesel as H_2 carrier is its renewable nature. First of all, the process for making biodiesel from vegetable / waste cooking oil and animal fat is well-known and a commercialised process. Use of biodiesel as hydrogen carrier would result in lower GHG emissions, since the CO_2 generated during H_2 production would be used by plants grown to produce oil for biodiesel. If ethyl esters are used for H_2 production, advantage of totally recyclable CO_2 cycle can be obtained since ethanol can be produced from biomass. Biodiesel production is predicted to increase from 21750 thousand tonnes per year in 2011 to 39150 by 2020. As a result, assured and continuous supply of biodiesel would be available for H_2 production. Biodiesel contains 11-12 wt % H_2. For e.g. steam

reforming of ethanol will produce 13 wt % of hydrogen from ethanol, which is considerably less in comparison to steam reforming of methyl oleate producing 23 wt % of methyl oleate. Biodiesel contains lower oxygen (11 wt %) which is considerably lower than ethanol (35 wt %) or bio-oil (65 wt %). The presence of oxygen would affect hydrogen production lowering hydrogen yield.

Biodiesel has shorter carbon chain length compared to vegetable oil making it easier to convert to H_2 and is expected to form relatively lower amount of carbon. Waste cooking oil contains free fatty acids formed as a result of cooking or frying processes. These free fatty acids are responsible for formation of aromatics which are known precursors for carbon formation during hydrogen production processes. The free fatly acids are removed during biodiesel production in turn affecting the life of catalyst during hydrogen production. Similarly biodiesel lacks aromatics present in diesel again responsible for carbon formation during hydrogen production. Similarly other catalyst poisons like sulphur, chlorine, phosphorus and calcium are absent in biodiesel, increasing catalyst life. Biodiesel is non-toxic, biodegradable, handling and storage are much safer than conventional petroleum diesel fuel due to high flash point. Biodiesel has higher energy density ~40 MJ/kg in comparison to 29.7 and 15-19 MJ/kg for ethanol and bio-oil respectively. As a result of high energy density, lower amount of biodiesel would be required to be combusted in hydrogen production process such as autothermal reforming to generate the internal heat required to drive the process. Other advantages like higher lubricity and lower viscosity would be useful for injectors and pumps used in hydrogen production processes. Absence of compounds like sulphur would prevent the formation of SO_2 in hydrogen production processes like autothermal and chemical looping reforming. Biodiesel produced from waste cooking oil is cheaper as cost of waste cooking oil is almost free. As of today the cost of biodiesel on a petrol station is £ 1/l in comparison to 1.3£/l for diesel. The hydrogen produced from this type of biodiesel would cheaper as compared to hydrogen produced from diesel. New sources of oil i.e. non edible oils like Jatropha, Karanja or algae are being investigated widely to reduce the cost of biodiesel and in turn reduce the cost of H_2 produced.

3.6 Aim and Objective

The aim of this research project is to investigate hydrogen production from biodiesel via steam and autothermal reforming. To accomplish this aim, the following objectives are drawn.

- Design and commission an experimental set up for hydrogen production via steam and autothermal reforming of biodiesel.

  The important tasks involved to fulfil this objective were design and building of vaporisers for biodiesel and water.

  - Building a frame for the installation of the vaporisers and the reactor.
  - Selection of PID controllers and building of the controller unit for mounting the PID controller and the necessary electronics.
  - Pipe work for connecting the vaporisers and the reactor.
  - Installing and commissioning of micro-GC for the analysis of the products coming out of the reactor. Building a condenser for cooling the reactor gases and separating the condensed vapours from the gases.
- Preparation of an effective H_2 production catalyst exhibiting high H_2 yield, biodiesel and steam conversion.
- Examining the effect of catalyst preparation methods and types via catalyst characterisation techniques for catalyst selection.
- Testing the prepared and commercial catalyst in the reactor. Performing mass balance calculations for determining H_2 yield, biodiesel and steam conversions in addition to H_2 selectivity along with selectivities of carbon gases. Comparison of experimental results with equilibrium counter parts to determine the process efficiency.

  Optimisation of operating parameters such as biodiesel preheating to maximize H_2 yield, biodiesel and steam conversion.

- Determine the optimum reactor temperature in order to maximize H_2 production.
- Determining the effect of S/C and WHSV on H_2 yield in addition to biodiesel and steam conversion.

To analyse the effect of biodiesel types on the performance of the steam reforming process.

Characterisation of used steam reforming catalyst and calculation of overall system efficiency by calculating the carbon balance of the process.

- The characterisation work would involve XRD of the used catalyst to determine the sintering of the catalyst.
- Similarly examining the surface area of the used catalyst to access signs of surface area reduction.

Examining autothermal reforming of biodiesel using the optimised parameters such as S/C ratio, WHSV, vaporiser temperatures and reactor temperature obtained from steam reforming experiments.

- The examination of O_2/C, S/C and WHSV on the performance of autothermal reforming process.
- Evaluation of process performance and efficiency by performing mass and energy balances.
- Comparing the experimental results with equilibrium results to determine process efficiency.
- The determination of autothermal conditions will be achieved using energy balance calculations. Determination on of overall system efficiency calculation using carbon balance of the process.

4. Methodology experimental methods and materials

This chapter describes the construction and building of the experimental set up. The problems associated with it and the solutions implemented to resolve the problems. This chapter also explains the preparation of biodiesel and catalyst used in the experiments and it also describes the various methods used for characterisation of the same.

4.1 Reactor design and experimental setup building

The reactor systems used for the experiments were designed and built at the Energy Research Institute, University of Leeds. They were a replica of an existing larger rig. Initially the reactor was placed at the top to provide an up flow arrangement. The setup had to be modified a few times due to the condensation of vapours and steam during the experiments. The rig consisted of two vaporisers, reactor, pumps, mass flow controllers, condenser and micro gas chromatograph for the analysis of the products. The vaporisers consisted of 180 mm long aluminium and stainless steel solid cylinders, heated with cartridge heaters supplied by Elmatic Cardiff, UK. The cylinders were provided with two ¼ " od stainless tubes in which actual vapourisation of biodiesel and water occurred by indirect heating. Due to absence of holding mechanism as a result of the size of the vapouriser tube inert material could not filled in the tubes. In the first of the setups, the vapourisers were mounted on aluminium plate connected to the frame as shown in Figure 4.1.

A ½ " od SS 310 tube was used as a reactor. The tube placed in an electric furnace (Elite thermal systems, UK). A special controller unit was built comprising of two limit based controllers (Watlow Ez zone) used to control the cartridge heaters. A Eurotherm controller present with the furnace was used for its control. The schematic of the rig with an up flow arrangement with reactor at the side is shown in the Figure 4.2.

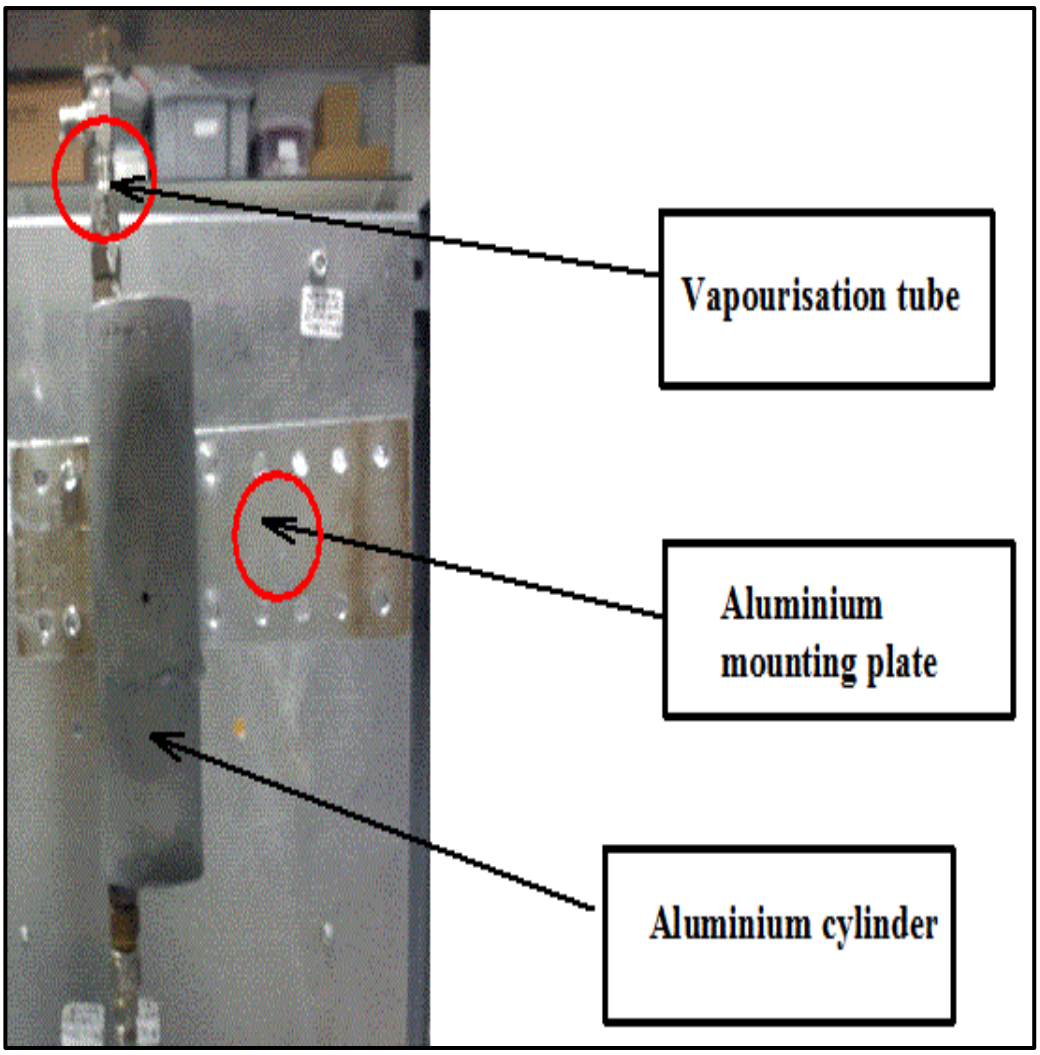

Figure 4.1: Schematic of vaporiser assembly.

Dual junction thermocouples supplied by TC direct, UK were placed in either vapourisation tubes to measure the temperature and provide a signal for the controllers (Watlow EZ-zone) controlling the power provided to the heaters. First junction of the dual junction thermocouples was connected to the controllers while the second junction was connected to a temperature logger (TC08, PicoTech). The vaporisers were fed with biodiesel and water by means of two syringe pumps (NE-1000) supplied by New era, Ltd, using 25 ml SGE gas tight glass syringes. Mass flow controllers supplied by MKS

instruments, UK were used to meter N_2 and air flow for SR and ATR experiments. A separate mass flow controller was used to control the flowrate of 5 vol% H_2/N_2 used for the reduction of the catalyst. The third mass flow controller used for the metering of 5 vol% H_2/N_2 mixture during catalyst reduction is not shown in the Figure 4.2.

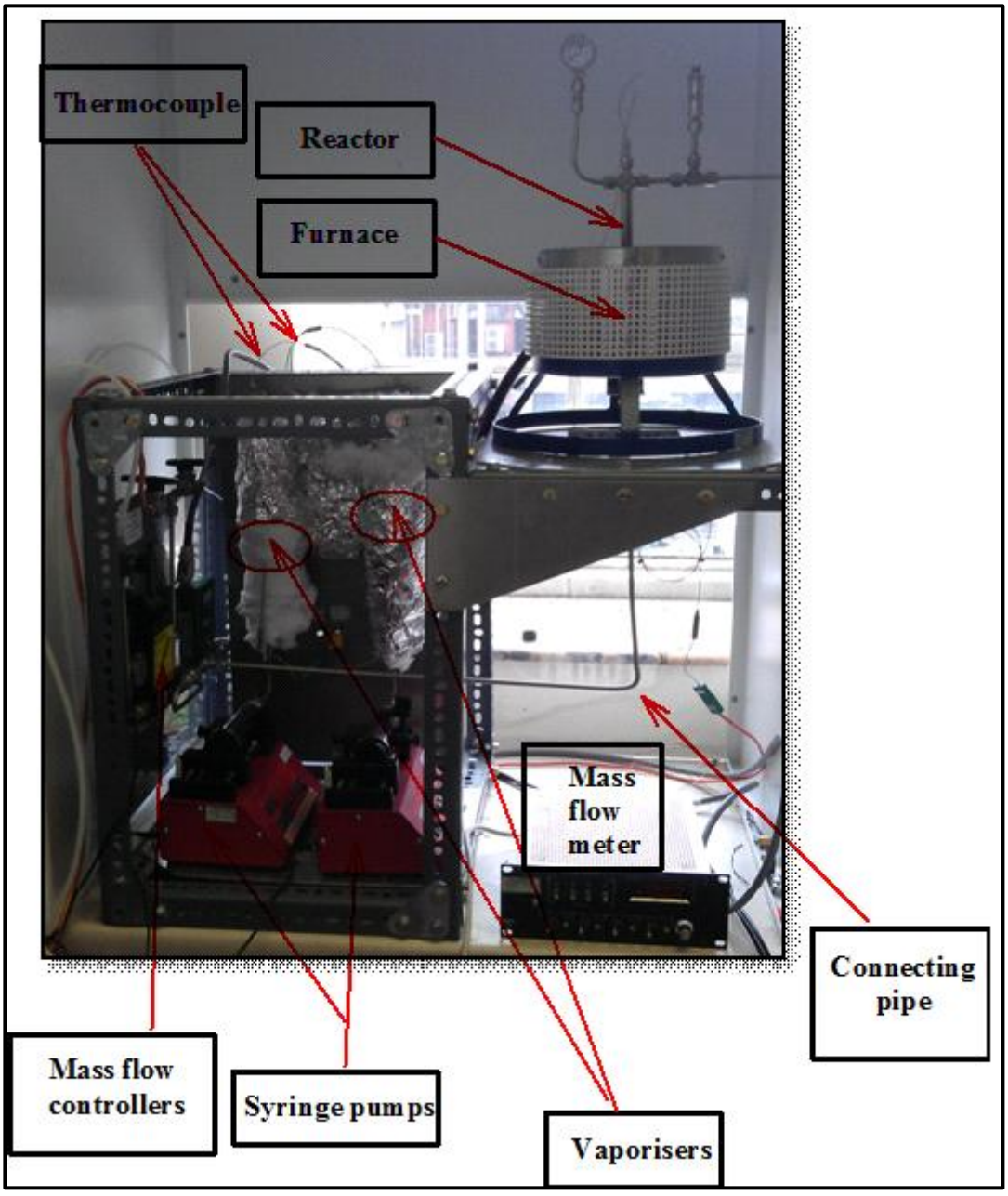

Figure 4.2: Schematic of up flow reactor with reactor at the side. In the Figure the first vapouriser on the left hand side was used for biodiesel.

The hot vapours from the vapourisers were mixed with N_2 below the reactor in a Swagelok cross provided with a thermocouple as shown in Figure 4.3. This thermocouple was known as the reactor inlet thermocouple. A second thermocouple was provided in the reactor bed. Both the thermocouples were connected to the pico-logger for recording the temperature. Both vaporisers and the furnace were insulated with super wool and aluminium foil (Figure 4.2) to minimise the heat loss and hence reduce the energy requirement of the system; the controller associated with each vaporiser was checked and tuned to the experimental specifications. A series of steam reforming experiments were performed by setting both the vaporisers at 365°C and reactor temperature of 600°C. Various different flow rates of biodiesel and steam and N_2 were tried.

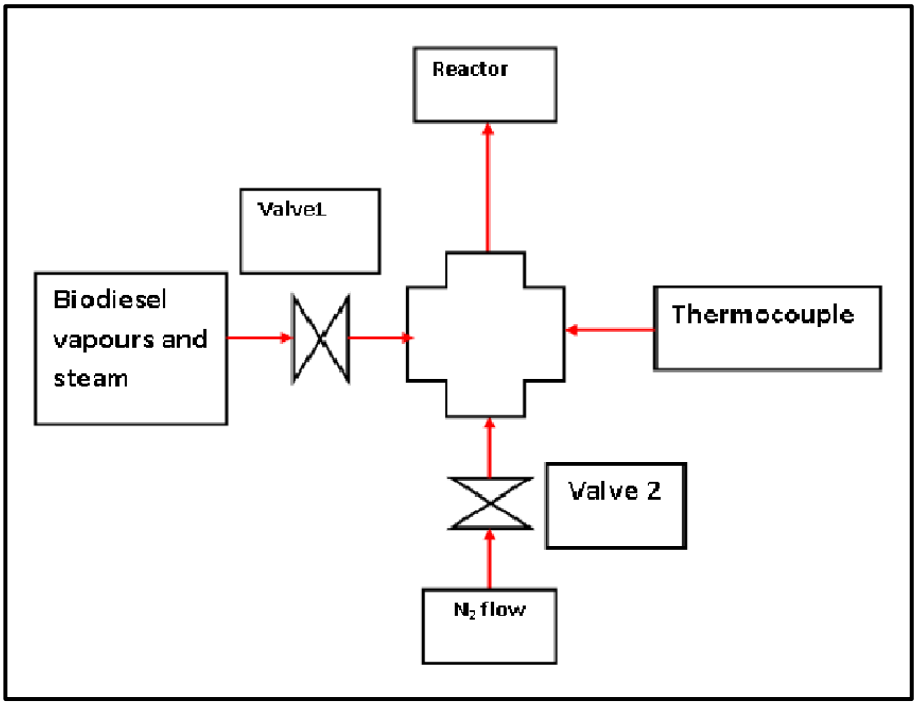

Figure 4.3: Schematic of up flow reactor inlet.

The condensation of hot biodiesel vapours and steam with cold N_2 resulted in unsteady reactor operation, resulting in low amounts or no products. In order to improve the reactor operation and minimise the condensation of reactants, it was decided to move the reactor at the top of the frame, in line with the vaporisers, and preheat the N_2 by making use of the heat from the heated vaporisers. The two N_2 preheating coils were made from 1/8" od copper tubing and were placed on the vaporisers surfaces as shown in the Figure 4.4.

The modified reactor setup with the reactor placed on the top of the vaporisers is shown in the Figure 4.5. In the figure the first vaporiser on the left hand side was used for biodiesel. As a result of insulation the N_2 preheating coils placed on the vaporisers (Figure 4.4) are not visible in this figure. In the modified set up the pipe length from the vaporisers to the reactor was reduced in order to prevent the condensation of the biodiesel vapours and steam. A non return valve (check valves Figure 4.6) was used to prevent the flow of the N_2 towards the vaporiser and divert it directly in the reactor (Figure 4.6).

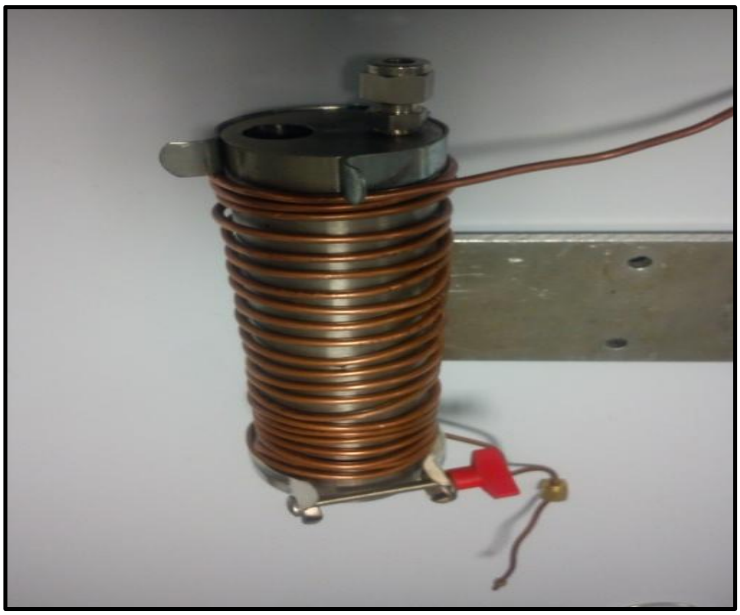

Figure 4.4: Schematic of the copper coil used for N_2 preheating.

As the vapour pressure of the steam and biodiesel was smaller than the cracking pressure of the check valve. The valve remained partially opened resulting in only small amount of vapours being carried in the reactor to achieve stable operation. The condensed vapours collected in the pipe and after a while created back pressure on the biodiesel pump, resulting in the pushing the syringe backwards causing spillage of biodiesel on the pump body and the experiments had to be stopped. The copper coils also were oxidised due to constant use. In order to prevent the entire condensation problem, the position of the reactor was changed a third and final time from up flow to down flow. Figure 4.7 shows a process and instrumentation diagram for down flow reactor system. Figure 4.8 shows the down flow reactor arrangement with stainless steel preheating coils. The coils were made from ¼" od stainless steel tubing by Swagelok, UK. The coils were made from 180 mm long ¼" od stainless steel tubing coiled to fit on the vaporisers. The biodiesel vaporiser was placed at the top of the reactor with water vaporiser to the left of it as shown in Figure 4.8, to facilitate direct injection of the biodiesel vapours into the reactor and prevent condensation.

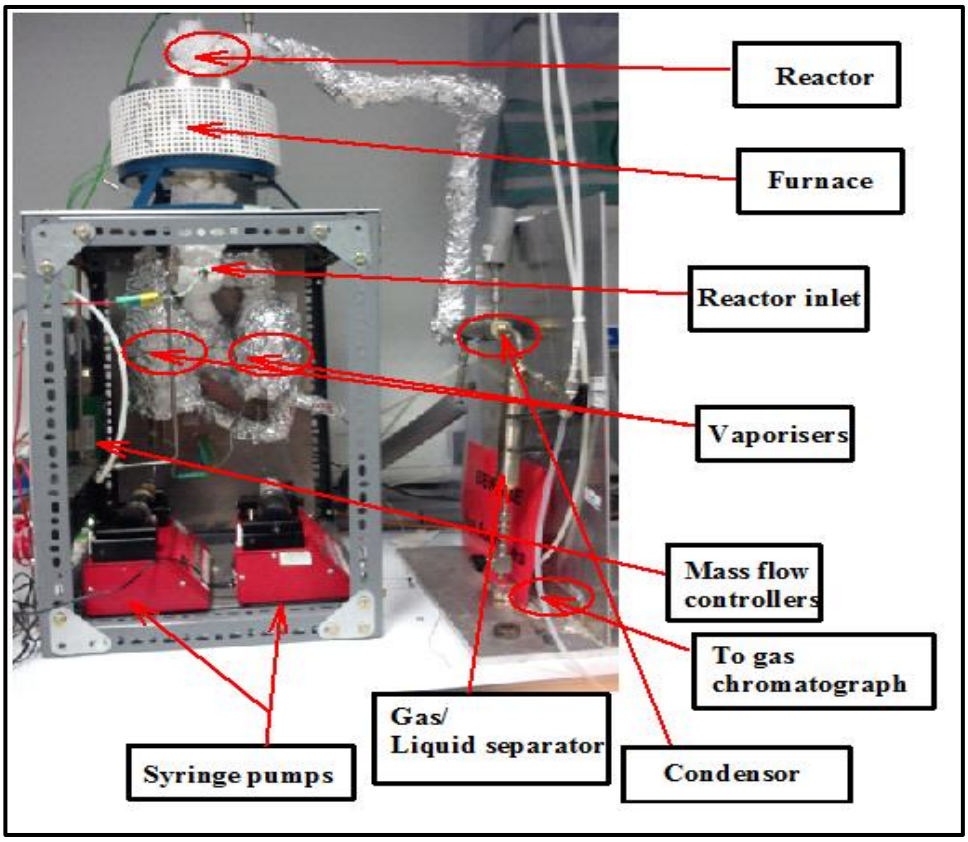

Figure 4.5: Modified reactor setup with up flow reactor at the top. In the Figure the first Vapouriser on the left hand side was used for biodiesel.

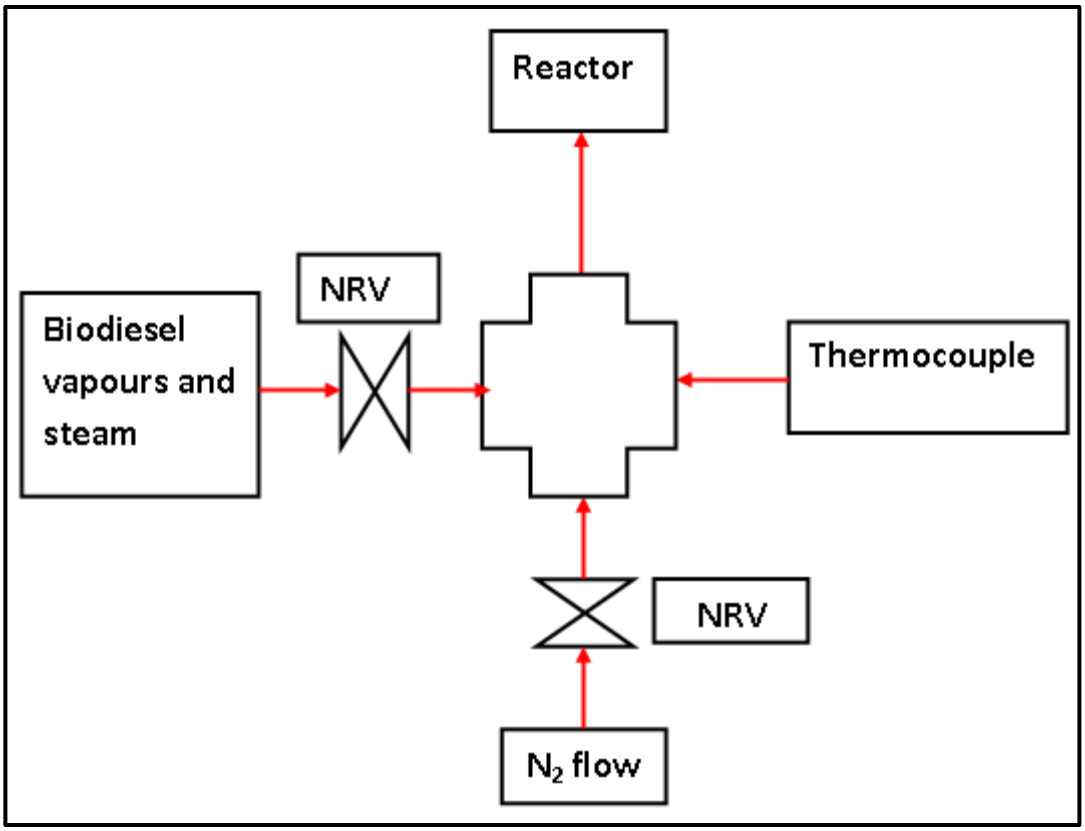

Figure 4.6: Schematic of valve assembly used in the modified reactor.

The biodiesel and water vaporisers were connected via ¼" od stainless steel tubing. During an experiment the biodiesel and water vaporisers were set to the desired temperature using the Watlow (Ez zone PM controller) and reactor. The desired biodiesel and water flowrates were maintained by means of the syringe pumps. Reactor temperature was set by the Eurotherm controller. The hot vapours were mixed with preheated N_2 in Swagelok cross provided with a thermocouple as shown in Figure 4.7.

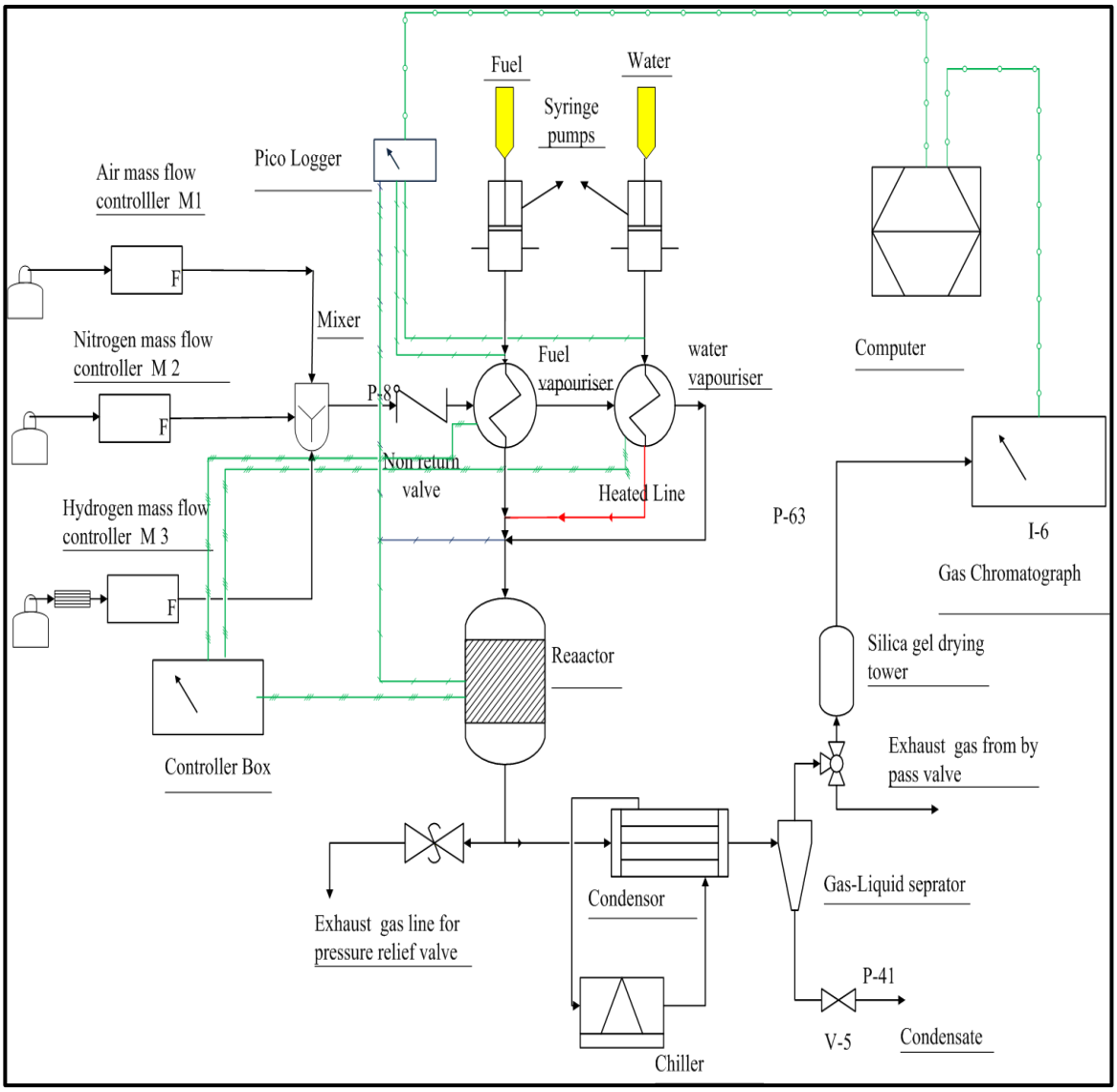

Figure 4.7: Process and instrumentation diagram of the down flow experimental set up. In the figure the green lines represents signal connections and the black are the processes connections.

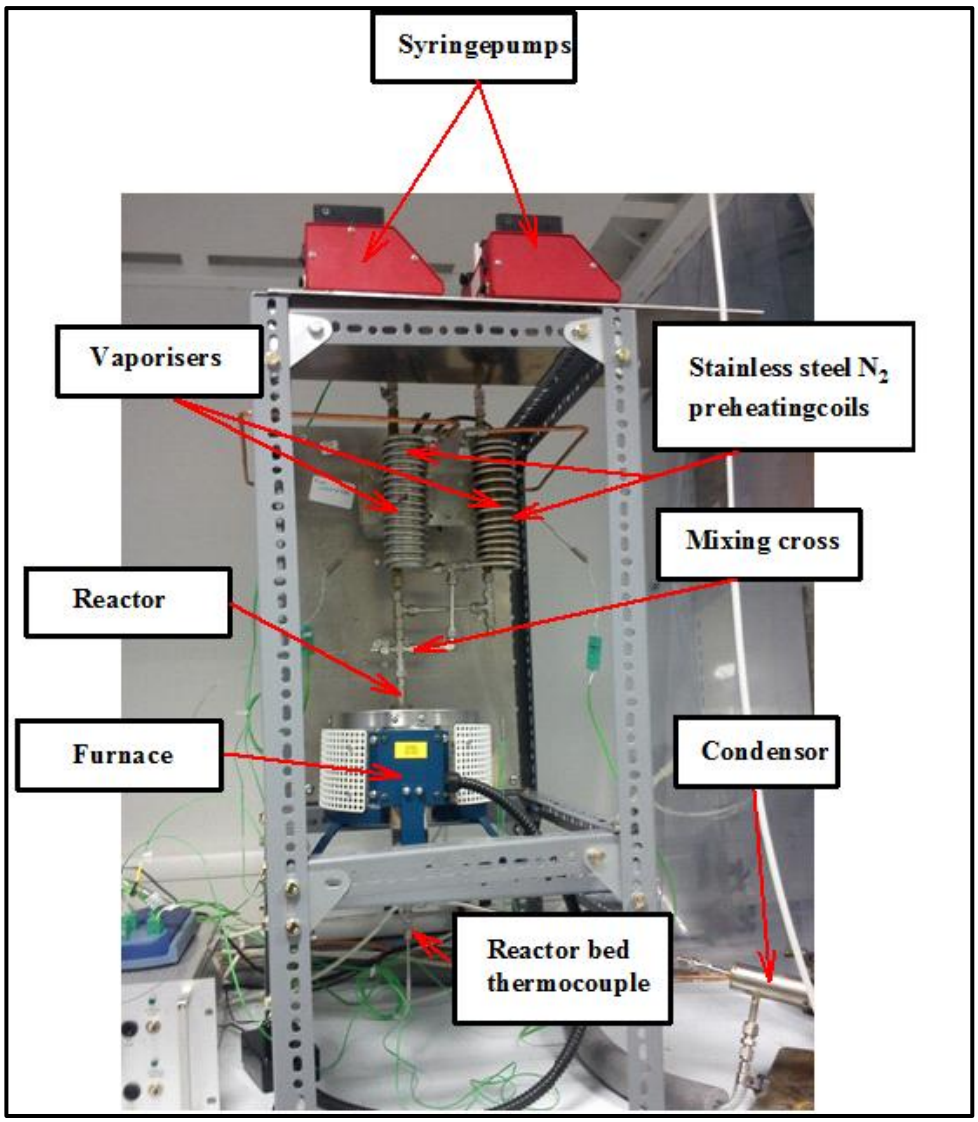

Figure 4.8: Schematic of un-insulated down flow reactor.

The flowrate of N_2 was controlled by mass flow controllers (MKS Instruments, UK) shown in the Figure 4.8. The arrangement of mass flow controllers had to be modified slightly from the previous arrangements. The three mass flow controllers were mounted on a stand and were placed near the controller box shown in the Figure 4.9. This mixture of vapour, steam and N_2 passed through the reactor maintained at the desired temperature. The condensed vapours and unreacted steam passed through the condenser

and were collected in the gas/ liquid separator connected to the condenser. The condenser was a double pipe type, in which the gases and the vapours flowed in the inner pipe and water was circulated in the annulus between the inner and the outer pipe. Cold water at 1°C was circulated by means of a chiller connected to the condenser. The condensed vapours and unreacted steam was collected and removed from the bottom of the gas-liquid separator (Figure 4.10). The product gases (H_2, CO, CO_2, CH_4, C-2 to C-3 hydrocarbons and N_2) leave the gas liquid separator and were passed through a silica gel trap to remove the moisture. The gases were finally transferred to an online gas chromatograph for composition analysis (Figure 4.10).

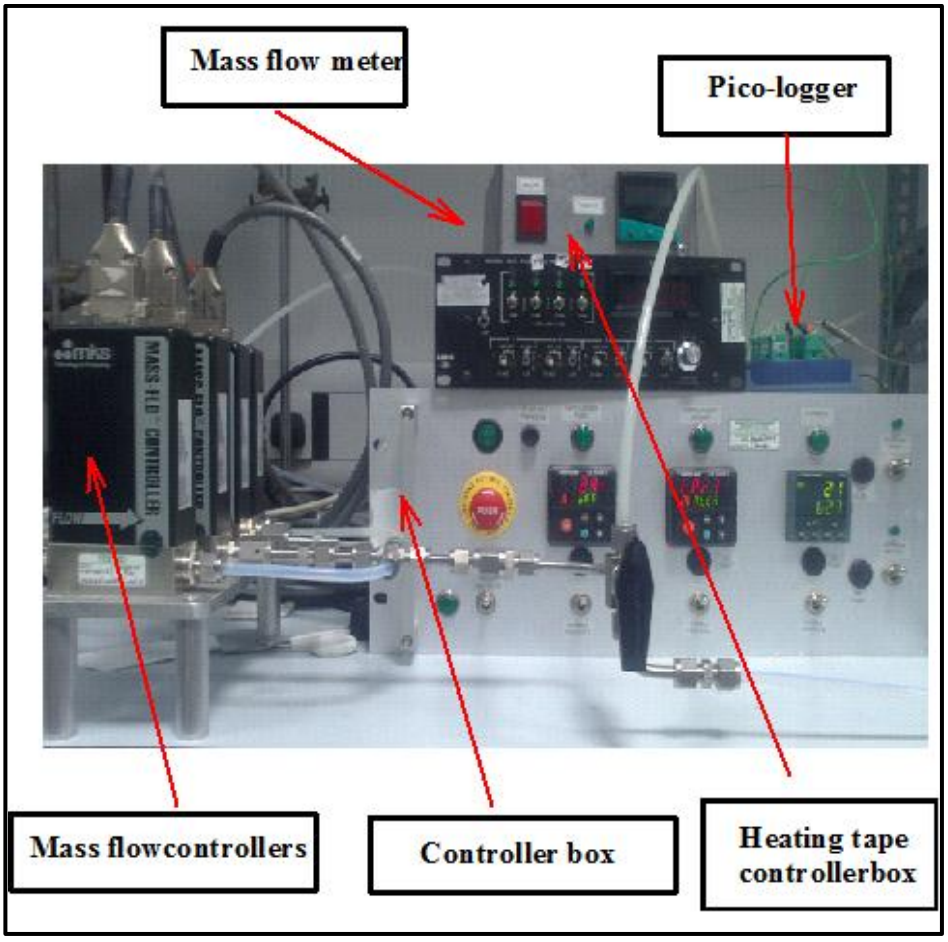

Figure 4.9: Arrangement of mass flow controllers and schematic of the controller box.

The vaporisers were insulated with super wool insulation material (Good fellows, UK) in order to prevent the heat loss from the preheating coils. To maintain the steam temperature in the tubing connecting the biodiesel vaporiser and the water vaporiser, a heating tape was provided as shown in Figure 4.11. The initial investigation, performed in the absence of the heating tape still revealed steam condensation in the tubing connecting both the vaporisers, which created back pressure on the water syringe pump. The heating tape was provided by the engine research group.

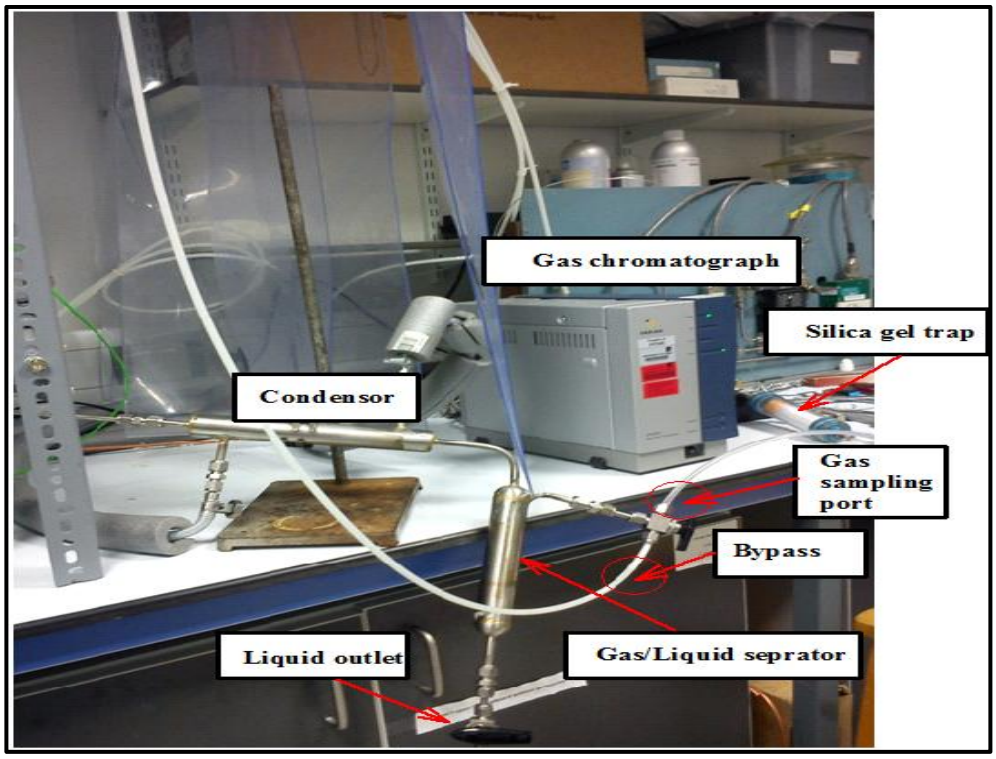

Figure 4.10: Condenser and gas drying schematic connected to the micro gas chromatograph.

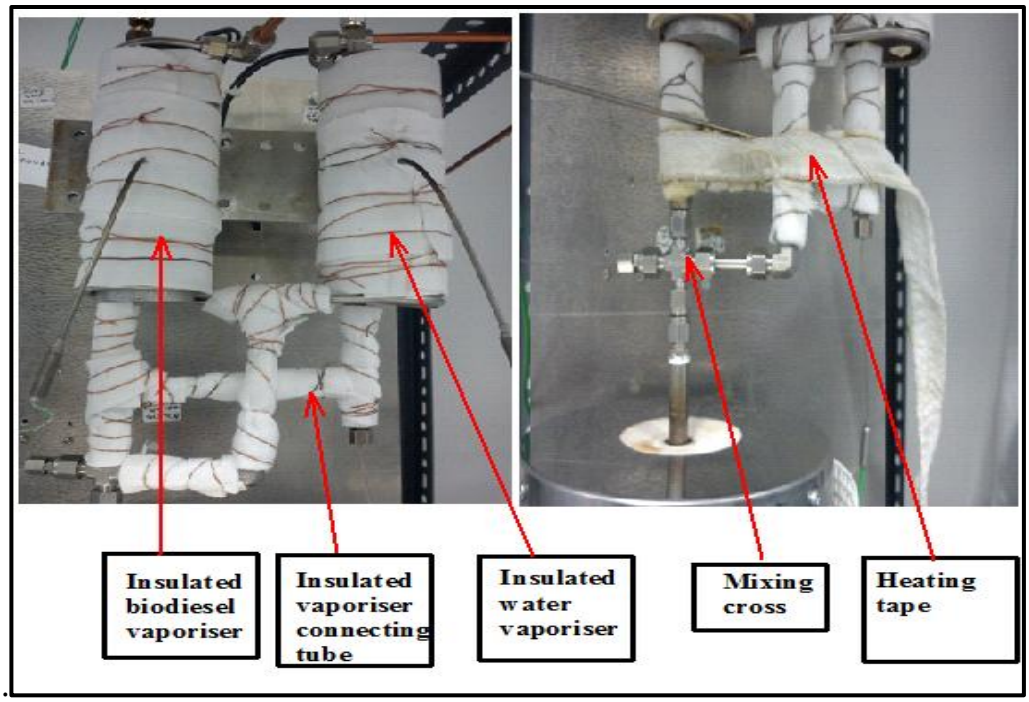

Figure 4.11: Insulated vaporisers and heating tape arrangement.

4.2 Gas chromatograph

The most important part of the experimental setup was the micro gas chromatograph (micro GC). Figure 4.12 shows the micro gas chromatograph (CP 4900) supplied by Varian Instruments, UK. The instrument was connected to a silica gel trap as shown in the Figure 4.10. The gas chromatograph was equipped with two thermal conductivity (TCD) detectors and two columns. Molecular sieve 5A plot and Pora Plot Q columns were provided with the gas chromatograph for the analysis of H_2 and carbon gases. The molecular sieve 5A (column 1) was 10 m long column with 0.32 mm id and was used for the analysis of H_2, O_2, N_2, CH_4 and CO. The Pora Plot Q (column 2) was used to detect CO_2, C_2H_4, C_2H_6, C_3H_6 and C_3H_8. In addition to these gases, column 2 also detected CH_4. Two pre columns were provided for both the columns to prevent unwanted condensate or moisture entering the columns. Column 1 was operated with a back flush of 13 s, which prevented CO_2 from entering the column. The presence of CO_2 disrupts stable column operation as it entered the pores of the molecular sieve column affecting

the column performance. The poisoned column had to be regenerated by heating to 180°C. This operation required a long time due to oven temperature limitation. In order to prevent this from happening, column 1 was always operated with back flush option. The columns were conditioned after every experiment by heating to 180°C to get rid of the moisture, which might enter the columns. Although the silica gel trap removed most of the moisture before the gas from the reactor was sampled by the gas chromatograph.

The run time for the gas chromatograph was about 2.5 min which is much faster than conventional gas chromatographs and therefore was more suited to the dynamic processes investigated. The column temperatures were set to 100°C at 100 kpa pressure. It was equipped with a pump which withdrew gas sample from the silica gel trap. The pump had a sampling time of 20's. The inlet sample line to the gas chromatograph was maintained at 45°C. The Galaxie data acquisition software was provided by the manufacturer to set the column conditions and other essential parameters for the instrument. An external standard method was used for the analysis of the products. The instrument was calibrated with various gas mixtures of different concentration to obtain a good calibration curve for all the gases (Appendix A).

Figure 4.12: Micro gas chromatograph used for gas analysis.

4.3 Biodiesel and catalyst preparation

This section describes the preparation of biodiesel and catalysts used in the study. It also explains the various techniques used to characterise biodiesel and the catalysts.

4.3.1 Biodiesel preparation

Three different kinds of biodiesels i.e. commercial, palm and in-house prepared biodiesel were used in this study. The commercial biodiesel was provided by the engine research group, Energy Research Institute, University of Leeds which was procured from a petrol station in Huddersfield, UK. Likewise palm oil based biodiesel was procured from the crystallisation science and engineering research group, Institute of Particle Science and Engineering, University of Leeds.

In house biodiesel was prepared using the method described in [231]. Waste cooking oil was collected from a local restaurant and was converted to biodiesel using acid-base transesterification processes due to the presence of high amount of free fatty acid in the waste cooking oil. Waste cooking oil was esterified using different concentration of sulphuric acid (1.5 to 3% w/w) at 65 ^{o}C with methanol/oil ratio of 3/7 (v/v). The esterified mixture was transesterified using KOH (1.5, 2 and 3% w/w) in methanol (methanol/oil ratio 3/7(v/v)). The acid-base transesterification was performed in a 500 cm^3 three neck flask fitted with a condenser and a thermometer as shown in Figure 4.12. The condenser was fitted with a condenser to condense methanol vapours formed during the processes. The waste cooking oil was filtered to remove insoluble impurities and was heated to 100° C for 15 min to remove the moisture.

A 250 g of waste cooking coil was measured and its volume was recorded. The waste cooking oil was heated to 65°C in a beaker on a hot plate and was poured in the three

neck flask as shown in Figure 4.12. Sulphuric acid was dissolved in methanol and was heated to 50 °C to prevent boiling. This mixture was the added to the hot oil in the three neck flask and was vigorously stirred for 3 h at 400 rpm by means of magnetic bar placed in the three neck flask. The esterified oil was cooled and was allowed to settle overnight and subjected to the base catalysed transesterification process using KOH as catalyst. The esterified oil was measured and the volume was recorded. It was heated to 50 °C on a hot plate and was poured in a clean three neck flask. Potassium hydroxide (1.5, 2 and 3 % w/w) was dissolved in methanol (methanol/oil ratio of 3/7 (v/v)) which was also heated to 50 °C and mixed with the hot oil. This mixture was stirred for 3 h at 50 °C with constant stirring. The transesterfied oil was cooled over night and was separated in a separating funnel where the heavier glycerol layer was separated from the lighter methyl ester (biodiesel). The biodiesel was washed with water to remove unreacted methanol and glycerol.

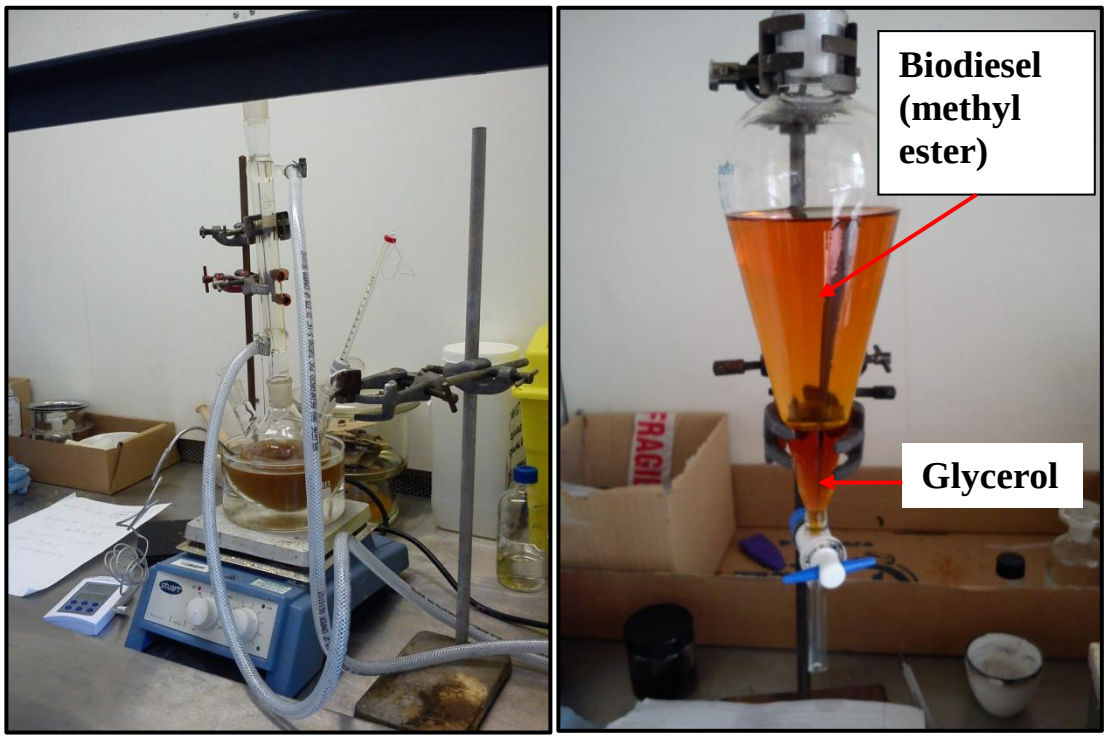

Figure 4.13: Acid- base catalysed transesterification set up.

4.3.2 Biodiesel characterisation

Biodiesel samples were subjected to elemental analysis (C/H/N/O), Thermogravimetric analysis (TGA), composition analysis (gas chromatography), acid value, and free fatty acid determination.

4.3.2.1 Elemental Analysis

The biodiesel samples were characterised using various techniques. Biodiesel samples were subjected to elemental analysis to determine the composition of C/H/N/S by means of a Thermo Flash EA 1112 series CE instrument. Biodiesel samples of 3 mg were placed in thin tin capsules and the capsules were folded to avoid air entrapment. The folded capsules were placed in the autosampler of the analyser which were further combusted in the reactor chamber with excess oxygen at 1800°C. The elemental C, H, N and S were converted to CO_2, H_2O, nitrogen oxides and SO_2. These gases were detected by a TCD detector and compared with standard to determine the percentage of C, H, N and S. An oat meal with BBOT (2, 5-Bis (5-tert-butyl-2-benzoxazolyl) thiophene was used as standard for the analysis. The oxygen content of the samples was determined by difference. It is important to note that biodiesel samples did not contain any N and S.

4.3.2.2 Thermogravimetric analysis (TGA)

A Stanton Redcroft TGH-1000 instrument was used to perform a proximate analysis of the biodiesel samples. This instrument makes use of horizontal differential balance to measure weight change of the sample with respect to time and temperature under isothermal conditions. The experiments were performed using 5 biodiesel samples (1.5, 2 and 3 wt% biodiesel, commercial biodiesel, and palm oil biodiesel), in order to compare

the volatile, carbon residue and ash content weight percentages. For every experiment 180 mg of sample was used. The samples were placed in the TGA and were subjected to the following heating program.

- 5 °C/min from ambient to 400 °C with 50ml/min of nitrogen.
- 25 °C/min from 400 °C to 900 °C with 50ml/min of nitrogen.
- Held at 900 °C for 10 minutes with 50ml/min of air.

The data obtained from the TGA was used to determine the wt% of the volatile, carbon residue and ash. The volatile percentage is given by the main mass loss around 200-500°C. The carbon residue is determined by the weight at which air is added to the system which is at 900°C. The ash content was the weight remaining at the end of the analysis as this material cannot be burnt thus remains in the pan. The weight (initial minus final for volatiles) given by the equipment in comparison to the initial weight was used to produce the percentage data.

4.3.2.3 Composition analysis

The composition analysis of the biodiesel samples were provided by crystallisation science and engineering research group, Institute of Particle Science and Engineering, University of Leeds. Clarus 500, Perkin Elmer fitted with flame ionisation detector, using a 100 m long, 0.25 mm i.d. and 0.25 μm film thicknesses, fused silica column (SUPELCO SP^{TM} 2380). The biodiesel sample was diluted in toluene before performing the analysis.

4.3.2.4 Acid value and free fatty acid determination

The acid value of the biodiesel and the waste cooking oil samples was determined using EN 14104 which is comparable to ASTM-D974. A 0.1 M solution of KOH in ethanol was prepared by dissolving 3.5 g KOH in 500 ml ethanol. Biodiesel or oil sample (10 g) was dissolved in toluene. This solution was titrated against 0.1 M alcoholic KOH using phenolphthalein as an indicator. The alcoholic KOH solution was placed in a micro burette and added drop wise to the oil-toluene mixture, with constant stirring. The end point was color change from light yellow to light pink that lasted at least for 15 s. The following Eqs 4.1 and 4.2 were used to determine the acid value and free fatty acid content.

$$\text{Acid value} = \frac{56.1 \times V \times c}{m} \tag{4.1}$$

$$\text{Free fatty acid as \% of oleic acid} = \frac{282.46 \times V \times c}{m} \tag{4.2}$$

In the above Eqs, V is the volume, in ml of standard KOH solution used, c is the concentration of the KOH solution in moles/lit and m is the mass of the sample (biodiesel or vegetable oil) in g. Finally 56.1 and 282.46 are the molar mass of KOH and $C_{18}H_{34}O_{2.}$

4.3.2.5 Bomb calorimetry

Bomb calorimetry was performed on the 5 biodiesel samples using a Parr Instruments model-6200 bomb calorimeter to determine the gross calorific value of the samples. The biodiesel samples were placed in a metallic bomb as shown in Figure 4.13 which was

pressurised to 3 bars in pure O_2 environment. The bomb was placed exactly 2 L of water and the sample was lit by a fuse. The rise in temperature of the water was correlated to the energy released by sample combustion which in turn provides the gross calorific value (GCV) of the sample. During the tests test sample sometimes did not ignite as a result biodiesel samples had to be spiked with kerosene or silicon tape to ensure ignition propagation to sample and achieve complete combustion. The calorific value of the spike is subtracted from the total to get the actual calorific value of the biodiesel sample.

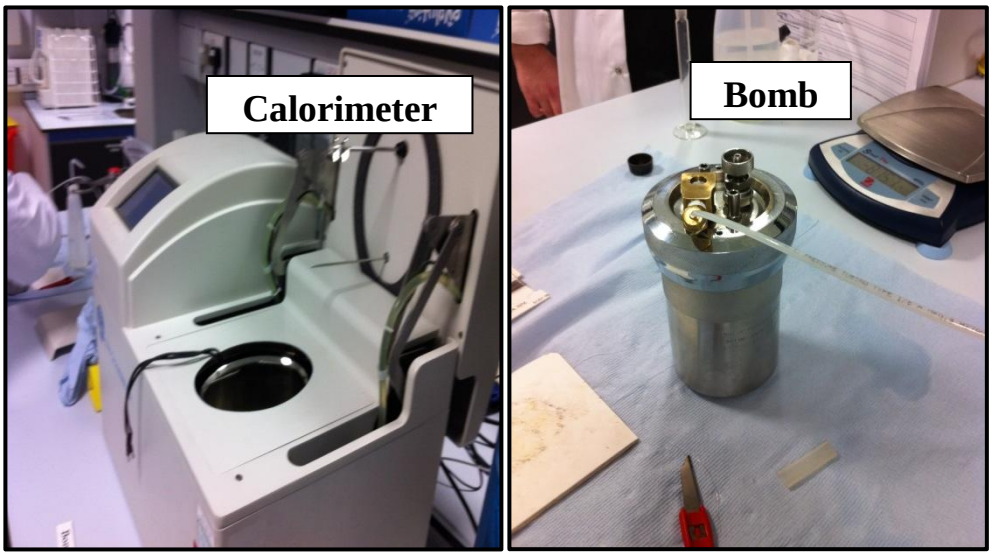

Figure 4.14: Parr instruments bomb calorimeter

4.3.3 Catalyst preparation

Nickel based catalyst were used in this investigation. Two commercial catalysts i.e. Ni supported on Al_2O_3 and Ni supported on calcium aluminate were tested in addition to in-house prepared catalysts. An 18 wt% Ni supported on α-Al_2O_3 was supplied by Johnson Matthey, Plc. On the other hand the 15 wt% Ni supported on calcium aluminate was provided by TST, Ltd. These two catalysts i.e. 18 wt % NiO supported on α-Al_2O_3 and 15 wt% supported on calcium aluminate will hence forth be referred as Ni/Al and Ni/Ca-Al. The difference between fresh and used will be pointed out by use NiO for fresh and Ni

for used e.g. NiO/Al will represent fresh 18 wt% NiO supported on α-Al_2O_3 and Ni/Al would be the used. This terminology will be used for rest of the catalysts as well. Figure 4.14 shows the commercial NiO/Ca-Al and NiO/Al catalysts supplied by TST, Ltd and Johnson matthey, Plc.

The 18 wt% Ni supported on α-Al_2O_3 was doped with K to obtain K doped catalyst. The commercial pellets (27.63 g) obtained from the manufacturer were soaked in a solution of KNO_3 in water (20 wt%) for 3h. The pellets were dried over night at 120°C in an oven and calcined in a furnace. The calcined pellets were weighed again (28.091 g). The loading of K was calculated to be 1.67 wt%. The K doped catalyst will be referred as Ni-K/Al throughout the thesis. The fresh catalyst would be NiO-K_2O/Al and used would be Ni-K/Al.

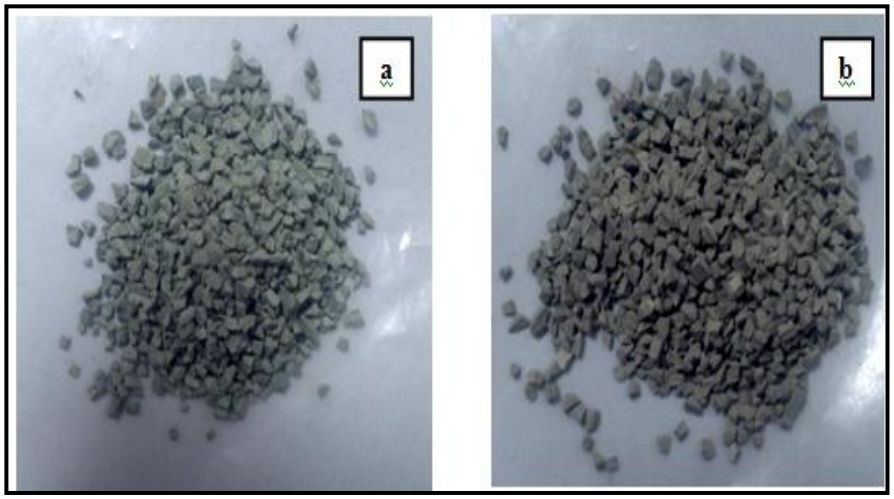

Figure 4.15: Commercial NiO/Ca-Al (a) and NiO/Al (b) catalysts.

The Ni-Co-Ce/γ-Al_2O_3 was prepared by Giannakeas et al.[178]. The Catalyst was prepared by wet impregnation of γ-Al_2O_3 stabilised by calcining at 600°C. The active metals Ni, Co and Ce were introduced by appropriate nitrate salts to give 6 wt% Ni, 3 wt % Co, and 5 wt% of Ce. This catalyst hence forth in the thesis will be referred to NiCoCe/Al. In case of fresh catalyst it will be referred as NiOCoOCeO/Al and used will stated by NiCoCe/Al.

Nickel impregnated catalysts were prepared using two different supports. One support was Ce rich support prepared in the lab, while the other was Zr rich support supplied by MEL Chemicals, UK.

4.3.3.1 Preparation Ni supported on Zr rich supports

A 17 wt% cerium doped zirconia oxide ($Ce_{0.12}Zr_{0.88}O_2$) and hydroxide supplied by MEL chemicals, UK were utilised in catalyst preparation. The hydroxide material was calcined and converted to oxide and was used in the preparation of the catalysts. This material was calcined at 600 °C for 6 h. Thus the oxide support obtained from the hydroxide hence forth will be referred as in house calcined Ce-Zr support and the oxide support provided by the manufacturer will be referred as pre calcined Ce-Zr support (Figure 4.15). The in house calcined support was used to prepare catalyst by two different methods i.e. wet impregnation and dry impregnation methods.

Figure 4.16: Ce-Zr support supplied by MEL chemicals, UK.

In wet impregnation method 6g of in house calcined Ce-Zr support was impregnated with different amounts of precursor to obtain 10, 20 and 30 wt% NiO loading, using $Ni_2NiO_6.6H_2O$ as Ni precursor. In case of 10 wt% NiO loading, 2.33 g of $Ni_2NiO_6.6H_2O$ was dissolved in 50 cm^3 of distilled water and in house calcined Ce-Zr was added to it and stirred continuously for 3 h using a magnetic needle on a hot plate without heating. The impregnated material was drilled in an oven at 120 °C to remove the water and the dried powder was calcined at 600 °C for 6 h in a furnace. Exact same procedure was adopted to prepare other catalysts with 20 and 30 wt% NiO loadings.

In the dry impregnation method, the calculated amount of nitrate salt was added to 50 cm^3 water which was slowly added to the catalyst support via a burette. Once a paste was formed the addition was stopped and the material was dried over a hot plate to evaporate the water; this procedure was repeated until all the solution had been added and the material was dry. The solid was then calcined using the same methodology (600 °C for 6 hours).

It was found that the wet impregnation method produced smaller Ni crystallite size. The surface area of the pre calcined material, supplied by MEL chemicals was higher as compared to the in house calcined support. As a result the precalcined support and wet impregnation method was used in the preparation of the catalyst. In preparation of 10 wt% NiO supported on pre calcined Ce-Zr, 30 g of Ce-Zr support was used. The precursor $Ni_2NiO_6.6H_2O$ (11.64 g) was dissolved in 50 cm^3 distilled water and the support was added and continuously stirred for 3 h. The impregnated material dried at 120 °C and calcined at 600 °C for 6 h. In addition to this two other catalysts with 2 wt% K_2O and SnO were also prepared using the same method. The dopants were simultaneously impregnated over the precalcined Ce-Zr support. In order to obtain K doped Ni catalyst, 1.28 g of KNO_3 and 11.36 g $Ni_2NiO_6.6H_2O$ were dissolved in same amount of water and the impregnation of the precalcined support was achieved. In the case of the Sn doped Ni catalyst, 0.23 g of SnC_2O_4 and 11.36 g $Ni_2NiO_6.6H_2O$ were used in the preparation. The NiO catalysts prepared using wet impregnation of precalcined

Ce-Zr support are represent in Figure 4.16. The fresh 10 wt% NiO supported on pre calcined Ce-Zr will be referred as NiO/Ce-Zr and other two with 10% Ni O and 2% dopants will be reported using NiO-K_2O/Ce-Zr, NiO-SnO/Ce-Zr. The used catalyst would be referred as Ni/Ce-Zr, Ni-K/Ce-Zr and Ni-Sn/Ce-Zr. This terminology will be used in rest of the thesis.

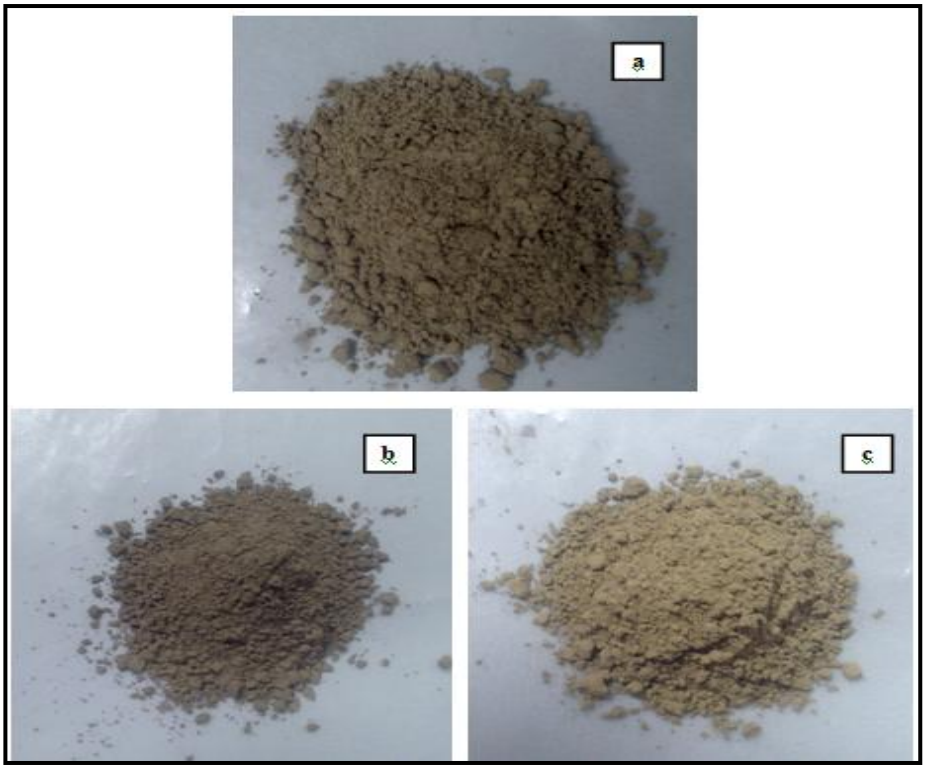

Figure 4.17: Nickel catalysts (NiO/Ce-Zr (a), NiO-K_2O/Ce-Zr (b) and NiO-SnO/Ce-Zr (c)) prepared by wet impregnation of pre calcined Ce-Zr support.

4.3.3.2 Preparation Ni supported on Ce-rich supports

The zirconia doped ceria (Ce-Zr) support was prepared in the laboratory, University of Leeds using a sol-gel method. Tamarind seed polysaccharide TSP (Xyloglucan) was used as a gelling agent. A stock solution of 3.5% (w/v) was prepared by dissolving 7 g of TSP

in 200 ml deionised water. The stock solution was heated on a hot plate at 65 °C under continuous stirring to obtain a viscous solution.

As the solution obtained was very viscous the use of magnetic stirrer present with the hot plate became difficult resulting in non homogeneity which was observed during initial trials. A skin formed on top surface where full mixing had occured, however the underneath of the solution was unhomogeneous and had not mixed completely. As a result an electrical mixer, mounted on a clamp was used to produce uniform mixing. A temperature probe was also placed within the solution to measure the bath solution and control the hot plate temperature.

At the same time on a separate hot plate catalyst precursors i.e. cerium ammonium nitrate and zirconyl oxy-nitrate with (Ce/Zr) molar ratio of 3/1 were mixed in alcohol. It was found that TSP does not form a gel with water, rather it forms gels with alcoholic solutions. Hence the precursors were dissolved in different alcohols. Three different alcohols such as methanol, ethanol, propanol and sugar were examined. In each experiment 5 g of cerium ammonium nitrate and 0.0702 g zirconyl oxy-nitrate was used. The amount of alcohol was varied from 10 and 17 wt% of the water used. The precursors, once mixed, were then added to the stock solution. The total solution was mixed once more using the electrical mixer at a temperature of ~45 °C for approximately one hour or until the solution had become a viscous gel (Figure 4.17). As temperature controlled hot plate was unavailable it was difficult to maintain the temperature of the solution to exact 45 °C. The obtained gels were dried using atmospheric and freeze drying. The dried gels were calcined at 600 °C for 6 h in a furnace. Alumina doped ceria (Ce-Al) was prepared using same method. Cerium ammonium (5g) nitrate and aluminium nitrate were dissolved in ethanol with Ce/Al molar ratio 3/1. The dissolved precursors were added to viscous TSP water solution and gel was obtained. The gel was freeze dried and calcined at 600 °C for 6 h. In order to differentiate and avoid confusion the Ce-Zr support prepared by sol gel synthesis will be referred as Ce-Zr-3/1.

Wet impregnation method was used to impregnate the Ce-Zr-3/1 and Ce-Al-3/1 supports to prepare 10 wt% NiO supported on Ce-Zr-3/1 and Ce-Al supports. To achieve this 4 g of each support and 1.55 g of $Ni_2NiO_6.6H_2O$ were used. The $Ni_2NiO_6.6H_2O$ was dissolved in 30 cm^3 water and the support was added to it and mixed thoroughly for 3 h. The impregnated support was dried at 120°C overnight in an oven and calcined at 600 °C for 6 h to obtain the catalyst. The 10 wt% NiO supported on sol gel synthesized Ce-Zr support will hence forth be referred as Ni/Ce-Zr-(3/1) to distinguish it from other Ce-Zr catalysts prepared from commercial support discussed in the previous section. Similarly Ni supported on Ce-Al-3/1 catalyst will be referred as Ni/Ce-Al. In case of fresh it would be NiO/Ce-Al and with used it would be refereed by Ni/Ce-Al. Similarly terminiolgy will apply to Ni/Ce-Zr-3/1.

Figure 4.18: Viscous gel obtained during sol gel synthesis of Ce-Zr (3/1) support.

4.3.4 Catalyst characterisation

The catalyst were characterised using X ray diffraction, specific surface area (BET), elemental analysis (C/H/N) and thermo gravimetric- Fourier transform infra red spectroscopy (TGA-FTIR). The presence of carbon in the condensate from the catalytic experiments was determined using Total organic carbon (TOC) analysis.

4.3.4.1 Surface area analysis (BET)

Adsorption is a surface phenomenon where a density of fluid in contact with solid increase. When a gas molecule strikes a solid surface, it can collide in two different ways i.e. elastically and in-elastically. During elastic collision no energy is exchanged as a result the gas molecule is reflected back to gas phase, unaffecting the system. In inelastic collision the gas molecule lacks energy to overcome the surface potential and sticks to the surface for a while before returning to the gas phase. The inelastic collisions lead to adsorption. Wan der Waals forces govern physical adsorption of gases on solid surface. The process of physical adsorption takes place when a gas is contact with solid and pressures and temperature conditions are manipulated so that the gas reaches it condensation point [232]. This is performed in a closed vessel where a solid is exposed to condensed gas usually N_2 and the pressure of the system is increased gradually. This causes the gas to condense in the large pores of the solid, until all the pore volume of the solid is filled with the condensate and the surface is saturated. The system pressure is then reduced so that the liquid boils and returns back to gas. This results in the formation of two separate operations in the processes known as adsorption and desorption [232].

Adsorption and desorption equilibria are represented by isothermal plots that show the volume of gas adsorbed onto the solid as a function of the relative pressure (P/P_0). The

relative pressure is the equilibrium pressure (P) of the gas in contact with the liquid over the saturated vapour pressure of the gas at the process temperature. The adsorption and desorption isotherms are never identical since they are governed by different controlling processes. This results in the formation of a hysteresis loop. These hysteresis loops are very useful to predict the geometry of the pores in the material. The adsorption desorption isotherms helps us identify the nature of the solid. IUPAC has classified the isotherms in 6 types to determine the pore size and nature of the solid.

Figure 4.18 shows 6 different kinds of isotherms classified by IUPAC [233]. Type 1 isotherms indicate pores of 2 nm or smaller associated with micropores solids. Non-porous i.e. macroporous solids having pores excess of 50 nm exhibit type 2 isotherm. Type 4 isotherms are exhibited by mesoporous solids having pore radius 2-50 nm. Type 3 and 5 isotherms are rare. An example of type 3 isotherms is adsorption of water vapour on non porous carbons. In this type of isotherms the adsorbent-adsorbate interactions are reported to be weaker as compared to adsorbate-adsorbate. Type 5 isotherms are related to type 3. In this type of isotherm the adsorbent-adsorbate interaction is weaker but is obtained with certain types of porous adsorbents. Type 6 isotherms indicative of multilayer adsorption on non-porous surfaces, e.g. argon or krypton on graphitised carbon black at liquid nitrogen temperatures. Type 6 indicates groups of adsorption sites that are homogeneous in regards to energy.

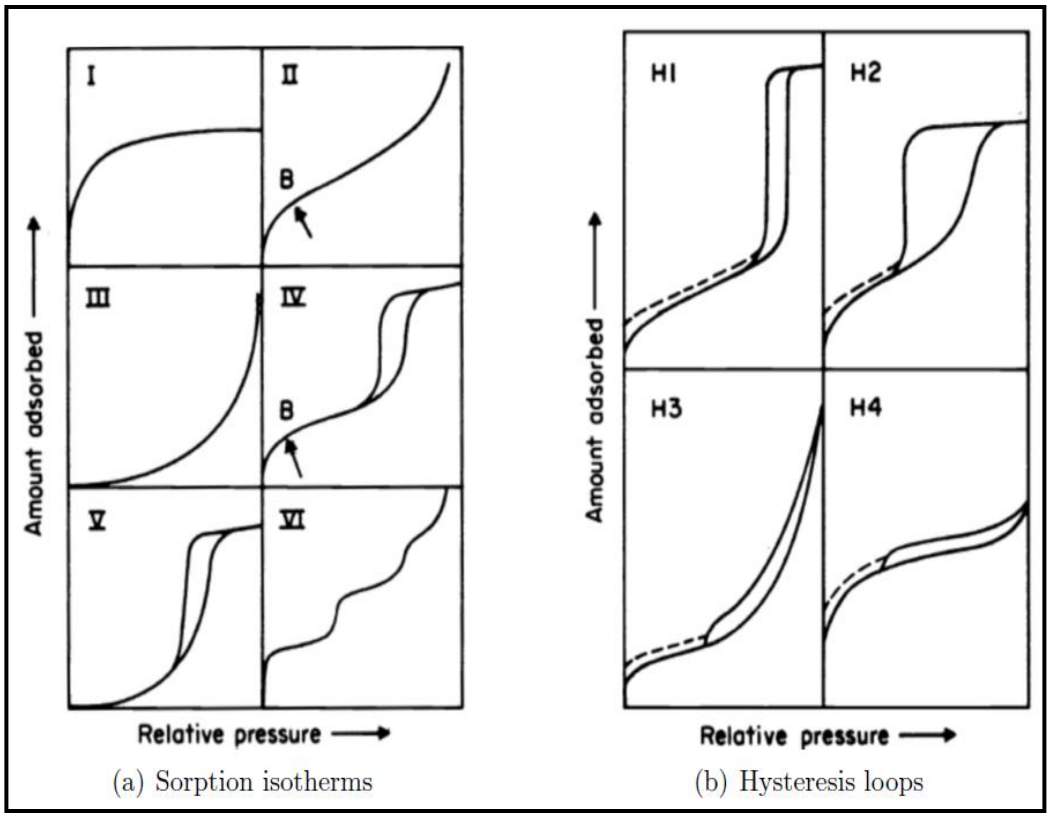

Figure 4.19: IUPAC classification of gas physical adsorption isotherms [233].

As a result of different controlling processes the adsorption and desorption isotherms are rarely if ever identical. This results in formation of a loop on the isothermal plot known as a hysteresis loop. In order to explain the relationship between the absorbed volume of gas and relative pressure, P/P_0 various models have been developed. The most commonly used model is Brunauer-Emmett-Teller (BET) model.

The surface area of all the catalysts was evaluated was measured using Brunauer-Emmett-Teller (BET) method. This method is widely used to determine the specific surface area and porosity. The method relies on the physical adsorption of inert gases line N_2 on the surface of the material. The model makes use of the following Eq.

$$\frac{P}{V(P_0 - P)} = \frac{1}{V_m C} + \frac{C-1}{V_m C}\frac{P}{P_0} \tag{4.3}$$

In the above Eq 4.3, Vm is the monolayer adsorbed gas quantity and P and Po are the equilibrium and saturation pressures. The model uses the following assumptions. Adsorption occurs on well defined pores and only one molecule adsorbs per site. The surface is assumed to be homogeneous and all the sites have same energy. The solid surface is assumed to be completely covered with gas molecule and the gas molecule is considered to be small enough to achieve this. The adsorbed molecules do not interact with each other. The gas and solid do not interact beyond a monolayer. The BET model is a mathematical technique that calculates specific surface area (SSA) of the material or catalyst. SSA is defined as surface area per unit mass of the material. The model can be used for meso and macroporous solids. The model Eq is valid when P/Po values are in the range of 0.05 and 0.35 i.e. 0.05<P/Po<0.35 [234]. A graph of I/ (V [Po-P]-1) is plotted against P/Po. The slope of the graph yields α and β is obtained as an intercept. The quantity of Vm is calculated using following formula

Vm=1/ (α+β) and C is ratio of α/β [235]

$$S_{BET} = \frac{NAV_m 10^{-20}}{mV_M} \tag{4.4}$$

The Eq 4.4 is used to determine the BET surface area where N is Avogadro's number, A is the area occupied by an absorbed gas molecule, m is the mass of the solid analysed and V_M is the molar volume of adsorbate.

The study of pore structure especially pore radius is very important especially in hysteresis loop. The pore properties of mesoporous solids are widely studied using Barrett, Joyner and Halenda (BJH) model. The small pore size of the mesoporous material results in the formation of a highly curved meniscus in the adsorption of the liquid on to the solid. As a result the liquid vapour pressure drops below the saturated vapour pressure Po which results in formation of a hysteresis loop during adsorption and desorption of gas [235]. This phenomenon is termed as capillary condensation. The formation of the hysteresis loop and capillary condensation modelling helps us to determine the pore size distribution, cumulative pore volume and specific surface area of

the catalyst. The condensation phenomenon is explained by means of Kelvin Eq 4.5 [236].

$$ln\frac{P}{P_0} = \frac{-f\gamma V cos\theta}{RT(r_p - t)} \quad (4.5)$$

In the above Eq, *f* is a form factor (depending on the meniscus), γ is the surface temperature of the adsorbate at temperature T, V is the molar volume of the liquid condensate, θ is the angle of contact equal to 0, R is the true gas constant r_p is the radius of the pore and t is the film thickness. The film thickness t of the adsorbate is calculated using the Eq 4.6.

$$t = 3.5\left(\frac{5}{2.303\log\left(P/P_0\right)}\right)^{1/3} \quad (4.6)$$

The Kelvin Eq 4.5 tries to predict the pressure at which adsorbate will spontaneously condense and evaporate in cylindrical pores of given size. This will only happen if there is an existing film of gas is adsorbed on the solid [237]. The BJH model uses a modified Kelvin Eq (4.6) and the statistical thickness (t curve). The Eq 4.6 is used to determine the change in pore volume and surface area by applying pore geometric pore models. Pore size distribution is also provided by the model by plotting change in pore volume with respect to change in pore radius against pore radius. Cumulative pore volume and the specific surface are also obtained from this model.

The shapes of the hysteresis loop present in the isotherm help us to identify the geometry of the pores in the mesoporous material. IUPAC has classified the hysteresis loops into four different types (Figure 4.18). Type H_1 suggest tubular pores at both end with various cross sections and slightly widened parts; termed ink bottle and trough shaped pores. Type H_2 also suggest ink bottle shaped pores but can also propose or voids between close packed particles [235]. The H_2 type adsorption hysteresis can occur due to interconnectivity of pores. In such systems the pore sizes and pore shapes are not well defined or they are irregular. The sharp steep of the desorption isotherms indicates the existence of interconnectivity among the pores [238]. Type H_3 hysteresis is associated

with plate such as particles which give rise to slit shaped pores, while H_3 type are associated with narrow slit pores.

A Quanta-chrome Instruments NOVA 2200e Surface Area and Pore Size analyser (Figure 4.19) was utilised in order to perform the surface area and isotherm analysis of the support and the catalysts. The instrument was provided with a degassing (left had side) and physical adsorption (right hand side) section. The instrument was used for the analysis of both fresh and used catalysts. The samples were vacuum degassed at 300°C for 3 h in order to eliminate gases such as CO_2 or moisture adsorbed on to the solid catalysts. The instrument was operated in batch manner to determine the amount of gas adsorbed. Volumetric technique was used by the instrument which relied on pressure sensors in a container with known volume to determine the adsorbed quantities.

Figure 4.20: Quanta-chrome Instruments NOVA 2200e Surface Area and Pore Size Analyser

Cylindrical glass tubes were used to perform the analysis. The tubes were initially weighed and the sample was added in the tubes and the actual mass of the sample was determined by subtracting the weight of the tube from the total (tube + sample). The

samples were degassed for 3 h; the tubes were cooled and weighed again to determine the loss in weight after degassing. This final mass was used to perform the analysis. The cooled tubes were then connected to the analysis section (right side of the instrument). The samples were left overnight for isotherm analysis.

4.3.4.2 X ray powder diffraction (XRD)

X-ray diffraction is widely used technique to study the crystallographic structure of the catalysts. In this method the sample is exposed to an electron beam that is accelerated across a high voltage field. The electrons of the atoms from the sample deflect some of the photons from the incident beam away from the original vector. This results in the formation of deflected X-rays which are measured during the experiments. The presence of different atoms and molecules in the sample interfere with one another resulting in the intensity distribution.

The term 'powder' really means that the crystalline domains are randomly oriented in the sample. Therefore when the 2-D diffraction pattern is recorded, it shows concentric rings of scattering peaks corresponding to the various d spacings in the crystal lattice [239]. The positions and the intensities of the peaks are used for identifying the underlying structure (or phase) of the material. For e.g. graphite, will exhibit different diffraction lines as compared to diamond, even though they consist of carbon atom. This phase identification is important because the material properties are highly dependent on structure (just think of graphite and diamond) [239, 240].

The Brucker D8 instrument by means of Cu Kα radiation was used to perform the X-ray diffraction studies. The samples were scanned with a steep size of 0.108°/s and the range of 2θ was set at 20-100°. The obtained diffraction patterns of the samples were compared

with the known standard diffraction patterns to identify phases present in the material. Phase analysis based on the XRD data was obtained using the X'Pert High Score Plus software. Rietveld refinement was used to measure the phase compositions of NiO, Al_2O_3 and Ce-Zr as well as the crystallite sizes (Scherrer Eq accounting for peak broadening by instrument and strain) [240]. The Scherrer Eq is given by Eq 4.7.

$$d_c = \frac{k\lambda}{\beta\cos\theta} \tag{4.7}$$

Where K is a dimensionless shape factor with typical values about 0.9, λ is the wave length of the X-rays, θ is the Bragg diffraction angle and β is full width at half-maximum.

4.3.4.3 Elemental analysis

The amount of carbon deposited on the catalyst surface was determined using elemental analysis by means Thermo Flash EA 1112 series CE instrument. For each analysis duplicate samples (17 mg) each of used catalysts were analysed. The samples were placed in thin tin capsules and the capsules were folded to avoid air entrapment. The folded capsules were placed in the autosampler of the analyser which were further combusted in the reactor chamber with excess oxygen at 1800°C, to obtain C, H in the form of CO_2 and H_2O detected by the TCD detector of the instrument.

4.3.4.4 TGA-FTIR and TOC analysis

In order to obtain an idea about the type of carbon present on the catalyst surface TGA-FTIR analysis was performed. Temperature programmed oxidation (TPO) of the catalyst was performed in a Stanton-Redcroft TGA connected to a FTIR (Nicolet iS10, Thermo scientific). During each test 100 mg of used catalyst was placed in the sampling pan of

the TGA and the temperature was increased from ambient to 900°C at the rate of 10°C/min in 50 cm^3/min air. The FTIR spectral scanning was repeated every 30 s, scanning from 4000 to 500 $cm^{-1}$to determine the gaseous products formed during the experiment.

The organic carbon of the condensate collected after the experiment was analysed using a Hach-Lange IL550 analyser. The samples were diluted 10 times before performing the analysis, 1 cm^3 of the condensate was placed in 10 cm^3 centrifuge tube and was diluted up to the mark using deionised water.

4.3.4.5 Scanning Electron Microscopy analysis (SEM) and Energy Dispersive X-ray (EDX)

SEM uses an electron microscope equipped with a high-energy beam of electrons for generating images. This beam is bombarded on the sample, after striking the sample surface they produce different signals which are detected by the detector resulting in the formation of an image. This technique is used to study the sample topography along with topology. The SEM is coupled with an energy-dispersive X-ray (EDX) source which is used for chemical characterisation of the sample. The EDX technique uses the principle of exciting electrons of sample using X-rays. At normal or ground state the atoms of the sample contain electrons which are bound to the nucleons. The bombarded X-ray beam excites the electron in the inner shell of atom. The excited electron is ejected from the shell creating an electron hole. This hole is filled with another electron from higher energy shell. This difference in energy between higher and lower energy shells releases some form of X- rays. This X rays are characteristics of the difference of energy of the shells and the atomic structure of the emitted electron, elemental composition can be determined using this principle. The SEM-EDX analysis was performed to observe the dispersion of the active metals i.e. Ni, K and Sn on the catalyst surface. It was also used to observe carbon formation on the catalyst surface.

A Hitachi SU8230 (Figure 4.20) was used for the SEM analysis. The EDX analysis of the samples was performed using an INCA 350 EDX system fitted with an 80 mm^2 X-Max SDD detector, Oxford Instruments. The chemical characterisation of all the samples was conducted by using INCA and Aztec software supplied by Oxford Instruments. The samples were prepared a day before the analysis. The samples were suspended in methanol and were placed on the stubs (Figure 4.21). The methanol was evaporated and the sample was decontaminated in an ozone treatment chamber (Figure 4.22) to remove unwanted hydrocarbons from the sample. The treated sample was stored in vacuum in the same chamber prior to analysis.

Figure 4.21: Hitachi SU8230 cold finger SEM.

Figure 4.22: SEM sample stubs.

Figure 4.23: Ozone decontaminator for Hitachi SU8230 SEM.

5. Characterisation of biodiesel and catalysts

5.1 Biodiesel Characterisation

The characterisation of biodiesel was performed to determine the ester content to be used for the equilibrium analysis of the experiments. The elemental analysis of biodiesel was to be used to set the flows of biodiesel and H_2O for the CSR experiments. Similarly the presence of fatty acid affecting the biodiesel performance during the CSR experiments would also be determined in biodiesel characterisation, useful for equilibrium analysis. Likewise, the free fatty acid and proximate analysis is used to determine the quality of biodiesel used for the experiments.

The gas chromatograph composition of the different biodiesel used in this study is shown in the Table 5.1. It can be seen from the table that biodiesel samples mainly consisted of methyl oleate, methyl linoleate and methyl palmitate. The three different biodiesel samples prepared using different amount of KOH (1.5, 2 and 3 wt%) showed very similar ester compositions. Highest composition of methyl oleate was found in the commercial biodiesel sample as compared to the other two. The in house prepared biodiesel exhibited the highest amount of methyl linoleate. As compared to commercial and in house prepared biodiesels, palm oil biodiesel showed the highest amount of methyl palmitate. In all the biodiesel samples, smaller chain methyl esters (C_{13}-$_{15}$) were negligible and so were higher methyl esters (C_{20}-C_{25}). The in house prepared biodiesel composition were comparable to literature Hoekman et al. [241] and Wang et al. [242] which both show biodiesel to contain ~≥40 wt% oleate, ~≥30 wt% linoleate and ~≥15 wt% palmitate.

Table 5.1: Gas chromatograph composition of three different biodiesels.

Biodiesel	Commercial	In-house	Palm
Methyl laurate (C13(0))	0.09	0.00	0.21
Methyl myristate (C15(0))	0.33	0.27	1.06
Methyl palmitate (C17(0))	16.86	15.07	40.19
Methyl palmitoleate (C17(1))	0.34	0.10	0.11
Methyl stearate (C19(0))	3.88	2.98	4.03
Methyl oleate (C19(1))	51.34	42.62	42.81
Methyl linoleate (C19(2))	21.29	32.24	10.56
Methyl linolenate (C19(3))	1.69	3.93	0.00
Methyl arachidate (C20(0))	0.56	0.43	0.29
Methyl gadoleate (C21(1))	0.90	0.96	0.00
Methyl behenate (C23(0))	0.16	0.16	0.00
Methyl erucate (C23(1))	0.43	0	0
Methyl lignocerate (C25(0))	0.16	0.13	0.00
Unknown	1.96	1.17	0.74

The elemental and the proximate analysis of all the biodiesel used in this study are shown in Table 5.2. In this (Table 5.2), 1.5, 2 and 3 wt% represents the amount of KOH used to prepare the biodiesel. These results show that the majority of the biodiesels are made up from carbon, accounting for around three quarters on a weight basis. H_2 is the next largest represented element accounting for around 13%, followed closely by oxygen accounting for around 9-12%. Among all the biodiesel samples, 2 wt% biodiesel showed the highest

carbon content while commercial biodiesel showed highest H_2 content. The oxygen content was highest in the 1.5 wt% biodiesel. The proximate analysis of all the biodiesel samples suggests that all the biodiesel samples analysed contain ≥99.5% volatiles which evaporates around 190°C (Figure 5.1). As a result formation of carbon residue and ash content are minimal. This is beneficial for the H_2 production process as 99% of the sample will convert to vapours in the vaporiser, with little amount of ash and carbon residue formation.

Table 5.2: Elemental and proximate analysis of 5 biodiesel samples.

wt (%)	Commercial biodiesel	In-house-1.5 wt %	In-house-2wt %	In-house-3wt %	Palm biodiesel
C	75.35	74.10	76.42	74.60	75.90
H	13.53	12.97	12.44	12.87	12.41
O	11.10	12.92	11.12	12.52	11.67
Volatile	99.63	99.91	99.92	99.65	99.88
Carbon residues	0.28	0.02	0.03	0.13	0.015
Ash	0.1	0.07	0.05	0.22	0.108

The ash content and the ultimate analysis of the samples obtained from elemental analysis of the biodiesel samples can be used to calculate the gross calorific value (GCV) by using the Eq 5.1 provided by Channiwalla & Parikh [243].

$$0.3491C + 1.1783H + 0.1005S - 0.1034O - 0.0151N - 0.0211A \quad (5.1)$$

These values were compared with the one obtained from bomb calorimetry. Table 5.3 compares the calculated and the experimental GCV of commercial and in house prepared biodiesel, obtained by bomb calorimetry. The calculated values were slightly higher as compared to the observed values.

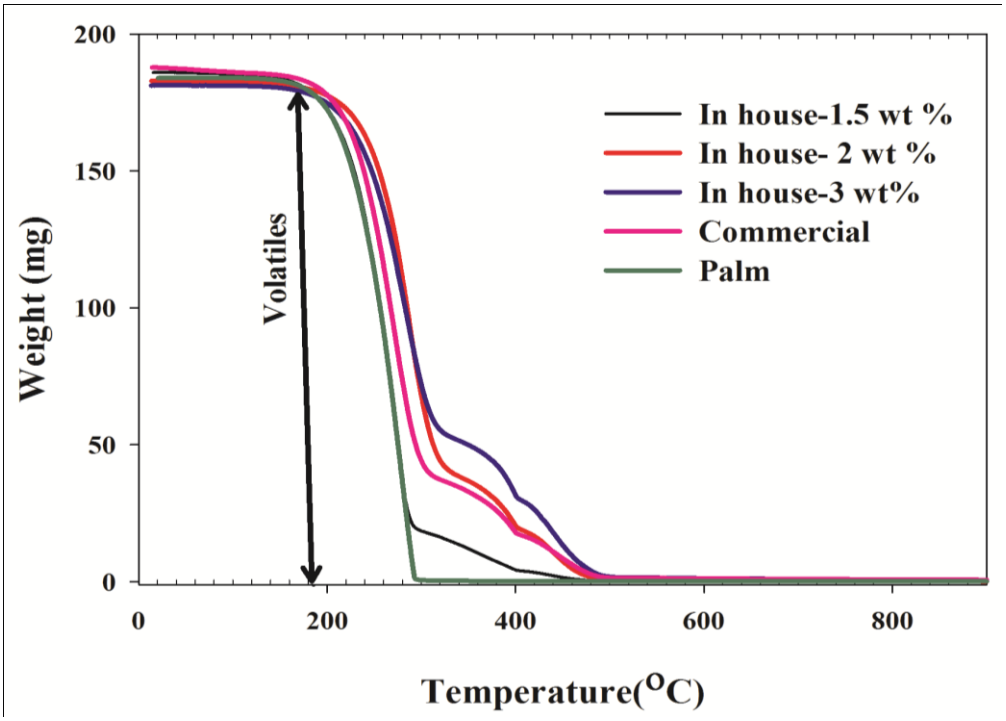

Figure 5.1: TGA analysis of the biodiesel samples.

Table 5.3: Comparison of calculated and experimental GCV of commercial and in house prepared biodiesel.

Biodiesel	Gross calorific value (MJ/kg)	
	Calculated	Observed
Commercial	45.81	41.08
In house-1.5 wt %	44.69	40.23
In house-2 wt %	44.95	41.31
In house-3 wt %	44.76	40.09
Palm	44.71	40.16

In addition to these properties, the acid value and presence of free fatty acid detection is also important to determine the quality of the biodiesel. Free fatty acid boils at higher temperatures and may affect the vaporisation process of biodiesel. Similarly free fatty acids are longer chain compounds and would affect the H_2 production resulting from higher carbon formation. Table 5.4 shows the free fatty acid and acid values of commercial and in house prepared biodiesel. All the biodiesel samples showed FFA

composition comparable to both ASTM D974-664 and EN14104. In all the biodiesel samples tested, in house 1.5 wt % biodiesel showed the lowest acid value as a result lowest free FFA content, in comparison in house 3 wt% biodiesel had the highest acid value and thus FFA content. The waste cooking oil used to prepare the biodiesel samples exhibited the highest higher acid value as a result highest free FFA content.

Table 5.4: Free fatty acid and acid values of commercial and in house prepared biodiesel.

Biodiesel	Free fatty acid (%)	Acid value mg KOH/g
Commercial	0.461	0.925
In house -1.5 wt %	0.381	0.757
In house -2 wt %	0.508	1.01
In house -3 wt %	2.965	5.89
Palm	0.392	0.781
Waste cooking oil	10.22	20.89

5.2 Catalyst Characterisation

5.2.1 Surface area analysis

The surface area of the fresh Al_2O_3 and Ce-Zr catalysts is provided in the Table 5.5. As seen in the Table the NiO-CoO-CeO/Al exhibits highest surface area followed by Ce-Zr and Ca-Al supported catalysts. Lowest surface area was shown by NiO/Al and NiO-K_2O/Al catalysts. The pre calcined Ce-Zr support supplied by the manufacturer showed higher surface area as compared to the in house calcined Ce-Zr support. The surface area of the pre calcined Ce-Zr support was 30% higher than the in house calcined support, suggesting that the in house calcination processes was not homogenous compared to the calcination processes employed by the company. The difference between the surface area values obtained from BET and BJH are far smaller when using the adsorption isotherm than when using the desorption isotherm. The pore size and pore volume of the pre calcined support was slightly smaller than the in-house calcined support. The catalyst prepared using dry impregnation method exhibited higher surface area as compared to the wet impregnation method. Increasing the loading of NiO showed to decrease the surface

area of the catalysts in both the methods. The decrease in BET surface area is associated with increase in NiO content observed in X-ray diffraction experiments.

Table 5.5: Surface area of fresh commercial and Ce-Zr catalysts.

Catalyst	BET (m^2/g)	BJH surface area (m^2/g)	Pore size (nm)	Pore volume cc/g
In-house calcined Ce-Zr	60.35	60.32	6.03	0.18
Pre calcined Ce-Zr	90.43	101.46	4.73	0.22
Catalyst prepared using in-house calcined Ce-Zr				
10wt%-NiO/Ce-Zr-wet	55.89	59.70	4.69	0.13
20wt%-NiO/Ce-Zr-wet	53.96	58.37	4.79	0.13
30wt%-NiO/Ce-Zr-wet	48.76	53.97	4.47	0.12
10wt%-NiO/Ce-Zr-dry	60.45	66.59	4.47	0.14
20wt%-NiO/Ce-Zr-dry	56.53	61.65	4.47	0.14
Catalyst prepared using pre calcined Ce-Zr				
NiO/Ce-Zr	79.61	88.78	3.58	0.18
NiO-SnO/Ce-Zr	61.12	63.96	4.68	0.16
NiO-K_2O/Ce-Zr	48.38	60.88	6.08	0.19
Commercial catalysts				
NiO/Al	05.31	-	-	-
NiO-K_2O/Al	02.27	-	-	-
NiO/Ca-Al	33.59	-	-	-
NiO-CoO-CeO/Al	106.38			

The pore volume of the catalyst decreased with increase in Ni loading in the wet impregnation method, while it remained unaffected in the dry impregnation method. This could be explained by the extensive restructuring of the catalysts surface as suggested by Haber et al [244]. As a result of loading NiO on to the support results in partial deposition of NiO in the pores reducing the pore volume of the catalyst. The catalysts prepared using the pre calcined Ce-Zr support was higher in surface area than catalyst obtained using the in house calcined Ce-Zr support. The NiO/Ce-Zr catalyst showed the highest surface area followed by NiO-SnO/Ce-Zr and finally NiO-K_2O/Ce-Zr. The pore volume and the pore size of the catalyst containing the dopants were higher as compared to bare Ni catalyst. Impregnation of 1 wt% Rh on 13 wt% CeO_2 doped ZrO_2 supplied by the same

manufacturer, calcined under similar conditions showed much smaller surface area (44 m^2/g) [245]. According to the authors there was no significant change before impregnation and after impregnation of Rh on the support.

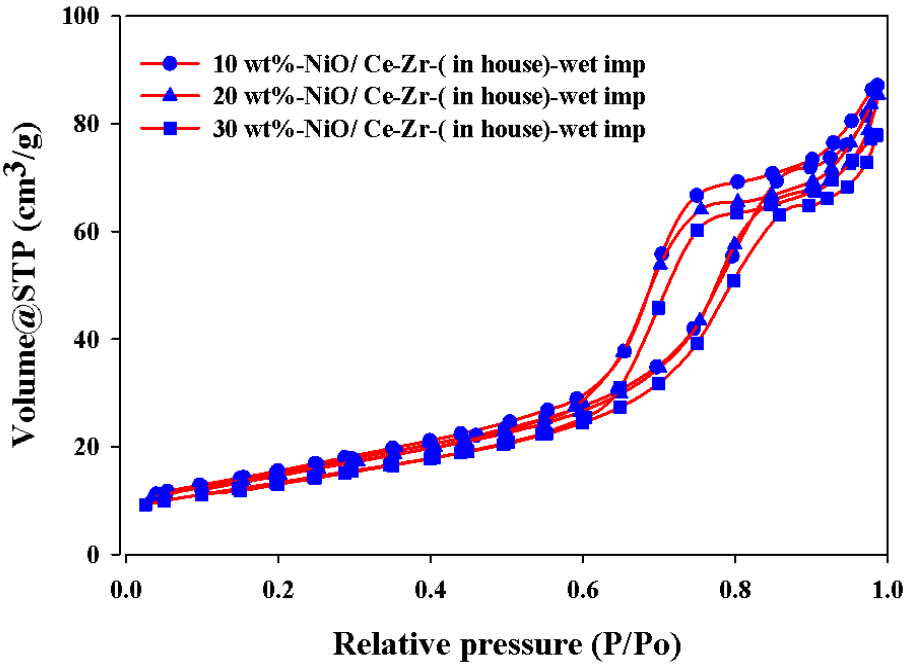

Figure 5.2: N_2 adsorption-desorption isotherms of NiO/Ce-Zr catalyst prepared by wet impregnation method using in-house calcined support.

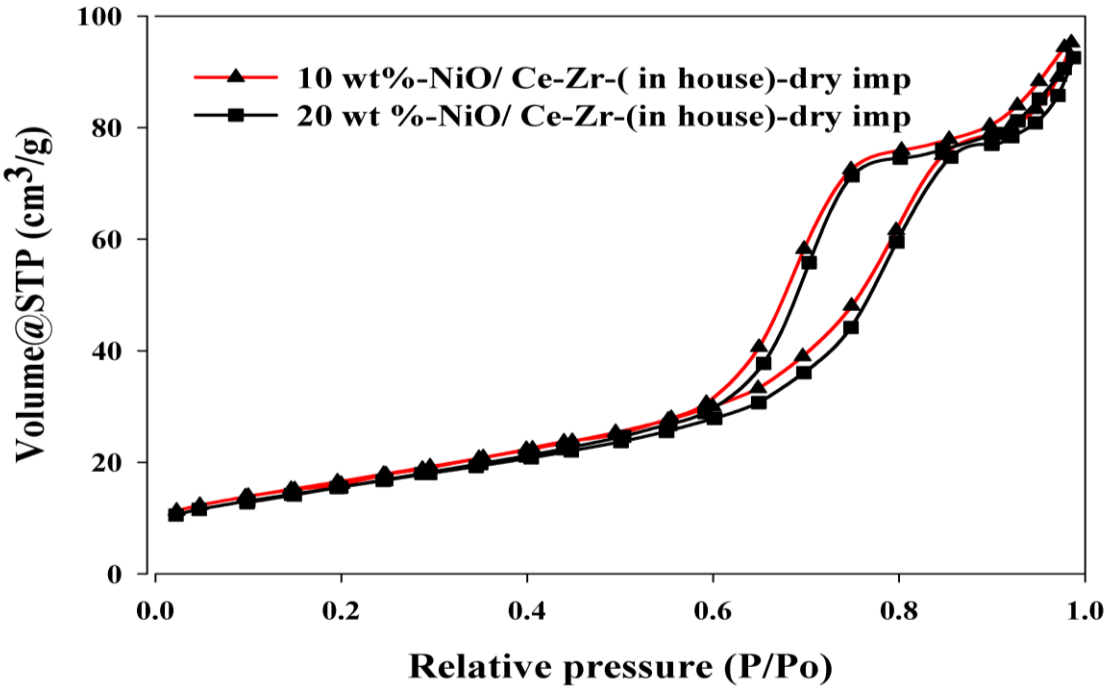

Figure 5.3: N_2 adsorption-desorption isotherms of NiO/Ce-Zr catalyst prepared by dry impregnation method using in-house calcined support.

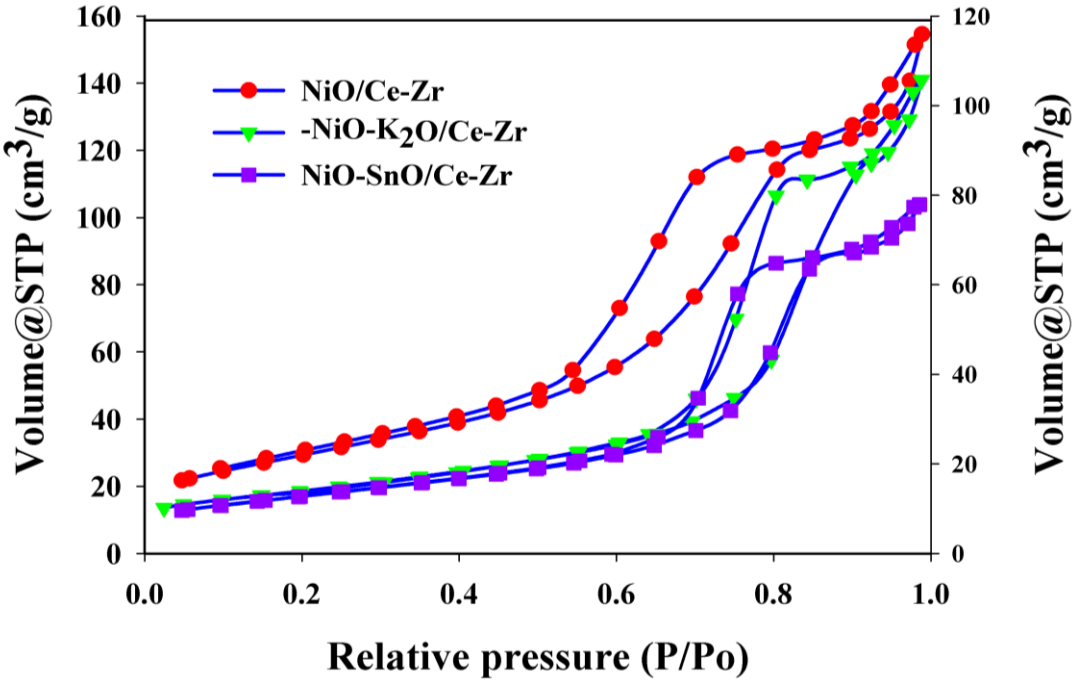

Figure 5.4: N_2 adsorption-desorption isotherms of NiO/Ce-Zr catalyst prepared by wet impregnation method using pre calcined Ce-Zr support.

The N_2 adsorption-desorption isotherms for the wet and dry impregnated in-house calcined Ce-Zr is shown in Figure 5.2 and 5.3 respectively. The isotherms obtained using in-house calcined and pre calcined Ce-Zr is very similar. Figure 5.4 shows the N_2 adsorption-desorption isotherms of Ni catalyst prepared using pre-calcined Ce-Zr support. The isotherm can be attributed to type IV and exhibits type H_1 hysteresis, which presents the typical characteristic of capillary condensation in mesopores (between 2 and 40nm) and contains either ink bottle or trough shaped pores [235]. Chen et al. [246] and Raju et al. [247] reported similar observations in the case of alumina and silica modified ceria-zirconia oxides. In the case of surfactant assisted preparation of 5wt% $Ni/Ce_{0.6}Zr_{0.4}O_2$ catalyst, Sukonket et al. [248] reported the existence of type IV isotherm exhibiting H_2 hysteresis. Ni supported on ceria-zirconia support prepared using improved evaporation induced self assemble strategy by Xu et al. [249] reported the presence of type IV isotherm exhibiting H_1 hysteresis, implying the presence of cylindrical pores.

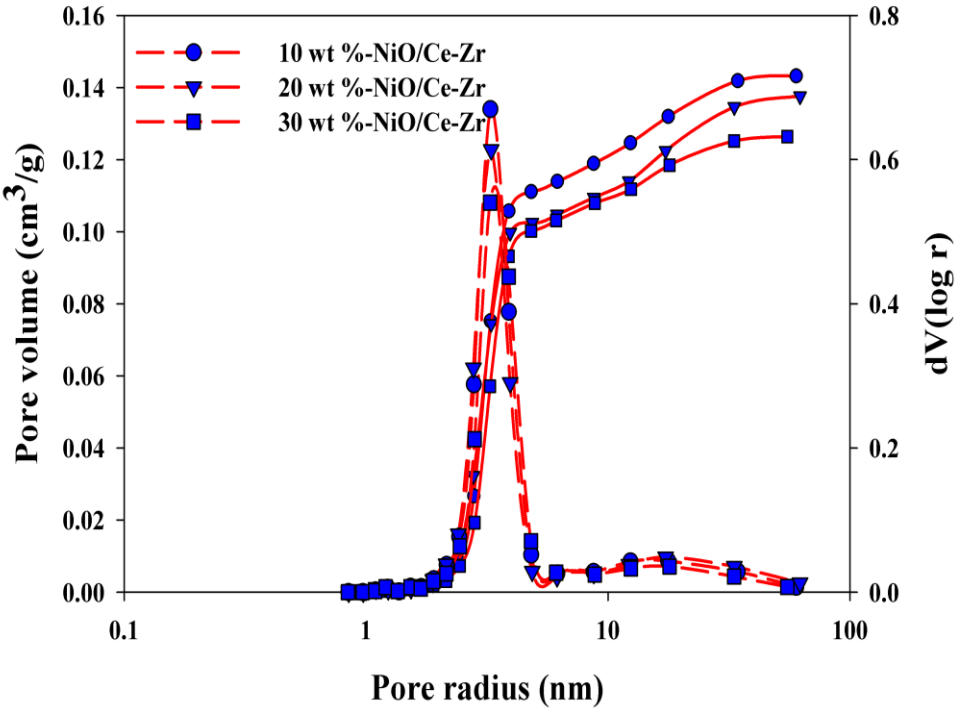

Figure 5.5: Pore-size distribution of NiO/Ce-Zr catalysts prepared using wet impregnation of in house calcined Ce-Zr support.

The pore size distribution of the wet impregnated in house and pre calcined Ce-Zr are shown in Figure 5.5 and 5.6 respectively. The distribution of pore were very close for the three catalysts prepared by wet impregnation of the in- house calcined Ce-Zr. Similar observation can also be made with the catalysts prepared using the pre calcined Ce-Zr support.

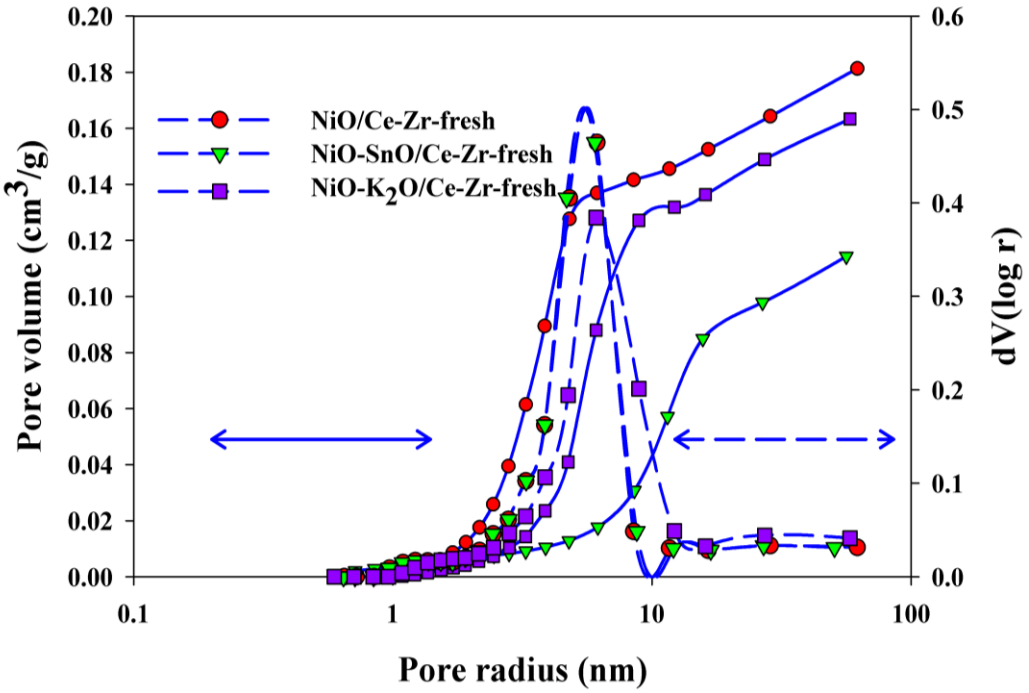

Figure 5.6: Pore-size distribution of NiO/Ce-Zr catalysts prepared using wet impregnation of pre calcined Ce-Zr support.

Table 5.6 shows the surface area of Ce-Zr-3/1 supports prepared by sol gel synthesis using various alcohols and TSP as a gelling agent. Among the alcohols, support prepared using 10 wt% methanol showed the highest surface area. It was found that atmospheric drying was not uniform and some of the polysaccharide was burnt. As a result freeze drying of the sample was implemented using ethanol for gel production. In order to prevent the utilisation of fossil based alcohols ethanol was selected for the investigation. It can be seen that freeze drying helps maintain the integrity of the gel and help increase the surface area of the support. Similarly increasing the alcohol content and freeze drying the sample was very beneficial to increase the surface area of the Ce-Zr-3/1 support.

Highest surface area of 118.21 m^2/g, was recorded for Ce-Zr-3/1 with 17 wt% ethanol using freeze drying. On the other hand Ce-Al-3/1 support exhibited much smaller area as compared to Ce-Zr-3/1 support. The Ce-Zr-3/1 support exhibited large surface area reduction during the impregnation of Ni on the support. The catalyst surface area prepared using Ce-Zr-3/1 support was 39.64 m^2/g. Comparatively the surface area of the NiO/Ce-Al catalyst was around 30.69 m^2/g.

Table 5.6: Surface area of fresh Ce-Zr-3/1 supports prepared by sol gel synthesis and catalyst prepared by impregnation method using Ni salts.

Alcohol	Drying	Support	Alcohol content wt %	BET Surface area m^2/g	BJH surface area m^2/g
Methanol	Atmospheric	Ce-Zr-3/1	10	40.84	-
Ethanol	Atmospheric	Ce-Zr-3/1	10	36.58	-
Propanol	Atmospheric	Ce-Zr-3/1	10	39.60	-
Sugar	Atmospheric	Ce-Zr-3/1	10	22.16	-
Ethanol	Freeze	Ce-Zr- 3/1	10	45.27	-
Ethanol	Freeze	Ce-Zr-3/1	17	118.21	-
Ethanol	Freeze	Ce-Al-3/1	17	35.03	46.54
Ethanol	Freeze	NiO/ Ce-Zr-(3/1)[a]	17	39.64	50.91
Ethanol	Freeze	NiO/ Ce-Al[a]	17	30.69	31.78

a- The NiO loading for the catalyst was 10 wt %.

Figure 5.7 shows N_2 adsorption-desorption isotherms of NiO/Ca-Al catalyst prepared using wet impregnation of sol gel synthesised support. Both the catalysts NiO/Ca-Al and NiO/Ce-Zr-3/1 exhibited type III isotherm with H_3 hysteresis curve with suggest the presence of plate-such as particles giving rise to slit-like pores [233]. As seen from Figures 5.8 and 5.9 the pore size distributions of NiO/Ce-Al and NiO/Ce-Zr-3/1 catalysts. The pore size distribution of these catalysts was very different as compared to the ones prepared using pre calcined and in house calcined supports. The distribution pore-size

obtained with the NiO/Ce-Al catalyst was the worst among all the catalysts. This suggests presence of non uniform pore structure resulting in uneven capillary condensation in the pores.

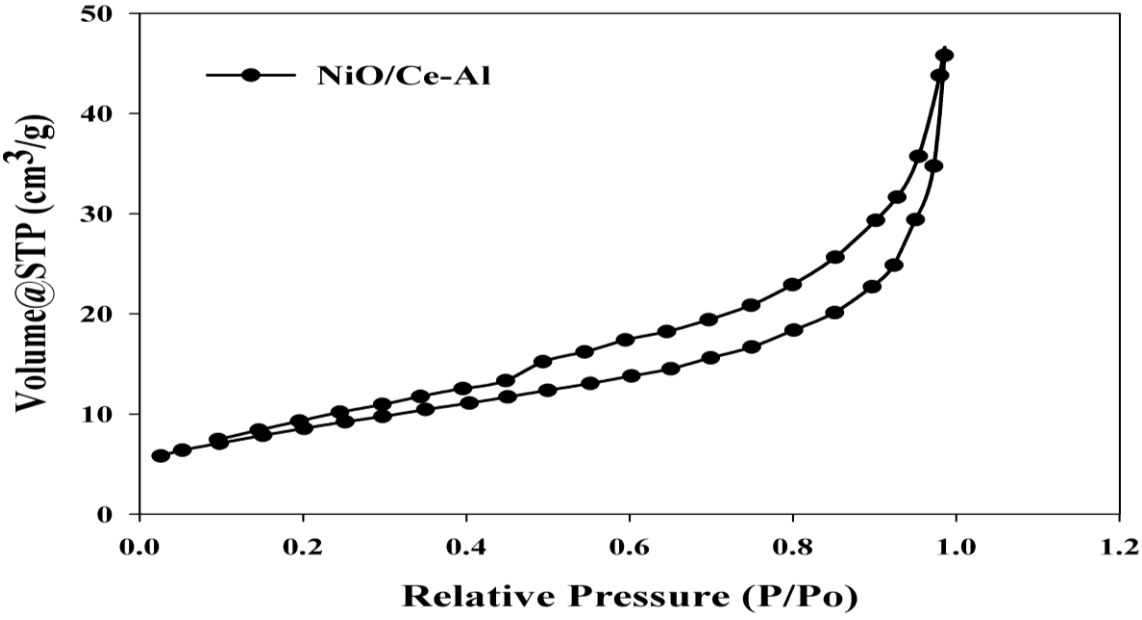

Figure 5.7: N_2 adsorption-desorption isotherms of NiO/Ce-Al catalyst prepared by wet impregnation method using pre calcined support.

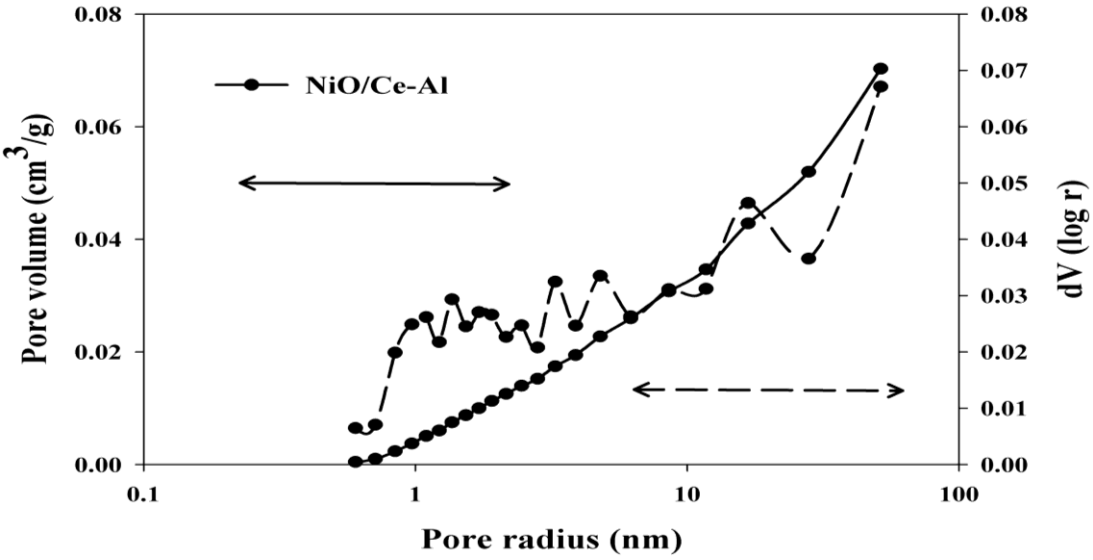

Figure 5.8: Pore-size distribution of NiO/Ce-Al catalyst prepared using wet impregnation of Ce-Al support prepared using sol gel synthesis.

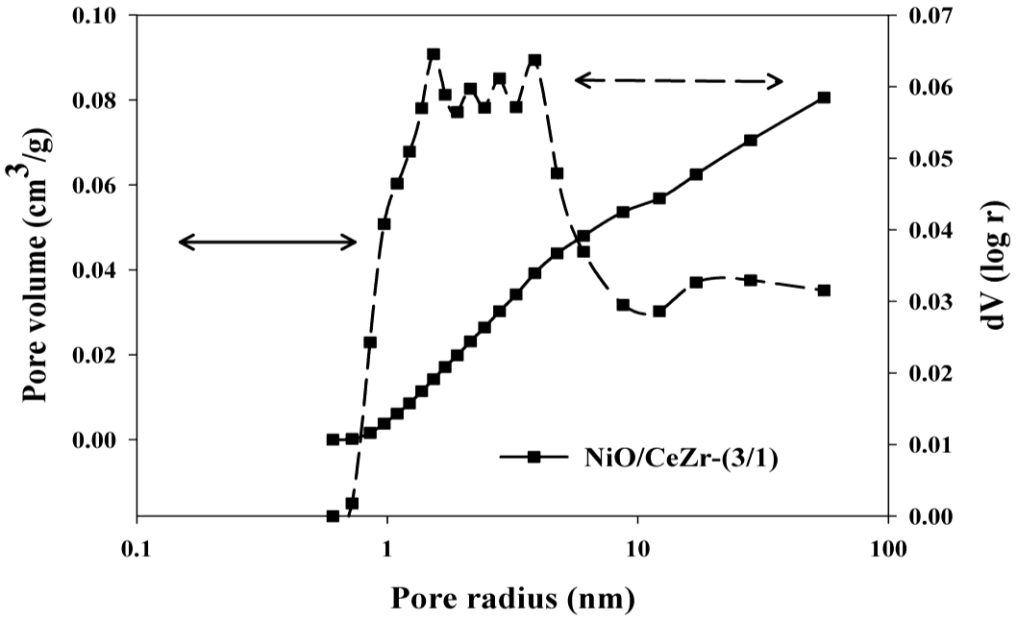

Figure 5.9:Pore-size distribution of Ni/Ce-Zr-3/1 catalyst, prepared by wet impregnation of Ce-Zr -3/1, support obtained using sol gel synthesis.

5.2.2 X-ray diffraction analysis

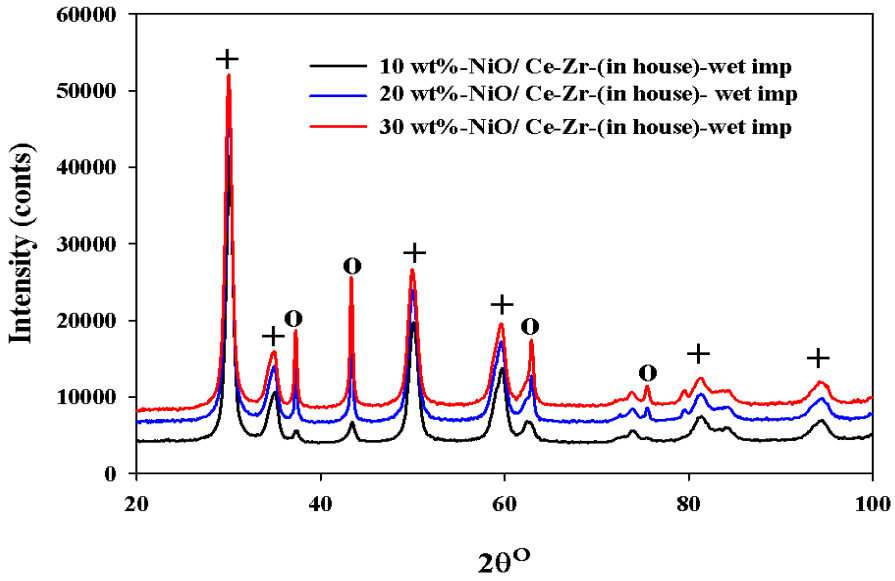

Figure 5.10: X-ray diffraction of NiO/Ce-Zr catalysts prepared using wet impregnation method using in house calcined Ce-Zr support. In the Figure (+) represents the Ce-Zr and (o) represents NiO.

The X-ray diffraction patterns for the NiO catalysts prepared by wet and dry impregnation methods employing in house calcined Ce-Zr support are shown in the Figure 5.10 and 5.11 respectively. Figure 5.12 shows the X-ray diffraction patterns of the in house and pre calcined Ce-Zr supports. The Figure 5.12 also includes the X-ray diffraction patterns of the NiO; NiO-K_2O and NiO-SnO catalysts prepared using wet impregnation of the pre calcined Ce-Zr support. The peaks observed at 29, 35, 49, 59, 81 and 94^o respectively, with highest intensity peak observed at around 29^o are attributed to diffraction peaks for Ce-Zr oxide. A cubic crystal system with tetragonal crystalline structure was observed. Absence of peaks responsible for pure ZrO_2 at 51^o (220) and 61^o (311) suggest the existence of a homogenous solid solution of Ce-Zr and complete incorporation of Zr in cerium crystal structure. Since both supports i.e. pre and in house calcined support (Figure 5.12) yielded identical data, inferring that both the supports consisted of the same components i.e. Ce-Zr mix oxide, and that the in house calcination of the cerium-zirconium hydroxide resulted in the complete formation of Ce-Zr mix oxide.

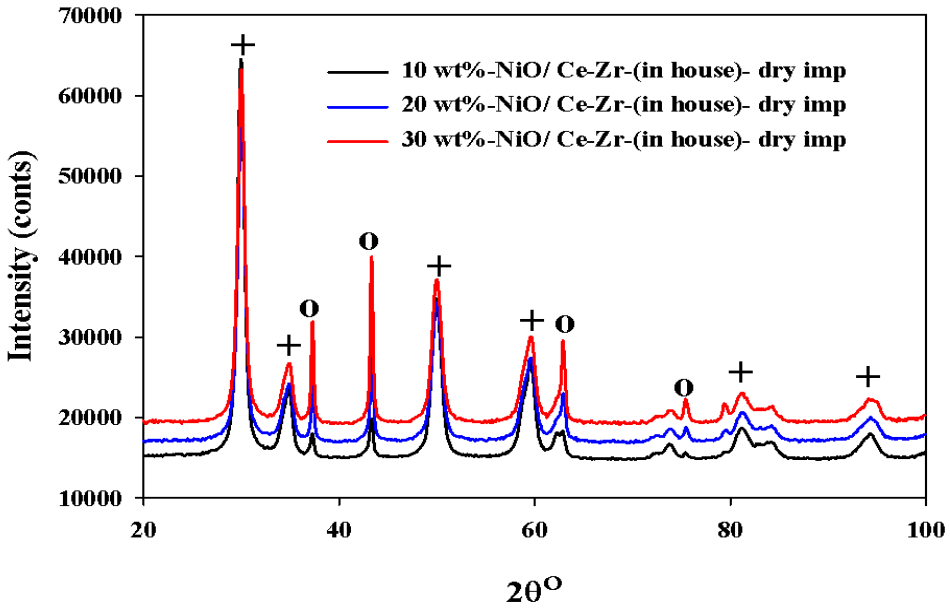

Figure 5.11:X-ray diffraction of NiO/Ce-Zr catalysts prepared using dry impregnation method using in house calcined Ce-Zr support. In the figure (+) represents the Ce-Zr and (o) represents NiO.

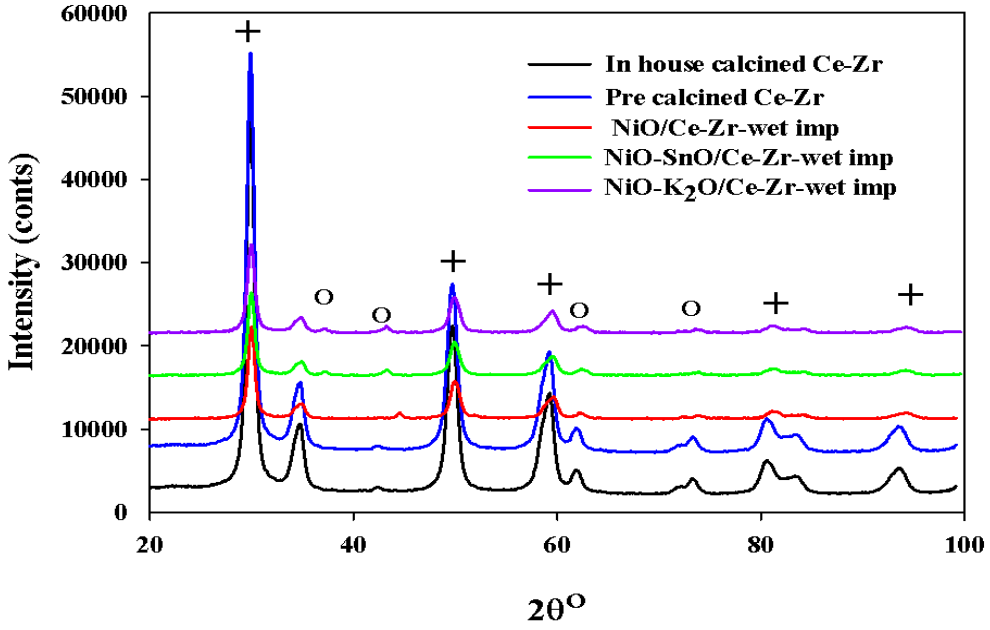

Figure 5.12: X-ray diffraction of NiO/Ce-Zr catalysts prepared using wet impregnation method employing pre-calcined Ce-Zr support. In the Figure (+) represents the Ce-Zr and (o) represents NiO.

The 2θ values of 37, 43 62-63, 75 and 79^{o} shown in Figure 5.11, 5.12 and 5.13 are attributed to the diffraction of NiO in the sample [250]. Highest intensity NiO peaks were obtained at similar 2θ angle in both the preparation methods. Increasing loading increased the NiO intensity in all the catalyst samples. The intensity of the NiO on the support changes and first doubles and then triples as the loading increases from 10 to 20 wt% and then to 30 wt%.

The Rietveld refinement summary of the NiO catalysts prepared using wet and dry impregnation methods on the in house calcined Ce-Zr is shown in Table 5.7. The difference between the desired and calculated loading increased with % loading. This difference reaches maxima at 30 wt% loading in both the methods, which suggests a decrease in the loading effectiveness. This could be as a result of NiO coating the outer surface of the Ce-Zr support rather than entering the pores of the support thus reducing the impregnation level [244].

Table 5.7: Rietveld refinement results of the catalysts prepared using in house calcined Ce-Zr support.

Loading wt %	Wet impregnation		Dry impregnation	
	Ce-Zr (wt%)	NiO (wt%)	Ce-Zr (wt%)	NiO (wt%)
10	90.70	9.30	90.50	9.50
20	79.60	20.40	81	19
30	71.70	28.30	74	26

The Rietveld refinement results of the catalysts prepared using pre calcined Ce-Zr support also showed results similar to that obtained using in house calcined Ce-Zr support. Table 5.8 shows the Rietveld refinement results of the catalysts prepared using pre calcined Ce-Zr support. The goodness of fit for all the catalysts mentioned in the Tables 5.7 and 5.8 was around 2 which suggest a very good match with the reference patterns. As a result the crystallite sizes obtained for the catalysts would be accurate.

Table 5.8: Rietveld refinement results of the catalysts prepared using pre calcined Ce-Zr support.

Catalyst	Ce-Zr (wt%)	NiO (wt%)
NiO/Ce-Zr	90.50	9.50
NiO-SnO/Ce-Zr	90.25	9.75
NiO-K_2O/Ce-Zr	90.13	9.87

The peaks attributed to K_2O and SnO were not observed in the diffractogram (Figure 5.12) suggesting fine dispersion of the dopants on the pre calcined Ce-Zr and hence they were not detected by XRD. Pengpanich et al., 2008 [227] reported similar results in case of Ni-Sn/$Ce_{0.75}Zr_{0.25}O_2$ catalysts utilised in partial oxidation of iso-octane. The existence of peaks attributable to single-phase Ni_3Sn, Ni_3Sn_2 and Ni_3Sn_4 were also not detected in Ni-Sn/$Ce_{0.12}Zr_{0.88}O_2$ catalysts [227].

The Ce-Zr and NiO crystallite sizes obtained from Rietveld refinement of the catalysts prepared by wet and dry impregnated in house Ce-Zr are shown in Table 5.9. The crystal size of Ce-Zr remained constant irrespective of the type of the impregnation processes employed. In contrast, the crystal size of NiO in the catalyst varied depending on loading and impregnation method. In the dry impregnation method, the NiO crystallite size increased linearly with the NiO loading. However, in the wet impregnation method, the NiO crystal size increased until 30 wt% loading, whereupon it decreased. This could be as a result of the surface coating effect explained previously. The increase in NiO particle size can lead to an increased plugging of the support pores, which causes a decrease of the accessible pore area for the reactant gas, in turn affecting the catalytic activity.

Table 5.9: Comparison of crystallite sizes obtained using wet and dry impregnation methods employing in house calcined Ce-Zr support.

Loading wt %	Wet impregnation		Dry impregnation	
	Ce-Zr (nm)	NiO (nm)	Ce-Zr (nm)	NiO (nm)
10	11.41	15.59	11.63	23.98
20	11.33	37.28	11.37	32.40
30	11.33	33.90	11.68	36.84

Table 5.10: Crystallite sizes of NiO catalysts prepared using wet impregnation of the pre calcined Ce-Zr support.

Catalyst	Ce-Zr (nm)	NiO (nm)
NiO/Ce-Zr	11.92	13.59
NiO-SnO/Ce-Zr	11.38	13.74
NiO-K_2O/Ce-Zr	12.19	13.54

Table 5.10 compares the NiO and Ce-Zr crystallite sizes obtained from the Rietveld refinement of the NiO/Ce-Zr catalysts prepared using pre calcined Ce-Zr support. It can be seen from Tables 5.9 and 5.10, the NiO crystallite size obtained in wet impregnated

pre calcined Ce-Zr is smaller than the in house calcined Ce-Zr. In the three catalysts NiO-K_2O/Ce-Zr was slightly higher than NiO/Ce-Zr and NiO-SnO/Ce-Zr catalysts. Similarly, the crystallite size for Ce-Zr in NiO-K_2O/Ce-Zr was slightly higher as compared to the other two. The addition of dopants induced some micro strain in NiO. At similar NiO loading (10 wt%) according to Dantas et al. [251] NiO crystallite sizes lie in the range of 15-50 nm when using Ce-Zr support. The smaller NiO crystallite results in better NiO reduction kinetics which would in turn affect the performance of the catalyst.

Figure 5.13 shows the X ray diffraction patterns for fresh NiO/Al and NiO-K_2O/Al catalysts. The 2θ values of 25, 35-37, 43 and 52-57^o are attributed to Al_2O_3 in the catalyst with highest intensity peak occurring at 43^o. The addition of K to fresh NiO/Al catalyst was shown to reduce significantly NiO crystallite size (from 48 to 35 nm). Higher micro strain was observed in case of the NiO-K_2O/Al catalyst in comparison to the bare NiO/Al catalyst. Like NiO-K_2O/Ce-Zr catalyst, no peaks for K_2O were observed in the NiO-K_2O/Al catalyst. In dry reforming of propane using Mo-Ni/γ-Al_2O_3 catalyst, Siahvashi and Adensia, 2013[252] reported that K_2O was finely dispersed over Mo-Ni/γ-Al_2O_3 catalyst and could not be detected by XRD. The Rietveld refinement allowed deriving the values 17.7 and 18 wt% for NiO content for the NiO/Al and NiO- K_2O/Al catalysts respectively.

The X-ray diffraction of Ce-Zr-3/1 prepared using different alcohol and sugar is shown in Figure 5.14. Absence of ZrO_2 peaks in all the samples suggested the formation of a homogenous solid solution in all the three samples. The Ce-Zr-3/1 support prepared using sugar showed the highest crystallite size of 12.79 nm. The CeZr-3/1 using propanol reduced the crystallite size to 8.8 nm.

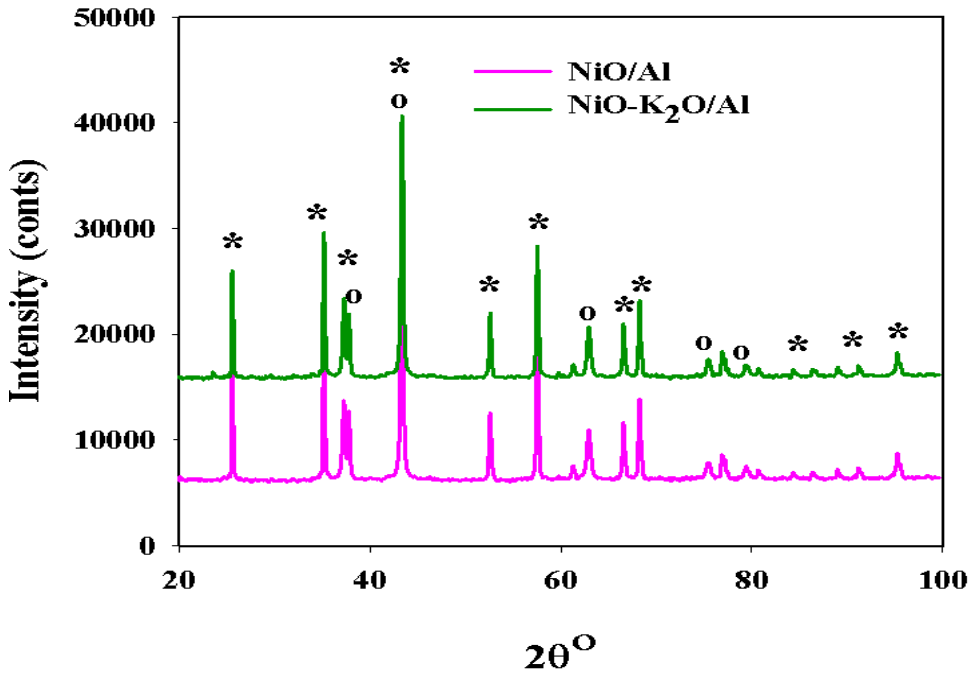

Figure 5.13: X-ray diffraction of NiO/Al and NiO-K_2O/Al catalysts. In the figure (*) represents the Al_2O_3 support and (o) represents NiO.

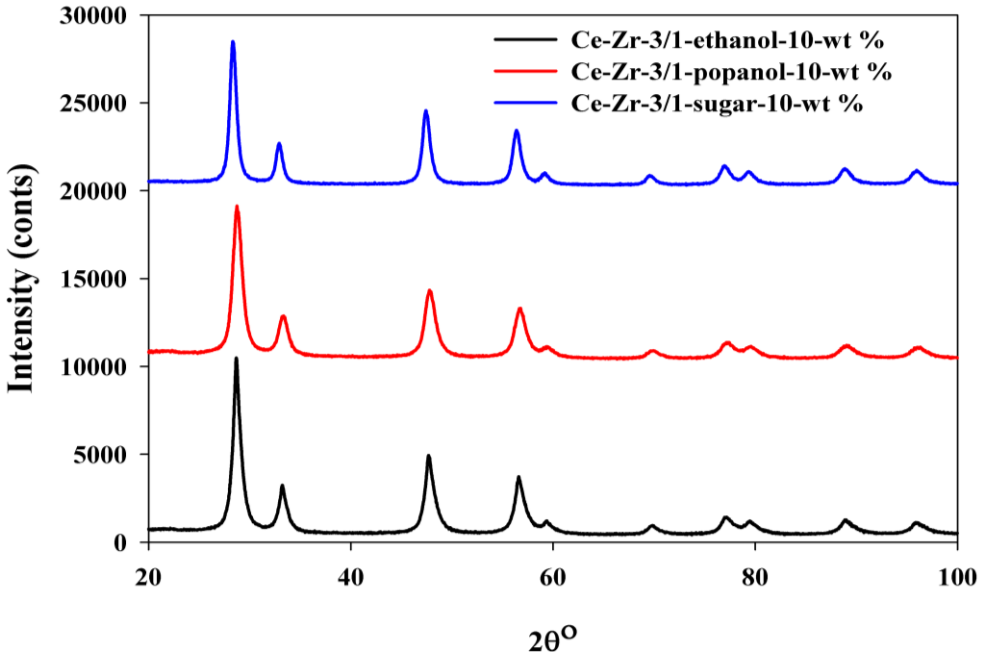

Figure 5.14: X-ray diffraction of Ce-Zr-3/1 prepared by sol-gel synthesis employing TSP as a gelling agent using 10 wt% alcohol and 10 wt% sugar in the preparation.

The X-ray diffraction pattern for Ce-Zr-3/1 and Ce-Al-3/1 supports prepared using 17 wt% ethanol and tamarind seed polysaccharide (TSP) as gelling agent is shown in Figure 5.15. No peaks of responsible for Al_2O_3 were detected which suggests the incorporation of Al_2O_3 in CeO_2. It is well known that the radius of Al^{3+} (0.057 nm) is much smaller than that of Ce^{4+} (0.097 nm), so incorporation of Al^{3+} ions into the ceria lattice inevitably leads to the shrinkage of the lattice [253]. The introduction of Zr and Al into the Ce lattice reduced the lattice parameters as shown in the Table 5.11. This shows that a solid solution between CeO_2, ZrO2 and Al_2O_3 was formed in Ce-Zr-3/1 and Ce-Al-3/1 supports. The crystallite sizes for the Ce-Zr-3/1 support were larger than Ce-Al-3/1. Sun et al.[253] reported similar results in the preparation of Ce-Al mix oxide by citric acid combustion method. The crystallite size decreased from 24 nm with CeO_2 to 9 nm with Ce-Al-3/1 oxide. The XRD pattern for the NiO/Ce-Zr-3/1 is shown in the Figure 5.16. Like other catalysts NiO/Al and NiO/Ce-Zr, the NiO peaks are observed at 2θ values of 37, 43, 63 and 79°, while Ce-Zr-3/1 peaks were observed at same 2θ as shown in Figure 5.15. The NiO crystallite size obtained with this catalyst was 21.21 nm which was higher than the other Ce-Zr based catalysts.

Unlike NiO/Al, NiO/Ce-Zr and NiO/Ce-Zr-3/1 catalyst the NiO/Ca-Al catalyst was unable to be refined due to the presence of large amount of amorphous material and complex pattern making it very difficult to refine. Figure 5.17 shows the XRD pattern for the NiO/Ca-Al catalysts. Likewise the XRD pattern for NiO-CeO-CoO/Al contained large amount of amorphous material making it difficult to perform Rietveld refinement. The sizes of size of CeO and CoO oxide were reported to be 9.64 and 15.8 nm, which were determined by Giannakeas et al. [178].

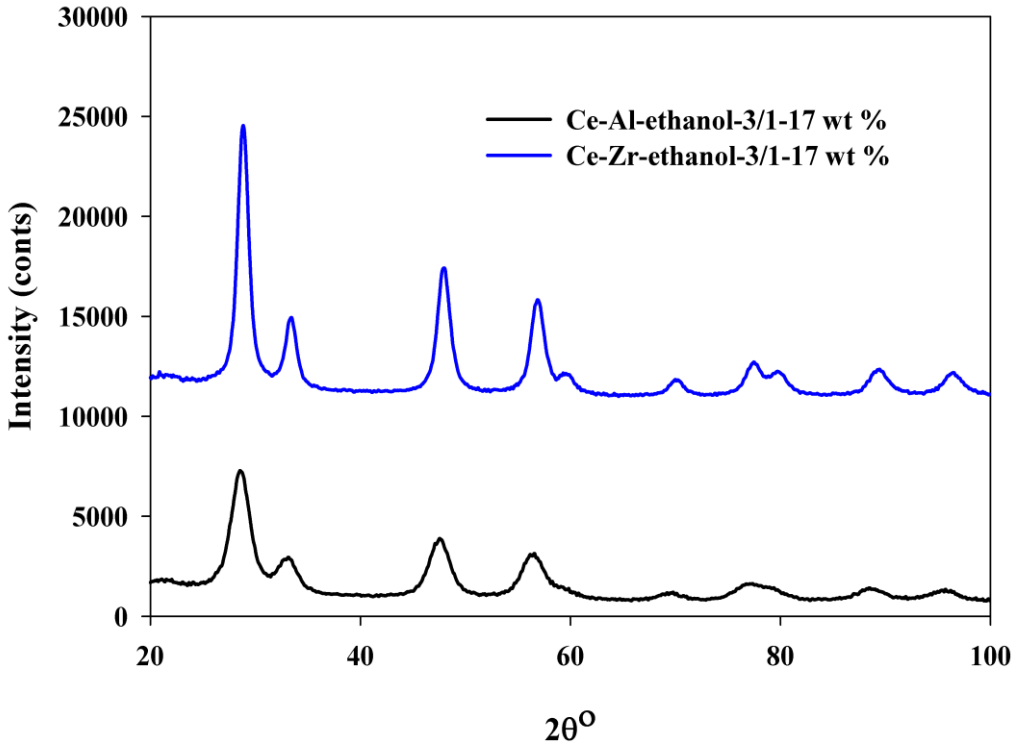

Figure 5.15: X-ray diffraction of Ce-Zr-3/1 and Ce-Al-3/1 prepared by sol-gel synthesis using 17 wt % ethanol in sol gel synthesis employing TSP and gelling agent.

Table 5.11: Properties of Ce-Zr- 3/1 and Ce-Al-3/1 mix oxides.

Sample	Lattice parameter (nm)	Crystallite size(nm)
CeO_2	0.54146	10
Ce-Zr-3/1[a]	0.53869	10.85
Ce-Zr-3/1[b]	0.53857	8.8
Ce-Zr-3/1[c]	0.53790	12.7
Ce-Zr-3/1[d]	0.53718	7.65
Ce-Al-3/1[d]	0.54092	4.18

a- The support was prepared using 10 wt% ethanol and 3 wt% TSP.

b- The support was prepared using 10 wt% sugar and 3 wt% TSP.

c- The support was prepared using 10 wt% propanol and 3 wt% TSP.

d- The supports were prepared using 17 wt% ethanol and 3 wt% TSP.

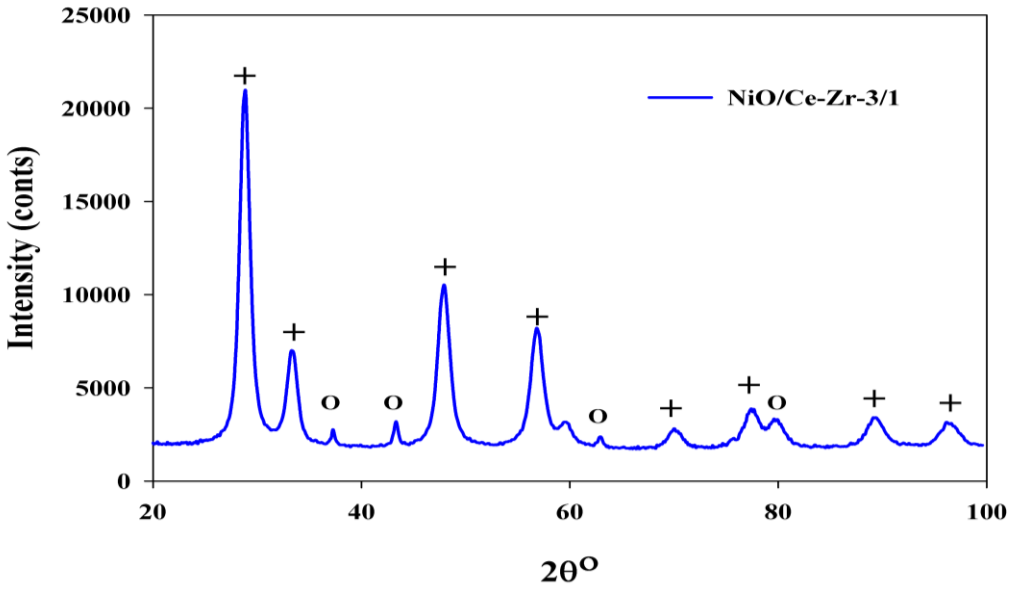

Figure 5.16: X-ray diffraction of NiO/Ce-Zr-3/1 prepared by sol-gel synthesis using 17 wt% ethanol in sol gel synthesis employing TSP and gelling agent. In the Figure (+) represents the Ce-Zr-3/1 support and (o) represents NiO.

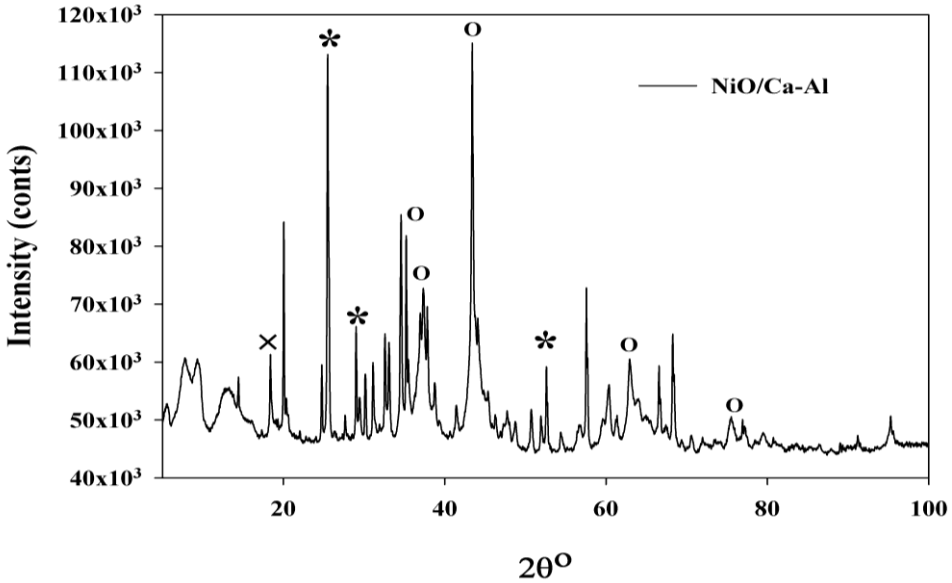

Figure 5.17: X-ray diffraction pattern of NiO/Ca-Al catalyst. In the Figure (+) represents the Ce-Zr-3/1 support and (o) represents NiO. In the Figure (×) Ca-Al, (*) represents Al_2O_3 and (o) represents NiO.

5.2.3 Scanning Electron Microscopy analysis (SEM) and Energy Dispersive X-ray (EDX)

Figure 5.18, 5.19 and 5.20 shows the SEM Images of NiO/Ce-Zr, NiO-SnO/Ce-Zr and NiO-K_2O/Ce-Zr catalyst.

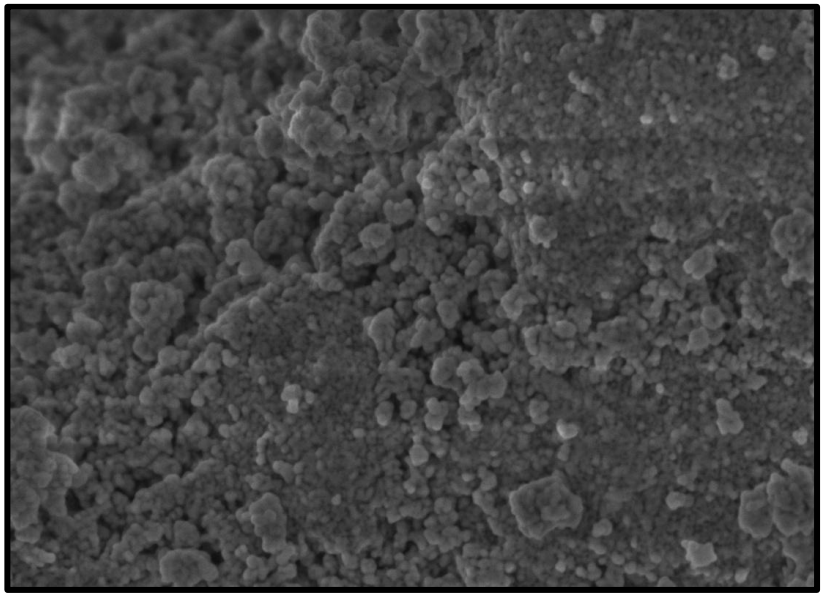

Figure 5.18: A SEM image of NIO/Ce-Zr prepared using wet impregnation of pre calcined Ce-Zr support with 50 K mag.

It can be seen from the Figures (5.18, 5.19 and 5.20) the morphology of the all the catalysts looks similar, although the presence different size particles can be seen in all the catalysts. In comparison to NiO/Ce-Zr, NiO-SnO/Ce-Zr and NiO-K_2O/Ce-Zr show the presence of slightly bigger particles. The elemental mapping of the NiO/Ce-Zr catalyst is shown in the Figures 5.21. It can be seen that Ni distributed uniformly over the catalyst surface. The elemental distribution of the NiO-SnO/Ce-Zr and NiO-K_2O/Ce-Zr showed that the dopants such as Sn and K along with Ni are uniformly distributed (Figure 5.22 and 5.23).

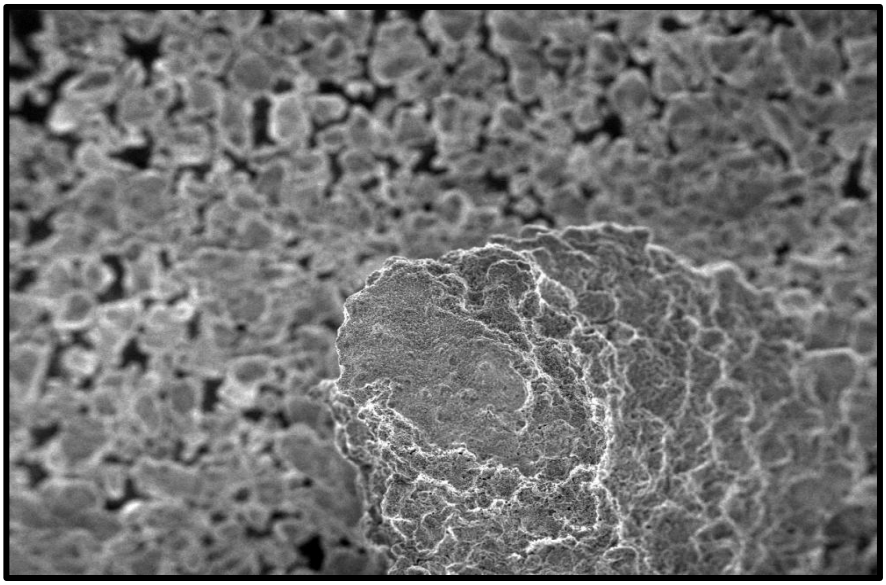

Figure 5.19 A SEM image of NiO-SnO/Ce-Zr prepared using wet impregnation of pre-calcined Ce-Zr support with 50 K mag.

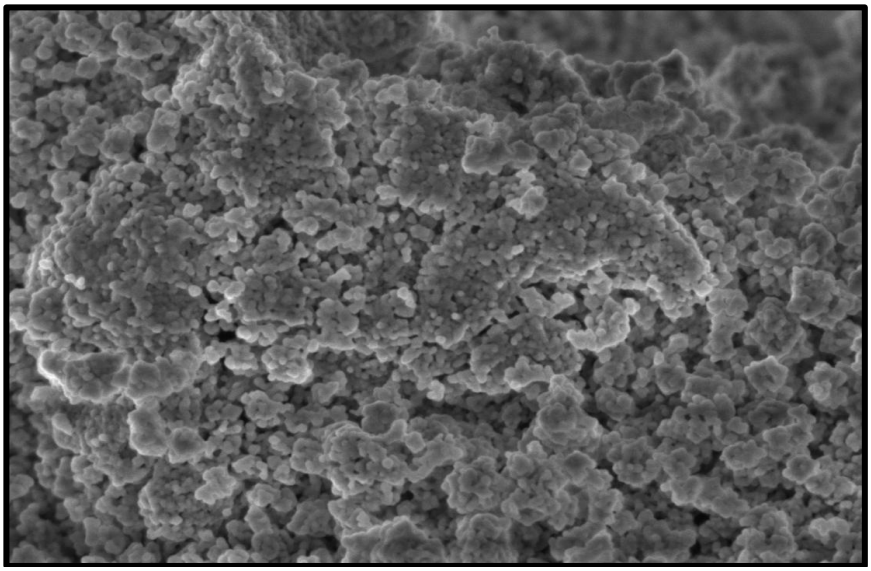

Figure 5.20 A SEM image of NiO-K_2O/Ce-Zr prepared using wet impregnation of pre calcined Ce-Zr support with 50 K mag.

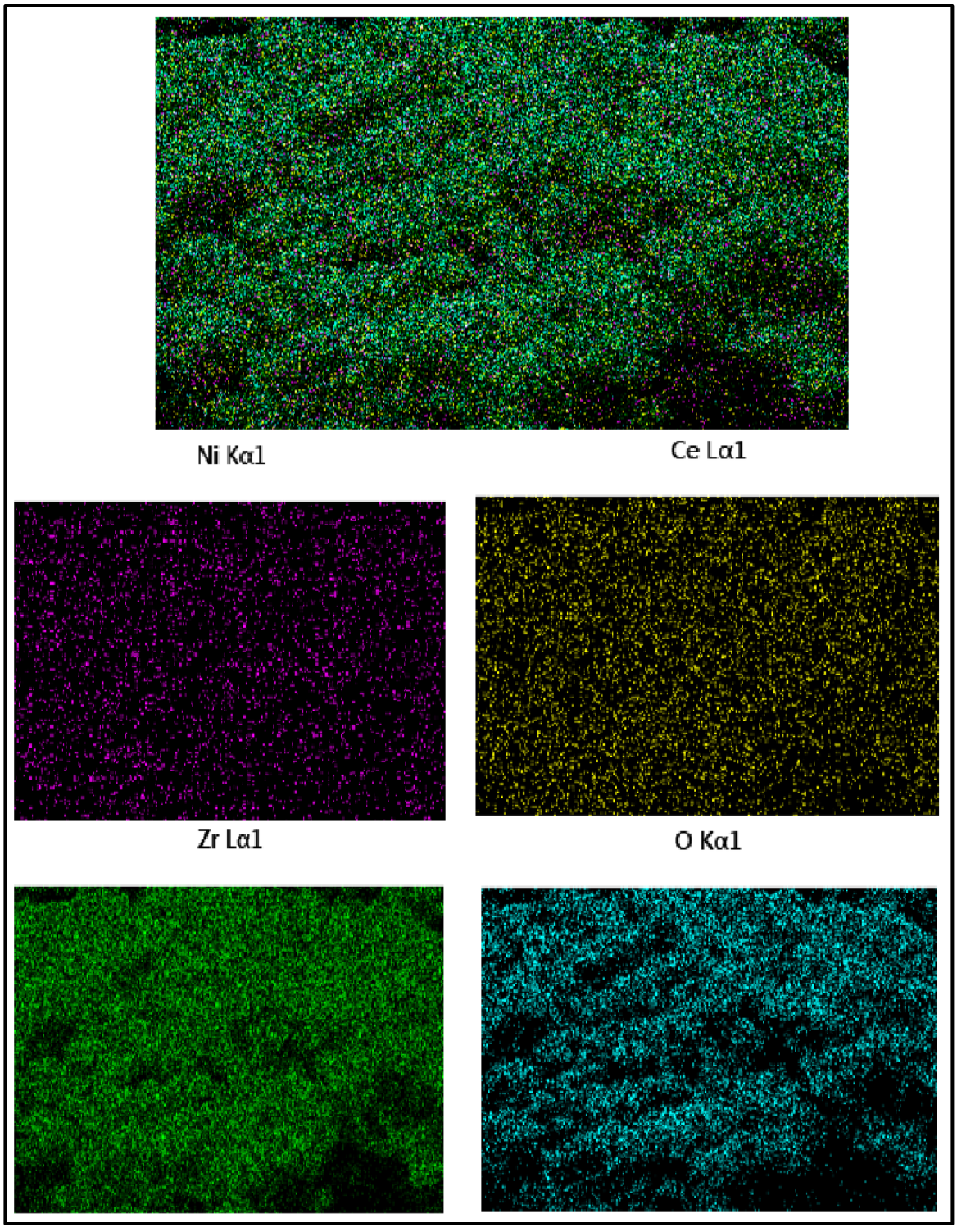

Figure 5.21: Elemental dispersion of the NiO/Ce-Zr prepared by wet impregnation of the precalcined Ce-Zr support.

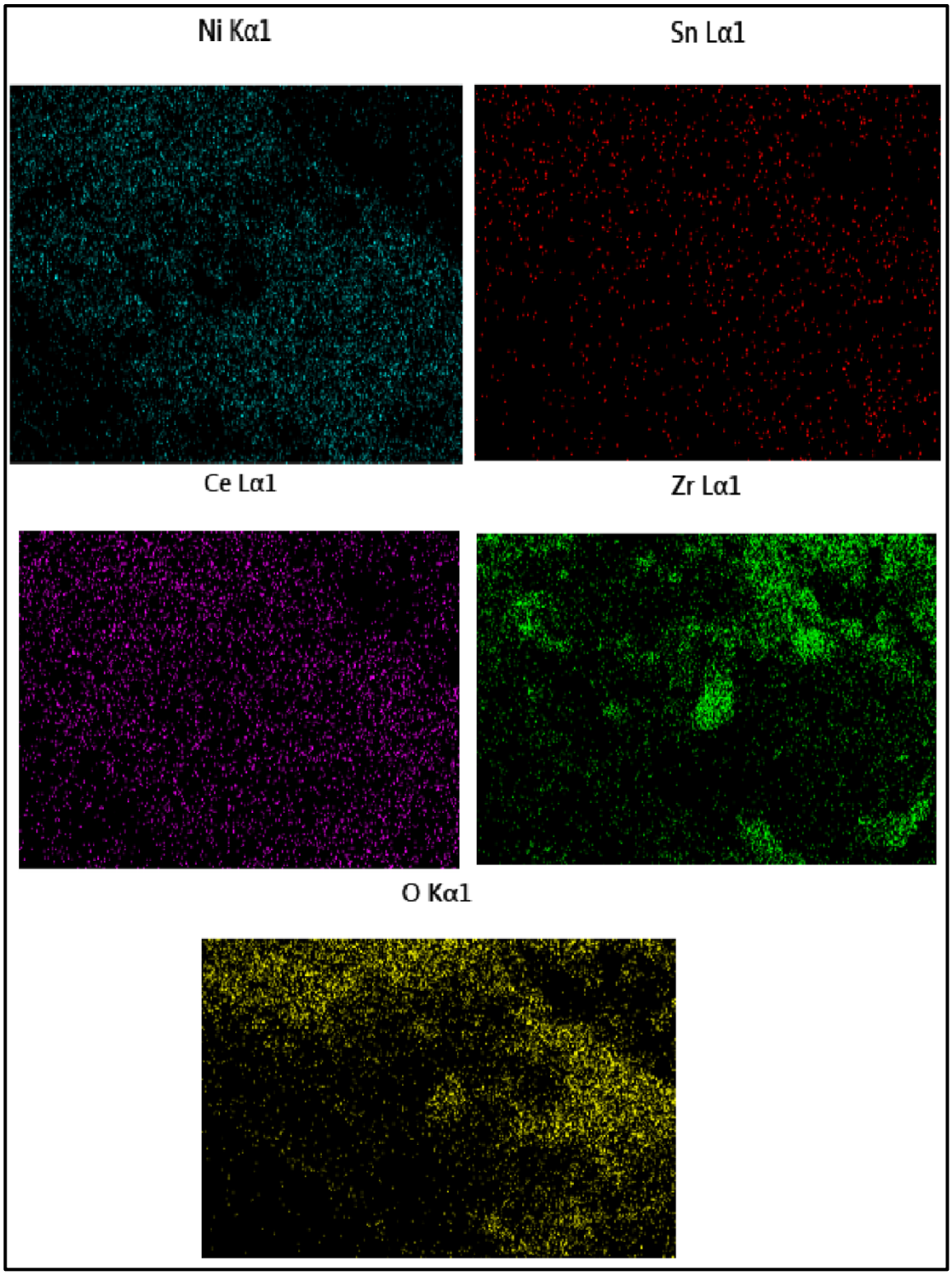

Figure 5.22: Elemental dispersion of the NiO-SnO /Ce-Zr prepared by wet impregnation of the precalcined Ce-Zr support.

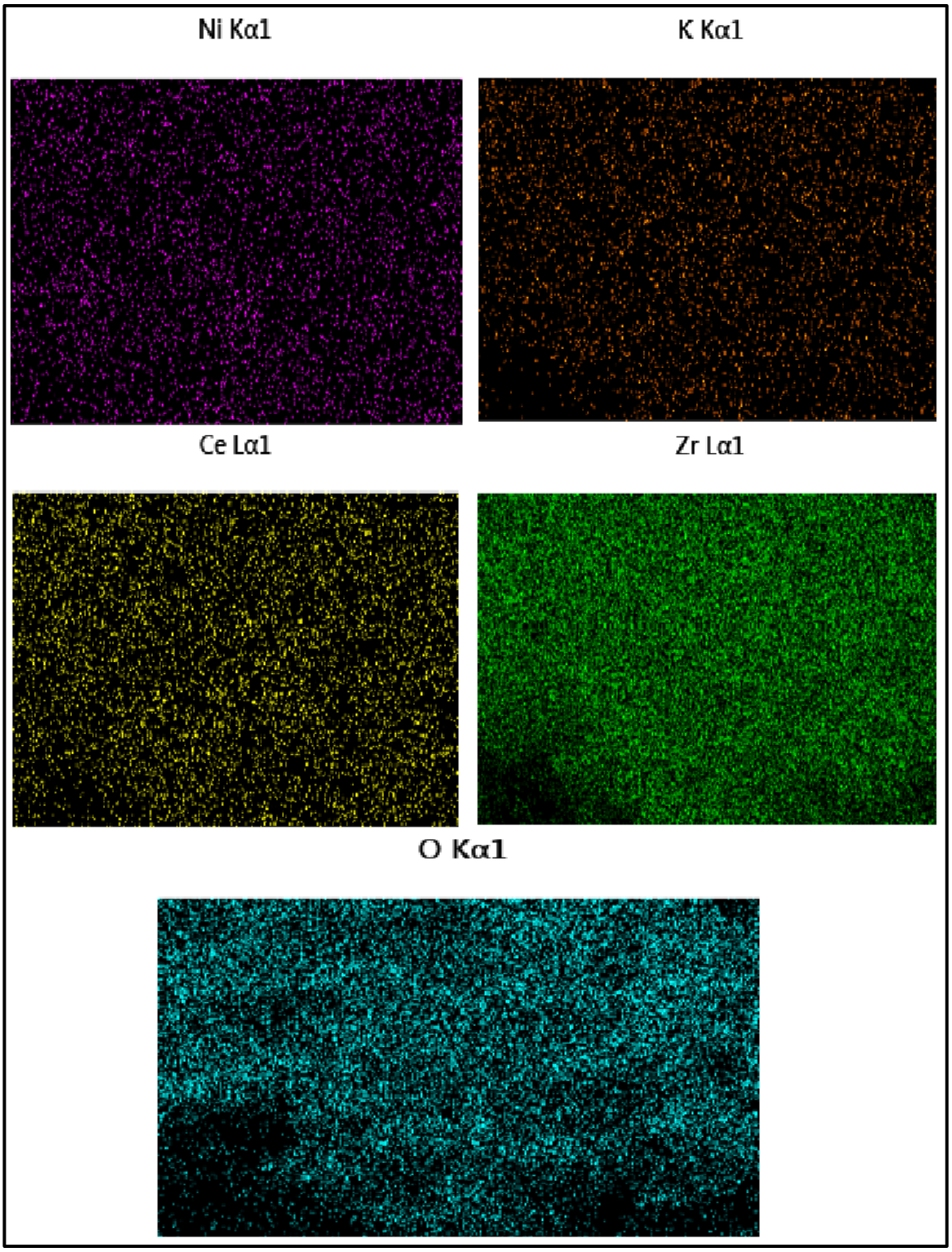

Figure 5.23: Elemental dispersion of the NiO-K_2O/Ce-Zr prepared by wet impregnation of the precalcined Ce-Zr support

6. Steam reforming of biodiesel

This evaluation was performed to determine the feasibility of H_2 production from biodiesel using CSR process. The experiments performed are divided into four series. In the first instance, effect of temperature on the processes performance was evaluated. For this part of the experiments, steam/carbon (S/C) molar ratio and weight hourly space velocity (WHSV) was kept constant and the reactor temperature was varied from 600-800^{o}C. Commercial catalysts (Ni/Al) and (Ni/Ca-Al) were utilised for this part of the experiments. The biodiesel and water vaporisers were set to 365 and 170^{o}C respectively. In the second series of experiments, the effect of biodiesel vaporiser temperature on the processes was examined. Water vaporiser temperature, WHSV, reactor temperature, and S/C ratio were kept constant at 170°C, 3.52h^{-1}, 650°C and 3 respectively for these experiments.

In the third series of experiments, the effect of WHSV on the performance of Ni/Ca-Al was evaluated using optimum reactor and vaporiser temperatures from series 1 and 2. Using the results of optimum residence time (WHSV) and reactor temperature, the effect of various catalysts and different biodiesel feedstocks on the CSR processes was explored. Various catalyst supports and i.e. ceria-zirconia, calcium aluminate and alumina on the process were investigated. Biodiesels from various origins i.e. palm oil, commercial, and prepared in house were used in these experiments. Finally the effect of molar steam to carbon ratio (S/C) on the performance of the Ni/Ca-Al catalyst was evaluated at a given WHSV and reactor temperature.

6.1 Reactions involved

Various reactions such as steam reforming (SR), water gas shift (WGS), decomposition (D), methanation (METH), carbon gasification (GS) and Boudouard reaction (BD) are

involved in SR processes. SR of oxygenated hydrocarbons such as acetic acid, ethanol, glycerol, and waste cooking oil and biodiesel is given by reaction (R-6.1). This reaction is an endothermic reaction and as such is feasible at high temperatures, depending up on the type of fuel which is steam reformed. For e.g. methanol CSR is carried out at lower temperatures i.e. 250-350°C. Ethanol CSR is performed in the temperature range of 500-600°C [254], while in case of glycerol, temperature above 600°C is preferred for SR reaction [255]. The oxygenated hydrocarbons react with steam over metallic catalysts to produce H_2, CO, CO_2, CH_4 and C. Other hydrocarbons such as C_2H_4, C_2H_6, C_3H_6 and C_4H_8 are also formed as a result of complex reactions such as dehydration, dehydrogenation etc.

$$C_nH_mO_k + (n\text{-}k)\ H_2O \xrightleftharpoons{Cat} nCO + \left(\frac{m}{2} + n - k\right)H_2 \quad \Delta H_{f,298K} > 0 \tag{6.1}$$

WGS (R-6.2) occurs simultaneously with SR reaction consuming the CO produced and making H_2 and CO_2 in the process.

$$CO + H_2O \xrightleftharpoons{cat} CO_2 + H_2 \quad \Delta H_{f,298K} = \text{-}41.2 \text{ kJ/mol CO} \tag{6.2}$$

The overall SR reaction (R-6.3) which is a combination of R-6.1 and R-6.2 is given by following reaction.

$$C_nH_mO_k + (2n\text{-}k)\ H_2O \xrightleftharpoons{cat} nCO_2 + \left(\frac{m}{2} + 2n - k\right)H_2 \quad \Delta H_{f,298K} > 0 \tag{6.3}$$

Side reactions such as thermal decomposition of oxygenated hydrocarbons (R-6.4) take place along with the SR reaction (R-6.1) leading to the formation of carbon on the catalyst surface affecting the catalyst performance.

$$C_nH_mO_k \xrightarrow{cat} (n-k)C + \left(\frac{m}{2}\right)H_2 + kCO \quad \Delta H_{f,298K} > 0 \tag{6.4}$$

In the above reactions n, m and k are the molar numbers of carbon, H_2 and oxygen atoms in the oxygenated hydrocarbon (biodiesel) of elemental formula $C_nH_mO_k$ (moisture free basis).

Other reactions which affect the H_2 yield and performance of the catalyst are given by (R-6.5) to (R-6.7).

$$CO + 3H_2 \overset{cat}{\rightleftharpoons} CH_4 + H_2O \; \Delta H_{f,298K} = -206.2 \text{ kJ/mol CO} \quad (6.5)$$

METH reaction (R-6.5) competes with SR reaction (R-6.1) consuming H_2 and affecting H_2 yield. Temperature plays an important role in governing the extent of this reaction. METH reaction (forward R-6.5) is dominant at low temperature up to 400°C, consuming H_2 and CO producing CH_4 and H_2O. Above 600°C, reverse R-6.5 i.e. steam methane reforming (SMR) is promoted, consuming CH_4 and H_2O and producing H_2 and CO.

In addition to the above reactions, (R-6.6) and (R-6.7) reactions are the important reactions which occur at high temperatures and are responsible for carbon removal from catalyst surface, affecting the life and the performance of the catalyst.

$$C + H_2O \overset{cat}{\rightleftharpoons} CO + H_2 \; \Delta H_{f,298K} = 131.3 \text{ kJ/mol C} \quad (6.6)$$

$$2CO \overset{cat}{\rightleftharpoons} CO_2 + C \; \Delta H_{f,298K} = -172.5 \text{ kJ/mol } CO_2 \quad (6.7)$$

6.2 Experimental procedure

As different types of catalysts were used in the evaluations, different procedures were adopted for loading the catalysts. In case of the commercial catalysts i.e. Ni/Al and Ni/Ca-Al were crushed from bigger pellets (5 mm diameter) and then sieved to obtain particle size of 0.85-2mm diameter. This size was chosen to prevent pressure drop in the system. For each evaluation 2.0506 g of catalyst was used. The catalysts were sandwiched in two quartz wool plugs of 4 μm size and were placed in the reactor for the evaluation. The powder catalysts were mixed with quartz sand of 150-200 μm size to make up 2.0506 g of reactor load. After every run the experimental set up was flushed overnight with nitrogen in order to remove the biodiesel vapours and steam and collect them in the gas liquid separation part of the condenser.

An experiment was performed in a day consisted of 4 main stages. The first stage involved reactor cleaning and unloading the used catalyst from the previous experiment. All the pipes and connections were thoroughly cleaned with acetone to remove condensed biodiesel. In second stage the reactor containing fresh catalyst was attached to the setup and all the pipes along with the connections were leak tested. The third stage consisted of reducing fresh catalyst with 5 vol % H_2/N_2 mixture (200 cm^3/min). Once the fresh catalyst was loaded in the reactor, the reactor temperature was increased to the desired set point by turning on the furnace under flowing N_2 (200 cm^3/min). Upon reaching the set point indicated by reactor bed thermocouple, the N2 flow was switched off and the H_2/N_2 flow was turned on. The completion of the catalyst reduction was shown by a return to steady state H_2 concentration (5% H_2) measured by gas chromatograph. Finally in the last stage the experimental set up was then flushed with pure N_2 to remove the H_2 used during reduction, and the vaporisers were turned on. Once the vaporisers reached the set point, the heating tape was turned on. Both these steps are performed using high N_2 flowrate in order to remove any unreacted biodiesel vapours from previous experiments. The flowrate of N_2 was then lowered to the desired value depending on the experiment and the syringe pumps were turned on. The flow rate of N_2 was set in the range 30-50 cm^3/min (STP), depending on the WHSV value chosen for the experiment. In the experiments performed using commercial biodiesel, biodiesel flowrate was set to 0.978 cm^3/h which gave a carbon input flowrate of 1.50×10^{-5} mol/s. The water flow rate was varied from 1.95 to 2.92 cm^3/h to obtain the desired S/C of 2 and 3 respectively. The flow rates of other biodiesel feedstocks examined were adjusted according to the elemental analysis and the density of the biodiesel to get the desired S/C.

6.3 Process outputs and elemental balances

The process performance was measured in terms of fuel and steam conversion (X_{biod} and X_{H2O}), H_2 yield ($Y_{H2,}$) and H_2 yield efficiency ($Y_{H2,}$ eff), selectivity to carbon containing products (S_{C-i}) and to H_2 containing products (S_{H-i}) using Eqs 6.8-6.28, respectively. In these Eqs, $\dot{n}$ is a molar flow rate, and *y* represents a dry gas mol fraction in the products,

dn/dt is a rate of accumulation of a species, e.g. dn_c/dt denotes an accumulation of moles of carbon element over the dt period of time. Similarly $dn_{H,HC}/dt$ denotes a rate of accumulation of moles of H_2 from hydrocarbons products other than those already listed.

Biodiesel conversion was calculated using Eq 6.8.

$$X_{biod} = \left(\frac{\dot{n}_{biod,\,in} - \dot{n}_{biod,\,out}}{\dot{n}_{biod,\,in}} \right) \times 100 \tag{6.8}$$

Applying carbon balance

$$\left[n \times \dot{n}_{biod,\,in} \right] = \frac{dn_c}{dt} + \left[\dot{n}_{out,\,dry} \times \left(\sum y_{i,C} \right) \right] + \left[n \times \dot{n}_{biod,\,out} \right] \tag{6.9}$$

In the above Eq

$$\dot{n}_{out,\,dry} \times \left(\sum y_{i,C} \right) = \dot{n}_{out,\,dry} \times \begin{bmatrix} y_{CO} + y_{CO_2} + y_{CH_4} + 2 \times y_{C_2H_4} + 2 \times y_{C_2H_6} + \\ 3 \times y_{C_3H_6} + 3 \times y_{C_3H_8} \end{bmatrix} \tag{6.10}$$

Rearranging the above Eq and substituting for $\dot{n}_{out,\,dry} \times \left(\sum y_{i,C} \right)$ we get

$$\left[\dot{n}_{biod,\,in} - \dot{n}_{biod,\,out} \right] = \frac{\dot{n}_{out,\,dry}}{n} \times \begin{bmatrix} y_{CO} + y_{CO_2} + y_{CH_4} + 2 \times y_{C_2H_4} + 2 \times y_{C_2H_6} \\ +3 \times y_{C_3H_6} + 3 \times y_{C_3H_8} \end{bmatrix} + \frac{dn_c}{dt} \tag{6.11}$$

In order to calculate biodiesel conversion, the term $\frac{dn_c}{dt}$ is set to zero, as this term represents the carbon in the condensate and formed on the catalyst surface, which has to measured separately by other techniques i.e. elemental (CHN) and total organic carbon (TOC) analysis of the used catalyst and collected condensate. X_{biod} is therefore interpreted as 'biodiesel conversion to CO, CO_2, and C1-C3 gases'.

Inserting the $\dot{n}_{biod,\,in} - \dot{n}_{biod,\,out}$ value in the Eq 6.8 we arrive at the following expression.

$$X_{biod} = \left(\frac{\begin{matrix} \dot{n}_{out,\,dry} (y_{CO} + y_{CO_2} + y_{CH_4} + 2 \times y_{C_2H_4} + 2 \times y_{C_2H_6} + \\ 3 \times y_{C_3H_6} + 3 \times y_{C_3H_8}) \end{matrix}}{n \times \dot{n}_{biod,\,in}} \right) \times 100 \tag{6.12}$$

Steam conversion is obtained using the Eq 6.13.

$$X_{H_2O} = \left(\frac{\dot{n}_{H_2O,in} - \dot{n}_{H_2O,out}}{\dot{n}_{H_2O,in}} \right) \times 100 \tag{6.13}$$

Applying hydrogen balance, Eq 6.14

$$\left[m \times \dot{n}_{biod,\,in} \right] + \left[2 \times \dot{n}_{H_2O,\,in} \right] = \left[m \times \dot{n}_{biod,\,out} \right] + \left[\dot{n}_{out,\,dry} \times \left(\sum y_{i,\,H} \right) \right] + \left[2 \times \dot{n}_{H_2O,\,out} \right] + \frac{dn_{H,HC}}{dt} \tag{6.14}$$

Rearranging the Eq 6.14 we get Eq 6.15.

$$2\left[\dot{n}_{H_2O,\,in} - \dot{n}_{H_2O,\,out} \right] - \left[m \times \dot{n}_{biod,\,out} \right] - \left[\frac{dn_{H,HC}}{dt} \right] = \left[-m \times \dot{n}_{biod,\,in} \right] + \left[\dot{n}_{out,\,dry} \times \left(\sum y_{i,H} \right) \right] \tag{6.15}$$

In the Eq 6.16, $\dot{n}_{out,\,dry} \times \left(\sum y_{i,H} \right)$ is substituted by the following term.

$$\dot{n}_{out,\,dry} \times \left(\sum y_{i,H} \right) = \dot{n}_{out,\,dry} \times \begin{bmatrix} 2 \times y_{H_2} + 4 \times y_{CH_4} + 4 \times y_{C_2H_4} + 6 \times y_{C_2H_6} \\ + 6 \times y_{C_3H_6} + 8 \times y_{C_3H_8} \end{bmatrix} \tag{6.16}$$

Finally the following expression (Eq 6.17) is derived by substituting $(\dot{n}_{H_2O,\,in} - \dot{n}_{H_2O,\,out})$ in Eq 6.13 and setting $\frac{dn_{H,HC}}{dt}$ to 0. This simplification may introduce a small error in the calculated value of water conversion only if the condensates are shown to contain significant amounts of organic H_2. It will be shown later in the results section that this amount was negligible based on the full carbon balance.

$$X_{H_2O} = \left(\frac{\dot{n}_{out,\,dry} \times (2 \times y_{H_2} + 4 \times y_{CH_4} + 4 \times y_{C_2H_4} + 6 \times y_{C_2H_6} + 6 \times y_{C_3H_6} + 8 \times y_{C_3H_8}) - 0.5m \times (\dot{n}_{biod,\,in} X_{biod})}{\dot{n}_{H_2O,\,in}} \right) \times 100 \tag{6.17}$$

Dry gas molar flowrate $\dot{n}_{out,\,dry}$ is calculated using nitrogen balance.

$$\left[\left(j\times\dot{n}_{biod,\,in}\right)+\left(2\times\dot{n}_{N_2,\,in}\right)\right]=\left[\dot{n}_{out,\,dry}\times\left(2\times y_{N_2,\,out}\right)\right]+\left[j\times\dot{n}_{biod,\,out}\right] \quad (6.18)$$

Where j is the elemental N in biodiesel, which is here is set to 0 due to its negligible contribution to the nitrogen balance.

Rearranging the Eq 6.18 we get

$$\dot{n}_{out,\,dry}=\left[\frac{\dot{n}_{N_{2,\,in}}}{y_{N_{2,\,out}}}\right] \quad (6.19)$$

In the above Eqs $\dot{n}_{biod,\,in}$ $\dot{n}_{H_2O,\,in}$ are the molar flow rates of biodiesel and water fed to the reactor, $\dot{n}_{outdry}$ is the molar flow rate of dry gases leaving the reactor and y_i is the mol fraction of *i* in the dry gas output. All the flowrates of biodiesel, water and dry gases are in mol/s. Molar flow rate of biodiesel and water are calculated using Eq 6.20 and 6.21, where ρ is kg/m^3 , $\dot{V}$ is the volumetric flowrate in m^3/s and W denotes a molar mass in kg/mol, relevant to biodiesel and water respectively.

$$\dot{n}_{biod,\,in}=\left[\frac{m_{biod,\,in}}{\bar{W}_{biod}}\right]=\left[\frac{\rho_{biod,\,in}\times\dot{V}_{biod,\,in}}{\bar{W}_{biod}}\right]\text{mol/s} \quad (6.20)$$

$$\dot{n}_{H_2O,\,in}=\left[\frac{m_{H_2O,\,in}}{\bar{W}_{H_2O}}\right]=\left[\frac{\rho_{H_2O,\,in}\times\dot{V}_{H_2O,\,in}}{\bar{W}_{H_2O}}\right]\text{mol /s} \quad (6.21)$$

H_2 yield was calculated using Eq 6.22.

$$Y_{H_2}(\text{wt\%})=\left(\frac{W_{H_2}\times y_{H_2}\times\dot{n}_{out,\,dry}}{W_{biod}\times\dot{n}_{biod,\,in}}\right)\times 100 \quad (6.22)$$

Eq 6.22 can also be applied to determine CH_4 yield,

Selectivities for the H_2 ($S_{H\text{-}H2}$) and carbon containing gases (S_C) were determined by using the following Eqs. Eq 6.23 and 6.24 provide selectivity to H_2 ($S_{H\text{-}H2}$) and to CH_4 ($S_{H\text{-}CH4}$) with respect to H_2 containing gases.

$$S_{H-H_2} = \left(\frac{y_{H_2}}{y_{H_2} + y_{CH_4} + y_{C_2H_4} + y_{C_2H_6} + y_{C_3H_6} + y_{C_3H_8}} \right) \times 100 \quad (6.23)$$

$$S_{H-CH_4} = \left(\frac{y_{CH_4}}{y_{H_2} + y_{CH_4} + y_{C_2H_4} + y_{C_2H_6} + y_{C_3H_6} + y_{C_3H_8}} \right) \times 100 \quad (6.24)$$

Selectivity of CO ($S_{C\text{-}CO}$) and CO_2 ($S_{C\text{-}CO2}$) with respect to carbon containing gases is given below.

$$S_{C-CO} = \left(\frac{y_{CO}}{y_{CO} + y_{CO_2} + y_{CH_4} + y_{C_2H_4} + y_{C_2H_6} + y_{C_3H_6} + y_{C_3H_8}} \right) \times 100 \quad (6.25)$$

$$S_{C-CO_2} = \left(\frac{y_{CO_2}}{y_{CO} + y_{CO_2} + y_{CH_4} + y_{C_2H_4} + y_{C_2H_6} + y_{C_3H_6} + y_{C_3H_8}} \right) \times 100 \quad (6.26)$$

Efficiencies of the process are defined with the following Eqs.

Fuel reforming efficiency is given by Eq 6.27.

$$\text{Reforming (eff \%)} = \left(\frac{\dot{n}_{H_2,\,out} \times LHV_{H_2}}{\dot{n}_{biod,\,in} \times LHV_{biod}} \right) \times 100 \quad (6.27)$$

In the above LHV refers to the lower heating values of H_2 and biodiesel in kJ/mol. The LHV for H_2 is 24.0 kJ/mol. A singe value of 37.5 kJ/mol was used for the LHV of biodiesel despite the small differences in C, H and O content due to the different feedstocks investigated in this work. H_2 and biodiesel molar flowrates in the Eq are represented by $\dot{n}_{H_2}$ and $\dot{n}_{biod,\,in}$ respectively.

H_2 yield and steam conversion efficiencies are defined as the ratio of H_2 yield or steam conversion obtained during the experiment to that predicted by chemical equilibrium.

$$Y_{H_2}\text{(eff \%)} = \left(\frac{(Y_{H_2})_{exp}}{(Y_{H_2})_{eq}} \right) \times 100 \quad (6.28)$$

$$H_2O \text{ conv (eff \%)} = \left(\frac{(X_{H_2O})_{exp}}{(X_{H_2O})_{eq}} \right) \times 100 \quad (6.29)$$

The balances took into account the input data (CHN, flowrate of biodiesel, water and carrier gas). The outputs i.e. the composition of all the gases i.e. CO, CO_2, N_2, H_2, CH_4, C_2H_4, C_2H_6, C_3H_6 and C_3H_8 in the product were obtained from the gas chromatograph. The mole fractions of these output products were calculated in the elemental balances.

6.4 Results and discussions

6.4.1 Thermodynamics of biodiesel steam reforming

Chemical equilibrium with application (CEA) software provided by NASA was used for this purpose. The software relied on minimisation of Gibbs free energy in order to get the equilibrium outputs. Nine input compounds from methyl laurate (C13) to methyl arachidate (C20) were considered along with steam and nitrogen as an inert gas. The actual composition of these nine compounds in biodiesel was obtained using GC. Solid carbon was not considered as potential product due to the variable properties of carbon formed on the catalyst during the experiments. Temperature range of 200-900°C at an increment of 50°C was chosen for the evaluation and S/C ratio was varied from 1 to 3 respectively. The equilibrium analysis showed that H_2, CO, CO_2, CH_4, H_2O and insignificant amount of NH_3 can be formed.

The effect of temperature and S/C on Y_{H2} and ($S_{H\text{-}CH4}$), in SR of commercial biodiesel at the experimental conditions is represented in Figure 6.1. Figure 6.2 and 6.3 shows the selectivities to various carbon containing products obtained by SR of commercial biodiesel. SR of biodiesel (R-6.1) would occur in sequence with WGS (R-6.2) and METH reaction (R-6.5). In the lower temperature range (200-400°C), high ($S_{H\text{-}CH4}$) irrespective of the S/C ratio is observed which would affect very significantly the YH_2.

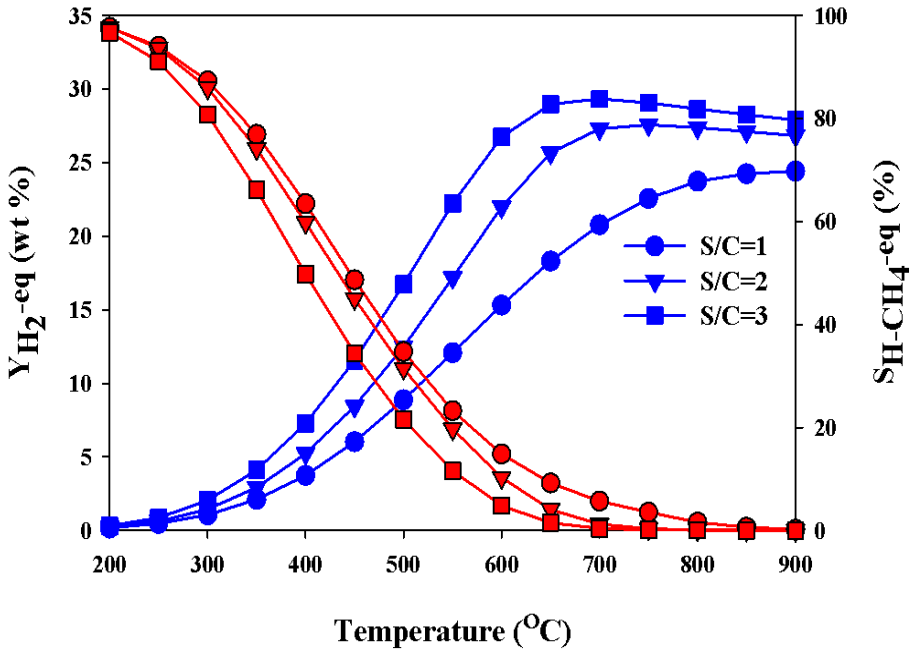

Figure 6.1: Effect of temperature on equilibrium H_2 yield (Y_{H2}) and CH_4 (S_C-CH_4) selectivity in steam reforming of commercial biodiesel at different S/C ratios, and 1 atm.

This could be the result of METH (R-6.5) reaction. It was considered that eliminating CH_4 from the potential equilibrium products would not be justified since in practice, Ni catalysts are active in both SR and METH reactions. WGS reaction (R-6.2) is also active in this temperature region, which could explain the presence of some amount of H_2 (lower yield) in this temperature range.

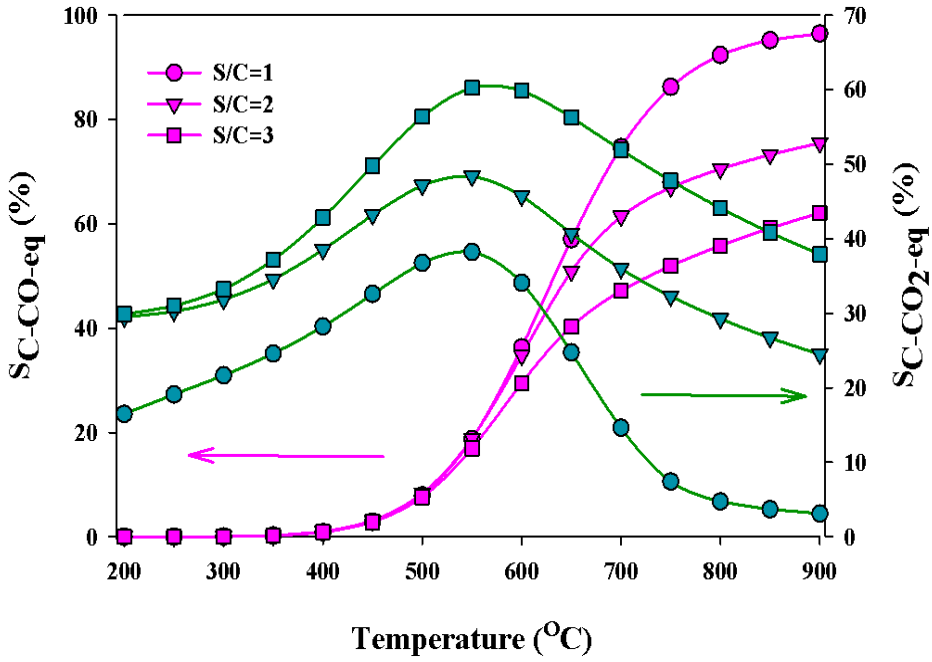

Figure 6.2: Effect of temperature on equilibrium selectivity to CO ($S_{C\text{-}CO}$) and CO_2 ($S_{C\text{-}CO2}$) in SR of commercial biodiesel at different S/C ratios, and 1atm.

It can be seen from Figure 6.2 and 6.3 that in the lower temperature range, CH_4 and CO_2 dominate the product distribution in the carbon containing products, supporting the theory of high METH activity (R-6.5) and some WGS (R-6.2) activity. Negligible ($S_{C\text{-}CO}$) irrespective of S/C can further strengthen the argument. Increasing temperature from 200 to 400^{o}C shows a shift in product distribution of carbon containing gases. This could suggest a shift from METH reaction (R-6.5) towards SR (R-6.1) and the WGS reaction (R-6.2) , revealed by slight increase in Y_{H2} (Figure 6.1) along with ($S_{C\text{-}CO2}$) and decrease in ($S_{C\text{-}CH4}$, Figure 6.3). Above 400°C, increase in SR of biodiesel could be promoted with the other two reactions (R-6.2 and R-.6.5). This is evident by slightly increased Y_{H2} (Figure 6.2) and ($S_{C\text{-}CO}$). The steep rise in Y_{H2} and ($S_{C\text{-}CO}$) above 500°C can be explained by the pronounced SR of biodiesel (R-6.1) and CH_4 (SMR reverse R-6.5). Both these reactions are endothermic in nature and increase in temperature shifts the equilibrium towards product side exhibited by increase in Y_{H2} and ($S_{C\text{-}CO}$). Significant reduction in CH_4 selectivities ($S_{H\text{-}CH4}$) and ($S_{C\text{-}CH4}$) show that high temperatures (700-900°C), favour SR (R-6.1 and reverse R-6.5) producing H_2 and CO.

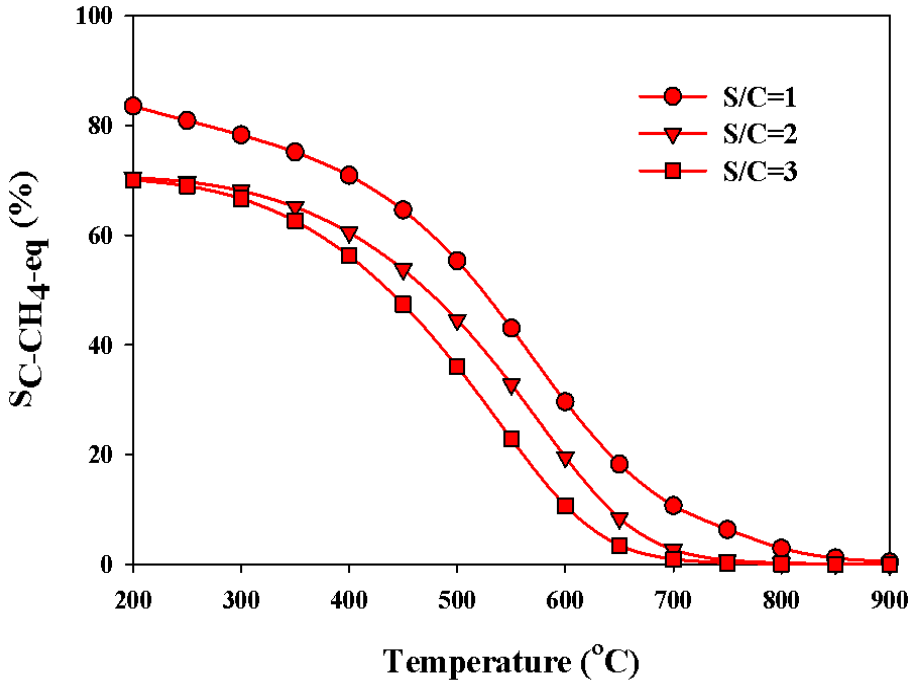

Figure 6.3: Effect of temperature on equilibrium selectivity to CH_4 (S_{C-CH4}) in SR of commercial biodiesel at different S/C ratios, and 1atm.

Although at these high temperatures (S_{C-CO}) also increases due to shift in equilibrium to reverse water shift reaction (reverse R-6.2) towards the reactants consuming H_2 and CO_2 thus affecting YH_2 (Figure 6.1).

The shallow dip in Y_{H2} at higher temperature and steep rise at lower temperatures can be explained by strong endothermic nature of SR reactions (biodiesel (R-6.1) and CH_4 (reverse R-6.5)) over weak exothermic WGS reaction (R-6.2). In addition to temperature, S/C plays an important role in SR reactions. According to Le Chatelier's principle increasing S/C ratio increases YH_2. The Y_{H2} peaked at different temperatures when S/C ratio was varied. At the lowest S/C of 1, Y_{H2} increased all the way up till 900°C. The peak yield temperature reduced to 750 and 700°C for S/C of 2 and 3 respectively. This could be as a result of stronger effect of S/C on SR reactions (R-6.1 and (reverse R-6.5) as compared to WGS (R-6.2).

Increasing S/C ratio promotes SR (R-6.1) increasing H_2 yield. Likewise SMR (reverse R-6.5), also increases with rise S/C ratio affecting Y_{H2} above 500°C. Increased S/C below 500°C, promoted WGS reaction as seen by decreased CO ($S_{C\text{-}CO}$) and increased CO_2 ($S_{C\text{-}CO2}$) selectivities (Figure 6.2). Thus increased S/C ratio has a positive impact on Y_{H2} and reduces formation of by products such as CH_4. Higher S/C ratio in practice would require larger reactor volumes to accommodate the high steam flowrates. It would also mean higher cost of steam generation and would increase volume of recycled water in the plant.

6.4.2 Effect of temperature

The effect of temperature on CSR of biodiesel was studied using commercial biodiesel in the temperature range of 600-800°C using the commercial Ni/Al catalyst is shown in Figure 6.4.

The CSR evaluations were performed using biodiesel liquid flow rate of 0.978 ml/h (20 ^oC) and liquid water flow of 2.92 ml/h (20 ^oC) with nitrogen gas flow rate of 50 ml/min (STP), using 365 and 170 ^oC vaporiser temperatures for biodiesel and water respectively. The biodiesel flow rate accounted for a carbon feed rate of 1.50×10^{-5} mol /s for all the experiments, which is used to perform the carbon balance as shown in Table 6.1.

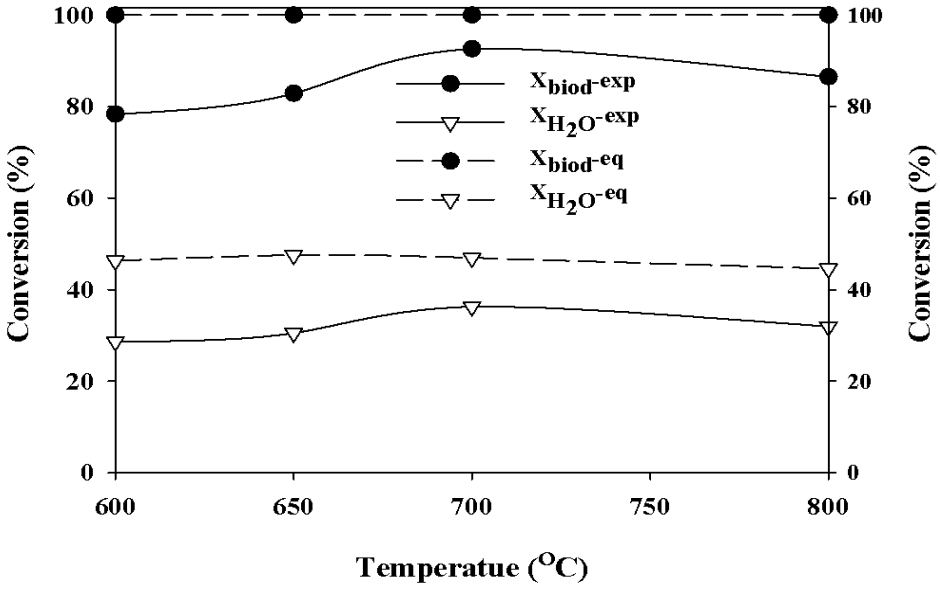

Figure 6.4: Effect of temperature on CSR of commercial biodiesel at S/C of 3 and WHSV of 3.52 h^{-1} using 365 and 170°C biodiesel and water vaporiser temperatures.

In order to check reproducibility of the experiments each experiment was performed twice, and the best one among the two in terms of stability of conversion biodiesel and water was chosen for further analysis i.e. to perform carbon balance and other characterisation work. The experiments were performed for duration of 7200 s. Table 6.1 lists the molar carbon balance consisting of gas ('C in gases') and volatiles products ('C in the condensate'), as well as carbon deposited as coke on the catalyst ('C on catalyst'). It is important to note that the term coke carbon carried the largest uncertainties, as it relied on samples taken from the catalyst bed, the difficulty residing in collecting thin layers of carbonaceous residue deposited on other parts of the reactor and seeping through the sample lines. Further as the catalysts were supported on quartz wool, some amount of carbon was deposited on the top layer of the quartz wool, which was not analysed. The used catalyst pellets were crushed before they were subjected to elemental analysis for detection of coke carbon on the catalyst surface, some carbon would have been lost during the crushing processes. All these reasons could explain why the carbon balance was in some cases within 12-13 mol% of the carbon feed. Another explanation

for the unaccounted carbon would be the presence of carbon containing compounds (carbon number >5) which were not measured by gas chromatograph.

The effect of temperature on Y_{H2} and (S_{H-H2}) is shown in Figure 6.5, and the selectivity to various carbon containing products in the gas phase is shown in Figure 6.6. The reproducibility of the experiments was checked by performing the experiments a second time. The selectivity to any given gas was in all cases very close to the corresponding equilibrium value. It is unlikely that SR (R-6.1) is involved directly in the reaction of steam with these very long molecules to produce CO and H_2. Instead, it is expected that the FAMEs first break up into smaller fragments under thermal and catalytic effects (catalytic cracking) and that the smaller fragments then undergo SR, similarly to what Marquevich et al [173] proposed for vegetable oil feedstock. Conversion of biodiesel to gas phase carbon products increased from 78% at 600 °C to 92% at 700 °C, and upon further temperature increase, it decreased slightly, with similar observations made for steam conversion (28% to 33%) (Figure 6.4).

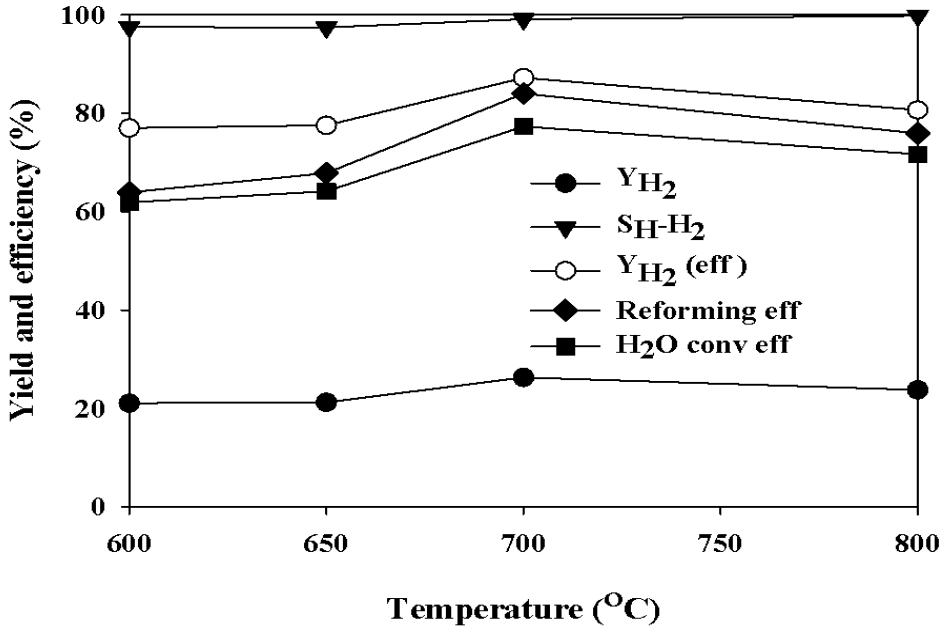

Figure 6.5: Effect of temperature on H_2 yield (Y_{H2}) and selectivity (S_{H-H2}) in CSR of commercial biodiesel using same conditions as Figure 6.4

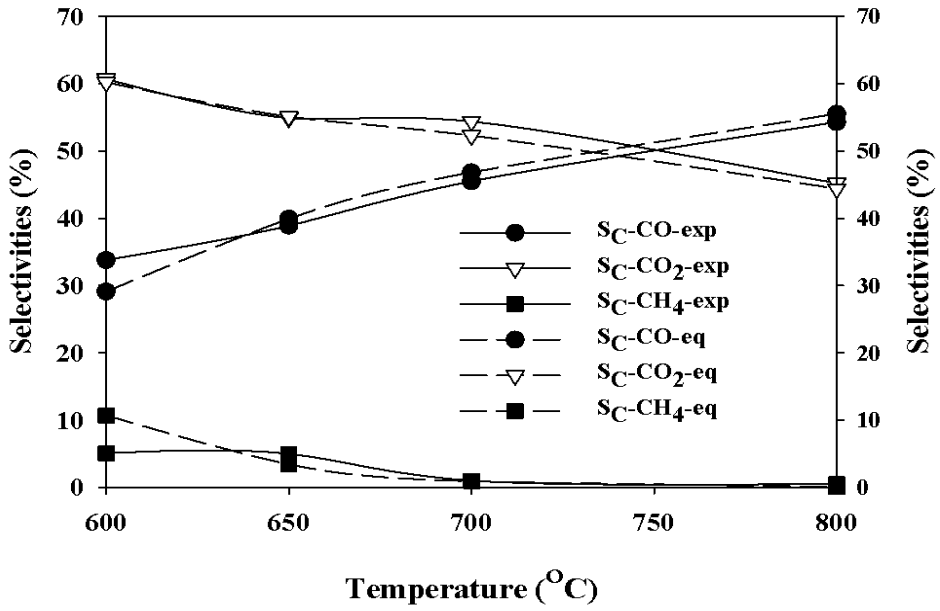

Figure 6.6: Effect of temperature of selectivities on carbon products (S_C) in CSR of commercial biodiesel using same conditions as Figure 6.4.

Marquevich et al. [132, 173] reported smaller fuel conversion (54%) in CSR of sunflower oil over commercial (ICI 46-1) catalyst at S/C of 3 and 650 °C. But when using hydrotalcite-like (HT) based catalyst with Ni^{2+}/Al^{3+} of 2, they obtained their largest fuel conversion (72%). At 600°C, X_{biod} (Figure 6.4) was lowest compared to other temperatures. This was as a result of higher carbon formation due to the decomposition reaction (R-6.4), which accounted for the 16% of the total carbon measured in the output (Table 6.1). For this run, 6 mol% of the carbon feed was unaccounted for, which could have been formed by thermal decomposition reaction (R-6.4) in some other parts of the parts of the reactor or could be contained in the quartz wool. Lower X_{H2O} of 28.6% resulting in a steam conversion efficiency of 62% of the equilibrium value (Figure 6.5) would support the interpretation. The argument was strengthened by the presence of small amount of alkenes such as C_2H_4, which is a known soot precursor [256] detected in the product gases.

At 650 °C, the amount of unaccounted carbon was high (13.2%), which suggested that the decomposition occurred in other parts of the reactor rather than on the catalyst surface (4% of total C-products, Table 6.1). This was likely due to the reverse Boudouard reaction (R-.6), shown by reduced carbon formation on catalyst (Table 6.1) in addition to ($S_{C\text{-}CO2}$) and increased ($S_{C\text{-}CO}$) (Figure 6.6). Similarly steam conversion efficiency (Figure 6.5) increased only by 3% which can backs the hypothesis. A Y_{H2} of 21.1 wt% (Y_{H2} (eff) of 77%) and 21.6 wt% (Y_{H2} (eff) of 77.5%) were measured at 600 and 650^{o}C (Figure 6.5). Reforming efficiency of the system was also unaffected significantly since there was no appreciable change in the YH_2.

At 700 ^{o}C, biodiesel X_{biod} and X_{H2O} increased (Figure 6.4) under combined effects of increase in SR (R-6.1), SMR (reverse R-6.5), and TD (R-6.4). The carbon balance for 700 °C was near zero, while carbon in the condensates was negligible; indicating the products were gases CO, CO_2, CH_4 and carbonaceous residue on the catalyst (7% of total C products). This implied the fuel conversion was now overwhelmingly consisting of catalytic reactions (R-6.1, reverse (R-6.5) and (R-6.4)) as seen by increased Y_{H2} (Figure 6.5) along with ($S_{H\text{-}H2}$) and ($S_{C\text{-}CO}$) (Figure 6.6) supporting the hypothesis. Highest biodiesel and steam conversions (X_{H2O}) of 92.3 and 36.3% at 700 ^{o}C resulted in the highest yield and Y_{H2} (eff)) (87.2%, Figure 6.5). At similar S/C of 2.5 and 700 ^{o}C with WHSV of 1.967 h^{-1}, Pimenidou et al [174] reported lower fuel (although this was waste cooking oil) and steam conversions i.e. 86.3% and 35.7%, respectively. Figure 6.7 shows the changes in biodiesel and steam conversion with respect to time at 700°C. Initially the values oscillate substantially. One of the reasons for this could be the smaller flowrates of biodiesel and water. As the flowrates of the biodiesel (0.978 cm^3/h) and water (2.92 cm^3/h) used are smaller and size of the vapourisation (1/4'') is bigger, it takes ~1800 s to generate enough vapours to assure continues flow over the catalyst bed to achieve steady state. The average X_{biod} and X_{H2O} values were selected from the point where steady readings of H_2 produced were observed (2250 s). The slandered deviation was quite small for both the X_{biod} and X_{H2O}. A deviation of 6.2 and 2.3 % was observed for X_{biod} and $X_{H2O.}$

Finally at 800°C, both X_{biod} and X_{H2O} decreased (Figure 6.4), decreasing Y_{H2} (Figure 6.5) and increasing ($S_{C\text{-}CO}$) at the expense of CO_2 (Figure 6.6). This was expected from equilibrium trend, as the reverse WGS reaction (reverse R-6.2) limited the conversions to H_2. However, Y_{H2} (eff) also decreased significantly between 700 and 800 °C from 87.2% to 80.6% (Figure 6.5), suggesting conditions moving further away from equilibrium. The ($S_{H\text{-}H2}$) at all the temperatures examined was above 95% at all the temperature examined which showed very small amount of other H_2 consuming gases. The ($S_{C\text{-}CH4}$) in the carbon containing gases (Figure 6.6) decreased with increase in temperature following equilibrium trends which were adverse to the METH reaction (R-6.5) and favourable to steam methane reforming (reverse R-6.5). The unaccounted carbon for this run was 12% and catalyst surface was 2%. The reduction in C on catalyst was as result of higher reforming temperature reducing C due to (R-6.6).

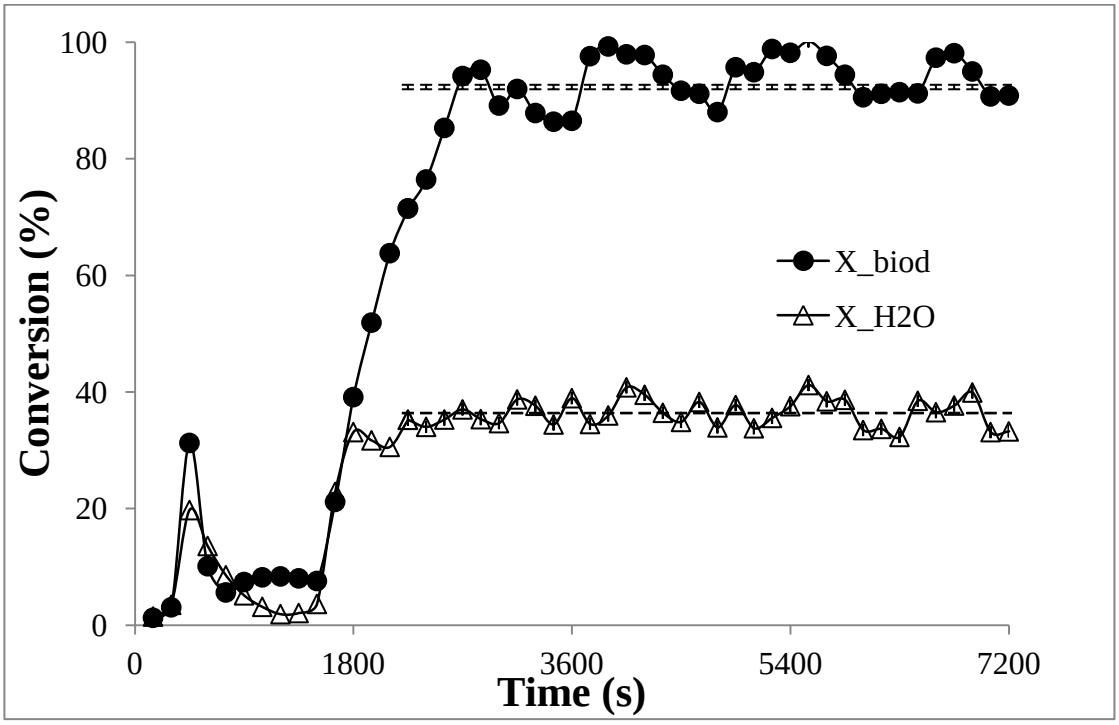

Figure 6.7: Biodiesel (X_{biod}) and steam (X_{H2O}) conversions during CSR using same conditions as Figure 6.4.

Table 6.1: Molar carbon balance of CSR of commercial biodiesel using Ni/Al catalyst at S/C of 3 at WHSV of 3.52h^{-1} and 170°C as water vaporiser temperature. The balance based on total input mol of C (=1.08 ×10^{-1}) over duration of experiment (7200 s) minus mol C converted to gases, volatiles in the condensate and deposited on catalyst.

React	Vap	1-(Cout/Cin)	C on catal		C in cond		C in gases	
T(°C)	T (°C)	%	mol	% C out	mol	% C out	mol	% C out
600	365	6.32	1.65×10^{-2}	16.32	7.27×10^{-4}	0.07	8.46×10^{-2}	83.60
650	365	13.23	4.03×10^{-3}	4.30	1.91×10^{-4}	0.20	8.95×10^{-2}	95.48
700	365	0.35	7.58×10^{-2}	7.04	3.62×10^{-5}	0.03	1.00×10^{-1}	92.92
800	365	11.97	1.67×10^{-3}	1.75	3.31×10^{-3}	0.03	9.34×10^{-2}	98.20
650	220	15.60	6.19×10^{-3}	10.19	5.14×10^{-5}	0.08	5.45×10^{-2}	89.72
650	190	14.25	7.11×10^{-3}	7.68	4.33×10^{-5}	0.04	8.54×10^{-2}	92.26

From the investigation it can be concluded that CSR of biodiesel is temperature dependent like other hydrocarbons and the performance of the system using Ni/Al catalyst peaked at 700 °C resulting in highest X_{biod} and X_{H2O}, resulting in highest H_2 yield, which was predicted by thermodynamic equilibrium calculations. The selectivity to any given gas i.e. H_2 (S_H), CO, CO_2 and CH_4 (S_C) was close to the value predicted at

equilibrium. Carbon balance for this particular temperature exhibited almost complete closure, which meant all the carbon entering the reactor was accounted for in the gas products and accumulated on the catalyst.

6.4.3 Effect of biodiesel preheating

Table 6.2 shows the effect of biodiesel preheating temperatures on CSR of commercial biodiesel at S/C of 3 using WHSV of 3.52 h^{-1} with 1.50 $\times 10^{-5}$ mol /s carbon molar feed flowrate. The reactor temperature was set to at 650 °C rand 170 °C as reactor and water vaporiser temperatures. The carbon balance for these runs is provided in Table 6.1. Lin et al. [257] showed that biodiesel is stable up to 275 °C and thermal decomposition starts at 275 °C and above. According to these authors, thermal decomposition of biodiesel involves isomerisation, polymerisation (Diels-Alder reaction) and pyrolysis reactions which occur in the temperature range of 275-400 °C, 300-425 °C and >350 °C.

Table 6.2: Effect of biodiesel preheating temperatures on CSR of biodiesel using Ni/Al catalyst at 650 °C, WHSV of 3.52 h^{-1} and S/C of 3. Water vaporiser was set to 170 °C.

Vaporiser T (°C)	X_{biod}	X_{H2O}	Reforming eff (%)	H_{2O} conv eff (%)	Y_{H2} (wt %)	Y_{H2} eff (%)
190	79.46	31.74	71.25	67.03	22.30	74.97
220	75.72	30.65	68.57	64.71	21.46	72.15
365	82.3	30.04	67.82	63.42	21.23	71.36

It is possible that at higher vaporiser temperature i.e. 365 °C, biodiesel decomposed and the products were steam reformed producing H_2, CO, CO_2, CH_4, C_2H_4 and C_2H_6. Lowering the vaporiser temperature reduced the X_{biod}, which means a higher amount of

longer chain compounds entered the reactor, which would have broken down on the surface of catalyst, forming smaller compounds that were steam reformed to produce H_2, CO, CO_2, and CH_4. As the vaporiser tubes were made of stainless steel it could have some catalytic effect on the decomposition of biodiesel at higher temperature (365 °C) resulting in X_{biod} due to thermal decomposition. Lower reforming and steam conversion efficiency could support the interpretation. Relatively higher reforming and steam conversion efficiencies suggest better SR activity with lower vaporiser (190 °C) temperature than higher (365 °C). As higher amount of intact biodiesel entered the reactor at lower vaporiser temperature, higher amount of carbon formation resulted. For 190 °C vapouriser temperature, 8% of the carbon feed ended up on the catalyst, while 14.3% was unaccounted carbon (Table 6.1). The unaccounted carbon could be present on the quartz wool. The carbon content of the condensate was negligible as compared to that of the gas and the carbon deposited on the catalyst. Carbon content of the condensate at 365 °C, although very small, was higher as compared to 190 °C, which suggested that at this vaporiser temperature more liquid products are formed by pyrolysis of biodiesel.

The better performance of the catalyst in terms of H_2 obtained at 190 °C and in order to prevent the thermal decomposition of biodiesel in the vaporiser, resulted in this temperature being chosen for the biodiesel vaporiser. TGA experiments also showed that at 190 °C, biodiesel vaporisation just begins.

6.4.4 Effect of catalyst

SR processes depend greatly on the type of catalyst used for the processes. Some catalysts have higher surface area, which results in higher activity compared to catalysts with lower surface area. The presence of dopants in the catalysts can also affect the activity positively as well negatively. The presence of elements such as Ca affects the activity of the catalyst by reducing carbon formation and maintaining the activity of the

catalyst. Ceria based catalysts are also helpful in reducing carbon formation and exhibit higher WGS activity. This section of results and discussion explores the effect of various Ni based catalysts on CSR of commercial biodiesel.

The performance evaluation of the catalysts was performed at constant WHSV (i.e. residence time) and S/C. The biodiesel flowrate to the reactor was kept constant at 0.978 cm^3/h and the steam flowrate was maintained at 2.92 cm^3/h, which provided an S/C of 3. These conditions corresponded to a carbon input flowrate of 1.50×10^{-5} mol/s while the N_2 flowrate was set to 40 cm^3/min to obtain a constant WHSV of 3.18 h^{-1}.

Figure 6.8 represents X_{biod} and X_{H2O} conversions in CSR of commercial biodiesel at constant S/C of 3 and WHSV of 3.18 h^{-1}. The reactor temperature was set to 650 ^oC. The molar carbon balance for these set of experiments is provided in Table 6.3. The previous experiments on the effect of temperature showed that 700 °C was found to be the optimum temperature in terms of Y_{H2} and with highest X_{biod} and X_{H2O}. The (S_{C-CO}) at this temperature was higher, inferring limitation of WGS activity. Similarly as some of the catalysts tested were powders, these might undergo sintering due to high reactor temperatures. For this reason the catalysts were compared at 650 °C. The biodiesel and water vaporisers were set to 190 and 170 °C respectively.

6.4.4.1 Alumina supported catalysts

Figure 6.8 represents the performance of alumina supported Ni catalysts in CSR of commercial at constant S/C of 3, with 650 °C as reactor temperature and WHSV of 3.18 h^{-1}. The biodiesel and water vaporisers were set to 190 and 170 °C. Table 6.3 shows the molar carbon balance for these experiments performed over 7200s with a carbon input of 1.08×10^{-1} mol. Biodiesel (X_{biod}) and steam (X_{H2O}) conversions with the commercial Ni/Al and Ni/K-Al catalysts were lower as compared to Ni/Ca-Al and NiCoCe/Al catalysts. The Ni/Ca-Al catalyst exhibited highest X_{biod} of 96.0% followed by NiCoCe/Al which showed 90.4% conversion. Steam conversions (X_{H2O}) of 37.8 and 34.9% were

observed for Ni/Ca-Al and NiCoCe/Al respectively compared to the equilibrium value of 47%.

6.4.4.2 Alumina supported catalyst

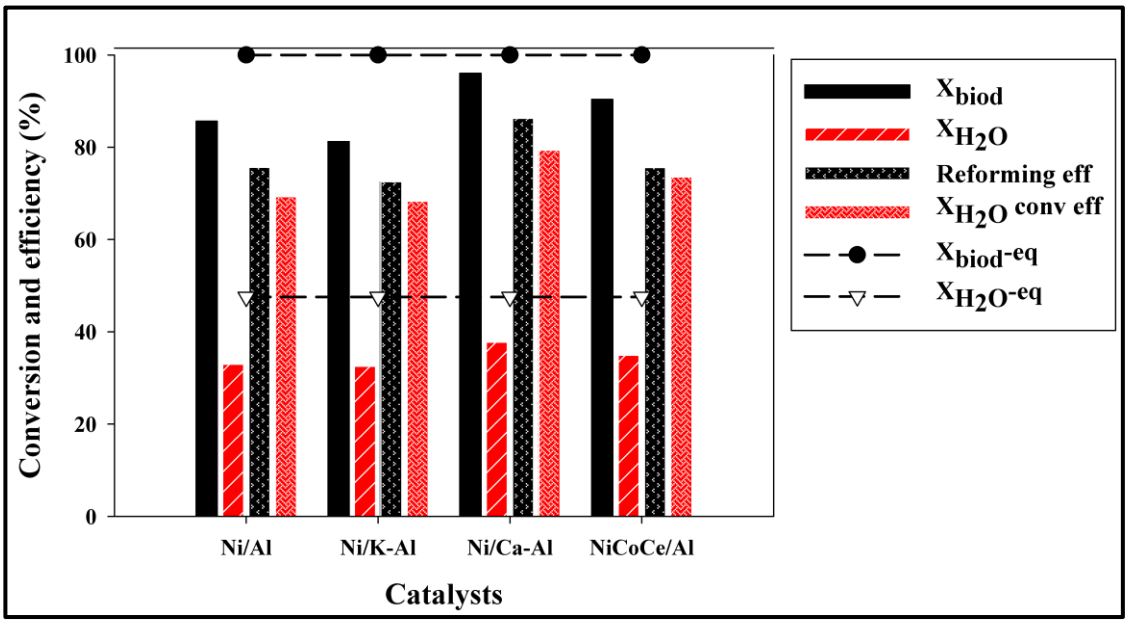

Figure 6.8: Performance of various alumina supported Ni catalysts in CSR of commercial biodiesel at 650 °C and constant S/C of 3 and WHSV of 3.18 h^{-1} with biodiesel and water vaporisers set to 190 and 170 °C.

Steam conversions (X_{H2O}) for Ni/Al and Ni/K-Al were very similar, but X_{biod} for Ni/Al catalyst was higher compared to Ni/K-Al catalyst, which infers that thermal decomposition of biodiesel was higher over alumina support of the Ni/Al catalyst (Figure 6.8). Although the carbon content in the condensates was insignificant as compared to the carbon conversion in gas phase and on the catalyst surface, Ni/Al catalyst exhibited higher organic carbon as compared to the Ni/K-Al catalyst (Table 6.3). According to Marquevich et al.[173], the acidic nature of alumina support can cause cracking of oxygenated hydrocarbons affecting the SR performance. The presence of K could have modified the acidic sites of alumina, resulting in lower TD. Addition of K increases steam adsorption on catalyst surface, which means steam covers the surface, restricting

the fragments of biodiesel broken by Ni to be adsorbed and steam reformed [228, 258]. Addition of K alters the hydrocarbon dissociative chemisorptions in SMR i.e. there is a decrease in CH_x *(a)* fragments formed on the Ni surface from the increase of interactions with water vapour resulting lower activity and coke formation[259]. The carbon content on the surface of Ni-K/Al catalyst was relatively lower compared to the Ni/Al catalyst. Approximately 4.2 and 3.63% of the total carbon in the products was found on the surface of the Ni/Al and Ni/K-Al catalysts. The unaccounted carbon for these runs was higher, suggesting formation carbon in other places of the reactor or quartz wool surface (Table 6.3).

From the two catalysts that yielded higher X_{biod}, i.e. Ni/Ca-Al and NiCoCe/Al, the latter exhibited higher carbon formation on its surface. A 4.8% of the output carbon was found on NiCoCe/Al as compared to 3.5% on Ni/Ca-Al (Table 6.3). This could explain why the X_{biod} was lower for the NiCoCe/Al catalyst as compared to Ni/Ca-Al. Similarly X_{H2O} over NiCoCe/Al was lower than Ni/Ca-Al, suggesting lower SR activity (R-6.1). Among all the catalysts, the highest amount of carbon in the condensate was found for NiCoCe/Al, which suggests this catalyst was more active in the biodiesel decomposition reaction. For these two catalysts (Ni/Ca-Al and NiCoCe/Al) only 0.5 and 5% of the carbon feed was unaccounted (Table 6.3). Vagia and Lemonidou [260] reported high catalytic activity in CSR of acetic acid over 5 wt% Ni/12CaO-7Al_2O_3. They reported that Ni was distributed at the boundaries of the grains facilitating a high degree of dispersion. Further, the smaller crystallites of Ni over the support contributed to the difference in dispersion and caused high reforming activity. The presence of Ca in the case of calcium aluminate based catalyst had an influence on the performance of the catalyst. Addition of Ca to 10% Ni/Al_2O_3 was shown to improve the performance of the catalyst in CSR of ethanol Choong et al [261]. Formation of less crystalline carbon was observed in Ca modified catalysts which was more easily gasified (R-6) during the CSR reaction. Addition of Ca decreased the acidity of the Al_2O_3 and increased the adsorption of steam while providing the Ni catalyst the proximity and abundance of adsorbed OH groups affecting the performance of the catalyst [261].

Higher conversion of X_{biod} and X_{H2O} in Ni/Ca-Al resulted in highest Y_{H2} from enhanced SR reaction (R-6.1). A Y_{H2} of 27.0 wt% was observed for Ni/Ca-Al, which resulted in YH_2 (eff) close to 93% (Figure 6.9). Steam conversion (X_{H2O}) and reforming efficiencies for this catalyst were also highest due to higher biodiesel and steam conversion. A steam conversion efficiency of 79.5% was seen with reforming efficiency of 86.3% (Figure 6.8). Lowest Y_{H2} of 22.8 wt% was exhibited by Ni/K-Al, which resulted in Y_{H2} (eff) of 78.9% (Figure 6.9). Reforming efficiency of 72.5% and steam conversion efficiency of 68.3% was recorded for Ni/K-Al (Figure 6.8).

Figure 6.9 represents yield (Y_{H2}) and (S_{H-H2}) to H_2 in addition selectivity to carbon gases (S_C) in CSR of commercial biodiesel at S/C of 3, WHSV of 3.18 h^{-1} for various alumina supported catalysts. Selectivity to any given gas was very close to its equilibrium value. The (S_{H-H2}), for all the catalysts was close to 100%. The (S_{C-CO}) and (S_{C-CO2}) was in the range of 38.7 to 42.4% and 55.8 to 58.5% respectively. The (S_{C-CO}) in case of Ni/K-Al was slightly lower than others, due to slight improvement WGS reaction (R-6.2). Ni/K-Al also showed highest (S_{C-CH4}) as compared to the other catalysts. Addition of K disrupts the CH_4 activation sites of the catalyst which would reduce SMR reaction (reverse R-6.5) increasing (S_{C-CH4}).

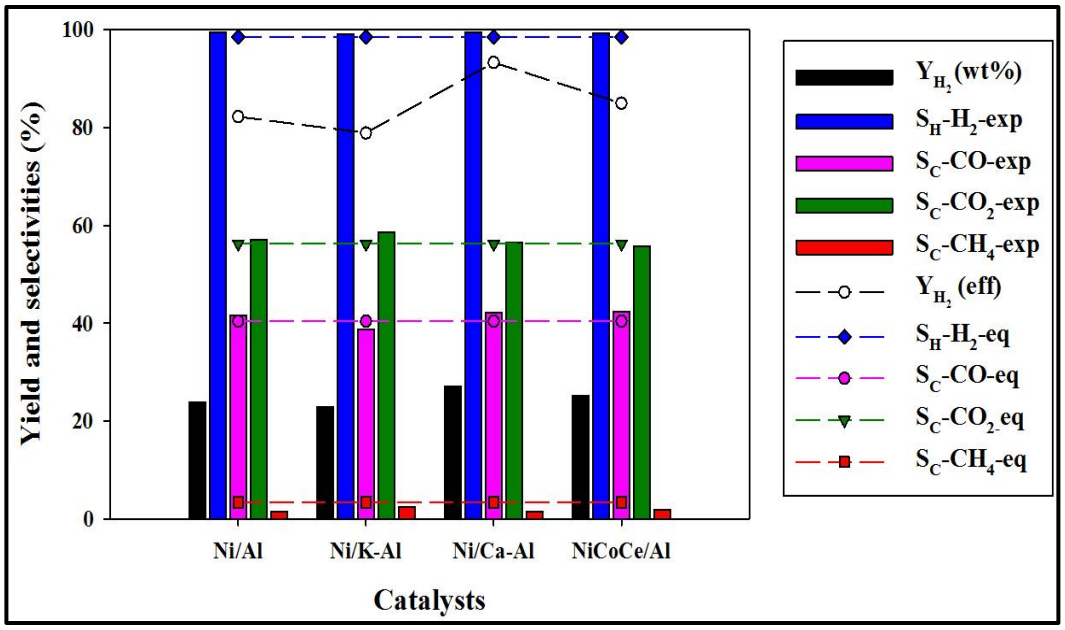

Figure 6.9: Yield of H_2 (Y_{H2}) and selectivity (S_{H-H2}) for H_2 with selectivities of carbon gases in CSR of commercial biodiesel over alumina supported catalysts, at same conditions as Figure 6.8.

6.4.4.3 Ceria-zirconia supported catalysts

Effect of ceria based Ni catalysts on (X_{biod} and steam X_{H2O} in CSR of commercial biodiesel, at 650 °C using S/C of 3 and constant WHSV of 3.18 h^{-1} is shown in Figure 6.10. The molar carbon balance for these set of experiments performed over 7200s with the carbon input of 1.08×10^{-1} mole is shown in Table 6.3. The vaporiser temperatures were set to 190 and 170 °C for biodiesel and water respectively. In the case of Ce-Zr supported catalyst, the presence of Ce resulted in higher conversion and WGS activity [262]. Addition of Ce is well known to promote metal activity and dispersion, resulting high catalytic activity. Similarly the presence of Ce increases adsorption of steam thereby promoting X_{H2O}. Higher (S_{C-CO2}) and X_{H2O} during the CSR reaction suggested higher WGS reaction (R-6.2) activity. It was reported that CeO_x enhances the dissociation of H_2O and accelerates the reaction of steam with adsorbed species on the Ni surface near the boundary area between metal and support, thus decreasing the carbon deposition (Table 6.3) and promoting the stability of the catalyst during reforming [216]. Ni/Ce-Zr-

1.5g showed the highest biodiesel and steam conversions compared to the others (Ni-K/Ce-Zr, Ni-Sn/Ce-Zr and Ni/Ce-Al). Biodiesel conversion (X_{biod}) of 96.1% with 41.3% X_{H2O} were observed with this catalyst, which resulted in 86.9 and 88.9% steam conversion and reforming efficiency respectively. For this catalyst 1.3% of the carbon fed was detected on the catalyst surface.

Decreasing the amount of catalyst resulted in reduction in X_{biod} and X_{H2O} with Ni/Ce-Zr-1g catalyst. Biodiesel (X_{biod}) and steam (X_{H2O}) conversion reduced to 90.2% and 33.3% with the use of Ni/Ce-Zr-1g. It is obvious that increasing the amount of sand in the bed, with reduction in catalyst mass, resulted in lower activity. Comparing the carbon formation on catalyst surface, use of 1 g catalyst showed slightly higher carbon formation (Table 6.3). The unaccounted carbon for Ni/Ce-Zr-1g and Ni/Ce-Zr-1.5 g were 7 and 2.5 % of the carbon fed respectively (Table 6.3) which suggests that the CSR process was very efficient. The unaccounted carbon could be present in the sand and over the quartz wool.

In case of Ni-K/Ce-Zr Ni-Sn/Ce-Zr catalysts, biodiesel and steam conversions (X_{H2O}) decreased, suggesting lower activity towards SR reaction (R-6.1). The reason for reduced activity for these catalysts differs from one another.The Ni-K/Ce-Zr catalyst showed reduced activity due to the presence of higher carbon on catalyst surface (Table 6.3). It was hoped that addition of K would reduce carbon formation, but this ability of the catalyst is dependent on the position and amount of K on the catalyst surface. According to Borowiecki et al. [263] location of K on the catalyst plays an important role in resistance of K containing catalyst to carbon formation. A part of K is in an intimate contact with Ni, whereas the other part is distributed over the support. In catalyst where K–Ni interaction dominates, K promoted catalyst exhibits lower resistance to carbon formation. A X_{biod} of 90.0% and X_{H2O} of 38.1% were exhibited by the Ni-K/Ce-Zr catalyst. A 6% of the carbon measured in the output was observed over the catalyst surface (Table 6.3), with 4% of the carbon fed was unaccounted.

Reduction in the catalytic activity of Ni-Sn/Ce-Zr compared to Ni/Ce-Zr, could be as a result of surface coverage of active Ni sites by Sn [227]. Similar behaviour was reported by Nikolla et al. [264] in SMR using S/C of 0.5 at 800 ^{o}C using Ni/YSZ catalyst. Addition of Sn was reported to increase the stability of the catalyst but was shown to reduce activity; a 25% decrease in the activity was reported with 5 wt% Sn doped Ni/YSZ catalyst. Formation of relatively higher amount of carbon (Table 6.3) on the surface of Ni-Sn/Ce-Zr compared to Ni/Ce-Zr could be one of the reasons for lower activity of the catalyst, resulting from formation of alkenes [256]. A 3% of the measured carbon in the output was detected on the catalyst surface of the Ni-Sn/Ce-Zr catalyst, with 7% unaccounted carbon. Biodiesel (X_{biod}) and steam (X_{H2O}) conversions of 90.0% and 39.4% were recorded with Ni-Sn/Ce-Zr catalyst.

Lowest conversions X_{biod} and X_{H2O} were observed with the Ni/Ce-Al catalyst. Biodiesel conversion (X_{biod}) of 75.9% with X_{H2O} of 30.4% was seen with this catalyst. The reason for low catalytic activity was the high amount of carbon formation on the catalyst surface. From the total output carbon, 18% was observed over the catalyst surface thus significantly affecting the performance of the catalyst. The unaccounted carbon was 8% of the carbon feed, which suggest most of the carbon was formed over the catalyst surface. As a result of poor biodiesel and steam conversions (X_{H2O}), 75.5 and 64.1% reforming and steam conversion efficiencies were obtained for the catalyst.

The selectivity (S_{H-H2}) and YH_2 with the selectivities of carbon gases (S_C) for Ce-Zr catalysts are shown in Figure 6.11. The highest Y_{H2} of 27.8 wt% was obtained with Ni/Ce-Zr-1.5 g catalyst, which resulted in an Y_{H2} (eff) of 93.5% (Figure 6.11). It decreased to 23.7 wt% with 79.0% Y_{H2} (eff) for Ni/Ce-Zr-1 g catalyst. H_2 yields of 26.2 and 25.7 wt% were found for the Ni-K/Ce-Zr and Ni-Sn/Ce-Zr catalysts. Among all the catalysts, the lowest yield was found for the Ni/Ce-Al catalyst (20.9 wt%), hence low Y_{H2} (eff)of 70.9%. The (S_{H-H2}) was above 97% for all the catalysts. The (S_{C-CO}) in Ni/Ce-Zr-1

g catalyst was higher compared to Ni/Ce-Zr-1.5 g, as a result of limited WGS reaction (R-6.2) due to lower amount of catalyst. This behaviour was also observed with Ni/Ce-Al catalyst. Ni-Sn/Ce-Zr catalyst, exhibited highest ($S_{C\text{-}CO2}$) among all the catalyst. On the other hand ($S_{C\text{-}CH4}$) was highest with Ni/Ce-Zr-1 g catalyst The ($S_{C\text{-}CH4}$) was highest for 1 g catalysts. Ni/Ce-Zr-1g showed highest $S_{C\text{-}CH4}$ (5.7%) from all the catalyst. But increasing the mass of catalyst to 1.5 g reduced ($S_{C\text{-}CH4}$) to 2.1%, which suggest higher SMR activity (reverse R-6.5) with 1.5 g catalyst.

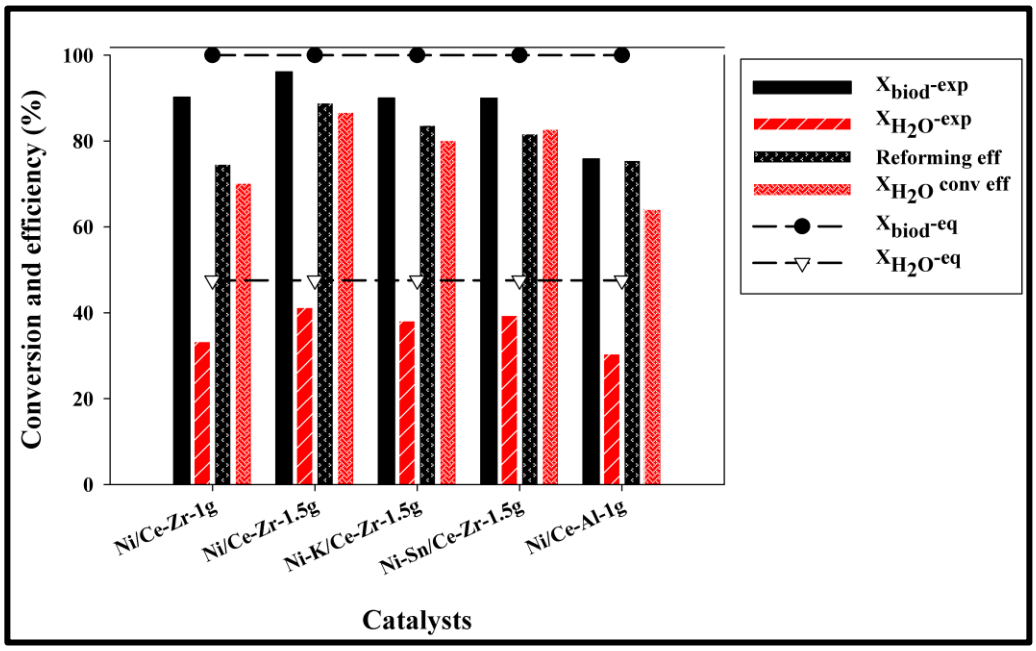

Figure 6.10: Performance of various ceria based Ni catalysts in CSR of commercial biodiesel at 650 °C and constant S/C of 3 and WHSV of 3.18 h^{-1} with biodiesel and water vaporisers were set to 190 and 170 °C. In this Figure, 1.5 and 1g of catalysts were mixed with appropriate amount of quartz sand to make 2.0506 g catalyst bed.

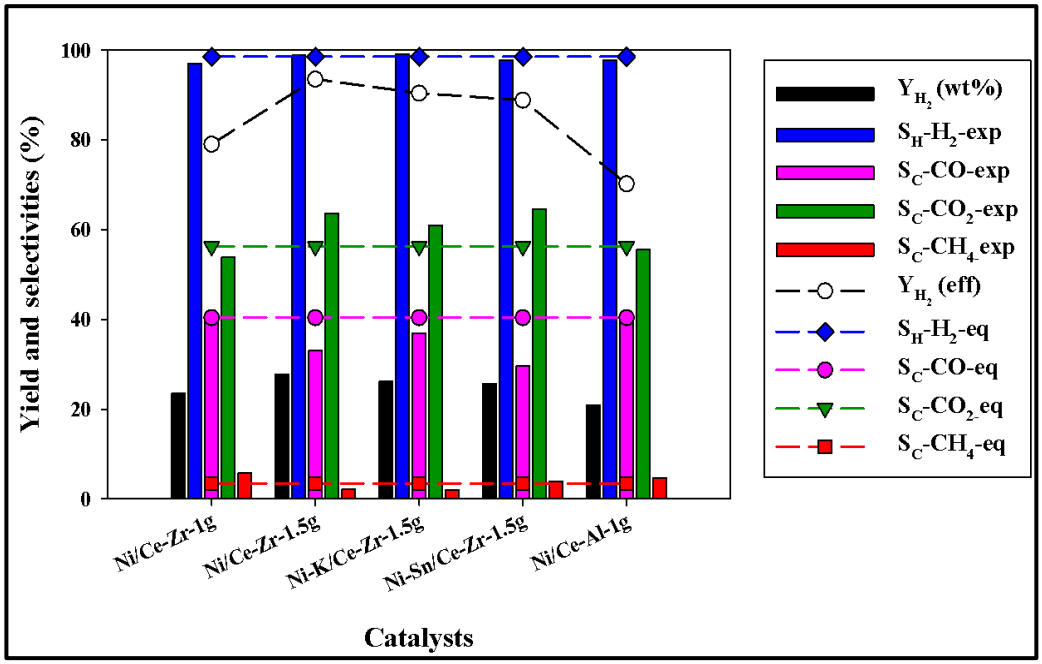

Figure 6.11: Yield (Y_{H2}) and selectivity (S_{H-H2}) to H_2 with selectivity to carbon gases in CSR of commercial biodiesel over Ce-Zr supported catalysts, at same conditions as Figure 6.10.

Table 6.3: Molar carbon balance of CSR of commercial biodiesel using alumina and Ce-Zr supported catalysts at S/C of 3 at WHSV of 3.18 h^{-1}. The biodiesel and water vaporiser were set to 190 and 170 °C. The balance is based on total input mol of C (=1.08 ×10^{-1}) over duration of experiment (7200 s) minus mol C converted to gases, volatiles in the condensate and deposited on catalyst. Superscript (a) - sand addition.

Catal	1-(Cout/Cin)	C on catal		C in cond		C in gases	
	%	mol	% C out	mol	% C out	mol	% C out
Ni/Al	10.56	4.04×10^{-3}	4.18	7.70×10^{-5}	0.07	9.24×10^{-2}	95.73
Ni/K-Al	15.70	3.31×10^{-3}	3.63	5.49×10^{-5}	0.06	8.77×10^{-2}	96.30
Ni/Ca-Al	0.46	3.75×10^{-3}	3.49	2.50×10^{-5}	0.02	1.00×10^{-1}	96.48
NiCoCe/Al	4.9	4.90×10^{-3}	4.77	1.91×10^{-4}	0.18	9.75×10^{-2}	95.04
Ni/Ce-Zr-1g[a]	7.10	2.77×10^{-3}	2.76	1.25×10^{-4}	0.12	9.74×10^{-2}	97.10
Ni/Ce-Zr-1.5g[a]	2.40	1.36×10^{-3}	1.29	2.60×10^{-4}	0.24	1.03×10^{-1}	98.46
Ni-K/Ce-Zr-1.5g[a]	3.86	6.55×10^{-3}	6.31	4.33×10^{-5}	0.04	9.72×10^{-2}	93.63
Ni-Sn/Ce-Zr-1.5g[a]	7.06	3.05×10^{-3}	3.04	1.47×10^{-4}	0.14	9.71×10^{-2}	96.80
Ni/Ce-Al-1g[a]	7.68	1.77×10^{-2}	17.77	5.52×10^{-5}	0.05	8.19×10^{-2}	82.17

6.4.5 Effect of WHSV

The effect of WHSV on the CSR of commercial biodiesel was performed using Ni/Ca-Al catalyst at 650 °C and constant S/C of 3. Biodiesel and water flowrates were kept constant at 0.978 cm^3/h (1.50 $\times 10^{-5}$ mol /s carbon molar feed flowrate) and 2.92 cm^3/h. The WHSV values were adjusted to 2.85, 3.18 and 3.52 h^{-1} by altering N_2 flowrate from 30 to 50 cm^3/min. Biodiesel and water vaporisers were set at 190 and 170 °C. Figure 6.12 illustrates the effect of WHSV on CSR of commercial biodiesel at constant S/C and reactor temperature of 650 °C. The molar carbon balances of these experiments are provided in Table 6.4 over 7200s with a carbon input of 1.08×10^{-1} mol.

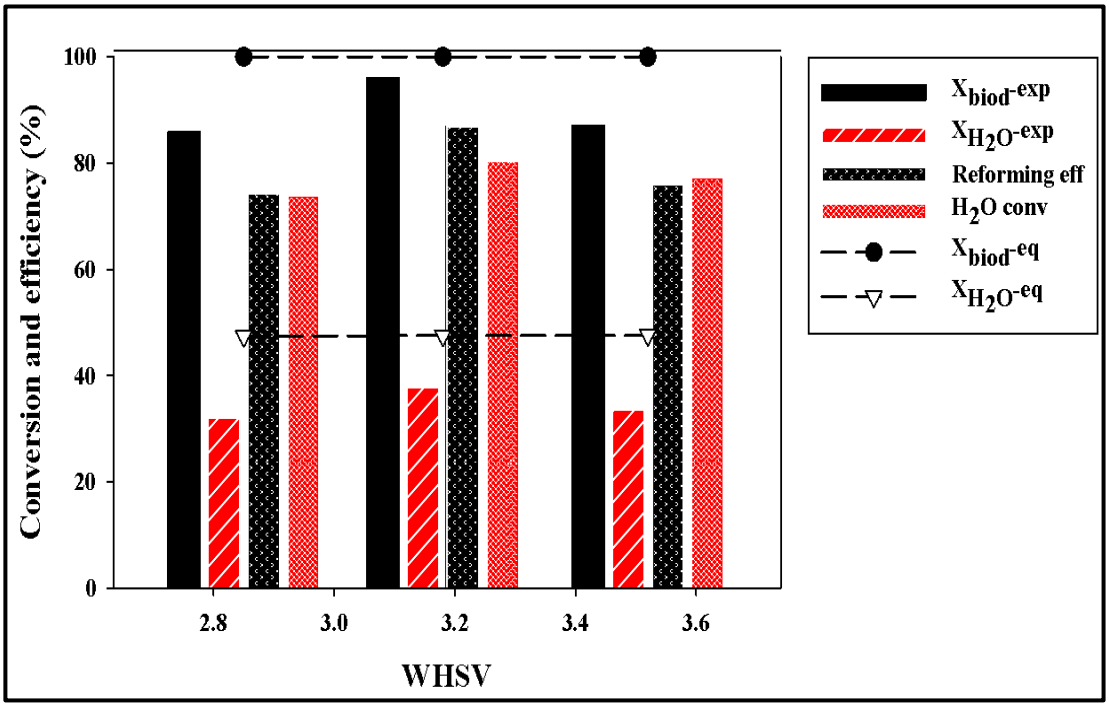

Figure 6.12: Effect of WHSV on the performance of Ni/Ca-Al catalyst in CSR of commercial biodiesel at 650 °C and S/C of 3. In this investigation biodiesel and water vaporisers were set to 190 and 170 °C respectively.

Increase in WHSV increased the amount of carbon in the condensate as observed by TOC analysis (Table 6.4) which could suggest increased pyrolysis of biodiesel. Similarly increasing the WHSV increased the amount of carbon deposited on the catalyst surface. At WHSV of 3.52 h^{-1}, 6% of the carbon output was found on the catalyst surface. This decreased to 2.8% with reduction in WHSV to 2.85 h^{-1}. This suggests that lower WHSV increases carbon steam gasification leading to net lower carbon deposition. Maximum conversions of both biodiesel and steam and therefore Y_{H2} (27 wt%, Figure 6.12) were observed at 3.18 h^{-1}, with very good mass balance closure (Table 6.4). Reforming and steam conversion efficiencies of 86.9 and 80.35% were observed for this WHSV value. Figure 6.13 represents selectivity ($S_{H\text{-}H2}$) and yield for H_2 (Y_{H2}) with the selectivities to CO, CO_2 and CH_4 (S_C). At all the WHSV values, H_2 selectivities ($S_{H\text{-}H2}$) values were above 98%, with 99.4 % at WHSV of 3.18 h^{-1}. The ($S_{C\text{-}CO}$) was shown to increase with WHSV value, in contrast to ($S_{C\text{-}CO2}$) which remained similar at all the WHSV values. The ($S_{C\text{-}CH4}$) was negligible as compared to the other gases, with WHSV of 3.18 h^{-1} showing the least.

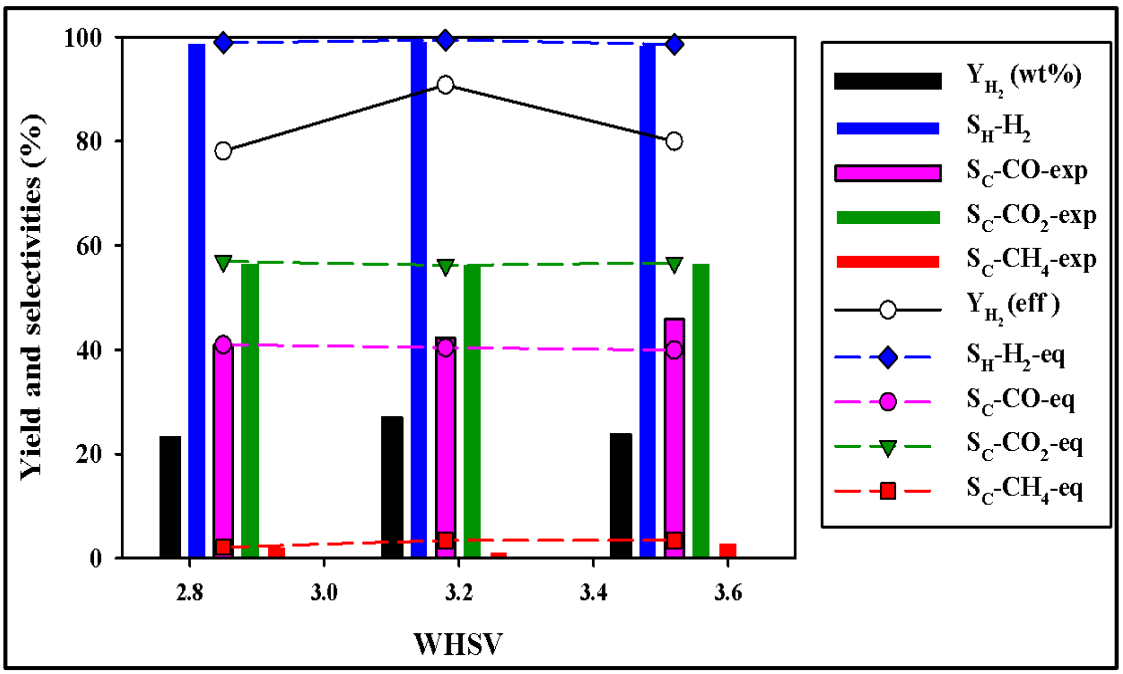

Figure 6.13: Effect of WHSV on yield (Y_{H2}) and selectivity ($S_{H\text{-}H2}$) to H_2 with selectivities of carbon gases in CSR of commercial biodiesel over Ni/Ca-Al catalyst, at 650 °C and constant S/C of 3.

6.4.6 Effect of biodiesel

Effect of biodiesel types (commercial, palm and in-house biodiesel) on the performance of the CSR was examined using Ni/Ca-Al catalyst at constant S/C of 3 and 650 °C with WHSV of 3.18 h^{-1} is shown in Figure 6.14 with molar carbon balance for the experiments are provided in Table 6.4. The biodiesel flows was adjusted to maintain a carbon molar feed flowrate of 1.50 $\times 10^{-5}$ mol /s. The steam flowrate was also adjusted to provide S/C ratio of 3. The WHSV for these experiments was 3.18 h^{-1}.

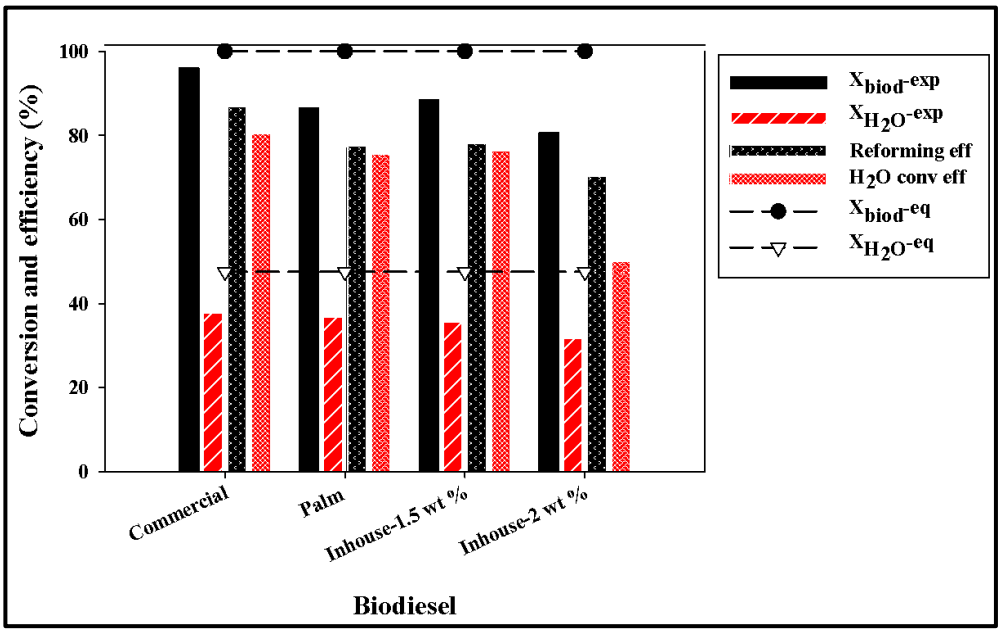

Figure 6.14: Effect of biodiesel origin on CSR process using Ni/Ca-Al catalyst at 650 °C and constant S/C of 3 with constant WHSV of 3.18 h^{-1}. The biodiesel and water vaporisers were set to 190 and 170 °C. In this Figure 1.5 and 2 wt% represents the amount of KOH catalyst used for biodiesel preparation.

Highest X_{biod} and X_{H2O} were observed with commercial biodiesel compared to other biodiesels examined. Biodiesel conversion (X_{biod}) with commercial biodiesel was 96% as compared to 86.5, 88.5 and 80.7% with palm, in-house 1.5 wt% and 2 wt%. Lower conversion in CSR of palm oil biodiesel was reported by Shiratori et al [140] using S/C

of 3.5 at 800 ^{o}C with GHSV of 3900 h^{-1} over a Ni/YSZ+Al_2O_3 based paper catalyst. Highest X_{H2O} was recorded with commercial biodiesel. The decreasing order of X_{H2O} was commercial biodiesel > palm > in-house -1.5 wt% and finally in-house -2 wt%. Commercial biodiesel also exhibited the lowest carbon formation on the catalyst surface as compared to other biodiesel. Commercial biodiesel showed 3.5% of the output carbon on the catalyst surface. For palm, in-house 1.5 wt% and 2 wt% biodiesels, carbon formation was 4.5, 5.5 and 6.5% of the carbon output. As a result of higher X_{biod} and relatively lower amount of carbon deposited on the catalyst surface, commercial biodiesel showed the best result in terms of carbon balance (Table 6.4). Only 0.5% of the carbon fed was unaccounted as compared to 13% with in-house- 2wt% biodiesel (Table 6.4). The reforming and steam conversion efficiency for commercial biodiesel reached the maxima of 86.9 and 80.3% (Figure 6.13) due to the above reasons.

The (S_{H-H2}) and (Y_{H2}) in addition to carbon containing gases (S_C) are shown in Figure 6.15. Highest X_{biod} and X_{H2O} conversions resulted in highest in Y_{H2} with commercial biodiesel (Figure 6.14). According to Shotipruk et al [265] higher H_2 production can be produced from palmitic acid and oleic acid using S/C of 3 at 900 ^{o}C, since commercial biodiesel has higher amount of these esters one could assume that this could be one of the factors affecting Y_{H2} in the CSR of the biodiesels examined. The yield of H_2 decreased from commercial biodiesel to in-house-2wt% biodiesel. This resulted in in-house-2wt% biodiesel showing the poorest Y_{H2} (eff) value of 74.0% (Figure 6.15) which suggested deviation from equilibrium conditions with this biodiesel. The (S_{H-H2}) was above 98% for all the biodiesels. Palm biodiesel exhibited the highest (S_{C-CO}) among all the biodiesels. In contrast, in-house-2wt% biodiesel recorded the highest (S_{C-CO2}). In-house-1.5 wt% biodiesel was responsible for highest (S_{C-CH4}) among the rest.

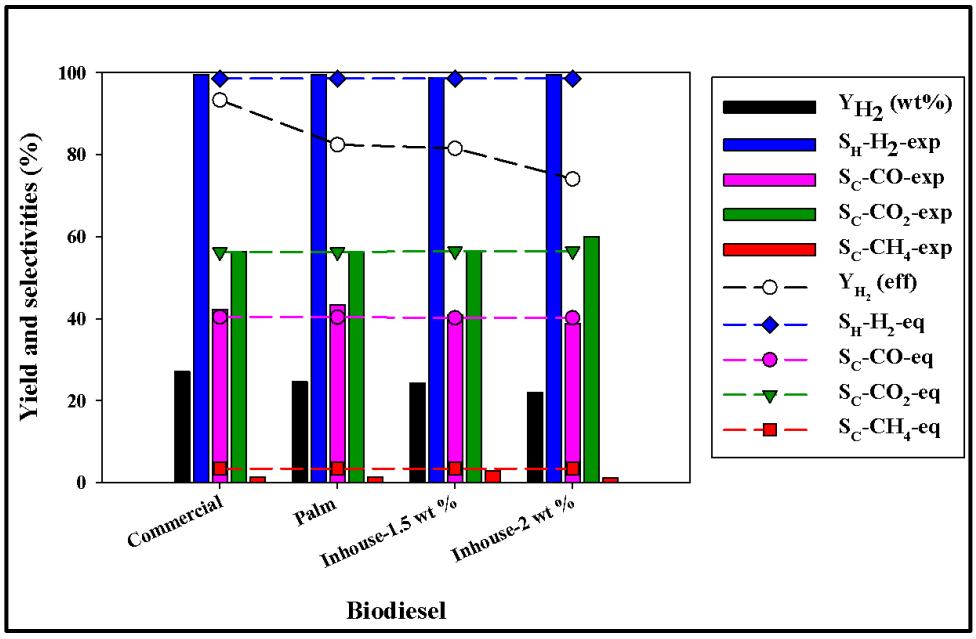

Figure 6.15: Effect of biodiesel origin on yield (Y_{H2}) and selectivity (S_{H-H2}) to H_2 with selectivity to carbon gases (S_C) in CSR process over Ni/Ca-Al catalyst, at same conditions as Figure 6.14.

6.4.7 Effect of molar S/C ratio

The effect of S/C on the performance of CSR process was investigated using Ni/Ca-Al. Biodiesel flowrate was kept constant at 0.978 cm^3/h in order to maintain same molar carbon feed of 1.50 $\times 10^{-5}$ mol/s. Water flowrate was adjusted from 1.95 and 2.92 cm^3/h to achieve S/C ratios of 2 and 3 respectively. In order to maintain the WHSV of 3.18 h^{-1}, the flow of N_2 was varied in from 40 to 54 cm^3/h.

Figure 6.16 represents the effect of S/C on CSR of commercial biodiesel at 650 °C and WHSV of 3.18 h^{-1} over Ni/Ca-Al catalyst. Molar carbon balance is provided in Table 6.4. Biodiesel conversion (X_{biod}) increased with S/C, while X_{H2O} decreased slightly. The decrease in X_{H2O} would be due to the presence of excess steam due to higher S/C ratio. Steam low excess conditions (S/C=2) could have resulted in the formation of carbonaceous deposits (Table 6.4) which would have reacted with steam resulting in

higher steam conversion X_{H2O}) [174]. A 7% of the carbon in the products was found on the catalyst surface with 7% unaccounted carbon at S/C of 2. Increasing the S/C reduced the carbon deposition by half, 3.5% of the output carbon was detected on the catalyst surface. The improved performance with higher S/C is as a result of lower carbon deposition resulting in improved SR reaction (R-6.1). Higher reforming and steam conversion efficiencies support this claim. In contrast to our results, higher temperature was required to obtain similar conversions in CSR of waste cooking oil [174]. At similar S/C of 2.5 and WHSV of 1.967 h^{-1}, waste cooking oil and X_{H2O} reached 86.3 and 35.7% at 700 °C over Ni/Al catalyst. Higher S/C of 4 was required to achieve 99.9% for waste cooking oil as compared to 96.0% at S/C of 3 for biodiesel. This could suggest that biodiesel would be easy to steam reform even at higher WHSV values.

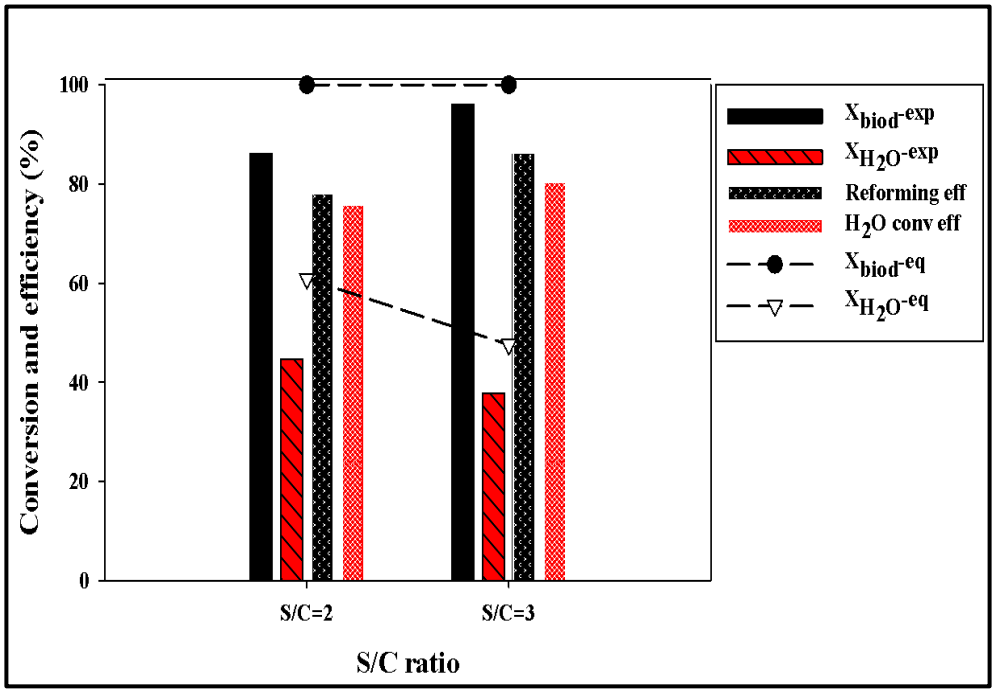

Figure 6.16: Effect of molar S/C on CSR process using Ni/Ca-Al catalyst at 650 °C and constant WHSV of 3.18 h^{-1}. The biodiesel and water vaporisers were set to 190 and 170 °C.

The yield of H_2 was lower at S/C of 2 compared to yield obtained at S/C of 3. A 21.9 wt% of Y_{H2} with (Y_{H2} (eff)) of 80.3% was observed at S/C of 2. Figure 6.17 represents yield (Y_{H2}) and ($S_{H\text{-}H2}$) to H_2 in addition to selectivities to carbon containing gases i.e.

CO, CO_2 and CH_4 (S_C). At higher S/C, higher WGS activity (R-6.2) was observed thus increasing YH_2. Lower CO and higher ($S_{C\text{-}CO2}$) were observed at S/C of 3, supports the interpretation. Similarly lower ($S_{C\text{-}CH4}$) under steam rich condition suggests higher SMR activity (reverse R-6.5). The ($S_{H\text{-}H2}$) in case of S/C of 2 was slightly lower than that observed at S/C of 3.

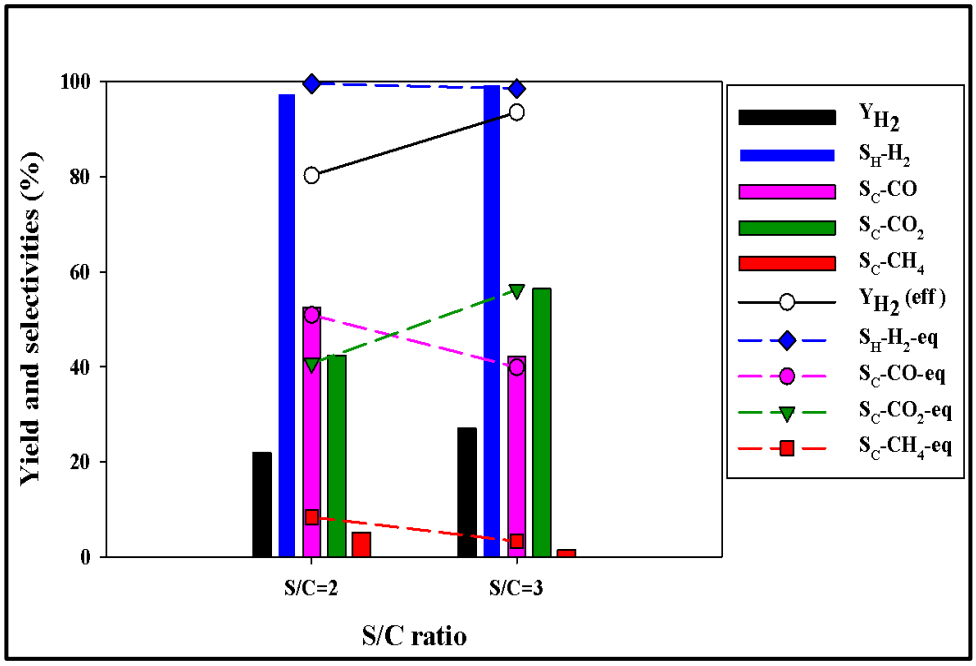

Figure 6.17: Effect of S/C on yield (Y_{H2}) and selectivity ($S_{H\text{-}H2}$) to H_2 with selectivity to carbon gases (S_C) in CSR process over Ni/Ca-Al catalyst, at same conditions as Figure 6.16.

Table 6.4: Molar carbon balance of CSR experiments using Ni/Ca-Al catalyst. The biodiesel and water vaporiser were set to 190 and 170 °C. The balance is based on total input mol of C (=1.08 ×10^{-1}) over duration of experiment (7200 s) minus mol C converted to gases, volatiles in the condensate and deposited on catalyst.

Biodiesel	1-(Cout/Cin)	C on catal		C in cond		C in gases	
	%	mol	% C out	mol	% C out	mol	% C out
Commercial[a]	07.12	6.04×10^{-3}	06.02	2.10×10^{-4}	00.21	9.40×10^{-2}	93.76
Commercial[b]	00.46	3.75×10^{-3}	03.49	2.50×10^{-5}	00.02	1.03×10^{-1}	96.48
Commercial[c]	11.64	2.70×10^{-3}	02.83	1.50×10^{-5}	00.01	9.26×10^{-2}	97.14
Commercial[d]	07.24	7.13×10^{-3}	07.12	0.00×10^{-5}	00.00	9.30×10^{-2}	92.87
Palm[b]	09.21	4.55×10^{-3}	04.64	3.74×10^{-5}	00.03	9.34×10^{-2}	95.31
In-house1.5 wt %[b]	06.42	5.46×10^{-3}	05.40	4.65×10^{-5}	00.04	9.54×10^{-2}	94.54
In-house 2 wt %[b]	13.56	6.19×10^{-3}	06.63	2.84×10^{-5}	00.03	8.71×10^{-2}	93.33

a- The performance was evaluated at S/C of 3 and WHSV of 3.52h^{-1}.

b- The performance was evaluated at S/C of 3 and WHSV of 3.18h^{-1}.

c- The performance was evaluated at S/C of 3 and WHSV of 2.85h^{-1}.

d- The performance was evaluated at S/C of 2 and WHSV of 3.18h^{-1}.

6.5 Catalyst Characterisation

The used catalyst was characterised using BET, XRD, SEM and TGA-FTIR.

6.5.1 Surface area

Table 6.5: The BET results of used Al_2O_3 supported catalysts used in CSR of biodiesel at S/C of 3. The water vaporiser temperature for these experiments was set to 170°C.

Catalyst	BET (m^2/g)	React °C	Vapr °C	WHSV h^{-1}
Ni/Al[a]	-	600	365	3.52
Ni/Al[a]	3.83	650	365	3.52
Ni/Al[a]	4.77	700	365	3.52
Ni/Al[a]	2.21	800	365	3.52
Ni/Al[a]	3.39	650	190	3.18
Ni-K/Al[a]	2.02	650	190	3.18
NiCoCe/Al[a]	83.11	650	190	3.18
Ni/Ca-Al[a]	19.09	650	190	3.52
Ni/Ca-Al[a]	22.25	650	190	3.18
Ni/Ca-Al[a]	20.31	650	190	2.85
Ni/Ca-Al[b]	22.52	650	190	3.18
Ni/Ca-Al[c]	21.13	650	190	3.18
Ni/Ca-Al[d]	20.30	650	190	3.18
Ni/Ca-Al[e]	17.50	650	190	3.18

a- The catalysts were examined using commercial biodiesel.

b- The catalyst was examined using S/C of 2.

c- The catalyst was examined using inhouse-1.5 wt % biodiesel.

d- The catalyst was examined using inhouse-2 wt % biodiesel.

e- The catalyst was examined using palm biodiesel.

Table 6.5 summarises the BET surface area of the used Al_2O_3 supported catalyst tested in CSR of biodiesel at S/C of 3. The surface area of the Ni/Al catalyst decreased with increase in reactor temperature (first 5 rows). The BET surface area of investigation CSR of commercial biodiesel at 600 °C is not reported. The sample produced large amount of

liquid on the analysis tube in spite of degassing for 24 h which was very difficult to be removed, hindering the analysis. The surface area of the catalyst at 650 °C, decreased by ~33% compared to the fresh NiO/Al catalyst. The most significant decrease in surface area was observed at 800 °C. The surface area decreased by 61.3% as compared to the fresh NiO/Al catalyst. The decrease in catalyst surface area at 700 °C was smaller than 650°C: ~17.5% compared to fresh Ni/Al, which was half the surface area loss observed at 650 °C. The decrease in surface area is as a result of sintering of the catalyst. In comparison to the Ni/Al, Ni-K/Al showed hardly any decrease in the surface area of the catalyst. The surface decreased only by ~2.64% in comparison to the NiO-K_2O/Al catalyst. In case of Ni/Ca-Al catalysts using commercial biodiesel, the smallest decrease in surface area was observed at WHSV of 3.18 h^{-1}, which accounted for a decrease of ~33 % compared to the fresh NiO/Ca-Al. In spite of lowering the S/C to 2, the decrease in surface area was very similar. In all the different biodiesels examined, palm biodiesel showed the highest decrease in surface area with the Ni/Ca-Al catalyst. A ~48% reduction in BET surface area was recorded with the Ni/Ca-Al catalyst in CSR of palm oil biodiesel. The surface area of used Ce-Zr catalyst in CSR of commercial biodiesel at 650 °C is shown in Table 6.6. Figure 6.18 and 6.19 shows the N_2 adsorption-desorption isotherms along with BJH pore size and pore volume distribution for the used Ni catalysts supported on pre calcined Ce-Zr support. The used catalyst also exhibited the same type IV isotherm with type H1 hysteresis with different size pores. In the three catalysts supported on the pre calcined Ce-Zr support, Ni-K/Ce-Zr catalysts showed the highest decrease in BET surface area. A ~45.5% decrease in BET surface area as compared to the fresh NiO-K_2O/Ce-Zr was observed. On the other hand, the smallest surface area loss was shown by the Ni-Sn/Ce-Zr catalyst, which accounted for ~17.3% in comparison to the fresh NiO-SnO/Ce-Zr catalyst. Similarly the pore radius of the Ce-Zr catalyst increased after the treatment in the reactor. The pore radius almost doubled in case of used Ni-K/Ce-Zr as compared to the fresh catalyst. In comparison to the fresh catalysts, the pore radii of the Ni/Ce-Zr and Ni-Sn/Ce-Zr catalysts, increased by 1.3 and 1.7%.

Table 6.6: Surface area results of Ce-Zr supported catalysts used in CSR of commercial biodiesel at S/C of 3 at 650 °C. The biodiesel and water vaporiser temperature for these experiments was set to 190 and 170 °C.

Catalyst	BET	BJH surface area	Pore size	Pore volume
	(m^2/g)	(m^2/g)	(nm)	cm^3/g
Catalyst prepared using pre calcined Ce-Zr				
Ni/Ce-Zr	48.33	60.49	6.04	0.19
Ni-Sn/Ce-Zr	50.53	59.66	6.06	0.21
Ni-K/Ce-Zr	22.08	31.69	11.41	0.11
Ni/Ce-Zr-3/1	35.61	43.41	0.62	0.11
Ni/Ce-Al	25.55	33.31	1.20	0.10

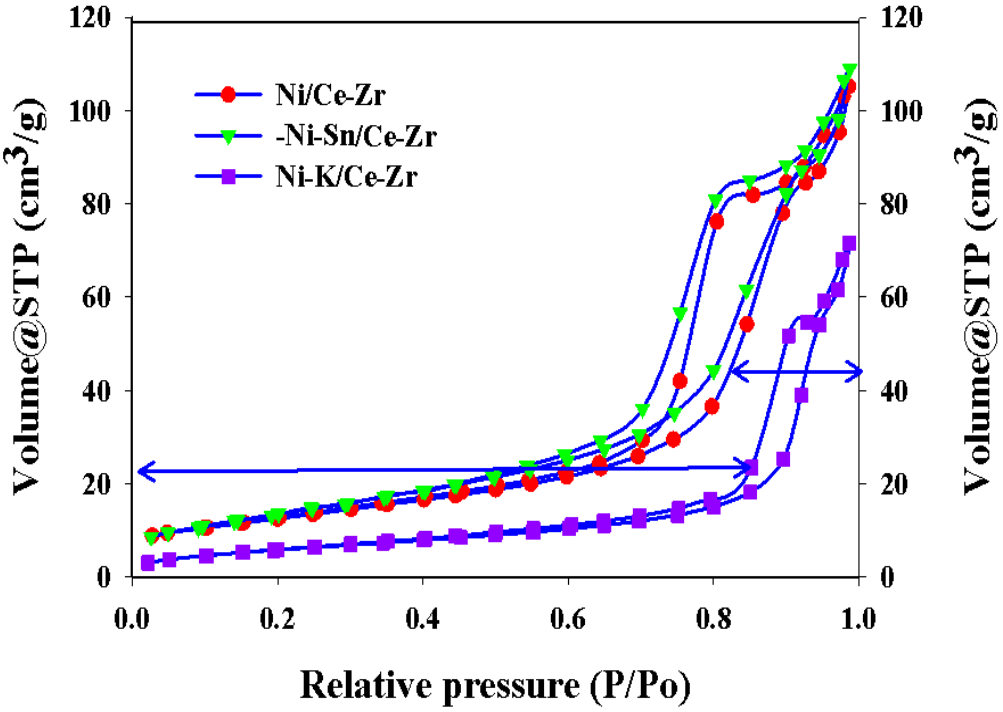

Figure 6.18: N_2 adsorption-desorption isotherms of used Ni catalysts supported on the pre calcined Ce-Zr support. The performance of the catalyst was examined at 650 °C and S/C of 3 with WHSV of 3.18 h^{-1}. The vaporiser temperatures for biodiesel and water were set to 190 and 170 °C.

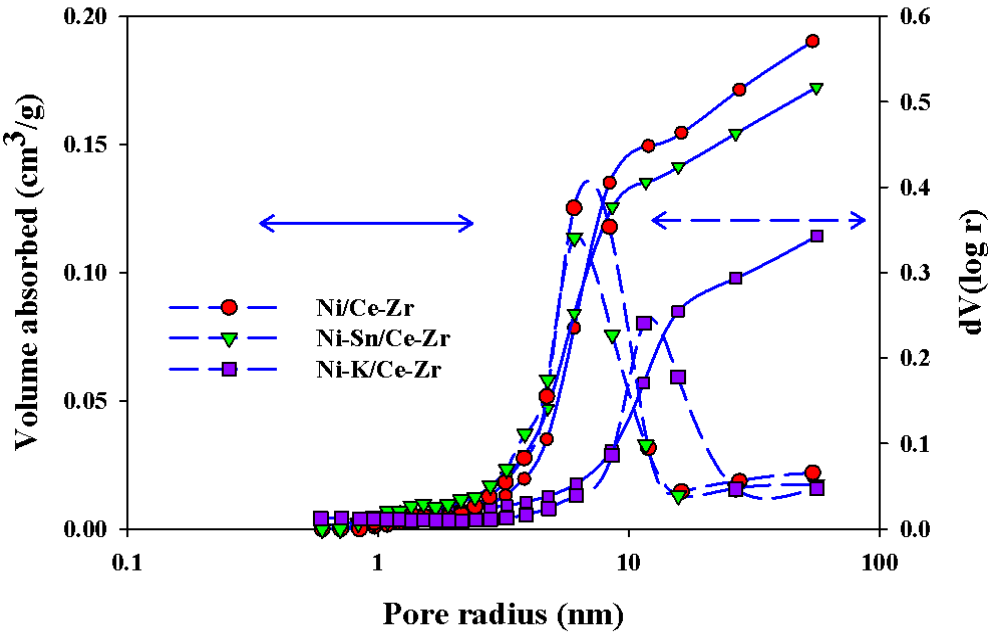

Figure 6.19: Pore-size distribution of used Ni/Ce-Zr catalysts prepared with wet impregnation of pre calcined Ce-Zr support. The performance of the catalyst was examined at 650 °C and S/C of 3 with WHSV of 3.18 h^{-1}. The vaporiser temperatures for biodiesel and water were set to 190 and 170 °C respectively.

In the case of the Ni/Ce-Zr-3/1 and Ni/Ce-Al catalysts, BET surface areas decreased by ~10.2 and 16.8% with the pore radii increasing to 0.62 and 1.20 respectively. The surface area reduction in case of NiCoCe/Al catalyst was 22%.

6.5.2 X-ray diffraction analysis

Figures 6.20 and 6.21 shows the XRD spectra for the used Al_2O_3 and Ce-Zr supported catalysts, respectively. Peaks attributed to Ni were observed at 2θ values of 44, 51, 76 and 91°, with highest intensity displayed at 44°. No peaks pertaining to NiO were observed in any of the catalysts, indicating effective reduction during the H_2 flow pre-

treatment and no deactivation of the catalyst by re-oxidation during their use. Phase composition and crystal sizes for the used Ni/Al catalysts are included in Table 6.7. The average Ni content of the used Al_2O_3-supported catalyst was around 13.8 wt% compared to the expected value of 14.5 wt% calculated from fully reducing the 17.7 wt% NiO of the fresh, oxidised catalyst. This would suggest that a small amount of Ni may have corroded from the catalyst and was carried out of the reactor into the condensate similarly to [266]. The Ni crystallite sizes of the Al_2O_3-supported catalyst increased slightly with temperature as expected by sintering of Ni (from 31 at 600 °C to 38 nm at 800 ºC in Table 6.7).

After use, Ni-K and Ni-Sn catalyst exhibited higher Ni content as compared to the undoped Ni/Ce-Zr catalyst. The Ni content in Ni-Sn/Ce-Zr catalyst was 9.2 wt% in comparison to 6.2 and 8.6 wt% in Ni/Ce-Zr and Ni-K/Ce-Zr catalyst. The Ni crystallite size of the used Ni-K/Ce-Zr catalyst was higher as compared to Ni/Ce-Zr and Ni-Sn/Ce-Zr catalysts.

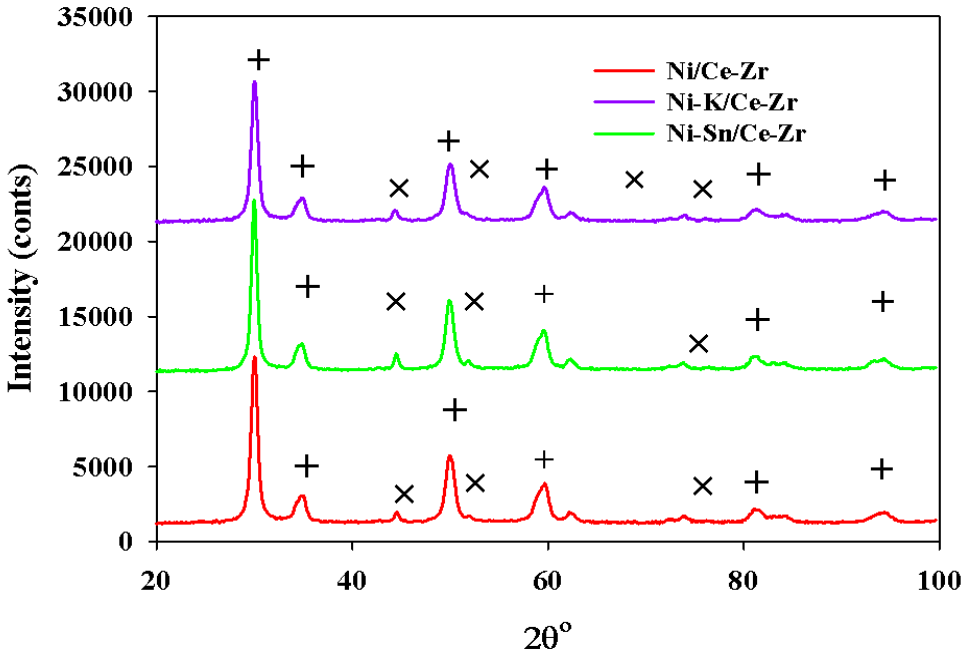

Figure 6.20: X ray diffraction patterns of used Ni catalysts supported on Ce -Zr (pre-calcined) supports. Ni peaks are marked with (×) and Ce-Zr supports are marked by (+).

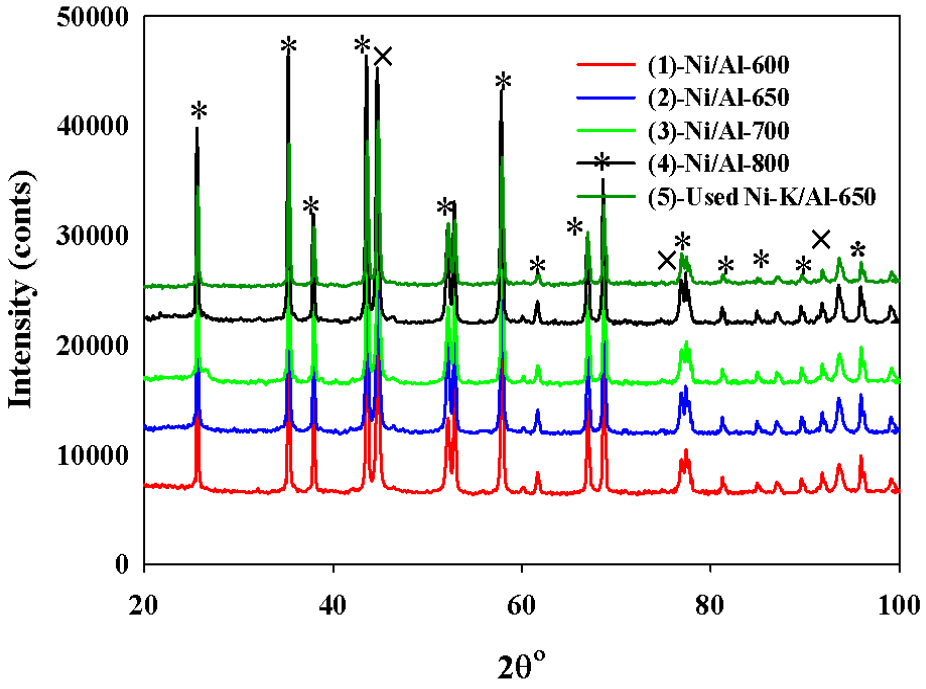

Figure 6.21: X ray diffraction patterns of used Ni/Al and Ni-K/Al catalysts. Ni peaks are marked with (×) and Al_2O_3 supports are marked by (∗).

Table 6.7: Rietveld refinement results of the used Al_2O_3 and Ce-Zr (pre calcined) supported catalysts.

Catalyst	React	Vap	WHSV	Ni	Support	Ni Cryst. size
	°C	°C	h^{-1}	wt. %	wt. %	nm
Ni/Al	600	365	3.52	13.8	86.2	30.91
Ni/Al	650	365	3.52	13.8	86.2	34.91
Ni/Al	700	365	3.52	13.9	86.1	31.87
Ni/Al	800	365	3.52	13.7	86.3	38.13
Ni/Al	650	190	3.18	13.7	86.3	31.06
Ni-K/Al	650	190	3.18	15.7	84.3	37.79
Ni/Ce-Zr	650	190	3.18	6.62	93.38	12.72
Ni-K/Ce-Zr	650	190	3.18	8.64	91.35	16.94
Ni-Sn/Ce-Zr	650	190	3.18	9.26	90.73	11.79

6.5.3 TGA-FTIR and SEM analysis

The TPO of the Ni/Al catalyst examined in the CSR of commercial biodiesel at constant S/C of 3 and WHSV of 3.52h^{-1} in the temperature range of 600-800 °C, is shown in the Figure 6.22. The vaporiser temperature of biodiesel and water for these experiments were set to 365 and 170°C. As seen in the Figure 6.22, there are two CO_2 emission peaks obtained from the TGA-FTIR analysis. The TGA-FTIR analysis was performed from 25 to 900°C at a temperature rate of 10°/C/min in 50 cm^3/min air flow. Normally the combustion temperature of the carbon deposits depends on the nature and deposition sites. It is assumed that the CO_2 peak observed at lower temperature i.e. around 330-350 °C is associated with the carbon deposited over the active metals while the higher temperature CO_2 peak is associated with carbon deposited on the catalyst support [266, 267]. It was reported that the low temperature CO_2 peak is associated with oxidation of surface metal carbides [268]. The high temperature peak is as a result of oxidation of graphite carbon in the form of filaments and nanotubes [269].

At 600 °C, the intensity of CO_2 was highest which decreased with temperature to 650 °C and up on further increase it increased to 700-800°C. This was explained as a result of Boudouard reaction (R-6.7), affecting accordingly the ($S_{C\text{-}CO}$) and to CO_2 ($S_{C\text{-}CO2}$) (Figure 6.6). In this temperature range 650-800 °C, the intensity of CO_2 was highest for the second peak which suggests that most of the carbon formed was present on the catalyst support.

The TPO of the pre calcined Ce-Zr supported Ni catalysts examined in the CSR of commercial biodiesel at constant S/C of 3 and 650°C with WHSV of 3.18 h^{-1} is shown in the Figure 6.23. The vaporiser temperature of biodiesel and water were set to 190 and 170°C respectively. It can be seen from the Figure 6.23, that two forms of carbon were observed with Ni/Ce-Zr and Ni-K/Ce-Zr catalysts, in comparison to only one form observed over Ni-Sn/Ce-Zr catalyst and Ni/Ca-Al (Figure 6.24).

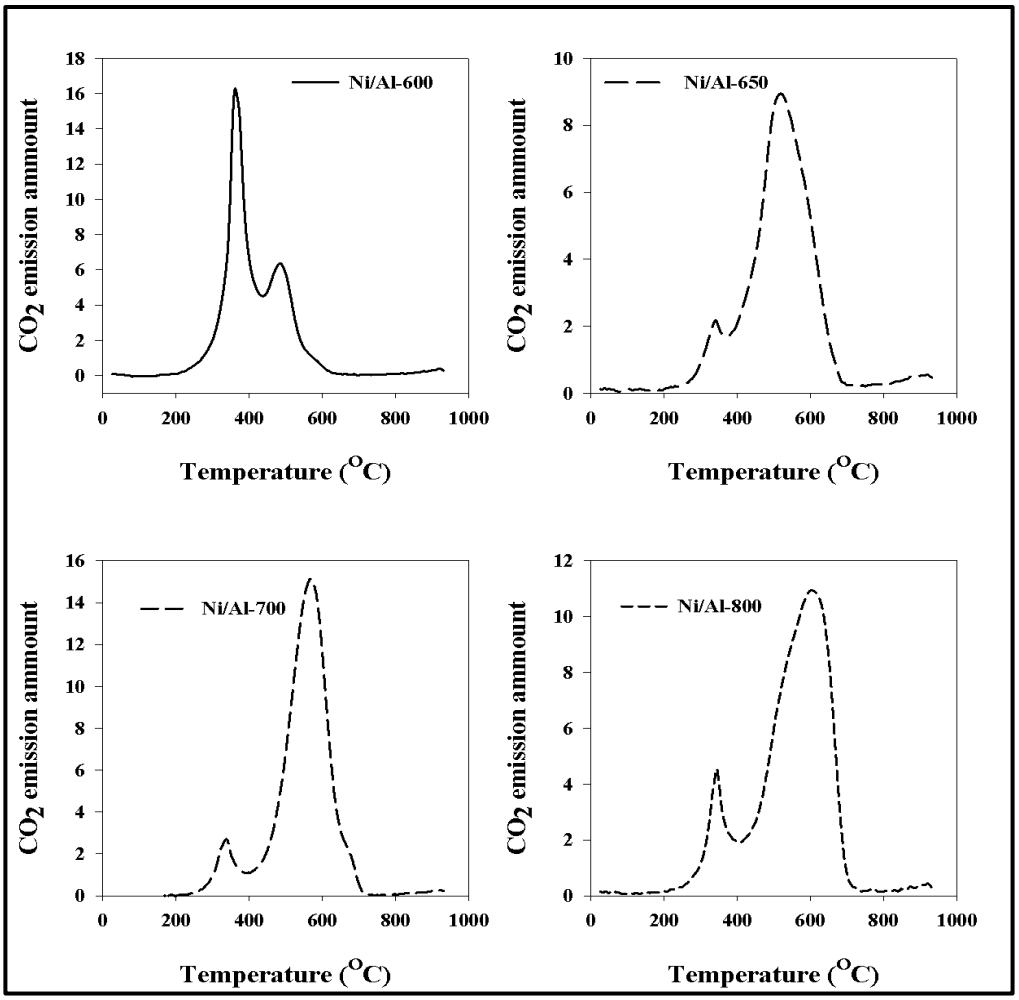

Figure 6.22: The TPO of Ni/Al catalyst examined in CSR of commercial biodiesel using constant S/C of 3 and WHSV of 3.52 h^{-1} in the temperature range of 600-800°C. The vaporiser temperature of biodiesel and water were set to 365 and 170°C respectively.

The intensity of CO_2 peak observed at lower temperature with Ni/Ce-Zr was higher as compared to Ni-K/Ce-Zr, which suggests that higher carbon formation over the metallic Ni as compared to the support. According to Li et al. presence of smaller Ni crystallite sizes in a catalyst help to reduce graphite carbon formation on the catalyst surface [270]. The low temperature CO_2 peak shifts towards lower temperature i.e. 255°C with Ni-K/Ce-Zr which could suggest that the addition of K to the catalyst is useful in oxidation of C. The addition of K lowers the activation energy of the oxidation process and shifts the spontaneous oxidation temperatures to lower values [271]. In comparison to Ni/Ce-

Zr catalyst, the intensity of the high temperature CO_2 peak was higher over Ni-K/Ce-Zr catalyst, suggesting higher carbon formation over the support. This was supported by SEM-EDX analysis.

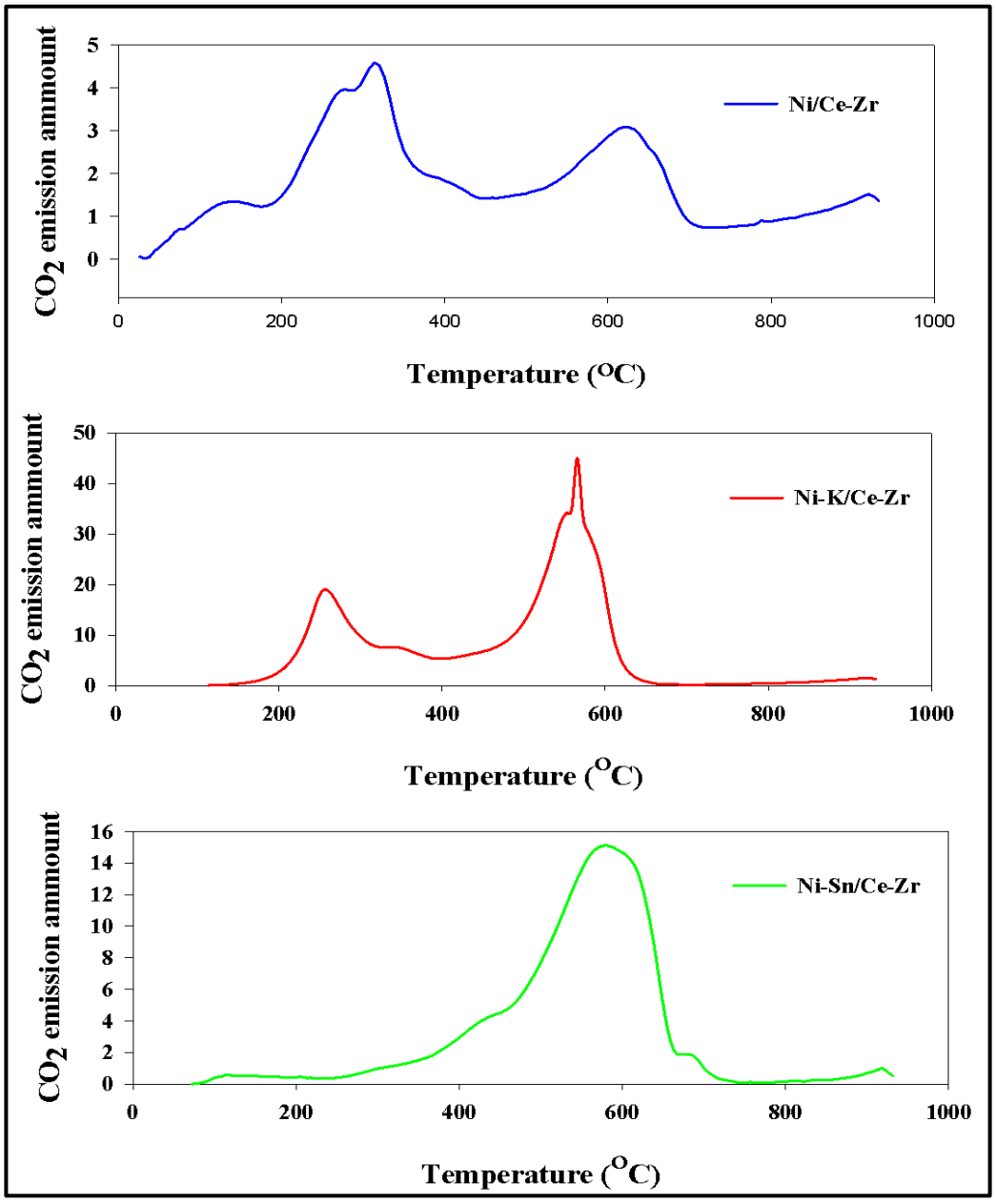

Figure 6.23: The TPO of pre calcined Ce-Zr catalysts examined in CSR of commercial biodiesel at constant S/C of 3 and WHSV of 3.18 h^{-1} with 650 °C. The vaporiser temperature of biodiesel and water were set to 190 and 170 °C respectively.

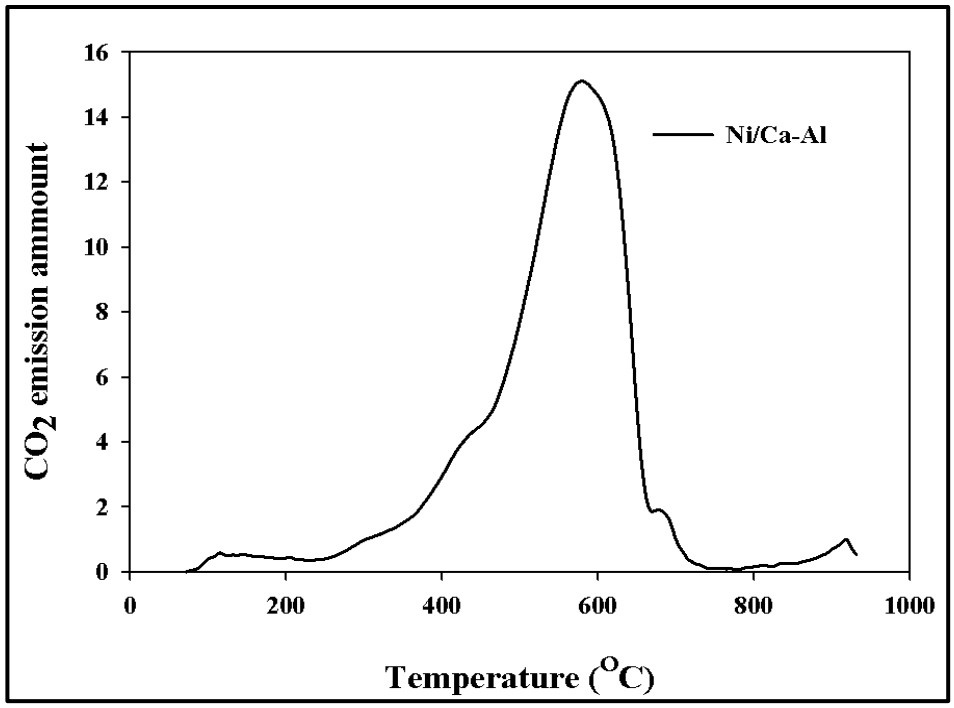

Figure 6.24: The TPO of Ni/Ca-Al catalyst examined in CSR of commercial biodiesel at constant S/C of 3 and WHSV of 3.18 h^{-1} at 650 °C. The vaporiser temperature of biodiesel and water were set to 190 and 170 °C respectively.

.

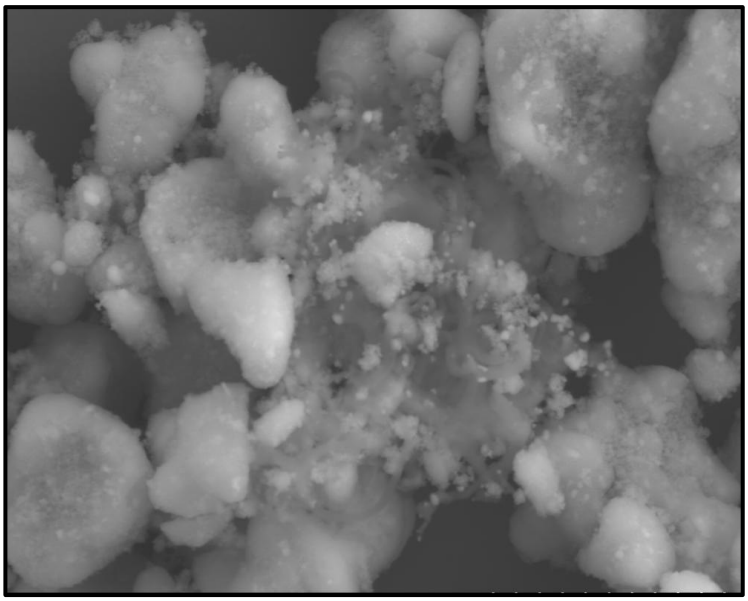

Figure 6.25: The SEM image used Ni-K/Ce-Zr catalyst at 8.00 K mag. The catalyst was used in CSR of commercial biodiesel using S/C of 3 and 650 °C and WHSV of 3.18 h^{-1}.

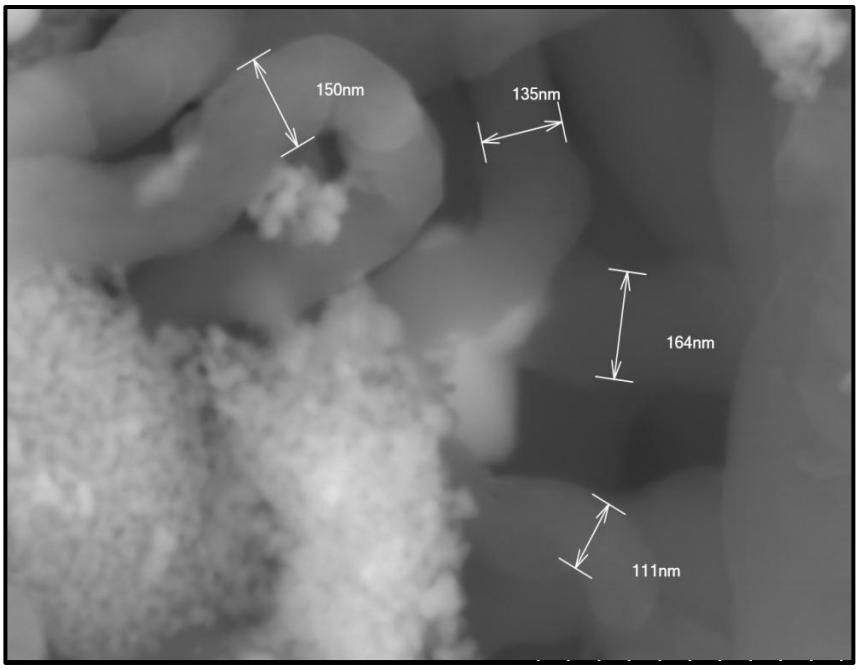

Figure 6.26: The SEM image used Ni-K/Ce-Zr catalyst at 90.00 K mag. The catalyst was used in CSR of commercial biodiesel using S/C of 3 and 650 °C and WHSV of 3.18 h^{-1}.

Figure 6.25 and 6.26 shows a SEM image of used Ni-K/Ce-Zr catalyst tested in CSR of commercial biodiesel at S/C of 3 and 650 °C with WHSV of 3.18 h^{-1}. It can be seen from the Figures that large amount of carbon was present over the catalyst surface. The presence of carbon nano tubes was observed as shown in the Figure 6.26. Carbon formation was concentrated in some areas although other areas were also covered with carbon. An EDX mapping of the used catalyst is shown in the Figure 6.27. The EDX spectrum of the catalyst surface shows the highest C intensity in both the spectrums. The SEM-EDX results were corroborated with TGA-FTIR results. The highest intensity of CO_2 observed in TGA-FTIR (Figure 6.23) and carbon balance (Table 6.3) of the catalyst supports the SEM-EDX results. There are also clusters observed in the Figures 6.25, 6.29 and 6.30 which could be as a result of sintering of Ni crystallites. The increase in Ni crystallite size and decrease in surface area observed during XRD and BET measurements of the used Ni-K/Ce-Zr catalyst (Table 6.6 and Table 6.7) also support this analysis.

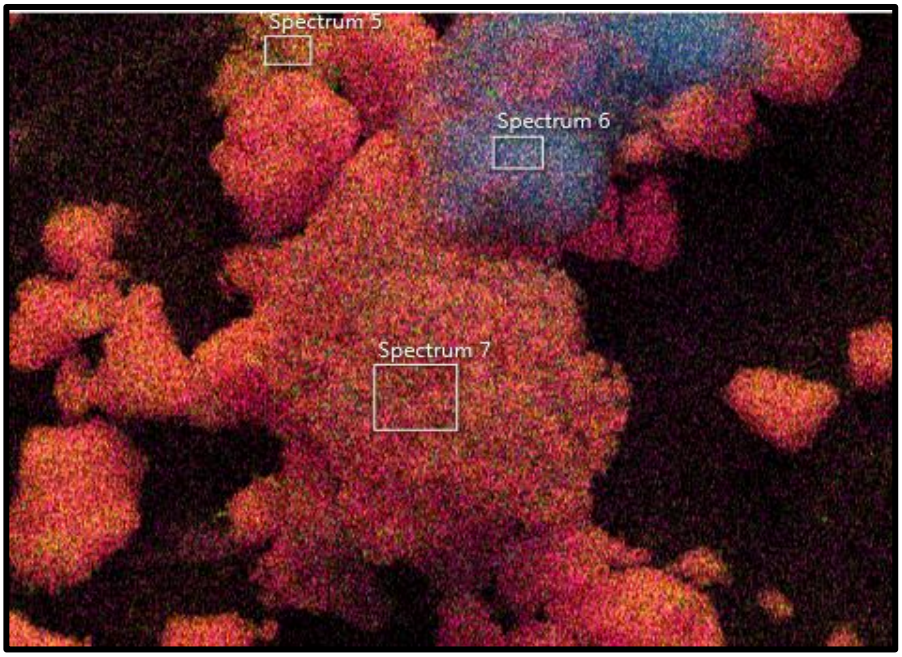

Figure 6.27: The EDX mapping of the used Ni-K/Ce-Zr catalyst tested in CSR of commercial biodiesel using S/C of 3 at 650°C and WHSV of 3.18h^{-1}.

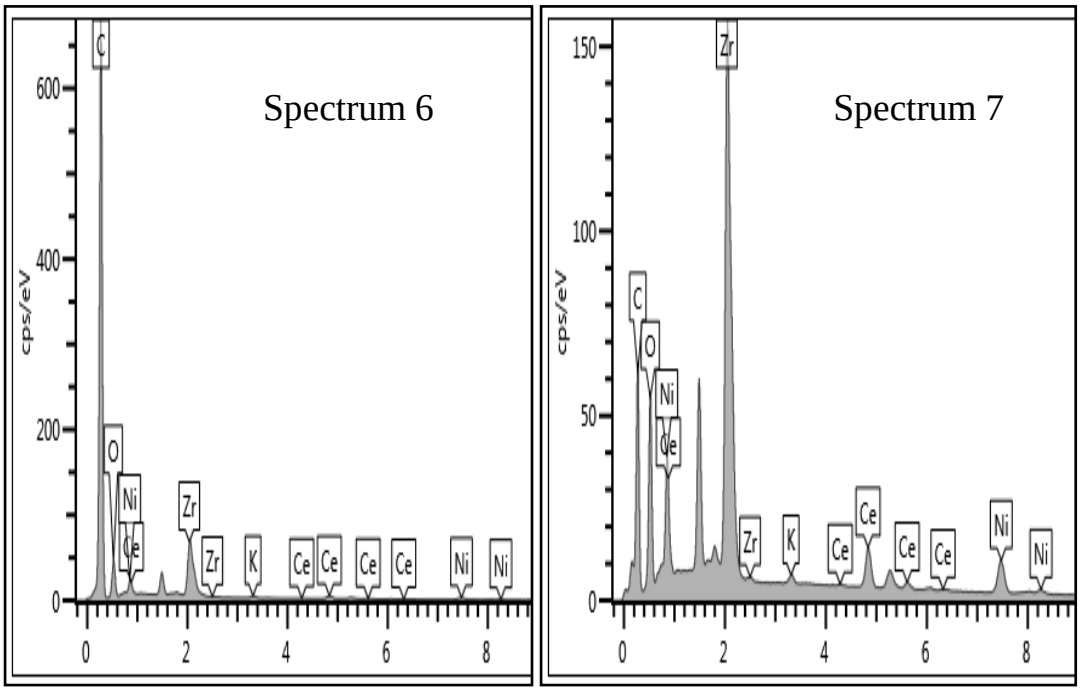

Figure 6.28: The EDX spectra of the used Ni-K/Ce-Zr catalyst tested in CSR of commercial biodiesel at S/C of 3 at 650 °C and WHSV of 3.18 h^{-1}.

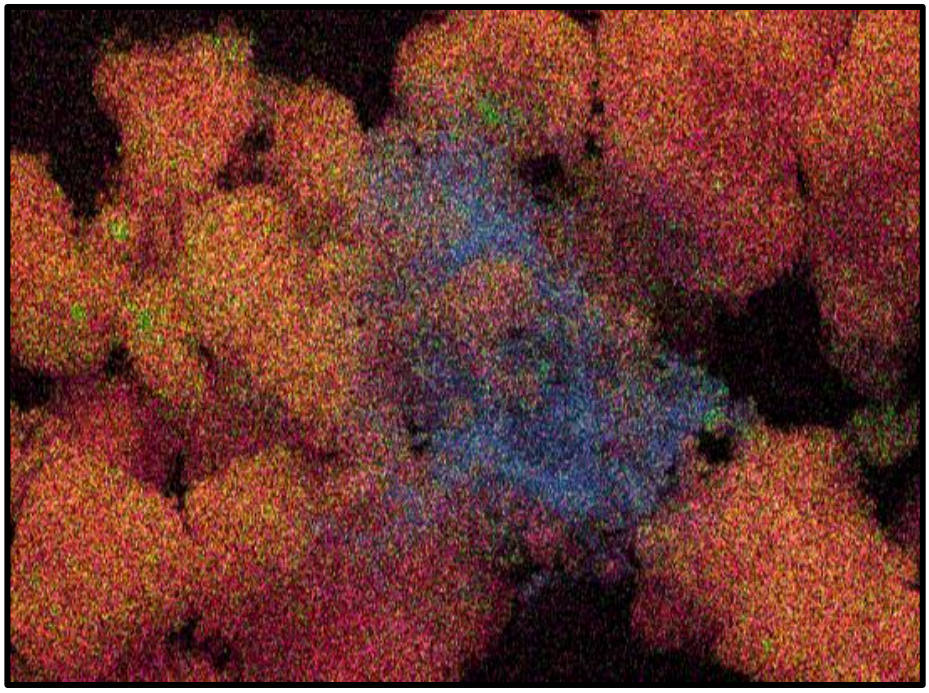

Figure 6.29: The EDX mapping of the SEM image shown in the Figure 6.25 using the same conditions as Figure 6.27.

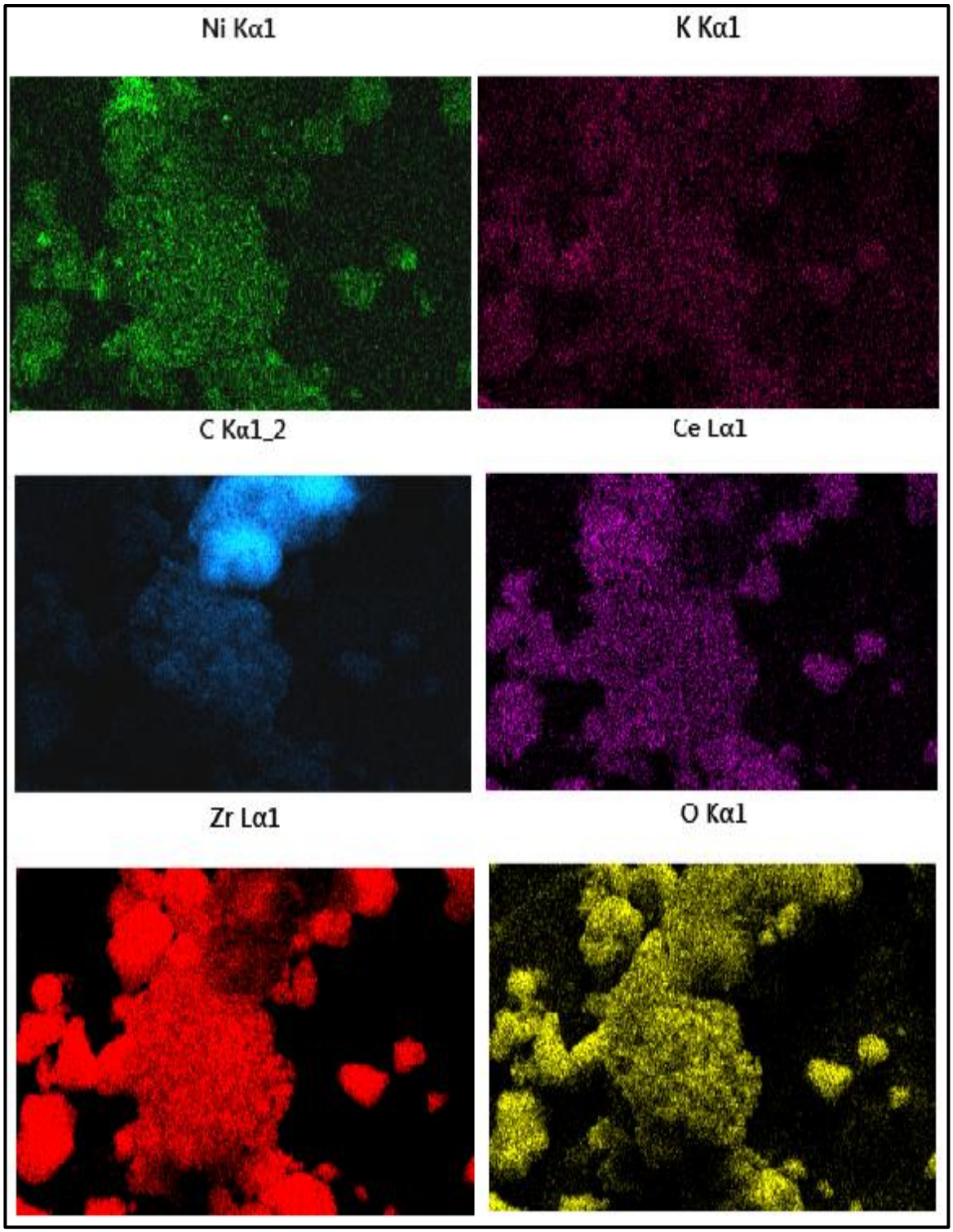

Figure 6.30: Elemental distribution of the (Figure 6.27) which represents used Ni-K/Ce-Zr catalyst tested using same conditions as Figure 6.27.

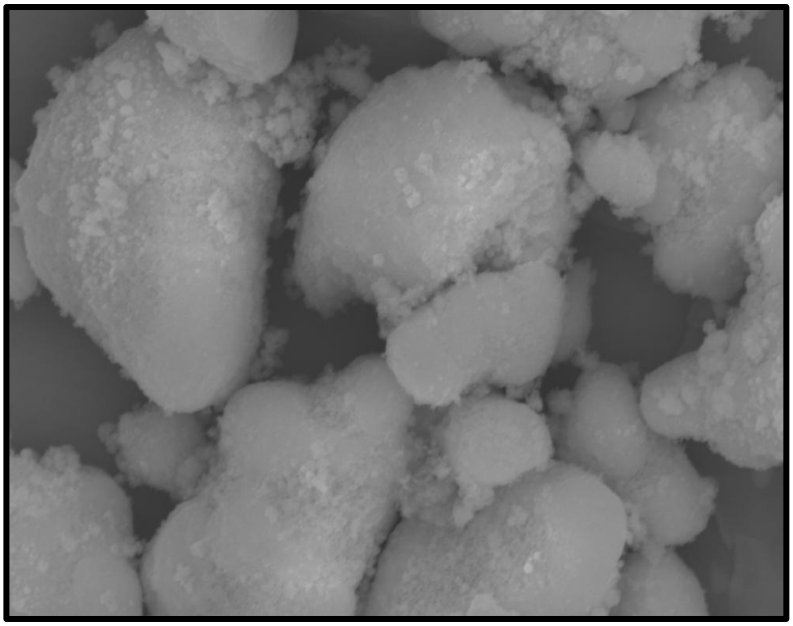

Figure 6.31: The SEM image used Ni/Ce-Zr catalyst at 11 K mag using upper detector. The catalyst was tested in CSR of commercial biodiesel using S/C of 3 at 650 °C and WHSV of 3.18 h^{-1}.

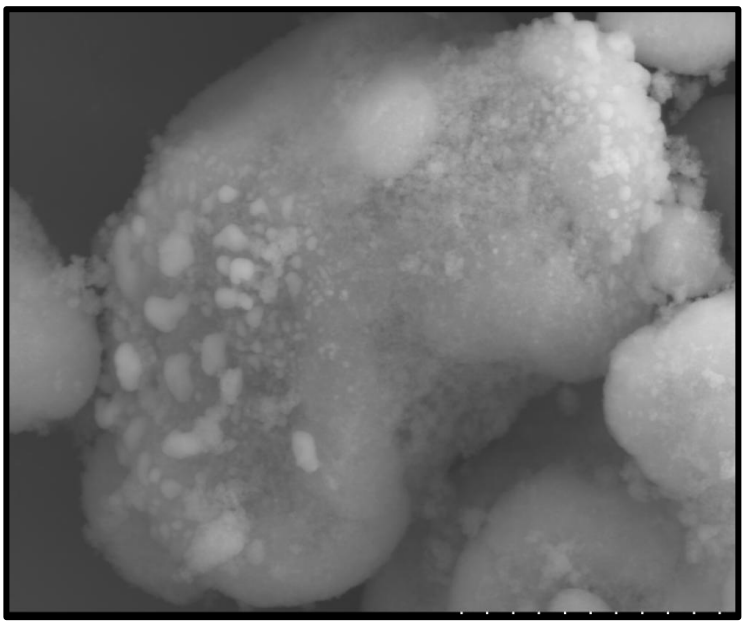

Figure 6.32: The SEM image used Ni/Ce-Zr catalyst at 15 K mag using secondary lower detector. The conditions were same as Figure 6.31.

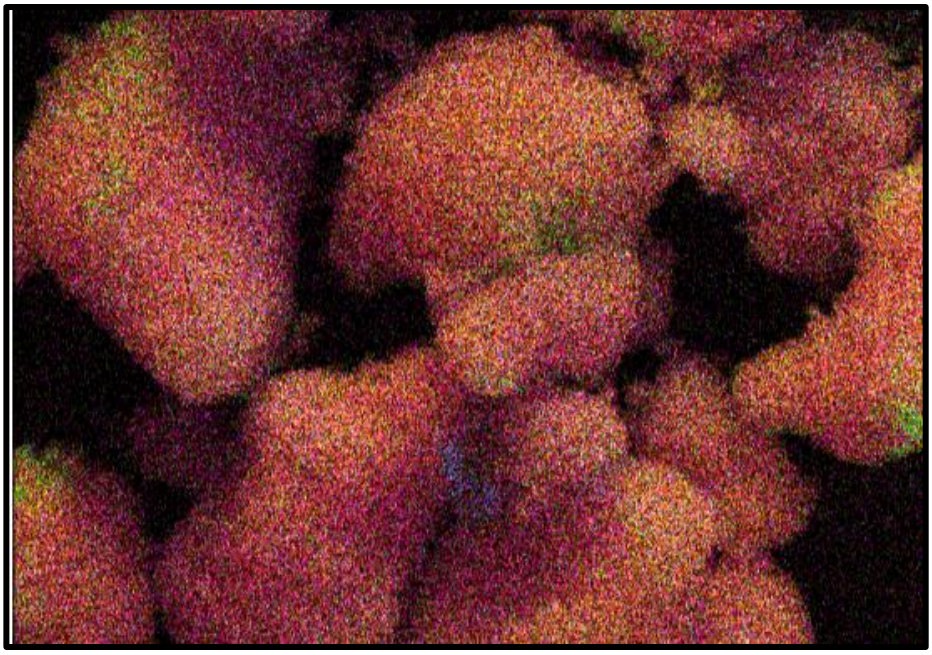

Figure 6.33: The EDX elemental mapping of the SEM image shown in Figure 6.31.

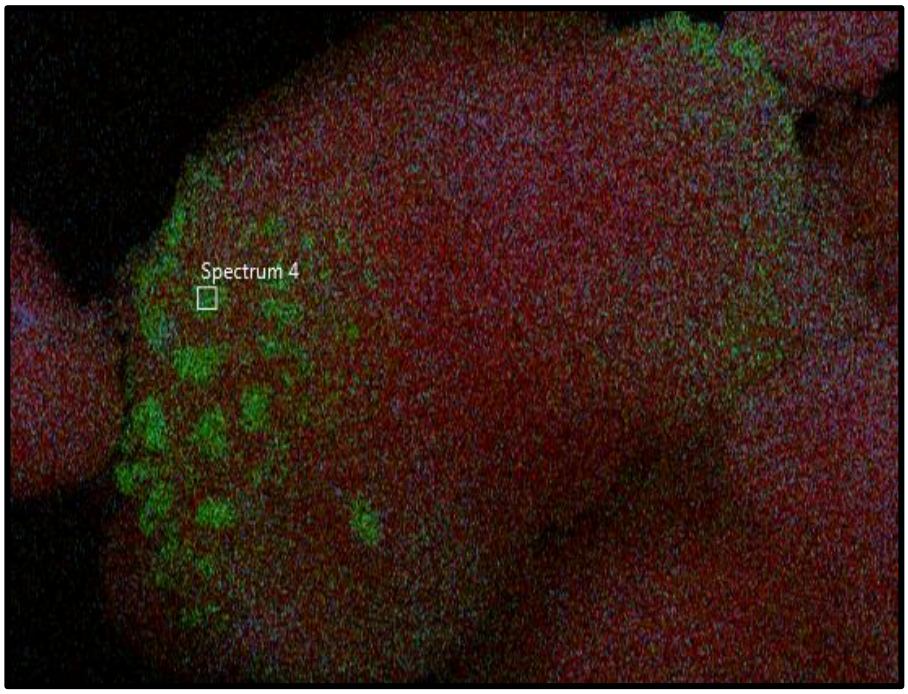

Figure 6.34: The EDX elemental mapping of the SEM image shown in Figure 6.32.

The SEM image of the used Ni/Ce-Zr catalyst tested in CSR of commercial biodiesel with S/C of 3 at 650 °C with WHSV of 3.18 h^{-1} is shown in the Figure 6.31 and 6.32. It can be seen from the Figure that the amount of carbon deposited on the catalyst surface was much less as compared to Ni/-K/Ce-Zr catalyst. The formation of the carbon on the catalyst is evenly distributed (Figure 6.33 and 6.34). The smaller intensity of CO_2 observed in TGA-FTIR (Figure 6.23) and carbon balance (Table 6.3) results for the catalyst supports the SEM-EDX results. On the other hand clusters of Ni were observed over the catalyst which shows signs of sintering of Ni crystallites (Figure 6.34). Figure 6.35 shows EDX spectra of the used Ni/Ce-Zr catalyst and the elemental distribution of the used Ni/Ce-Zr catalyst is shown in the Figure 6.36. The EDX spectra revealed the presence of the Ni clusters; high Ni intensity (Figure 6.35) supports the result. The reduction in BET surface area, observed with Ni/Ce-Zr catalyst also showed sintering of the catalyst (Table 6.6).

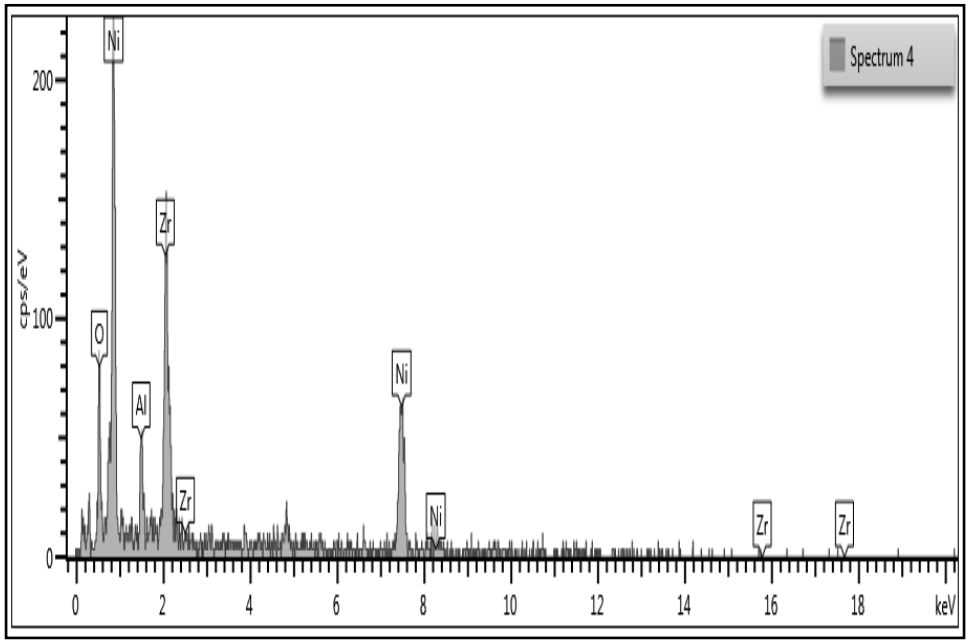

Figure 6.35: The EDX spectra of the used Ni/Ce-Zr catalyst tested in CSR of commercial biodiesel at S/C of 3 using 650 °C and WHSV of 3.18 h^{-1}.

Like Ni/Ce-Zr catalyst, carbon formation over Ni-Sn/Ce-Zr was uniformly distributed over the catalyst surface as shown in the Figure 6.37. Figure 6.23 shows that only one form of carbon was formed with Ni-Sn/Ce-Zr catalyst. The distribution of carbon seen from the elemental distribution was uniform over the catalyst surface (Figure 6.39). The existence of Ni sintering in this catalyst could be smaller in this catalyst as compared to the other two catalysts. This can be seen in the elemental distribution for the catalyst and Ni in the Figures 6.40 and 6.41. The reduction in surface area as a result of sintering was lowest for this catalyst in comparison to the other two Ni/Ce-Zr and Ni-K/Ce-Zr catalyst. Thus combining the BET and SEM-EDX results, one can say that this catalyst suffers less sintering for both the support and Ni.

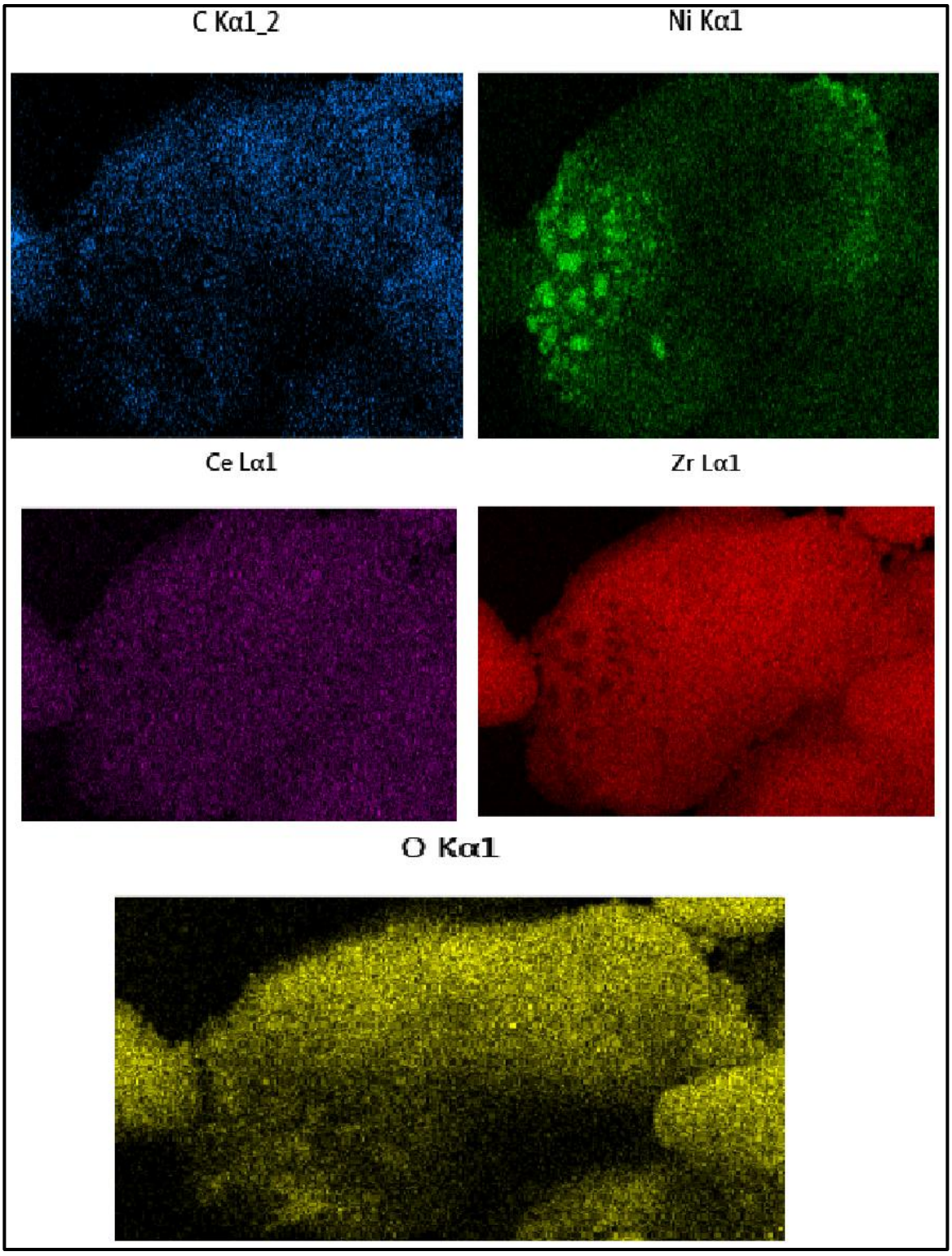

Figure 6.36: Elemental distribution for the used Ni-/Ce-Zr catalyst using same conditions as Figure 6.30.

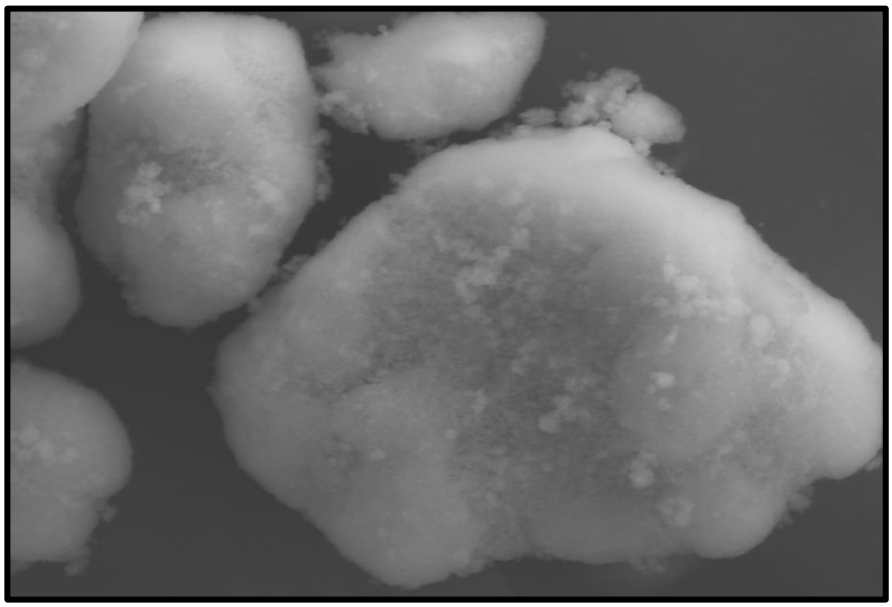

Figure 6.37: The SEM image of used Ni-Sn/Ce-Zr catalyst at 11 K mag. The catalyst was tested for CSR of commercial biodiesel using S/C of 3 at 650 °C and WHSV of 3.18 h^{-1}.

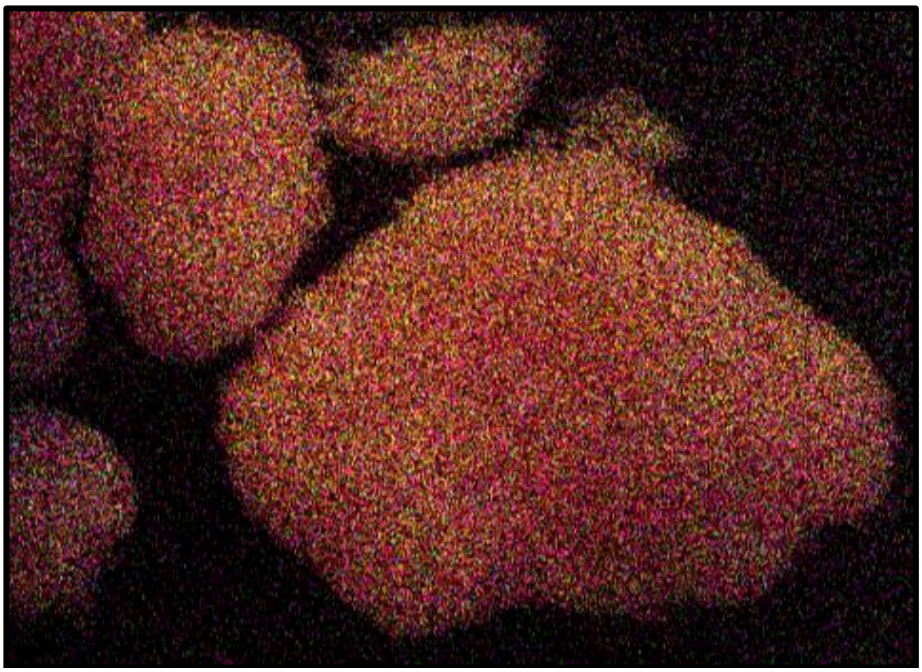

Figure 6.38: The EDX elemental mapping of the SEM image shown in Figure 6.37.

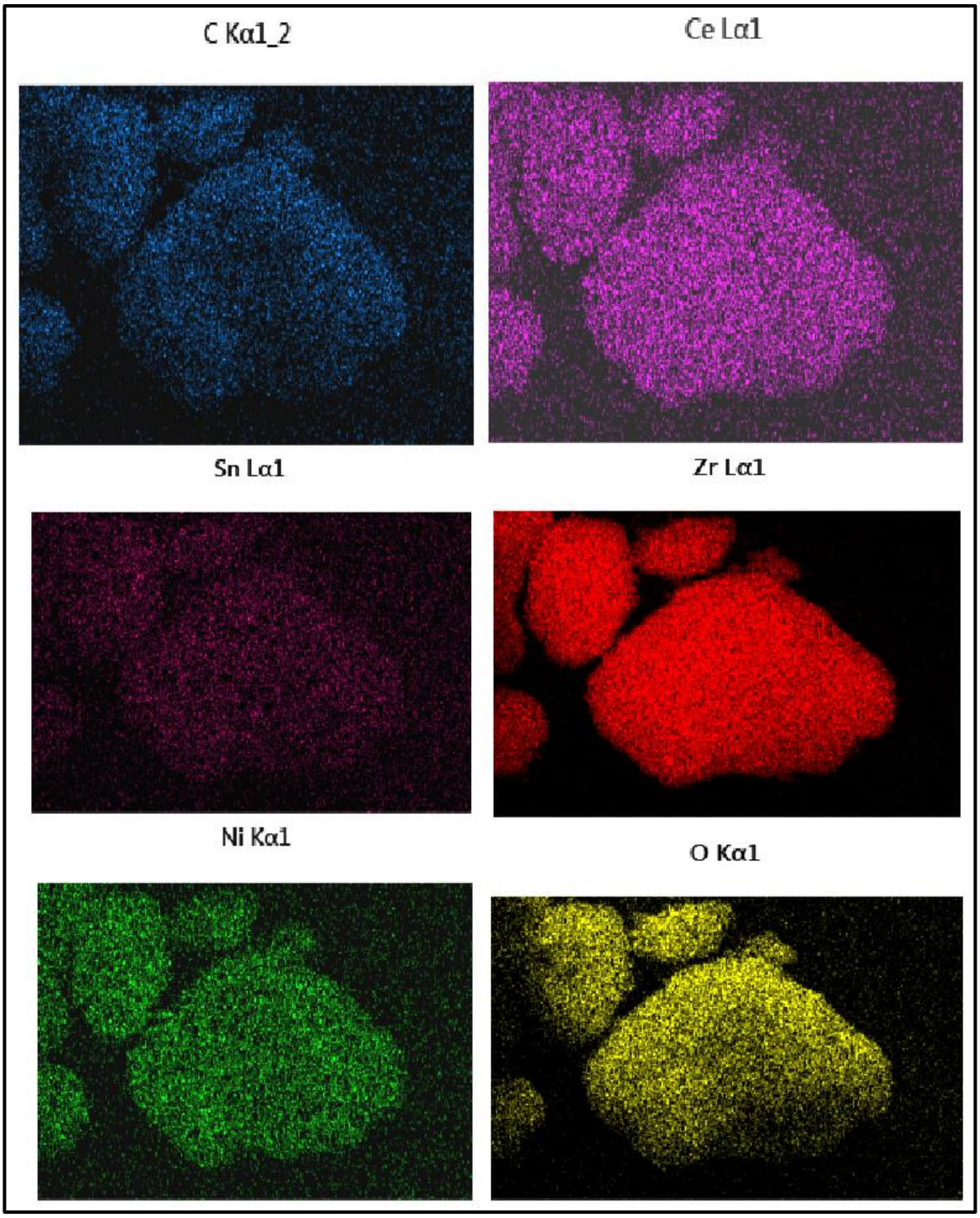

Figure 6.39: Elemental distribution for the used Ni-Sn/Ce-Zr catalyst using same conditions as Figure 6.38.

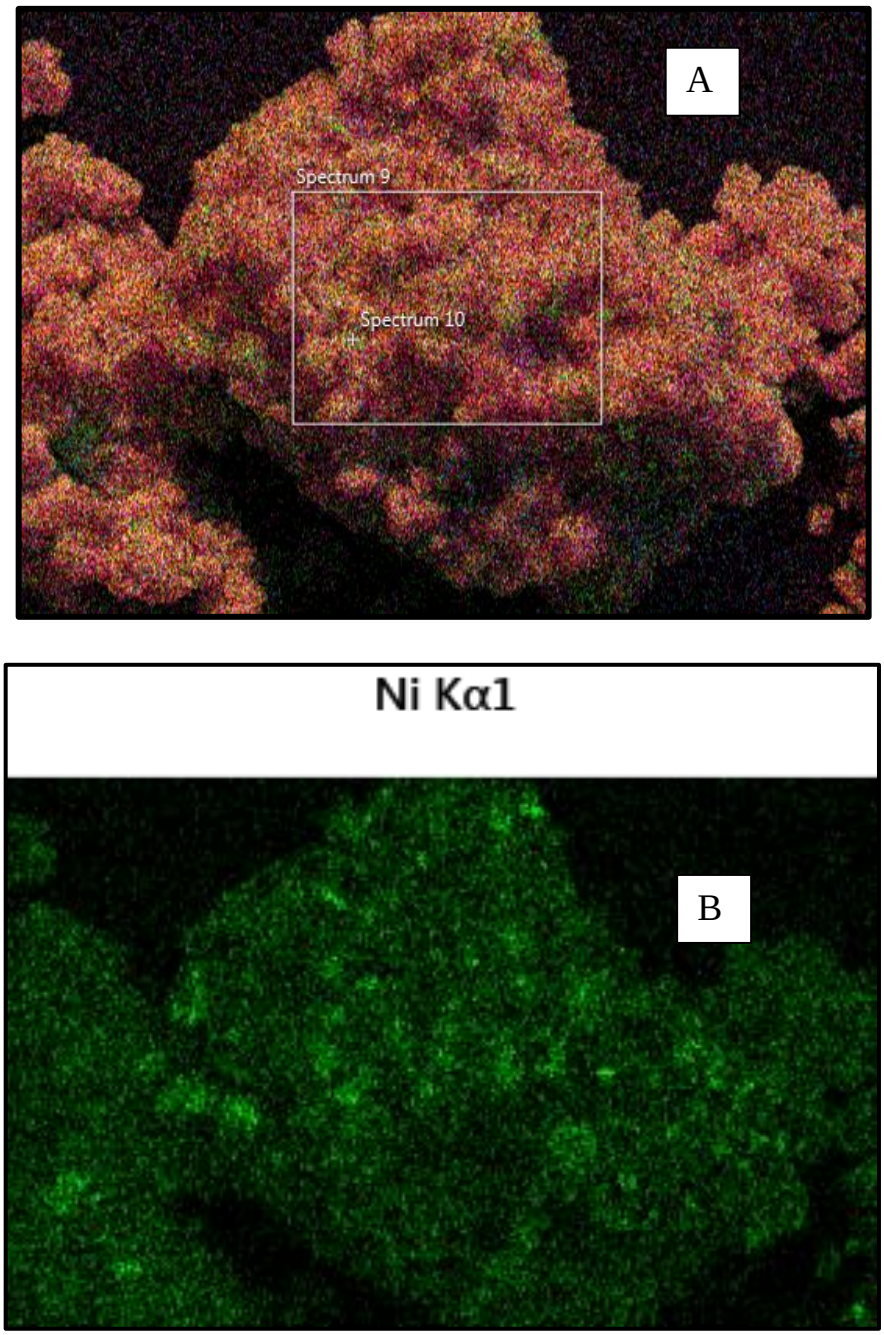

Figure 6.40: Elemental distribution for the used Ni-Sn/Ce-Zr catalyst using same conditions as Figure 6.37. In the figure (A) is elemental mapping of the catalyst and (B) is the Ni mapping for the catalyst.

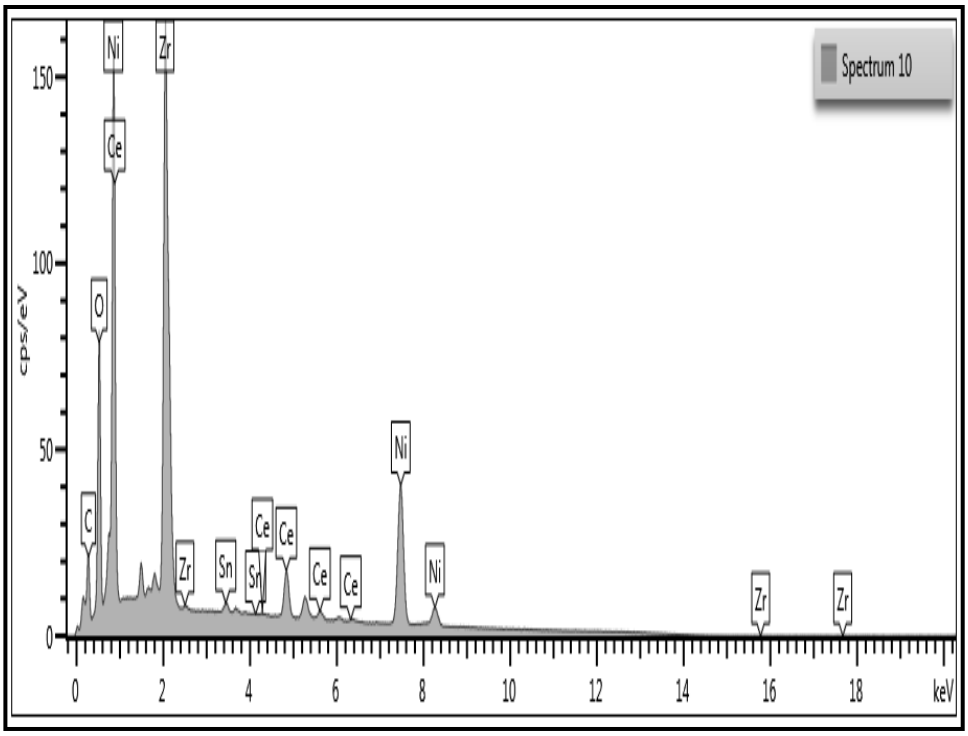

Figure 6.41: The EDX spectra of the used Ni-Sn/Ce-Zr catalyst tested in CSR of commercial biodiesel using S/C of 3 at 650 °C and WHSV of 3.18 h^{-1}

6.6 Conclusion

The experimental results show that biodiesel can be converted to H_2 rich gas efficiently. The optimum temperature for H_2 production by CSR of biodiesel is in the range of 650-700 °C which was also predicted by equilibrium. The optimum biodiesel vaporiser temperature was found to be 190 °C. Molar S/C ratio played an important role to determine the right conditions to perform the experiments, with S/C of 3 showing the best performance. It was found that WHSV of 3.18 h^{-1} provided the best results. The four different biodiesels examined showed that the commercial biodiesel exhibited the highest Y_{H2} and X_{biod}. Both the catalysts, commercial and in house prepared catalyst i.e. Ni/Ce-Zr and Ni/Ca-Al provided the best performance in terms of H_2 yield, along with X_{biod} and X_{H2O}. In comparison to Ni/Ce-Zr, Ni-Ce-Zr-3/1 catalyst was ineffective and showed very

high carbon formation about 25.7% of the carbon feed was observed on the catalyst making it very difficult to operate the reactor and calculate the conversion as a result the experimental results were not shown above for this particular catalyst.

Surface area analysis of the used catalysts indicated that the Ni/Ca-Al, Ni/Ce-Zr and Ni-K/Ce-Zr catalysts were prone to higher sintering as compared to the other Ni/Al and Ni-K/Al catalysts. The SEM-EDX analysis showed the presence of Ni sintering in the Ni/Ce-Zr, Ni-K/Ce-Zr and Ni-Sn/Ce-Zr catalysts. The TPO results performed using TGA-FTIR showed that two forms of carbon were deposited on the Ni/Al, Ni/Ce-Zr and Ni-K/Ce-Zr catalysts. On the other hand Ni-Sn/Ce-Zr and Ni/Ca-Al showed the presence of only one form of carbon.

7. Autothermal reforming

The ATR of biodiesel was examined by Specchia et al [146] and the authors reported the conditions to run an ATR reformer. The authors reported that S/C of 2-2.5 and O_2/C of 0.39-0.41 were good starting conditions to operate an ATR reformer. As a result the ATR experiments were performed using similar conditions. From the CSR experiments Ni/Ca-Al catalyst was an effective catalyst exhibiting highest biodiesel and water conversion thus highest H_2 yield. The experiments were performed at two S/C of 2-3, O_2/C of 0.3 - 0.38 and WHSV of 3.23-2.54 h^{-1} using commercial biodiesel. As this catalyst showed highest conversion at 650°C this temperature was selected for the investigation. The experiments were performed using same input carbon molar flowrate as the CSR experiment. In the experiments performed, biodiesel flowrate was set to 0.978 cm^3/h which gave a carbon input flowrate of 1.50 $\times 10^{-5}$ mol/s. The water flow rate was varied from 1.95 to 2.92 cm^3/h to obtain the desired S/C of 2 and 3 respectively. In comparison to CSR, O_2 was used in the experiment. As use of pure O_2 was not allowed for the experiments, air was used. In order to adjust the WHSV, N_2 was used in addition with air. The air flowrates of 26 and 40 cm^3/min were used to obtain an O_2/C ratio of 0.3 and 0.38.

7.1 Experimental procedure and reactions involved

In addition to the reactions involved in SR discussed in 6.1, catalytic partial (CPO) and complete oxidation (CPO) happen in the ATR processes. Reaction 7.1 and 7.2 show the partial and complete oxidation reactions.

$$C_nH_mO_k + \frac{(n-k)}{2}O_2 \longrightarrow nCO + \frac{m}{2}H_2 \quad \Delta H_{f,298K} < 0 \tag{7.1}$$

$$C_nH_mO_k + \left(n + \frac{m}{4} - \frac{k}{2}\right)O_2 \longrightarrow nCO_2 + \frac{m}{2}H_2O \quad \Delta H_{f,298K} < 0 \tag{7.2}$$

Other oxidation reactions like oxidation of CO, H_2 and C takes in ATR processes.

$$CO+\frac{1}{2}O_2 \longrightarrow CO_2 \ \Delta H_{f,298K}=\text{-}283.6 \text{ kJ/mol} \tag{7.3}$$

$$H_2+\frac{1}{2}O_2 \rightleftharpoons H_2O \ \Delta H_{f,298K}=\text{-}241.6 \text{ kJ/mol} \tag{7.4}$$

$$C+\frac{1}{2}O_2 \longrightarrow CO \ \Delta H_{f,298K}=\text{-}110.5 \text{ kJ/mol} \tag{7.5}$$

$$C+O_2 \longrightarrow CO_2 \ \Delta H_{f,298K}=\text{-}395.6 \text{kJ/mol} \tag{7.6}$$

For measuring the performance of ATR same Eqs i.e. (6.12, 6.17 and 6.22) used in CSR were used to determine the conversion of biodiesel (X_{biod}), steam (X_{H2O}) and hydrogen yield (Y_{H2}). The oxygen conversion is determined using the following Eq 7.7. The selectivities of carbon gases were calculated in similar fashion as the CSR using Eqs 6.24-26. The selectivity for H_2 ($S_{H\text{-}H2}$) was calculated using Eq 7.8, which contains addition H_2O term in addition to the others. The efficiency of the process was measured by comparing the experimental results to the equilibrium predictions.

$$X_{O_2}=\left(\frac{\dot{n}_{O_2,\,in}\text{-}\dot{n}_{O_2,\,out}}{\dot{n}_{O_2,\,in}}\right)\times 100 \tag{7.7}$$

$$S_{H-H_2}=\left(\frac{y_{H_2}}{y_{H_2}+y_{CH_4}+y_{C_2H_4}+y_{C_2H_6}+y_{C_3H_6}+y_{C_3H_8}+y_{H_2O}}\right)\times 100 \tag{7.8}$$

The reaction contribution of the reactions was also calculated. Let the moles of biodiesel reacted by POX (R-7.1), CSR (R-6.3), COX (R-7.2) and TD(R-6.4) be $\dot{n}_{POX}$, $\dot{n}_{CSR}$, $\dot{n}_{COX}$ and $\dot{n}_{TD}$.

Applying mass balance we get

$$\dot{n}_{CO_{out}} = (n \times \dot{n}_{POX} + k \times \dot{n}_{TD}) \quad (7.9)$$

$$\dot{n}_{H_{2out}} = \frac{m}{2} \times (\dot{n}_{POX} + \dot{n}_{TD}) + (\frac{m}{2} + 2n - k) \times \dot{n}_{CSR} \quad (7.10)$$

$$\dot{n}_{CO_{2out}} = n \times (\dot{n}_{CSR} + \dot{n}_{COX}) \quad (7.11)$$

$$\dot{n}_{Cs} = (n\text{-}k) \times \dot{n}_{TD} \quad (7.12)$$

Solving for $\dot{n}_{POX}$, $\dot{n}_{CSR}$, $\dot{n}_{COX}$ and $\dot{n}_{TD}$ we get

$$\dot{n}_{TD} = \left(\frac{\dot{n}_{Cs}}{n\text{-}k} \right) \text{ mol/s} \quad (7.13)$$

$$\dot{n}_{COX} = \left(\frac{\dot{n}_{CO_2 out}}{n} - \dot{n}_{CSR} \right) \text{mol/s} \quad (7.14)$$

$$\dot{n}_{CSR} = \left(\frac{\dot{n}_{H_2,out} - 0.5m \times (\dot{n}_{POX} + \dot{n}_{TD})}{(\frac{m}{2} + 2n\text{-}k)} \right) \text{mol/s} \quad (7.15)$$

$$\dot{n}_{POX} = \left(\frac{\dot{n}_{CO\,out} - k \times \dot{n}_{TD}}{n} \right) \text{mol/s} \quad (7.16)$$

$$\dot{n}_{POX}(\%) = \left(\frac{\dot{n}_{POX}}{\dot{n}_{TD} + \dot{n}_{POX} + \dot{n}_{CSR} + \dot{n}_{COX}} \right) \times 100 \quad (7.17)$$

In the above equations n, m and k are the elemental composition of C, H and O of biodiesel respectively.

It is important to note that the C balance for ATR runs had an additional term which involved char collected from the reactor inlet.. Figure 7.1 shows the char formed in

reactor inlet in the ATR experiments. Also O_2 conversion for all the experiments was 100%.

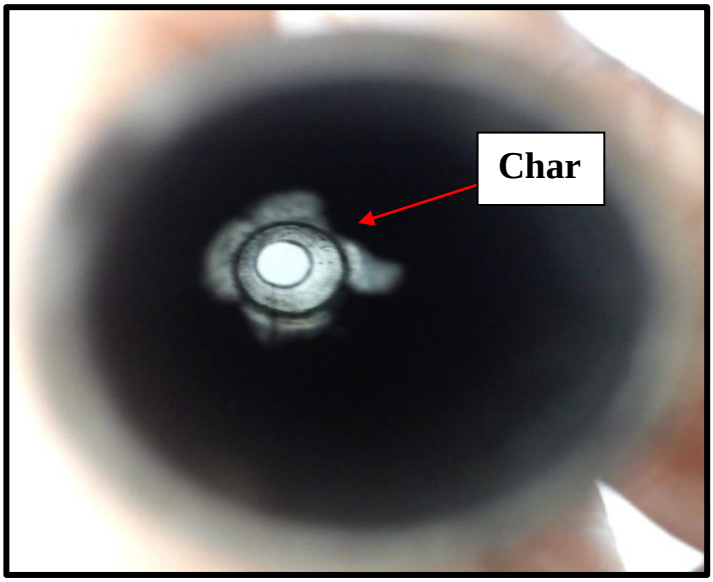

Figure 7.1: Char formed in the reactor inlet during ATR experiments.

7.2 Results and discussion

Figure 7.2 shows the performance of Ni/Ca-Al catalyst in attempted ATR of commercial biodiesel at 650 °C with 190 and 170 °C as vaporiser temperatures. The X_{biod} was highest at S/C of 3 and O_2/C of 0.38 at WHSV of 3.23 h^{-1}. The molar carbon balance for these set of experiments is provided in Table 7.1 performed over 7200s with the carbon input of 1.08×10^{-1} mol. Biodiesel conversion (X_{biod}) of 84.03% was observed at these conditions. In CSR, with same conditions X_{biod} of 96.04% was observed. As compared to CSR, under attempted ATR conditions, X_{H2O} was drastically affected. The X_{H2O} decreased from 37.8 to 13.1% when the ATR equilibrium value was in excess of 25%. At the same O_2/C and WHSV value, decreasing the S/C had a negative effect on the

X_{biod}. At S/C of 2, biodiesel conversion decreased to 75.8%. On the other hand the change in steam conversion was mere 0.43% at this S/C.

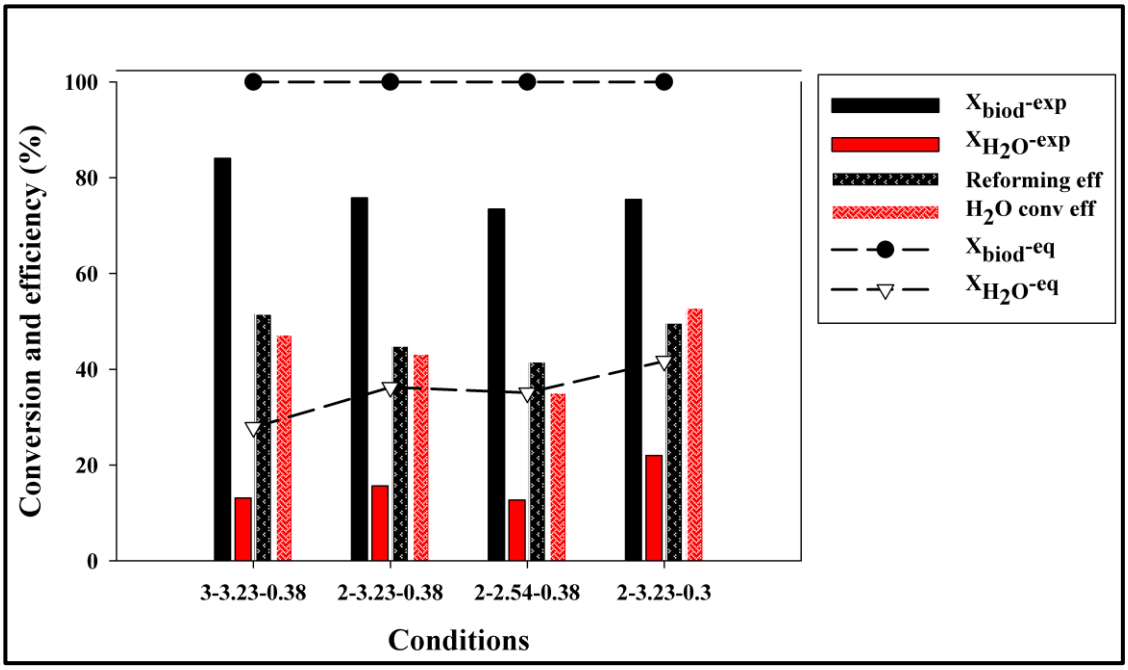

Figure 7.2: Performance Ni/Ca-Al catalyst in ATR of commercial biodiesel at 650°C with biodiesel and water vaporisers set to 190 and 170°C respectively. In the Figure 3-3.23-0.38 represents the experimental conditions. The first value represents S/C, the second value shows the WHSV (h^{-1}) and the last value is O_2/C.

In both these experiments, carbon formation on the catalyst surface was minimal: 2.8 and 2.3% of the carbon output was deposited on the catalyst surface (Table 7.1). On the other hand the carbon deposited at the reactor inlet was higher with S/C of 2 compared to S/C of 3. At S/C of 3, 10.8% carbon was formed in the reactor inlet which increased to 19.3% with reduction in S/C to 2. Similarly at S/C of 2, decreasing WHSV to 2.54 h^{-1} reduced the X_{biod} to 73.5% but water conversion slightly increased to 15.6%. Lowering O_2/C to 0.3 at S/C of 2 and WHSV of 3.23 h^{-1} had no significant effect on X_{biod}, while X_{H2O} increased from 12.7 to 22.0%. This could be as a result of lowering O_2/C ratio.

The highest Y_{H2} was observed at S/C of 3 and O_2/C of 0.38, with a value of 16.13 wt % obtained with Y_{H2} eff of 70.8% (Figure 7.3). Figure 7.3 shows the Y_{H2} and ($S_{H\text{-}H2}$) along with carbon gas selectivities (S_C) in ATR of commercial biodiesel using Ni/Ca-Al catalyst using 190 and 170°C biodiesel and water vaporiser temperatures respectively.

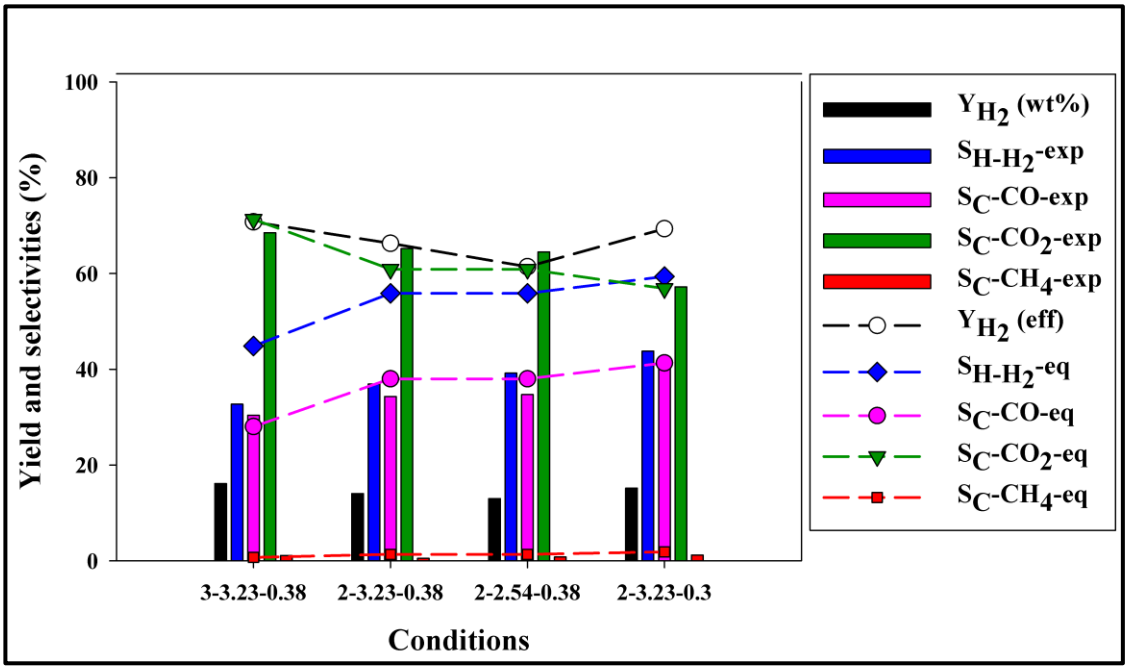

Figure 7.3: Yield (Y_{H2}) and selectivity for H_2 ($S_{H\text{-}H2}$) with selectivity's of carbon gases (Sc) in ATR of commercial biodiesel over Ni/Ca-Al catalyst at 650°C with biodiesel and water vaporisers set to 190 and 170°C respectively. In the Figure 3-3.23-0.38 represents the experimental conditions. The first value represents S/C, the second value shows the WHSV (h^{-1}) and the last value is O_2/C.

The selectivity to all the gases were close to their corresponding equilibrium values (Figure 7.3). As compared to CSR the ($S_{H\text{-}H2}$) was significantly reduced. Similarly ($S_{C\text{-}CO}$) is reduced and ($S_{C\text{-}CO2}$) increased in comparison to CSR. This could be as result of biodiesel oxidation via (R-7.2).

Figure 7.4 shows the contribution of various reactions i.e. TD, POX, CSR and COX occurring in the ATR of commercial biodiesel, using 190 and 170 °C as the biodiesel and water vaporiser temperature over Ni/Ca-Al catalyst. The highest contribution of CSR (R-

6.3) was observed at S/C of 3 and constant O_2/C of 0.38 and WHSV of 3.23 h^{-1}. At these conditions CSR (R-6.3) contributed 32% and the other two reactions POX (R-7.1) and COX (R-7.2) contributed to 24 and 27%. Among the four reactions the contribution of TD (R-6.4) was lowest about 18 %. The higher CSR (R-6.3) contribution resulted in higher X_{biod} and X_{H2O} conversions resulting in higher (Y_{H2}) (Figure 7.2 and 7.3). Lowering the S/C to 2 at the same O_2/C and WHSV was unfavourable as it reduced the contribution of the desired CSR (R-6.3) by 10 % and POX (R-7.1) by 1.2 %, with increasing contribution of the undesired TD (R-6.4) by 7.2% resulting in lower X_{biod} (Figure 7,2) ultimately lowering (Y_{H2}) (Figure 7.3). The reduced S/C ratio marginally affected contributions of COX (R-7.2) increasing by 2.6 %. The higher steam conversion and reforming efficiencies (Figure 7.2) with S/C of 3 and O_2/C of 0.38 corroborates the interpretation of the results. The amount of carbon formed on the catalyst surface for these two runs were similar but the carbon formed in the reactor inlet was higher with S/C of 2 as result of higher TD (R-6.4) contribution of 25.2%.

The reduction of O_2/C from 0.38 to 0.3 at S/C of 2 and same WHSV of 3.23 h^{-1} lowered the contribution of COX (R-7.2) by 12 % and increased POX (R-7.1) by 13 %. At these conditions of O_2/C of 0.3 with S/C of 2, CSR (R-6.3) contribution increased by 5% and TD (R-6.4) decreased by 6%. As a result Y_{H2} increased from 14.1 to 15.2 wt % when O_2/C was lowered from 0.38 to 0.3.

At the same S/C of 2 and O_2/C ratio of 0.38, decreasing the WHSV to 2.54 h^{-1} had no significant effect on the reaction contributions. The contributions of POX (R-7.1) and COX (R-7.2) increased by 3 and 1 %, but TD (R-6.4) decreased by 2.5 %. Even though the contributions of POX and CSR (R-6.3) increased, the reduced X_{biod} and X_{H2O} conversions (Figure 7.2) were responsible for the lower Y_{H2}. This also reflected by the decreased fuel and steam conversion efficiencies which are a supporting evidence for the interpretation.

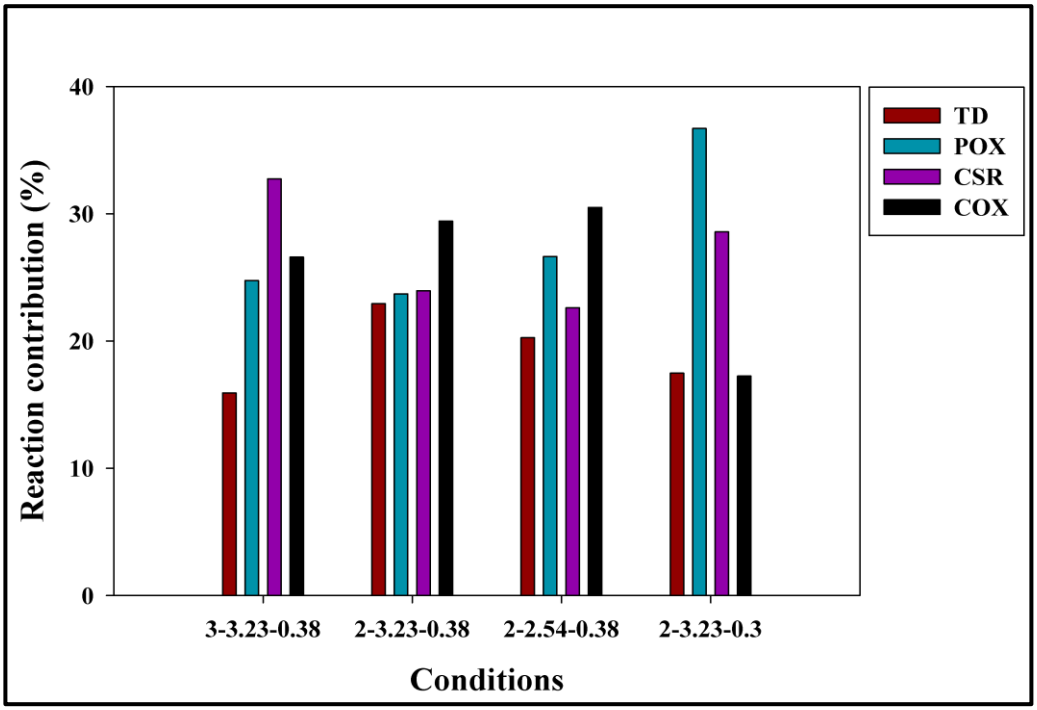

Figure 7.4: Reaction contribution in ATR of commercial biodiesel over Ni/Ca-Al catalyst at 650°C with biodiesel and water vaporisers set to 190 and 170°C respectively. In the Figure 3-3.23-0.38 represents the experimental conditions. The first value represents S/C, the second value shows the WHSV (h^{-1}) and the last value is O_2/C.

Table 7.1: Molar carbon balance of ATR of commercial biodiesel using Ni/Ca-Al catalyst. The biodiesel and water vaporiser were set to 190 and 170°C. The balance is based on total input mol of C (=1.08 ×10^{-1}) over duration of experiment (7200 s) minus mol C converted to gases, volatiles in the condensate, deposited on catalyst and carbon formed in the reactor.

		C on catal		C in cond		Char -reactor		C in gases	
O_2/C	1-Cin/Cout	mol	% C out	mol	% C out	mol	% C out	mol	% C out
0.38[a]	2.62	2.89×10^{-3}	02.75	1.73×10^{-4}	00.16	1.13×10^{-2}	10.78	9.07×10^{-2}	86.29
0.38[b]	3.24	2.37×10^{-3}	02.26	9.66×10^{-5}	00.09	2.01×10^{-2}	19.30	8.18×10^{-2}	78.32
0.38[c]	9.00	1.35×10^{-3}	01.38	5.93×10^{-5}	00.06	1.75×10^{-2}	17.83	7.93×10^{-1}	80.71
0.3[b]	10.32	2.58×10^{-3}	02.66	3.53×10^{-5}	00.03	1.27×10^{-2}	13.15	8.14×10^{-2}	84.13

a- The experiment was performed using S/C of 3 with WHSV of 3.23 h^{-1}.
b- The experiment was performed using S/C of 2 with WHSV of 3.23 h^{-1}.
c- The experiment was performed using S/C of 2 with WHSV of 2.54 h^{-1}.

7.3 Energy Balance:

In order to determine if autothermal conditions are achieved an energy balance was performed assuming isothermal conditions. The enthalpy of component i is calculated using Eq 7.18 from CEA thermodynamic analysis software using NASA coefficients. The values of the the coefficients a_1-b_1 is provided in Appendix E. The magnitude of the balance (ΔH_{EC}, for enthalpy change of reaction) was expressed in % of the total output enthalpy given by following Eq 7.19.

$$\frac{H_i}{RT} = -a_1 T^{-2} + a_2 T^{-1} \ln T + a_3 + a_4 \frac{T}{2} + a_5 \frac{T^2}{3} + a_6 \frac{T^3}{4} + a_7 \frac{T^4}{5} + \frac{b_1}{T} \quad (7.18)$$

$$\Delta H_{EC} = \left(\frac{\sum H_p - \sum H_r}{\sum H_p} \right) \times 100 \quad (7.19)$$

The enthalpies of reactants and products in the inlet and outlet are shown in Tables 7.2 and 7.3, at isothermal conditions of 650°C and atmospheric pressures. In both inlets and outlet enthalpies, enthalpy term of H_2O completely dominates all the others (reactants and products). In the inlet the enthalpy of H_2O and biodiesel were negative while the other reactants O_2 and N_2 were positive.

Table 7.2: Enthalpies of inlet reactants, calculated at isothermal conditions of 650 °C and 1 atm. In the Table 3-3.23-0.38 represents the experimental conditions. The first value represents S/C, the second value shows the WHSV (h^{-1}) and the last value is O_2/C. The enthalpy calculation was performed for duration of 7200 s.

Conditions	**3-3.23-0.38**		**2-3.23-0.38**		**2-2.54-0.38**		**2-3.23-0.3**	
Enthalpy	J	%	J	%	J	%	J	%
Biod	-9.62×10^{2}	1.4	-9.62×10^{2}	2.2	-9.62×10^{2}	2.2	-9.62×10^{2}	2.2
H_2O	-7.09×10^{4}	104.1	-4.73×10^{4}	109.5	-4.73×10^{4}	109.5	-4.73×10^{4}	109.7
O_2	8.25×10^{2}	-1.2	8.25×10^{2}	-1.9	8.25×10^{2}	-1.9	6.60×10^{2}	-1.5
N_2	2.94×10^{3}	-4.3	4.24×10^{3}	-9.8	4.24×10^{2}	-9.8	4.49×10^{3}	-10.4

Table 7.3: Enthalpies of outlet products, calculated at isothermal conditions of 650 °C and 1 atm. In the Table 3-3.23-0.38 represents the experimental conditions. The first value represents S/C, the second value shows the WHSV (h^{-1}) and the last value is O_2/C. The enthalpy calculation was performed for duration of 7200 s.

Conditions	**3-3.23-0.38**		**2-3.23-0.38**		**2-2.54-0.38**		**2-3.23-0.3**	
Enthalpy	J	%	J	%	J	%	J	%
H_2O	-6.16×10^3	76	-3.99×10^4	72.0	-4.13×10^4	74.0	-3.71×10^4	75.4
CO_2	-2.25×10^4	27.8	-1.97×10^4	35.6	-1.83×10^4	32.9	-1.57×10^4	32.0
CO	-2.54×10^3	3.1	-2.44×10^3	4.4	-2.56×10^3	4.6	-3.42×10^3	6.9
CH_4	-4.14×10^1	0.1	-3.35×10^1	0.1	-2.87×10^1	0.1	-2.73×10^1	0.1
C	1.51×10^2	-0.2	2.37×10^2	-0.4	1.99×10^2	-0.4	1.61×10^2	-0.3
H_2	2.52×10^3	-3.1	2.19×10^3	-4	2.03×10^3	-3.6	2.42×10^3	-4.9
N_2	2.94×10^3	-3.6	4.24×10^3	-7.6	4.24×10^3	-7.6	4.49×10^3	-9.1

Likewise in the outlet the enthalpies of H_2O, CO and CO_2 were negative while those of N_2, H_2 and C were positive. The enthalpies of CH_4 and C terms were negligible as compared to the other products H_2, CO, CO_2 and N_2. This phenomenon was evident in all the experimental conditions of varying S/C, O_2/C and WHSV values. The overall balance for all the runs (total output enthalpy-total input enthalpy) was negative, demonstrating exothermic conditions in the isothermal reactor. At constant O_2/C of 0.38 and WHSV of 3.23 h^{-1}, increasing S/C from 2 to 3: in agreement with both total input and output enthalpies dominated by the H_2O enthalpy term, changing the S/C from 2 to 3 increased significantly (in absolute values) the total input and output flow terms. The balance over the isothermal reactor was almost constant, as expressed by ~ (-13) kJ

(Figure 7.5) over the 7200 s of the experiment. However expressed in terms of relative energy flows, the difference between input and output appeared to reduce. With autothermality expressed by ΔH_{EC} of zero, a reduction from 22.1% to 16.0% (Figure 7.5) in this parameter reflected conditions getting closer to autothermality from the exothermal side. This is explained by equilibrium conditions shifted towards reactions that utilise steam, such as SR (R-6.1) and WGS (R-6.2), where SR is significantly more endothermic than the mildly exothermic WGS (R-6.2) (Figure 7.4).

Decreasing O_2/C from 0.38 to 0.3 at constant S/C of 3 and WHSV of 3.23 h^{-1}, did not affect the total input enthalpy, as the O_2 term is a negligible contributor to the inflow of energy compared to the overwhelming effect of steam. Varying the O_2/C affects the output enthalpy flow, via the effects on the CO and CO_2 products. Decreasing O_2/C hinders the COX (R-7.2), and shifts the equilibrium towards the less exothermic POX (R-7.1) (Figure 7.4). With CO_2 being a dominant term in the output enthalpy, a lower yield of CO_2 product and higher yield of CO reduces overall the total output enthalpy and brings the conditions closer to autothermality. This is reflected in the large drop in ΔH_{EC} from 22.1% to 12.7% (Figure 7.5). The condition O_2/C of 0.3 for S/C of 2 at WHSV of 3.23h^{-1} represented the closest to autothermal conditions for this set of runs.

Changing the WHSV by varying the catalyst mass in the reactor would have the effect of reducing the time available for homogeneous reactions in the reactor and for heterogeneous reactions on the catalyst bed. Accordingly, lowering the WHSV corresponded to higher reaction times and could have created conditions closer to chemical equilibrium. However, it was found here that the energy balance was hardly affected by the variation of WHSV from 3.23 to 2.54 h^{-1} at constant S/C of 2 and O_2/C of 0.38, by increasing the catalyst mass from 2 g to 2.6 g. It is ventured that the reactor as close to chemical equilibrium for 2g of catalyst as permitted by the set up and conditions used, and that adding catalyst volume did not change that.

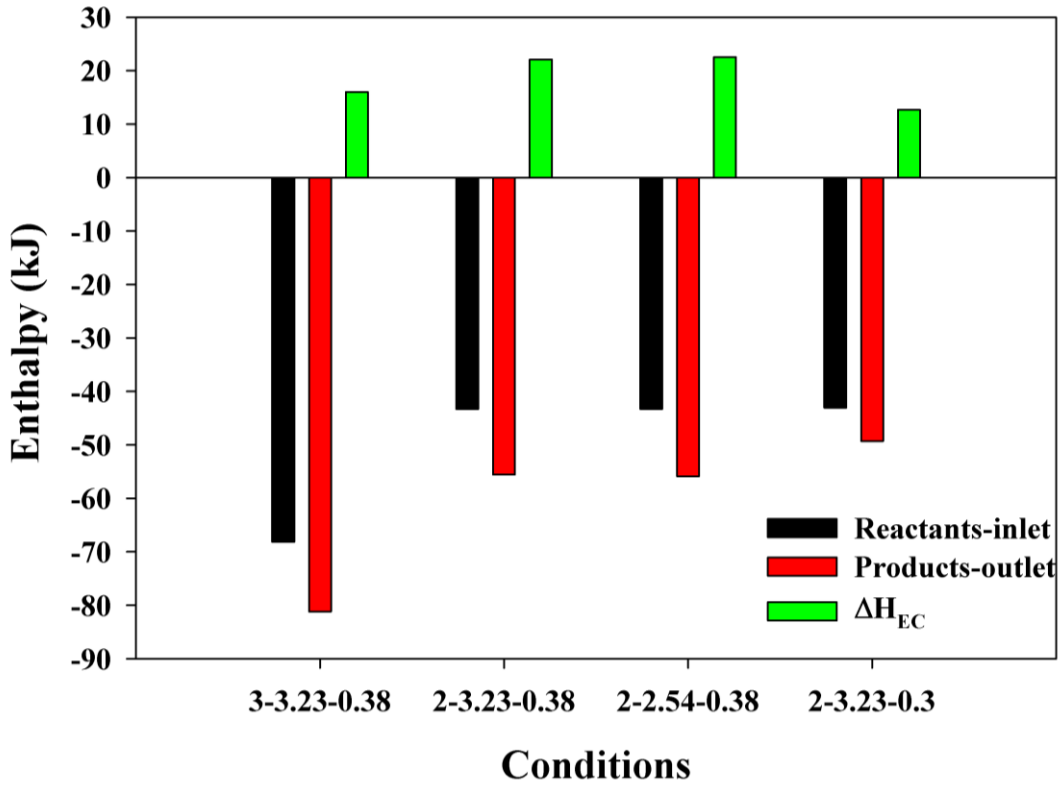

Figure 7.5: Enthalpy balance of the ATR reforming experiments.

7.4 Conclusion

Although the attempted ATR experiments were successful in demonstrating the simultaneous occurrence and respective contributions of the desired reactions of POX, steam reforming and complete oxidation, which form the backbone of autothermal reforming, the reactor designed did not appear to convert the biodiesel to the same efficient degree as was measured during the previous CSR experiments. A different approach must be adapted to feeding the reactants, and recommendations on this issue are made in the Future Work section. The main problem associated with the attempted ATR experiments was excessive formation of carbon in the reactor inlet, affecting the conversion of biodiesel to produce high yield of H_2 gas.

8. Conclusion and future work

An experimental set-up was designed and successfully evaluated for H_2 production from biodiesel. An up flow reactor arrangement was difficult to operate as a result of condensation occurring due to the mixing of cold N_2 carrier gas and hot biodiesel vapours and steam. The use of N_2 preheating coils placed on the vaporisers in addition to changing the configuration to down flow proved to be the right option for the prevention of condensation of the biodiesel and steam vapours and correct operation of the system. In order to evaluate the performance of the reactor set-up, a micro gas chromatograph was installed and an analysis method was developed and successfully tested. The designed set up was very effective for steam reforming while autothermal reforming indicated further optimization was required. Effects of molar steam to carbon ratio in the feed (S/C), temperature, weight hourly space velocity (WHSV, i.e. an inverse measure of residence time in the reformer), catalyst and biodiesel characteristics on the steam reforming outputs were examined at constant carbon input of 1.50×10^{-5} mol of C/s. The optimum temperature conditions to convert biodiesel to H_2 were found to be in the temperature range 600-700°C, with 190 and 170°C as biodiesel and water vaporiser temperatures respectively. The performance of the process was examined in terms of H_2 yield, as well as X_{biod} and X_{H2O} and selectivity to products. The experimental values were compared with the equilibrium values to determine the efficiency of the system and allow comparisons between catalysts and operating conditions.

The catalysts examined in this study were prepared by impregnation of commercial Ce-Zr support and of supports prepared by sol gel synthesis. The commercial Ce-Zr was supplied MEL Chemicals, UK. The manufacturer supplied the support in the form of hydroxide and oxide. The hydroxide was calcined in the laboratory to form oxide and was used to prepare the catalyst using two methods (wet and dry impregnation) with different Ni loading. It was found that smaller Ni crystallite sizes and higher surface area with good pore size distribution was exhibited by catalysts prepared with the wet impregnation method. As a result, this method was used in catalyst preparations. Further

the oxide pre calcined by the manufacturer had higher surface area thus it was chosen for the preparation of the catalysts Ni/Ce-Zr, N-K/Ce-Zr and Ni-Sn/Ce-Zr. Tamarind seed polysaccharide was used for the first time as a gelling agent in sol gel synthesis for the preparation of catalyst supports (Ce-Zr-3/1 and Ce-Al-3/1). As the polysaccharide is stable up to 100°C and can work in high ph this would assist in good gel formation. The formation of nanoparticles using green approach can be achieved. The higher chain length of the polysaccharide resulted in formation of nano crystals.

Three different kinds of biodiesel (commercial, palm and in house) were used to evaluate the characteristics of biodiesel on the process. It was found that commercial biodiesel exhibited the best performance in terms of reactants conversion and Y_{H2} over the Ni/Ca-Al catalyst among the three biodiesels tested and was thus used for evaluating the other catalysts.

The performance of the in house prepared Ni catalysts was compared with the commercial (Ni/Al) catalyst provided by Johnson Matthey, Plc and the Ni/Ca-Al catalyst provided by TST, Ltd. For Ni/Al catalysts, highest Y_{H2} of 26.3 wt% of the biodiesel feed was obtained with Y_{H2} (eff) of 87.2% (i.e. % of the chemical equilibrium value) at 700 ^{o}C and S/C of 3 at WHSV of 3.52 h^{-1}. A biodiesel conversion of 92% with 36.3% steam conversion was obtained for the catalyst, representing 84% and 77% of the chemical equilibrium values respectively. On the other hand Ni/Ca-Al and Ni/Ce-Zr supported catalysts exhibited the best performance at lower temperature (650 ^{o}C) and WHSV of 3.18 h^{-1} at S/C of 3. A Y_{H2} of 27.0 wt% (93.3% of equilibrium), was seen with the Ni/Ca-Al catalyst as a result of high biodiesel and steam conversions of 96% and 37.5%. On the other hand, Ni/Ce-Zr was responsible for slightly higher Y_{H2} of 27.9 wt%, equivalent to 96% of the equilibrium value, caused by the highest steam conversion among all the catalysts examined. The Ni/Ca-Al and the Ni/Ce-Zr catalysts exhibited a fuel reforming efficiencies as expressed by the ratio of H_2 to biodiesel calorific values of 86.4 and 88.9%.

The addition of dopants such as K and Sn had a negative effect on the catalytic activity of the Ni/Ce-Zr catalyst, especially Ni-K/Ce-Zr which showed higher C deposition on the catalyst surface and exhibited lower reforming activity as a result. The Ni catalysts prepared using sol gel made supports (Ce-Zr-3/1 and Ce-Al-3/1) were ineffective compared to the ones prepared using commercial Ce-Zr support supplied by MEL chemicals, UK. The catalysts prepared using sol gel syntheses were prone to carbon deposition and exhibited low surface area along with uneven pore structure, affecting their activity and catalyst performance. On the other hand the catalyst prepared using commercial Ce-Zr support had high surface area and had a uniform pore structure thus providing good catalytic activity.

In comparison to steam reforming, H_2 production via autothermal reforming was not as successful. A hydrogen yield of 16.1 wt%, i.e. just 70.8% of equilibrium was achieved at S/C of 3 and molar oxygen to carbon ratio (O_2/C) of 0.38 with WHSV of 3.23 h^{-1} at 650 °C, resulting from X_{biod} and X_{H2O} of just 84.0 and 13.1%, respectively. Enthalpy balances on the reformer for the experiments performed at 650 °C for the constant run durations of 7200 s showed that the enthalpy balance (ΔHr) for all the runs (total output enthalpy minus total input enthalpy) was negative, demonstrating exothermic conditions in the isothermal reactor. The negative enthalpy term of H_2O (steam) dominated over all the other reactants input enthalpy terms (biodiesel, O_2, N_2). In the total output enthalpy, the enthalpies of H_2O, CO_2, CH_4 and CO were negative while those of N_2, O_2, C and biodiesel, were positive, with, again the steam term dominating over all the others. The magnitude of the balance ΔH_{EC} showed that lower S/C of 2, resulted in conditions getting closer to autothermality from the exothermal side. The ΔH_{EC} value reducing from 22% to 16% of the total output enthalpy when lowering S/C from 3 to 2 at constant O_2/C of 0.38 and WHSV of 3.23 h^{-1} supported this interpretation. Likewise lowering the O_2/C from 0.38 to 0.3 at constant at S/C of 2 and WHSV of 3.23 h^{-1} also had a significant effect on ΔH_{EC}, suggesting conditions moving closer to autothermality, supported by reduced ΔH_{EC} value from 22.1% to 12.7%. At 650 °C, the condition O_2/C of 0.3 for S/C of 2 at WHSV of 3.23 h^{-1} represented the closest to autothermal conditions for the experiments.

Future work

It can be seen from this evaluation that H_2 can be successfully produced from biodiesel via steam reforming. The long term evaluation of the process has to be carried out to determine the stability of the catalyst in terms of activity and carbon deposition. The reasons responsible for carbon formation should be investigated to improve the stability and activity of the catalyst. The forms of carbon formed during hydrogen production must be investigated. This would help in selection or modification of catalyst to resist or minimise carbon formation. Further characterisation of catalyst using chemisorptions should be performed in order to determine the active sites of the catalyst in order to have a clear idea of the performance of the catalyst. Evaluation of the catalyst in kinetic regime rather than the thermodynamic regime should be performed in order to have a clear picture on the activity of the catalysts. The optimisation of particle size to eliminate internal diffusion limitation must be determined. In order eliminate the effects of thermodynamic regime; experiments must be performed in lower temperature range from 500-600°C.

The formation of liquid products during the hydrogen production processes has to be examined to determine their effect on the overall performance of the process. The presence of certain compounds in the liquid products like aromatics responsible for carbon formation, would give an idea of the reaction mechanisms involved and steps leading to the formation of the carbon precursors. The factors responsible for formation of the carbon precursors must be indentified and steps to avoid them should be investigated. For e.g. the effect of reactor temperature steam/carbon ration, residence time and catalyst support on the formation of carbon precursors like aromatics or ethylene should be investigated. The investigation of these conditions would help in selection of operating conditions for hydrogen production from biodiesel.

The effects of wall on the reactor on the performance of process have been examined. The stainless steel contains Ni and other elements such Cr which would catalyse some reactions during hydrogen production. Likewise the presence of sand used in the reactor would also affect reactions like decomposition during hydrogen production. As a result both these important aspects need to be examined under the chosen operating conditions.

The influence of biodiesel type on hydrogen production is not fully understood. In order to investigate the effect of biodiesel type on H_2 production, use of biodiesel derived from animal fat such as beef tallow or non edible oil derived biodiesel i.e. Jatropha could be evaluated. Further the hydrogen production from model compounds like methyl palmitate or linoleate etc should be studied. The percentage of the methyl esters vary depending on the source of biodiesel. The examination of H_2 production from model compounds would provide clues to the variation in performance of biodiesel in steam reforming processes. Likewise this could also provide an insight into the reasons for carbon formation during the process. Similarly, biodiesel production using algae oil has been investigated widely in recent times and algal biodiesel could also be investigated for steam reforming. The use of algae-derived biodiesel could be essential in resolving the problems of using edible oil for biodiesel production and competition between food and non-food crops. The use of sinter resistant Ni catalyst containing Ce-Zr needs to be developed for long term H_2 production from biodiesel.

It is known that steam reforming is an energy consuming process, in order to minimize energy expenditure of H_2 production autothermal reforming must be optimised and further evaluated. Different flow arrangements of reactants and oxidant for autothermal reforming may improve the processes effectiveness and increase H_2 yield while reducing carbon formation. Other processes such as chemical looping and sorption enhanced steam reforming could be evaluated for H_2 production from biodiesel. These processes are energy efficient and improve H_2 yield, when low H_2 yield is a drawback of conventional autothermal reforming.

9. References

1. Akorede, M.F., et al., *Mitigating the anthropogenic global warming in the electric power industry*. Renewable and Sustainable Energy Reviews, 2012. **16**(5): p. 2747-2761.
2. John, H., *Global warming.* Reports on Progress in Physics, 2005. **68**(6): p. 1343.
3. Hanley, I., *Unmixed steam reforming of methane and vegetable oil for production of hydrogen rich gas*, in *Energy research Institute*. 2007, University of Leeds: Leeds. p. 194.
4. MHTRE. *Global warming*. 2014 [cited 2014 May 30]; Available from: http://www.revisescience.co.uk/2011/schools/hach/sc1air2.asp.
5. Council., N.R., *Advancing science of climate change*. 2010, National Research Council. p. 4.
6. Florides, G.A. and P. Christodoulides, *Global warming and carbon dioxide through sciences.* Environment International, 2009. **35**(2): p. 390-401.
7. Neftel, A., et al., *Evidence from polar ice cores for the increase in atmospheric CO2 in the past two centuries.* Nature, 1985. **315**(6014): p. 45-47.
8. US and IEA, *CO2 emissions from fuel coombustion* 2013, International energy agency. p. 7-142.
9. Doman, L.E., *World energy demand and economic outlook*. 2013 U.S.EIA: Washington. p. 9-19.
10. BP, *BP Energy outlook 2035*. 2014.
11. Monirul Qader Mirza, M., *Global warming and changes in the probability of occurrence of floods in Bangladesh and implications.* Global Environmental Change, 2002. **12**(2): p. 127-138.
12. Niranjan Kumar, K., et al., *On the observed variability of monsoon droughts over India.* Weather and Climate Extremes, 2013. **1**(0): p. 42-50.
13. Kharraz, J.E., et al., *Water scarcity and drought in WANA countries.* Procedia Engineering, 2012. **33**(0): p. 14-29.
14. Sanghi, A. and R. Mendelsohn, *The impacts of global warming on farmers in Brazil and India.* Global Environmental Change, 2008. **18**(4): p. 655-665.
15. Peng, S., et al., *Rice yields decline with higher night temperature from global warming.* Proceedings of the National Academy of Sciences of the United States of America, 2004. **101**(27): p. 9971-9975.
16. Walthall, C.L., J. Hatfield, P. Backlund, L. Lengnick, E. Marshall, M. Walsh, S. Adkins, M. Aillery, E.A. Ainsworth, , et al., *Climate Change and Agriculture in the United States.USDA Technical Bulletin 1935.* . 2012, U.S. Department of Agriculture,: Washington, DC. p. 186.
17. Stern, N., *The Economics of Climate Change* 2006, The Office of Climate Change: Exter United Kingdom. p. 27.
18. Wang, G., et al., *A comprehensive risk analysis of coastal zones in China.* Estuarine, Coastal and Shelf Science, 2014. **140**(0): p. 22-31.
19. Crowell, M., et al., *An Estimate of the U.S. Population Living in 100-Year Coastal Flood Hazard Areas.* Journal of Coastal Research, 2010: p. 201-211.

20. Hinrichsen, D., *Coastal Waters of the World Trends, Threats, and Strategies*. 1998, Washington DC: Island Press. 270.
21. Adam Parri, et al., *Global Sea Level Rise Scenarios for the United States National Climate Assessment*. 2012, Natioanl Oceanic and Atmospheric Administration: Sliver spring, Maryland. p. 1-29.
22. UCS, *Causes of Sea Level Rise: What the Science Tells Us*. 2013, Union of concerned scientists: Washington, DC. p. 1-7.
23. Nicholls, R.J., F.M.J. Hoozemans, and M. Marchand, *Increasing flood risk and wetland losses due to global sea-level rise: regional and global analyses.* Global Environmental Change, 1999. **9, Supplement 1**(0): p. S69-S87.
24. Parizek, B.R. and R.B. Alley, *Implications of increased Greenland surface melt under global-warming scenarios: ice-sheet simulations.* Quaternary Science Reviews, 2004. **23**(9–10): p. 1013-1027.
25. Chapman, M.R., N.J. Shackleton, and J.-C. Duplessy, *Sea surface temperature variability during the last glacial–interglacial cycle: assessing the magnitude and pattern of climate change in the North Atlantic.* Palaeogeography, Palaeoclimatology, Palaeoecology, 2000. **157**(1–2): p. 1-25.
26. Bajracharya, S.R., P.K. Mool, and B.R. Shrestha, *Impact of Climate Change on Himalayan Glaciers and Glacial Lakes Case Studies on GLOF and Associated Hazards in Nepal and Bhutan*. 2007, Kathmandu, Nepal: Quality Printers. 120.
27. Bajracharya, S.R. and P. Mool, *Glaciers, glacial lakes and glacial lake outburst floods in the Mount Everest region, Nepal.* Annals of Glaciology, 2010. **50**(53): p. 81-86.
28. Tarnocai, C., et al., *Soil organic carbon pools in the northern circumpolar permafrost region.* Global Biogeochemical Cycles, 2009. **23**(2): p. GB2023.
29. Mastny, L. *Melting of Earth's Ice Cover Reaches New High*. 2000 [cited 2014 6 June 2014]; Available from: http://www.worldwatch.org/melting-earths-ice-cover-reaches-new-high.
30. Michieka, N.M. and J.J. Fletcher, *An investigation of the role of China's urban population on coal consumption.* Energy Policy, 2012. **48**(0): p. 668-676.
31. WCES, *Steel Statistical Yearbook* 2013, Worldsteel Committee on Economic Studies: Brussel. p. 116.
32. Mellish, M.L., *International Energy Outlook*. 2013, U.S. Eenergy Information Administration: Washington. p. 67-84.
33. Awan, A.B. and Z.A. Khan, *Recent progress in renewable energy – Remedy of energy crisis in Pakistan.* Renewable and Sustainable Energy Reviews, 2014. **33**(0): p. 236-253.
34. WSA, *Crude steel production* March 2014, World steel association. p. 1.
35. McCaffrey, R. *Global Cement India-review*. in *The 2nd Global Cement India Conference and Exhibition* 2013. Mumbai, India.
36. Findler, S., *Rising Coal Use Clouds Europe's Future.* The wall street journal, 2014.
37. Barden, J.L. and M. Ford, *International Energy Outlook*. 2013, U.S. Eenergy Information Administration. p. 67-84.

38. U.S.EIA. *Dy natural gas consumption*. 2012; Available from: http://www.eia.gov/cfapps/ipdbproject/iedindex3.cfm?tid=3&pid=26&aid=2&cid=regions&syid=2008&eyid=2012&unit=BCF.
39. Metelitsa, A. and M. Leahy, *International energy outlook*. 2013, U.S. Eenergy Information Administration: Washington. p. 23-37.
40. U.S.EIA, *Country Analysis Brief: India*. 2013, U.S. Energy Information Administration: Washington.
41. U.S.EIA, *Country Analysis Brief: China*. 2014, U.S. Eenergy Information Administration.
42. Agrawal, P., *India's Petroleum Demand: Empirical Estimations and Projections for the Future* 2012, Institute of Economic Growth. p. 1-26.
43. Ashraful, A.M., et al., *Production and comparison of fuel properties, engine performance, and emission characteristics of biodiesel from various non-edible vegetable oils: A review.* Energy Conversion and Management, 2014. **80**(0): p. 202-228.
44. Rutledge, D., *Estimating long-term world coal production with logit and probit transforms.* International Journal of Coal Geology, 2011. **85**(1): p. 23-33.
45. Kreft, E. *Supreme Court Upholds EPA Ruling That Will Likely Shut Down Critical Coal Plants*. 2014; Available from: http://www.theblaze.com/stories/2014/04/29/supreme-court-upholds-epa-ruling-that-will-likely-shut-down-critical-coal-plants/.
46. Tandjaoui, M.N., et al., *The Impact of Wind Power Implantation in Transmission Systems.* Energy Procedia, 2013. **36**(0): p. 260-267.
47. Denny, E., *The economics of tidal energy.* Energy Policy, 2009. **37**(5): p. 1914-1924.
48. Li, Y., B.J. Lence, and S.M. Calisal, *An integrated model for estimating energy cost of a tidal current turbine farm.* Energy Conversion and Management, 2011. **52**(3): p. 1677-1687.
49. Ramos, V., et al., *Tidal stream energy impacts on estuarine circulation.* Energy Conversion and Management, 2014. **80**(0): p. 137-149.
50. European Parliament, C.o.t.E.U., *The promotion of the use of energy from renewable sources and amending and subsequently repealing Directives 2001/77/EC and 2003/30/EC (Text with EEA relevance)* 2009.
51. Berndes, G., M. Hoogwijk, and R. van den Broek, *The contribution of biomass in the future global energy supply: a review of 17 studies.* Biomass and Bioenergy, 2003. **25**(1): p. 1-28.
52. Agency, E.E., *Renewable Energy Road Map:Renewable energies in the 21st century: building a more sustainable future* 2007: Brusselss. p. 1-60.
53. Demirbaş, A., *Biomass resource facilities and biomass conversion processing for fuels and chemicals.* Energy Conversion and Management, 2001. **42**(11): p. 1357-1378.
54. Long, H., et al., *Biomass resources and their bioenergy potential estimation: A review.* Renewable and Sustainable Energy Reviews, 2013. **26**(0): p. 344-352.
55. McKendry, P., *Energy production from biomass (part 1): overview of biomass.* Bioresource Technology, 2002. **83**(1): p. 37-46.

56. Clifton-brown, J.C., P.F. Stampfl, and M.B. Jones, *Miscanthus biomass production for energy in Europe and its potential contribution to decreasing fossil fuel carbon emissions.* Global Change Biology, 2004. **10**(4): p. 509-518.
57. Demba Diop, et al., *Assessing the impact of biofuels production on developing countries from the point of view of Policy Coherence for Development*. 2013, The European Union's Framework Contract Commission 2011. p. 168.
58. Biradar, C.H., K.A. Subramanian, and M.G. Dastidar, *Production and fuel quality upgradation of pyrolytic bio-oil from Jatropha Curcas de-oiled seed cake.* Fuel, 2014. **119**(0): p. 81-89.
59. Shadangi, K.P. and R.K. Singh, *Thermolysis of polanga seed cake to bio-oil using semi batch reactor.* Fuel, 2012. **97**(0): p. 450-456.
60. Jang, Y.-S., et al., *Butanol production from renewable biomass by clostridia.* Bioresource Technology, 2012. **123**(0): p. 653-663.
61. Czernik, S. and A.V. Bridgwater, *Overview of Applications of Biomass Fast Pyrolysis Oil.* Energy & Fuels, 2004. **18**(2): p. 590-598.
62. IRENA, *Renewable Power Generation Costs*. 2012, International Renewable Energy Agency.
63. Silitonga, A.S., et al., *A review on prospect of Jatropha curcas for biodiesel in Indonesia.* Renewable and Sustainable Energy Reviews, 2011. **15**(8): p. 3733-3756.
64. Tolbert, V.R. and L.L. Wright, *Environmental enhancement of U.S. biomass crop technologies: research results to date.* Biomass and Bioenergy, 1998. **15**(1): p. 93-100.
65. Lemus, R., et al., *Biomass yield and quality of 20 switchgrass populations in southern Iowa, USA.* Biomass and Bioenergy, 2002. **23**(6): p. 433-442.
66. Staubmann, R., et al., *Biogas production fromJatropha curcas press-cake.* Applied Biochemistry and Biotechnology, 1997. **63-65**(1): p. 457-467.
67. Huerga, I.R., et al., *Biodiesel production from Jatropha curcas: Integrated process optimization.* Energy Conversion and Management, 2014. **80**(0): p. 1-9.
68. Pandey, V.L. and A. Chaubal, *Comprehending household cooking energy choice in rural India.* Biomass and Bioenergy, 2011. **35**(11): p. 4724-4731.
69. Romijn, H., R. Raven, and I. de Visser, *Biomass energy experiments in rural India: Insights from learning-based development approaches and lessons for Strategic Niche Management.* Environmental Science & Policy, 2010. **13**(4): p. 326-338.
70. Niu, H., et al., *Rural household energy consumption and its implications for eco-environments in NW China: A case study.* Renewable Energy, 2014. **65**(0): p. 137-145.
71. Larminie, J. and A. Dicks, *Fuel Cell Systems Explained (2nd Edition)*, John Wiley & Sons.
72. Services, E.G.T., *Fuel cells Handbook*. 2004, EG&G Technical Services: Morgantown, West Virginia. p. 427.
73. James Larmine, A.d., *Fuel cell systems explained.* Wiley, 2001: p. 1-35.
74. Singhal, S.a.K.K., *High temperature solid oxide fuel cells: Fundamentals design and applications.* Elsevier advanced technology, 2003: p. 405.

75. Wang, Y., et al., *A review of polymer electrolyte membrane fuel cells: Technology, applications, and needs on fundamental research.* Applied Energy, 2011. **88**(4): p. 981-1007.
76. Kirubakaran, A., S. Jain, and R.K. Nema, *A review on fuel cell technologies and power electronic interface.* Renewable and Sustainable Energy Reviews, 2009. **13**(9): p. 2430-2440.
77. Kandepu, R., et al., *Modeling and control of a SOFC-GT-based autonomous power system.* Energy, 2007. **32**(4): p. 406-417.
78. Pérez, L.C., et al., *Effect of fuel utilization on the carbon monoxide poisoning dynamics of Polymer Electrolyte Membrane Fuel Cells.* Journal of Power Sources, 2014. **258**(0): p. 122-128.
79. Singhal, S.C. and K. Kendall, *Introduction to SOFCs*, in *High Temperature and Solid Oxide Fuel Cells*, C.S. Subhash and K. Kevin, Editors. 2003, Elsevier Science: Amsterdam. p. 1-22.
80. Karatzas, X., et al., *Autothermal reforming of low-sulfur diesel over bimetallic RhPt supported on Al2O3, CeO2–ZrO2, SiO2 and TiO2.* Applied Catalysis B: Environmental, 2011. **106**(3–4): p. 476-487.
81. Gould, B.D., A.R. Tadd, and J.W. Schwank, *Nickel-catalyzed autothermal reforming of jet fuel surrogates: n-Dodecane, tetralin, and their mixture.* Journal of Power Sources, 2007. **164**(1): p. 344-350.
82. USDOE, *Fuel cell hand book.* 7 ed. 2004, West Virginia, United States: EG&G Technical Services, Inc. 1-427.
83. Nahar, G., *Biodiesel Formulations as Fuels for Micro-tubular Solid Oxide Fuel Cells.*, in *Chemical Engineering*. 2007, University of Birmingham: Birmingahm. p. 112.
84. Mizutani, Y., et al., *From rare earth doped zirconia to 1 kW solid oxide fuel cell system.* Journal of Alloys and Compounds, 2006. **408-412**: p. 518-524.
85. Edwards, P.P., et al., *Hydrogen and fuel cells: Towards a sustainable energy future.* Energy Policy, 2008. **36**(12): p. 4356-4362.
86. Clark, W.W., et al., *Hydrogen energy stations: along the roadside to the hydrogen economy.* Utilities Policy, 2005. **13**(1): p. 41-50.
87. Knight, E., *Optimisation of unmixed steam reforming*, in *Energy research Institute*. 2009, University of Leeds: Leeds. p. 217.
88. Wang, Y.D., et al., *An experimental investigation of the performance and gaseous exhaust emissions of a diesel engine using blends of a vegetable oil.* Applied Thermal Engineering, 2006. **26**(14–15): p. 1684-1691.
89. Knothe, G., *Historical Perspectives on Vegetable Oil-Based Diesel Fuels* Inform, 2001. **12**: p. 1103-1107.
90. Reddy, B. and A. Khan, *Nanosized CeO2–SiO2, CeO2–TiO2, and CeO2–ZrO2 Mixed Oxides: Influence of Supporting Oxide on Thermal Stability and Oxygen Storage Properties of Ceria.* Catalysis Surveys from Asia, 2005. **9**(3): p. 155-171.
91. Jones, S. and C.L. Peterson, *Using Unmodified Vegetable Oils as a Diesel Fuel Extender*, in *Bioenergy* 2002: Boise, Idaho, USA.
92. Demirbaş, A., *Fuel properties and calculation of higher heating values of vegetable oils.* Fuel, 1998. **77**(9–10): p. 1117-1120.

93. Hazar, H. and H. Aydin, *Performance and emission evaluation of a CI engine fueled with preheated raw rapeseed oil (RRO)–diesel blends.* Applied Energy, 2010. **87**(3): p. 786-790.
94. Prasad, L. and A. Agrawal, *Experimental Investigation of Performance of Diesel Engine Working On Diesel and Neem Oil Blends.* Journal of Mechanical and Civil Engineering (2012. **1**(4): p. 48-51.
95. Agarwal, A.K., *Biofuels (alcohols and biodiesel) applications as fuels for internal combustion engines.* Progress in Energy and Combustion Science, 2007. **33**(3): p. 233-271.
96. manufacturers, E. and association, *Use of Raw Vegetable Oil or Animal Fats in Diesel Engines* 2006: Chicago, Illinois ,USA.
97. Harwood, H., *Oleochemicals as a fuel: Mechanical and economic feasibility.* Journal of the American Oil Chemists' Society, 1984. **61**(2): p. 315-324.
98. Agarwal, A.K. and L.M. Das, *Biodiesel Development and Characterization for Use as a Fuel in Compression Ignition Engines.* Journal of Engineering for Gas Turbines and Power, 2000. **123**(2): p. 440-447.
99. Nwafor, O.M.I., *Emission characteristics of diesel engine running on vegetable oil with elevated fuel inlet temperature.* Biomass and Bioenergy, 2004. **27**(5): p. 507-511.
100. Nwafor, O.M.I. and G. Rice, *Performance of rapeseed oil blends in a diesel engine.* Applied Energy, 1996. **54**(4): p. 345-354.
101. Sisarwal, V. and A.C. Tiwari, *Experimental Investigation of Effect of Straight Vegetable Oil Fuel on Engine Performance Parameters* International Journal of Engineering Research and Applications, 2013. **3**(1): p. 12091-2094.
102. Samuel T. Jones, C.L.P., Joseph C. Thompson. *Used Vegetable Oil Fuel Blend Comparisons Using Injector Coking in a DI Diesel Engine.* . in *ASAE Meeting Paper* 2001. Sacramento, California, USA ASAE.
103. Saravanan, N., G. Nagarajan, and S. Puhan, *Experimental investigation on a DI diesel engine fuelled with Madhuca Indica ester and diesel blend.* Biomass and Bioenergy, 2010. **34**(6): p. 838-843.
104. Atabani, A.E., et al., *Non-edible vegetable oils: A critical evaluation of oil extraction, fatty acid compositions, biodiesel production, characteristics, engine performance and emissions production.* Renewable and Sustainable Energy Reviews, 2013. **18**(0): p. 211-245.
105. Kumar, N., Varun, and S.R. Chauhan, *Performance and emission characteristics of biodiesel from different origins: A review.* Renewable and Sustainable Energy Reviews, 2013. **21**(0): p. 633-658.
106. Agarwal, A.K. and A. Dhar, *Experimental investigations of performance, emission and combustion characteristics of Karanja oil blends fuelled DICI engine.* Renewable Energy, 2013. **52**(0): p. 283-291.
107. Agarwal, A.K. and K. Rajamanoharan, *Experimental investigations of performance and emissions of Karanja oil and its blends in a single cylinder agricultural diesel engine.* Applied Energy, 2009. **86**(1): p. 106-112.
108. Agarwal, D. and A.K. Agarwal, *Performance and emissions characteristics of Jatropha oil (preheated and blends) in a direct injection compression ignition engine.* Applied Thermal Engineering, 2007. **27**(13): p. 2314-2323.

109. Sahoo, P.K., et al., *Biodiesel development from high acid value polanga seed oil and performance evaluation in a CI engine.* Fuel, 2007. **86**(3): p. 448-454.
110. Chavanne, C.G., *Procedures for the transformation of vegetable oils for their use as fuel*. 1937: Belgium.
111. Mittelbach, M. and C. Remschmidt, *Biodiesel: The Comprehensive Handbook*. 2004.
112. Amezaga, J.M., Boyes, S.L. and Harrison, J.A. , *Biofuels Policy in the European Union* in *7th International Biofuels Conference*. 2010, Indian Oil Corporation Ltd. and International Union for Conservation of Nature New Delhi. p. 1-10.
113. board, E.b. *European biodiesel board*. 2014; Available from: www.ebb-eu.org/stats.php.
114. Sun, J., J.A. Caton, and T.J. Jacobs, *Oxides of nitrogen emissions from biodiesel-fuelled diesel engines.* Progress in Energy and Combustion Science, 2010. **36**(6): p. 677-695.
115. Lapuerta, M., O. Armas, and J. Rodríguez-Fernández, *Effect of biodiesel fuels on diesel engine emissions.* Progress in Energy and Combustion Science, 2008. **34**(2): p. 198-223.
116. Murugesan, A., et al., *Bio-diesel as an alternative fuel for diesel engines—A review.* Renewable and Sustainable Energy Reviews, 2009. **13**(3): p. 653-662.
117. Basha, S.A., K.R. Gopal, and S. Jebaraj, *A review on biodiesel production, combustion, emissions and performance.* Renewable and Sustainable Energy Reviews, 2009. **13**(6–7): p. 1628-1634.
118. Demirbas, A., *Relationships derived from physical properties of vegetable oil and biodiesel fuels.* Fuel, 2008. **87**(8–9): p. 1743-1748.
119. Balat, M. and H. Balat, *A critical review of bio-diesel as a vehicular fuel.* Energy Conversion and Management, 2008. **49**(10): p. 2727-2741.
120. Dhar, A. and A.K. Agarwal, *Performance, emissions and combustion characteristics of Karanja biodiesel in a transportation engine.* Fuel, 2014. **119**(0): p. 70-80.
121. Dhar, A., R. Kevin, and A.K. Agarwal, *Production of biodiesel from high-FFA neem oil and its performance, emission and combustion characterization in a single cylinder DICI engine.* Fuel Processing Technology, 2012. **97**(0): p. 118-129.
122. Jindal, S., et al., *Experimental investigation of the effect of compression ratio and injection pressure in a direct injection diesel engine running on Jatropha methyl ester.* Applied Thermal Engineering, 2010. **30**(5): p. 442-448.
123. Kalligeros, S., et al., *An investigation of using biodiesel/marine diesel blends on the performance of a stationary diesel engine.* Biomass and Bioenergy, 2003. **24**(2): p. 141-149.
124. Misra, R.D. and M.S. Murthy. *Comparative performance evaluation of karanja vegetable oil and karanja biodiesel blends with diesel in C.I. engine*. in *Clean Energy and Technology (CET), 2011 IEEE First Conference on*. 2011.
125. Shi, X., et al., *Emission characteristics using methyl soyate–ethanol–diesel fuel blends on a diesel engine.* Fuel, 2005. **84**(12–13): p. 1543-1549.

126. Lapuerta, M., J. Rodríguez-Fernández, and J.R. Agudelo, *Diesel particulate emissions from used cooking oil biodiesel.* Bioresource Technology, 2008. **99**(4): p. 731-740.
127. Agarwal, A.K., T. Gupta, and A. Kothari, *Particulate emissions from biodiesel vs diesel fuelled compression ignition engine.* Renewable and Sustainable Energy Reviews, 2011. **15**(6): p. 3278-3300.
128. Pinzi, S., et al., *The Ideal Vegetable Oil-based Biodiesel Composition: A Review of Social, Economical and Technical Implications.* Energy & Fuels, 2009. **23**(5): p. 2325-2341.
129. Knothe, G., A.C. Matheaus, and T.W. Ryan Iii, *Cetane numbers of branched and straight-chain fatty esters determined in an ignition quality tester☆.* Fuel, 2003. **82**(8): p. 971-975.
130. Knothe, G., C.A. Sharp, and T.W. Ryan, *Exhaust Emissions of Biodiesel, Petrodiesel, Neat Methyl Esters, and Alkanes in a New Technology Engine†.* Energy & Fuels, 2005. **20**(1): p. 403-408.
131. Sarathy, S.M., et al., *A comparison of saturated and unsaturated C4 fatty acid methyl esters in an opposed flow diffusion flame and a jet stirred reactor.* Proceedings of the Combustion Institute, 2007. **31**(1): p. 1015-1022.
132. Marquevich, M., F. Medina, and D. Montané, *Hydrogen production via steam reforming of sunflower oil over Ni/Al catalysts from hydrotalcite materials.* Catalysis Communications, 2001. **2**(3–4): p. 119-124.
133. Mittelbach, M. and H. Enzelsberger, *Transesterification of heated rapeseed oil for extending diesel fuel.* Journal of the American Oil Chemists' Society, 1999. **76**(5): p. 545-550.
134. Lin, J., C.W. Babbitt, and T.A. Trabold, *Life cycle assessment integrated with thermodynamic analysis of bio-fuel options for solid oxide fuel cells.* Bioresource Technology, 2013. **128**(0): p. 495-504.
135. Xuan, J., et al., *A review of biomass-derived fuel processors for fuel cell systems.* Renewable and Sustainable Energy Reviews, 2009. **13**(6–7): p. 1301-1313.
136. Kraaij, G.J., et al., *Biodiesel fuel processor for APU applications.* International Journal of Hydrogen Energy, 2009. **34**(10): p. 4495-4499.
137. Martin, S. and A. Wörner, *On-board reforming of biodiesel and bioethanol for high temperature PEM fuel cells: Comparison of autothermal reforming and steam reforming.* Journal of Power Sources, 2011. **196**(6): p. 3163-3171.
138. Nahar, G.A., *Hydrogen rich gas production by the autothermal reforming of biodiesel (FAME) for utilization in the solid-oxide fuel cells: A thermodynamic analysis.* International Journal of Hydrogen Energy, 2010. **35**(17): p. 8891-8911.
139. Lin, J., et al., *Bio-fuel reforming for solid oxide fuel cell applications. Part 2: Biodiesel.* International Journal of Hydrogen Energy, 2014. **39**(1): p. 183-195.
140. Shiratori, Y., et al., *Paper-structured catalyst for the steam reforming of biodiesel fuel.* International Journal of Hydrogen Energy, 2013. **38**(26): p. 11278-11287.
141. Nahar, G. and K. Kendall, *Biodiesel formulations as fuel for internally reforming solid oxide fuel cell.* Fuel Processing Technology, 2011. **92**(7): p. 1345-1354.
142. Quang-Tuyen, T., Y. Shiratori, and K. Sasaki, *Feasibility of palm-biodiesel fuel for a direct internal reforming solid oxide fuel cell.* International Journal of Energy Research, 2013. **37**(6): p. 609-616.

143. Zhou, Z.F., et al., *Direct oxidation of waste vegetable oil in solid-oxide fuel cells.* Journal of Power Sources, 2007. **171**(2): p. 856-860.
144. N. Abatzoglou, C. Fauteux-Lefebvre, and N. Braidy, *Biodiesel reforming with a NiAl2O4/Al2O3-YSZ catalyst for the production of renewable SOFC fuel.* WIT Transactions on Ecology and the Environment, 2011. **143**: p. 145-154.
145. Sgroi, M., et al., *BIOFEAT: Biodiesel fuel processor for a vehicle fuel cell auxiliary power unit: Study of the feed system.* Journal of Power Sources, 2005. **149**(0): p. 8-14.
146. Specchia, S., et al., *Conceptual design and selection of a biodiesel fuel processor for a vehicle fuel cell auxiliary power unit.* Journal of Power Sources, 2005. **145**(2): p. 683-690.
147. Swami, S.M. and M.A. Abraham, *Integrated Catalytic Process for Conversion of Biomass to Hydrogen.* Energy & Fuels, 2006. **20**(6): p. 2616-2622.
148. Ospinal-Jimenez, M., *Hydrogen production study usingautothermal reforming of biodiesel and other hydrocarbons for fuel cell applications*, in *Chemical Engineering*. 2006, Uiversity of Puerto Rico. p. 126.
149. Colucci, J.A., *Hydrogen Production Using Autothermal Reforming of Biodiesel and Other Hydrocarbons for Fuel Cell Applications.* ASME Conference Proceedings, 2006. **2006**(47454): p. 483-484.
150. Siefert, N.S., et al., *Operation of a solid oxide fuel cell on a reformed FAME mixture.* Biomass and Bioenergy, 2012. **47**(0): p. 362-371.
151. Pena, M.A., J.P. Gómez, and J.L.G. Fierro, *New catalytic routes for syngas and hydrogen production.* Applied Catalysis A: General, 1996. **144**(1-2): p. 7-57.
152. Leite, L., E. Benazzi, and N. Marchal-George, *Hydrocracking of phenanthrene over bifunctional Pt catalysts.* Catalysis Today, 2001. **65**(2-4): p. 241-247.
153. Roussel, M., et al., *Mechanisms of n-decane hydrocracking on a sulfided NiW on silica-alumina catalyst.* Journal of Catalysis, 2003. **218**(2): p. 427-437.
154. Guo, X.-j., et al., *Preparation of CuO/ZnO/Al2O3 catalysts for methanol synthesis using parallel-slurry-mixing method.* Journal of Fuel Chemistry and Technology, 2007. **35**(3): p. 329-333.
155. Kojima, R., et al., *Cesium-promoted rhenium catalysts supported on alumina for ammonia synthesis.* Applied Catalysis A: General, 2003. **246**(2): p. 311-322.
156. Liu, Y., et al., *Fischer-Tropsch synthesis in slurry-phase reactors over Mn- and Zr-modified Co/SiO2 catalysts.* Fuel Processing Technology. **90**(7-8): p. 901-908.
157. Ahmed, S. and M. Krumpelt, *Hydrogen from hydrocarbon fuels for fuel cells.* International Journal of Hydrogen Energy, 2001. **26**(4): p. 291-301.
158. Harrison, D.P., *Sorption-Enhanced Hydrogen Production: A Review.* Industrial & Engineering Chemistry Research, 2008. **47**(17): p. 6486-6501.
159. *Hot spot elimination in partial oxidation of hydrocarbons.* Focus on Catalysts, 2007. **2007**(10): p. 7-7.
160. De Groote, A.M. and G.F. Froment, *The role of coke formation in catalytic partial oxidation for synthesis gas production.* Catalysis Today, 1997. **37**(3): p. 309-329.
161. Huang, T.-j. and S.-W. Wang, *Hydrogen production via partial oxidation of methanol over copper-zinc catalysts.* Applied Catalysis, 1986. **24**(1-2): p. 287-297.

162. Ersoz, A., et al., *Autothermal reforming as a hydrocarbon fuel processing option for PEM fuel cell.* Journal of Power Sources, 2003. **118**(1-2): p. 384-392.
163. Ersoz, A., H. Olgun, and S. Ozdogan, *Reforming options for hydrogen production from fossil fuels for PEM fuel cells.* Journal of Power Sources, 2006. **154**(1): p. 67-73.
164. Freni, S., G. Calogero, and S. Cavallaro, *Hydrogen production from methane through catalytic partial oxidation reactions.* Journal of Power Sources, 2000. **87**(1-2): p. 28-38.
165. Cheekatamarla, P.K. and A.M. Lane, *Catalytic autothermal reforming of diesel fuel for hydrogen generation in fuel cells: I. Activity tests and sulfur poisoning.* Journal of Power Sources, 2005. **152**: p. 256-263.
166. Kang, I. and J. Bae, *Autothermal reforming study of diesel for fuel cell application.* Journal of Power Sources, 2006. **159**(2): p. 1283-1290.
167. Joensen, F. and J.R. Rostrup-Nielsen, *Conversion of hydrocarbons and alcohols for fuel cells.* Journal of Power Sources, 2002. **105**(2): p. 195-201.
168. Faungnawakij, K., R. Kikuchi, and K. Eguchi, *Thermodynamic analysis of carbon formation boundary and reforming performance for steam reforming of dimethyl ether.* Journal of Power Sources, 2007. **164**(1): p. 73-79.
169. Faungnawakij, K., et al., *Influence of solid–acid catalysts on steam reforming and hydrolysis of dimethyl ether for hydrogen production.* Applied Catalysis A: General, 2006. **304**(0): p. 40-48.
170. Zhang, B., et al., *Hydrogen production by steam reforming of ethanol over an Ir/CeO2 catalyst: Reaction mechanism and stability of the catalyst.* International Journal of Hydrogen Energy, 2008. **33**(16): p. 4377-4386.
171. Zhang, B., et al., *Hydrogen production from steam reforming of ethanol and glycerol over ceria-supported metal catalysts.* International Journal of Hydrogen Energy, 2007. **32**(13): p. 2367-2373.
172. Marquevich, M., R. Coll, and D. Montané, *Steam Reforming of Sunflower Oil for Hydrogen Production.* Industrial & Engineering Chemistry Research, 2000. **39**(7): p. 2140-2147.
173. Marquevich, M., et al., *Hydrogen Production by Steam Reforming of Vegetable Oils Using Nickel-Based Catalysts.* Industrial & Engineering Chemistry Research, 2001. **40**(22): p. 4757-4766.
174. Pimenidou, P., et al., *Chemical looping reforming of waste cooking oil in packed bed reactor.* Bioresource Technology, 2010. **101**(16): p. 6389-6397.
175. Kumar, R.V., R.K. Lyon, and J.A. Cole, *Unmixed Reforming: A Novel Autothermal Cyclic Steam Reforming Process*

Advances in Hydrogen Energy, C.E. Grégoire Padró and F. Lau, Editors. 2002, Springer US. p. 31-45.
176. Holladay, J.D., et al., *An overview of hydrogen production technologies.* Catalysis Today, 2009. **139**(4): p. 244-260.
177. Faur Ghenciu, A., *Review of fuel processing catalysts for hydrogen production in PEM fuel cell systems.* Current Opinion in Solid State and Materials Science, 2002. **6**(5): p. 389-399.

178. Giannakeas, N., *Development of Oxygen Transfer Materials for Chemical Looping Reforming Processes*, in *Energy Resources Institute*. 2012, The University of Leeds: Leeds. p. 250.
179. Marquevich, M., R. Coll, and D. Montane, *Steam Reforming of Sunflower Oil for Hydrogen Production.* . Industrial & Engineering Chemistry Research, 2000. **39**(7): p. 2632-2632.
180. French, R.J. and S. Czernik, *Hydrogen production by steam reforming of waste vegetable oils.* Prepr. Pap.-Am. Chem. Soc., Div. Fuel Chem, 2003. **48**(2): p. 592.
181. Pimenidou, P., et al., *High purity H2 by sorption-enhanced chemical looping reforming of waste cooking oil in a packed bed reactor.* Bioresource Technology, 2010. **101**(23): p. 9279-9286.
182. Alberton, A.L., M.M.V.M. Souza, and M. Schmal, *Carbon formation and its influence on ethanol steam reforming over Ni/Al2O3 catalysts.* Catalysis Today, 2007. **123**(1-4): p. 257-264.
183. Chen, H., et al., *A comparative study on hydrogen production from steam-glycerol reforming: thermodynamics and experimental.* Renewable Energy, 2011. **36**(2): p. 779-788.
184. Dou, B., et al., *Hydrogen production by sorption-enhanced steam reforming of glycerol.* Bioresource Technology, 2009. **100**(14): p. 3540-3547.
185. Dou, B., et al., *Steam reforming of crude glycerol with in situ CO2 sorption.* Bioresource Technology, 2010. **101**(7): p. 2436-2442.
186. He, L., et al., *Towards efficient hydrogen production from glycerol by sorption enhanced steam reforming.* Energy & Environmental Science, 2010. **3**(8): p. 1046-1056.
187. Hu, X. and G. Lu, *Comparative study of alumina-supported transition metal catalysts for hydrogen generation by steam reforming of acetic acid.* Applied Catalysis B: Environmental, 2010. **99**(1-2): p. 289-297.
188. Trovarelli, A., et al., *The utilization of ceria in industrial catalysis.* Catalysis Today, 1999. **50**(2): p. 353-367.
189. Lahaye, J., et al., *Influence of cerium oxide on the formation and oxidation of soot.* Combustion and Flame, 1996. **104**(1–2): p. 199-207.
190. Matatov-Meytal, Y.I. and M. Sheintuch, *Catalytic Abatement of Water Pollutants.* Industrial & Engineering Chemistry Research, 1998. **37**(2): p. 309-326.
191. Murray, E.P., T. Tsai, and S.A. Barnett, *A direct-methane fuel cell with a ceria-based anode.* Nature, 1999. **400**(6745): p. 649-651.
192. Scott L. Swartz, D., et al., *Fuel processing catalysts based on nanoscale ceria.* Fuel Cells Bulletin, 2001. **4**(30): p. 7-10.
193. Zhou, G. and R.J. Gorte, *Thermodynamic Investigation of the Redox Properties for Ceria−Hafnia, Ceria−Terbia, and Ceria−Praseodymia Solid Solutions.* The Journal of Physical Chemistry B, 2008. **112**(32): p. 9869-9875.
194. Bernardo, C.A., I. Alstrup, and J.R. Rostrup-Nielsen, *Carbon deposition and methane steam reforming on silica-supported Ni□Cu catalysts.* Journal of Catalysis, 1985. **96**(2): p. 517-534.

195. Thormann, J., et al., *Steam reforming of hexadecane over a Rh/CeO2 catalyst in microchannels: Experimental and numerical investigation.* International Journal of Hydrogen Energy, 2009. **34**(12): p. 5108-5120.
196. Sato, K., et al., *Oxidative reforming of n-C4H10 triggered at ambient temperature over reduced Ni/CeO2.* Catalysis Communications, 2009. **10**(11): p. 1478-1481.
197. Swartz, S.L., et al., *Hydrogen production from E85 fuel with ceria-based catalysts.* Journal of Power Sources, 2009. **188**(2): p. 515-520.
198. Laosiripojana, N., et al., *Role and advantages of H2S in catalytic steam reforming over nanoscale CeO2-based catalysts.* Journal of Catalysis, 2010. **276**(1): p. 6-15.
199. Laosiripojana, N. and S. Assabumrungrat, *Hydrogen production from steam and autothermal reforming of LPG over high surface area ceria.* Journal of Power Sources, 2006. **158**(2): p. 1348-1357.
200. Laosiripojana, N. and S. Assabumrungrat, *Catalytic dry reforming of methane over high surface area ceria.* Applied Catalysis B: Environmental, 2005. **60**(1-2): p. 107-116.
201. Udani, P.P.C., et al., *Steam reforming and oxidative steam reforming of methanol over CuO-CeO2 catalysts.* International Journal of Hydrogen Energy, 2009. **34**(18): p. 7648-7655.
202. Zhang, B., et al., *Steam reforming of bio-ethanol for the production of hydrogen over ceria-supported Co, Ir and Ni catalysts.* Catalysis Communications, 2006. **7**(6): p. 367-372.
203. Mizuno, T., et al., *Effect of support on catalytic properties of Rh catalysts for steam reforming of 2-propanol.* International Journal of Hydrogen Energy, 2003. **28**(12): p. 1393-1399.
204. Kašpar, J., P. Fornasiero, and N. Hickey, *Automotive catalytic converters: current status and some perspectives.* Catalysis Today, 2003. **77**(4): p. 419-449.
205. Laosiripojana, N. and S. Assabumrungrat, *Methane steam reforming over Ni/Ce-ZrO2 catalyst: Influences of Ce-ZrO2 support on reactivity, resistance toward carbon formation, and intrinsic reaction kinetics.* Applied Catalysis A: General, 2005. **290**(1-2): p. 200-211.
206. Laosiripojana, N., D. Chadwick, and S. Assabumrungrat, *Effect of high surface area CeO2 and Ce-ZrO2 supports over Ni catalyst on CH4 reforming with H2O in the presence of O2, H2, and CO2.* Chemical Engineering Journal, 2008. **138**(1-3): p. 264-273.
207. Aneggi, E., et al., *Insights into the redox properties of ceria-based oxides and their implications in catalysis.* Journal of Alloys and Compounds, 2006. **408-412**: p. 1096-1102.
208. Liang, Q., et al., *Role of Surface Area in Oxygen Storage Capacity of Ceria–Zirconia as Soot Combustion Catalyst.* Catalysis Letters, 2007. **119**(3-4): p. 265-270.
209. Mamontov, E. and T. Egami, *Structural defects in a nano-scale powder of CeO2 studied by pulsed neutron diffraction.* Journal of Physics and Chemistry of Solids, 2000. **61**(8): p. 1345-1356.
210. Bernal, S., et al., *Some recent results on metal/support interaction effects in NM/CeO2 (NM: noble metal) catalysts.* Catalysis Today, 1999. **50**(2): p. 175-206.

211. Nagai, Y., et al., *X-ray absorption fine structure analysis of local structure of CeO2–ZrO2 mixed oxides with the same composition ratio (Ce/Zr=1).* Catalysis Today, 2002. **74**(3–4): p. 225-234.
212. Roh, H.-S., et al., *Highly active and stable Ni/Ce–ZrO2 catalyst for H2 production from methane.* Journal of Molecular Catalysis A: Chemical, 2002. **181**(1–2): p. 137-142.
213. Lemaux, S., et al., *Understanding of Enhanced Oxygen Storage Capacity in Ce0.5Zr0.5O2: The Presence of an Anharmonic Pair Distribution Function in the Zr−O2 Subshell as Analyzed by XAFS Spectroscopy.* The Journal of Physical Chemistry B, 2001. **105**(21): p. 4810-4815.
214. Fornasiero, P., et al., *Relationships between Structural/Textural Properties and Redox Behavior in Ce0.6Zr0.4O2 Mixed Oxides.* Journal of Catalysis, 1999. **187**(1): p. 177-185.
215. Vlaic, G., et al., *Relationship between the Zirconia-Promoted Reduction in the Rh-Loaded Ce0.5Zr0.5O2Mixed Oxide and the Zr-O Local Structure.* Journal of Catalysis, 1997. **168**(2): p. 386-392.
216. Dong, W.-S., et al., *Methane reforming over Ni/Ce-ZrO2 catalysts: effect of nickel content.* Applied Catalysis A: General, 2002. **226**(1–2): p. 63-72.
217. Roh, H.-S., et al., *Highly stable Ni catalyst supported on Ce–ZrO2 for oxy-steam reforming of methane.* Catalysis Letters, 2001. **74**(1): p. 31-36.
218. Fan, J., et al., *Influence of the oxidative/reductive treatments on the activity of Pt/Ce0.67Zr0.33O2 catalyst.* Applied Surface Science, 2005. **245**(1–4): p. 162-171.
219. Wu, X., et al., *Effect of preparation methods on the structure and redox behavior of platinum–ceria–zirconia catalysts.* Chemical Engineering Journal, 2005. **109**(1–3): p. 133-139.
220. Fornasiero, P., et al., *Modification of the Redox Behaviour of CeO2Induced by Structural Doping with ZrO2.* Journal of Catalysis, 1996. **164**(1): p. 173-183.
221. Trovarelli, A., et al., *Nanophase Fluorite-Structured CeO2-ZrO2Catalysts Prepared by High-Energy Mechanical Milling.* Journal of Catalysis, 1997. **169**(2): p. 490-502.
222. Trimm, D.L., *Catalysts for the control of coking during steam reforming.* Catalysis Today, 1999. **49**(1-3): p. 3-10.
223. Trimm, D.L., *Coke formation and minimisation during steam reforming reactions.* Catalysis Today, 1997. **37**(3): p. 233-238.
224. Mariño, F., et al., *Cu-Ni-K/γ-Al2O3 supported catalysts for ethanol steam reforming: Formation of hydrotalcite-type compounds as a result of metal–support interaction.* Applied Catalysis A: General, 2003. **238**(1): p. 41-54.
225. Zhang, Y., et al., *Potassium catalytic hydrogen production in sorption enhanced gasification of biomass with steam.* International Journal of Hydrogen Energy, 2014. **39**(9): p. 4234-4243.
226. Alstrup, I., et al., *Promotion of steam reforming catalysts*, in *Studies in Surface Science and Catalysis*, D.S.F.F.A.V. A. Parmaliana and A. F, Editors. 1998, Elsevier. p. 5-14.
227. Pengpanich, S., et al., *iso-Octane partial oxidation over Ni-Sn/Ce0.75Zr0.25O2 catalysts.* Catalysis Today, 2008. **136**(3–4): p. 214-221.

228. Espinal, R., et al., *Cobalt hydrotalcites as catalysts for bioethanol steam reforming. The promoting effect of potassium on catalyst activity and long-term stability*. Applied Catalysis B: Environmental, 2012. **127**(0): p. 59-67.
229. Iwasa, N., T. Yamane, and M. Arai, *Influence of alkali metal modification and reaction conditions on the catalytic activity and stability of Ni containing smectite-type material for steam reforming of acetic acid.* International Journal of Hydrogen Energy, 2011. **36**(10): p. 5904-5911.
230. Yu, X., et al., *Hydrogen production from steam reforming of kerosene over Ni–La and Ni–La–K/cordierite catalysts.* Fuel, 2006. **85**(12–13): p. 1708-1713.
231. Jain, S., M.P. Sharma, and S. Rajvanshi, *Acid base catalyzed transesterification kinetics of waste cooking oil.* Fuel Processing Technology, 2011. **92**(1): p. 32-38.
232. Bloom, R., *The autothermal reforming of biodiesel*, in *School of Process, Environmental and Material Engineering*. 2013, University of Leeds: Leeds. p. 65.
233. Sing, K.S.W., *Reporting physisorption for gas solid systems*. 1982, International union of pure and applied chemistry: Uxbridge. p. 2202-2218.
234. Lynch, j., *Physico-chemical analysis of industrail catlysts:A practical guide to chracterisation*. 2003, Paris: Institut Francais DU Petrole. 305.
235. Anderson, J.R. and K.C. Pratt., *Introduction to characterization and testing of catalysts* 1985, Sydney: Orlando Academic Press
236. Quantachrome, *Physisorption methods and techniques*. 2005, Ountachrome instruments
237. Quantachrome, *An Introduction to calculation methods for surface area and pore size from gas sorption data*. 2005, Ountachrome instruments
238. Naumov, S., *Hysteresis Phenomena in Mesoporous Materials*, in *Physics and earth sciences*. 2009, Universit¨at Leipzig: Leipzig. p. 95.
239. California, U.o. *UCSB X-ray Basics*. 2014; Available from: http://www.mrl.ucsb.edu/centralfacilities/x-ray/basics.
240. McCusker, L.B., et al., *Rietveld refinement guidelines.* Journal of Applied Crystallography, 1999. **32**(1): p. 36-50.
241. Hoekman, S.K., et al., *Review of biodiesel composition, properties, and specifications.* Renewable and Sustainable Energy Reviews, 2012. **16**(1): p. 143-169.
242. Wang, R., et al., *Biodiesel preparation, optimization, and fuel properties from non-edible feedstock, Datura stramonium L.* Fuel, 2012. **91**(1): p. 182-186.
243. Parikh, J., S.A. Channiwala, and G.K. Ghosal, *A correlation for calculating HHV from proximate analysis of solid fuels.* Fuel, 2005. **84**(5): p. 487-494.
244. J. Haber', J.H.Block, and B. Delmon, *Manual of methods and procedures for catalyst characterization.* Journal of Pure and Applied Chemistry, 1995. **67**: p. 1267-1306.
245. Roh, H.-S., Y. Wang, and D. King, *Selective Production of H₂ from Ethanol at Low Temperatures over Rh/ZrO₂–CeO₂ Catalysts.* Topics in Catalysis, 2008. **49**(1): p. 32-37.

246. Chen, H., et al., *A novel mesostructured alumina–ceria–zirconia tri-component nanocomposite with high thermal stability and its three-way catalysis.* Microporous and Mesoporous Materials, 2011. **143**(2–3): p. 368-374.
247. Aasberg-Petersen, K., et al., *Technologies for large-scale gas conversion.* Applied Catalysis A: General, 2001. **221**(1-2): p. 379-387.
248. Sukonket, T., et al., *Influence of the Catalyst Preparation Method, Surfactant Amount, and Steam on CO2 Reforming of CH4 over 5Ni/Ce0.6Zr0.4O2 Catalysts.* Energy & Fuels, 2011. **25**(3): p. 864-877.
249. Xu, L., H. Song, and L. Chou, *Mesoporous nanocrystalline ceria–zirconia solid solutions supported nickel based catalysts for CO2 reforming of CH4.* International Journal of Hydrogen Energy, 2012. **37**(23): p. 18001-18020.
250. Biswas, P. and D. Kunzru, *Steam reforming of ethanol for production of hydrogen over Ni/CeO–ZrO catalyst: Effect of support and metal loading.* International Journal of Hydrogen Energy, 2007. **32**(8): p. 969-980.
251. Dantas, S.C., et al., *Effect of different promoters on Ni/CeZrO2 catalyst for autothermal reforming and partial oxidation of methane.* Chemical Engineering Journal, 2010. **156**(2): p. 380-387.
252. Siahvashi, A. and A.A. Adesina, *Synthesis gas production via propane dry (CO2) reforming: Influence of potassium promotion on bimetallic Mo-Ni/Al2O3.* Catalysis Today, 2013. **214**(0): p. 30-41.
253. Sun, S., W. Chu, and W. Yang, *Ce-Al Mixed Oxide with High Thermal Stability for Diesel Soot Combustion.* Chinese Journal of Catalysis, 2009. **30**(7): p. 685-689.
254. Fishtik, I., et al., *A thermodynamic analysis of hydrogen production by steam reforming of ethanol via response reactions.* International Journal of Hydrogen Energy, 2000. **25**(1): p. 31-45.
255. Adhikari, S., et al., *A thermodynamic analysis of hydrogen production by steam reforming of glycerol.* International Journal of Hydrogen Energy, 2007. **32**(14): p. 2875-2880.
256. Yoon, S., I. Kang, and J. Bae, *Effects of ethylene on carbon formation in diesel autothermal reforming.* International Journal of Hydrogen Energy, 2008. **33**(18): p. 4780-4788.
257. Lin, R., Y. Zhu, and L.L. Tavlarides, *Mechanism and kinetics of thermal decomposition of biodiesel fuel.* Fuel, 2013. **106**(0): p. 593-604.
258. Borowiecki, T., G. Giecko, and M. Panczyk, *Effects of small MoO3 additions on the properties of nickel catalysts for the steam reforming of hydrocarbons: II. Ni□Mo/Al2O3 catalysts in reforming, hydrogenolysis and cracking of n-butane.* Applied Catalysis A: General, 2002. **230**(1–2): p. 85-97.
259. Meeyoo, V., et al., *Steam reforming of ethanol over Ni/Ce0.75Zr0.25o2 and Ni-K/Ce0.75Zr0.25O2 catalysts*, in *Chemeca 2011 (39th : 2011 : Sydney, N.S.W.)*. 2011, Engineers Australia: Barton, A.C.T. p. [807]-[816].
260. Vagia, E.C. and A.A. Lemonidou, *Hydrogen production via steam reforming of bio-oil components over calcium aluminate supported nickel and noble metal catalysts.* Applied Catalysis A: General, 2008. **351**(1): p. 111-121.

261. Choong, C.K.S., et al., *Effect of calcium addition on catalytic ethanol steam reforming of Ni/Al2O3: II. Acidity/basicity, water adsorption and catalytic activity.* Applied Catalysis A: General, 2011. **407**(1–2): p. 155-162.
262. Hilaire, S., et al., *A comparative study of water-gas-shift reaction over ceria-supported metallic catalysts.* Applied Catalysis A: General, 2004. **258**(2): p. 271-276.
263. Borowiecki, T., et al., *Studies of potassium-promoted nickel catalysts for methane steam reforming: Effect of surface potassium location.* Applied Surface Science, 2014. **300**(0): p. 191-200.
264. Nikolla, E., J. Schwank, and S. Linic, *Promotion of the long-term stability of reforming Ni catalysts by surface alloying.* Journal of Catalysis, 2007. **250**(1): p. 85-93.
265. Shotipruk, A., et al., *Reactivity of CeO2 and Ce-ZrO2 toward steam reforming of palm fatty acid distilled (PFAD) with co-fed oxygen and hydrogen.* Chemical Engineering Science, 2009. **64**(3): p. 459-466.
266. Cheng, F. and V. Dupont, *Nickel catalyst auto-reduction during steam reforming of bio-oil model compound acetic acid.* International Journal of Hydrogen Energy, 2013. **38**(35): p. 15160-15172.
267. Zhenga, J., et al., *Comparative study of carbon formation on supported NI catalysts during CH4 reforming using TEOM, TPO-IR and TGA techniques.* Prepr. Pap.-Am. Chem. Soc., Div. Fuel Chem, 2003. **48**(2): p. 801.
268. Swaan, H.M., et al., *Deactivation of supported nickel catalysts during the reforming of methane by carbon dioxide.* Catalysis Today, 1994. **21**(2–3): p. 571-578.
269. Świerczyński, D., et al., *Steam reforming of tar from a biomass gasification process over Ni/olivine catalyst using toluene as a model compound.* Applied Catalysis B: Environmental, 2007. **74**(3–4): p. 211-222.
270. Li, D., et al., *Self-activation and self-regenerative activity of trace Rh-doped Ni/Mg(Al)O catalysts in steam reforming of methane.* Applied Catalysis A: General, 2007. **332**(1): p. 98-109.
271. Silvie Vallová, E.P., Věra Valovičová, Martin Hummel, *The Effect of potassium carbonate on Thermal Oxidation of Cokes and Carbonaceous Materials.* Fuels, 2013. **3**: p. 100-104.

10. Appendices

10.1. Appendix A: Gas chromatograph calibration

The gas chromatograph used an external standard method to determine the reactor outlet gas composition. The different gas mixtures were used for the calibration of the gas chromatograph. The calibration gas mixture was connected to the gas chromatograph and samples were injected in the columns via the sampling pump. The calibration point was taken when the area of the sampling gases was constant and there was no residual O_2 From air left in the gas sampling tube.

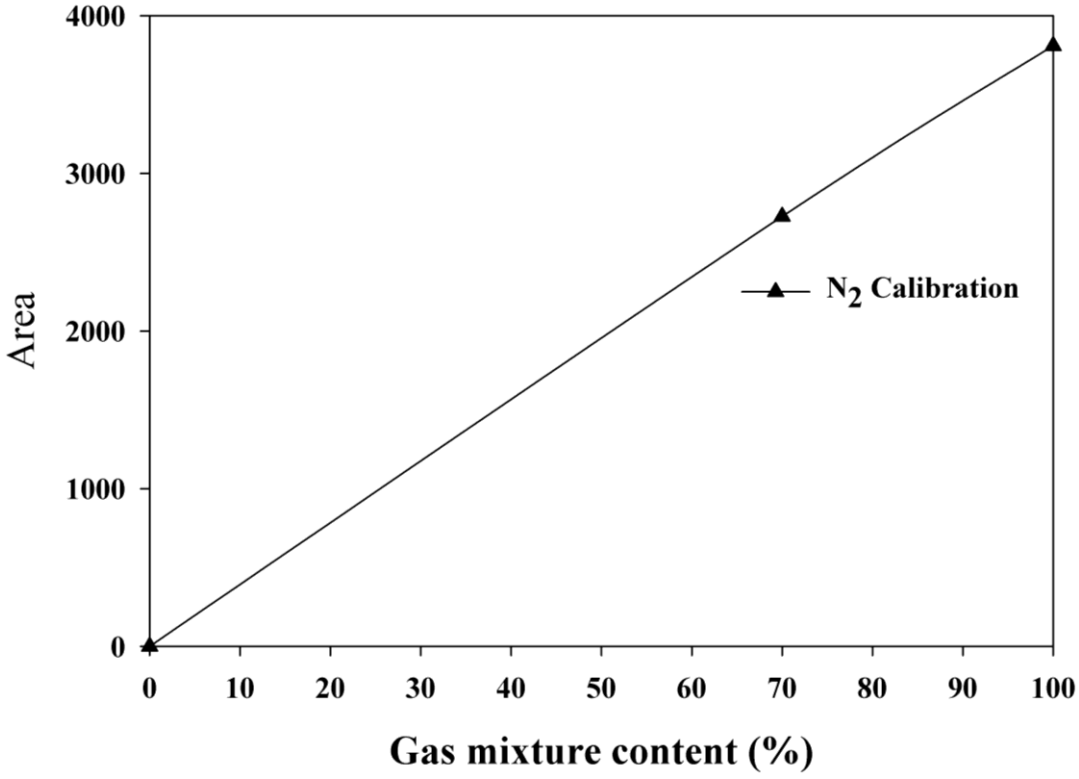

Figure 10.1: Channel 1, N_2 calibration for the GC.

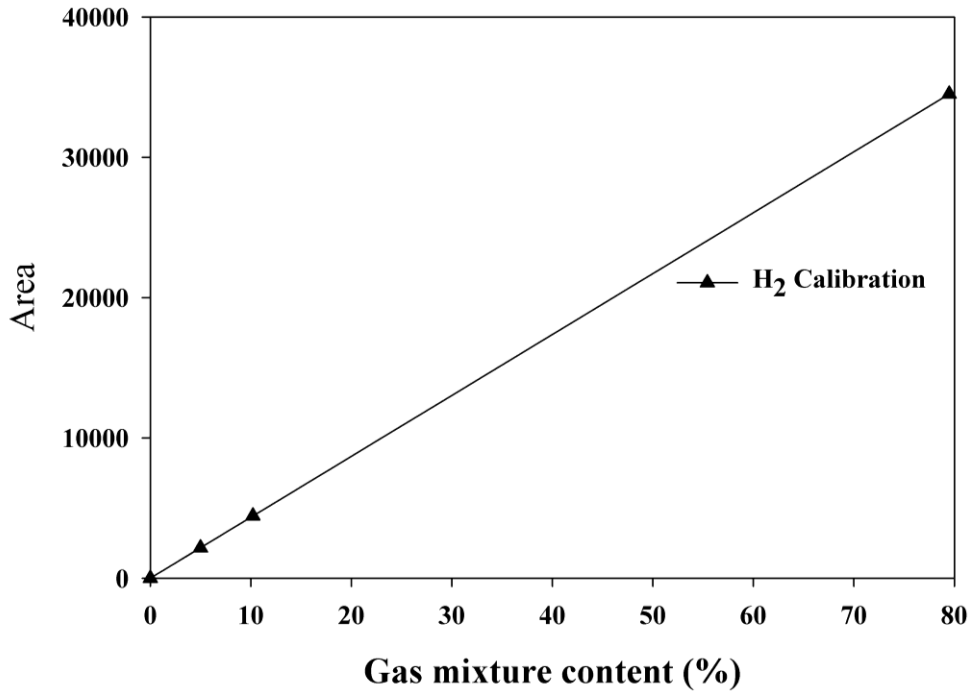

Figure 10.2: Channel 1, H_2 calibration for the GC.

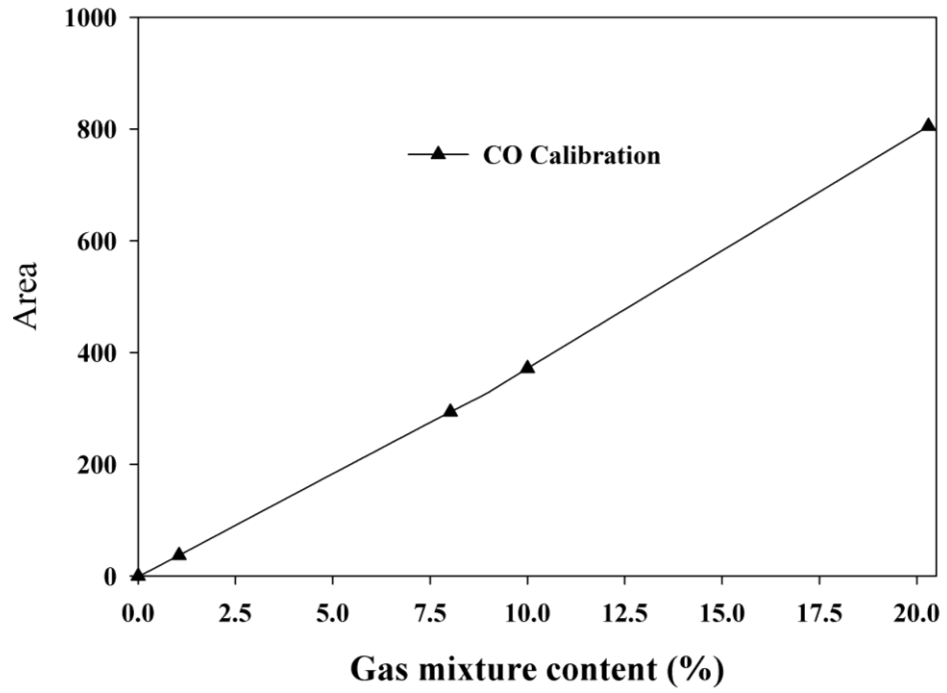

Figure 10.3: Channel 1, CO calibration for the GC.

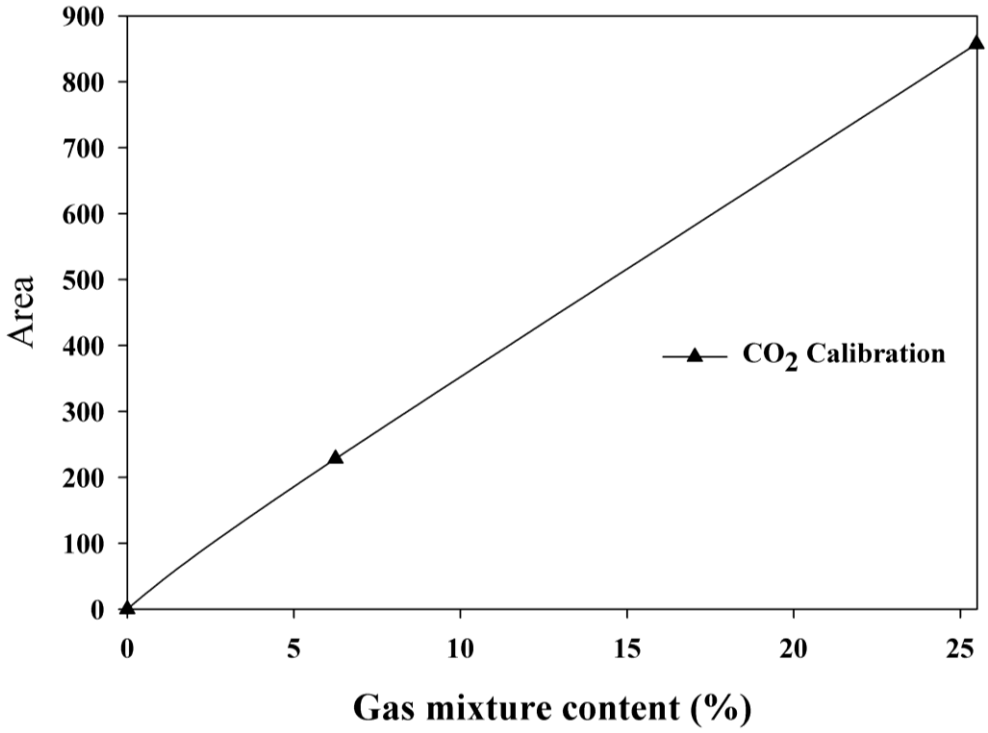

Figure 10.4: Channel 1, CO_2 calibration for the GC.

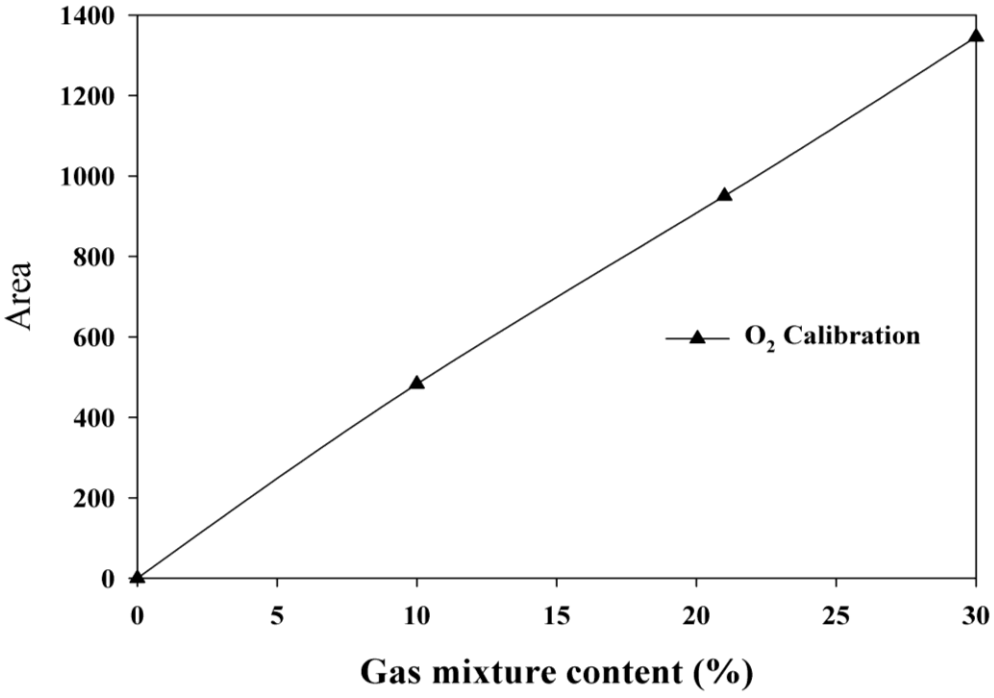

Figure 10.5: Channel 2, O_2 calibration for the GC.

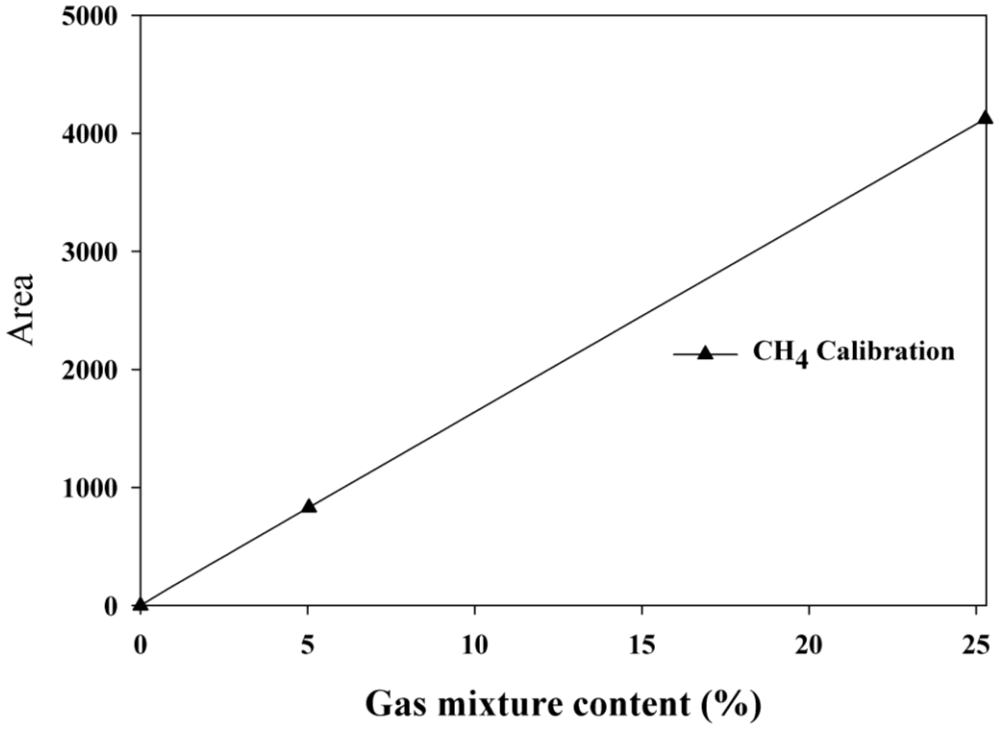

Figure 10.6 Channel 2, CH_4 calibration for the GC.

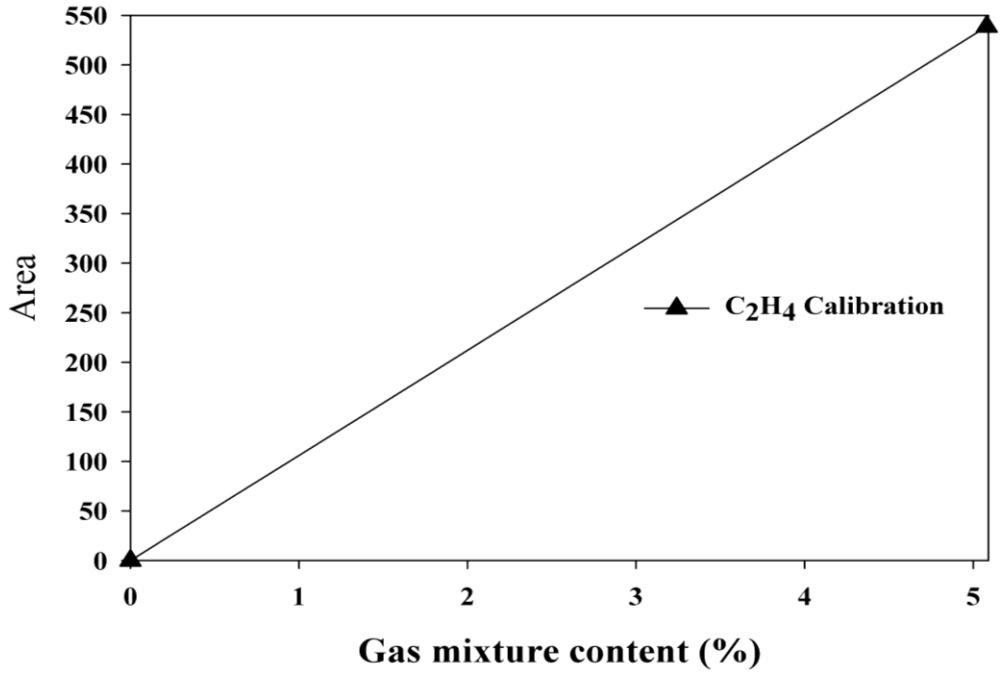

Figure 10.7 Channel 2, C_2H_4 calibration for the GC.

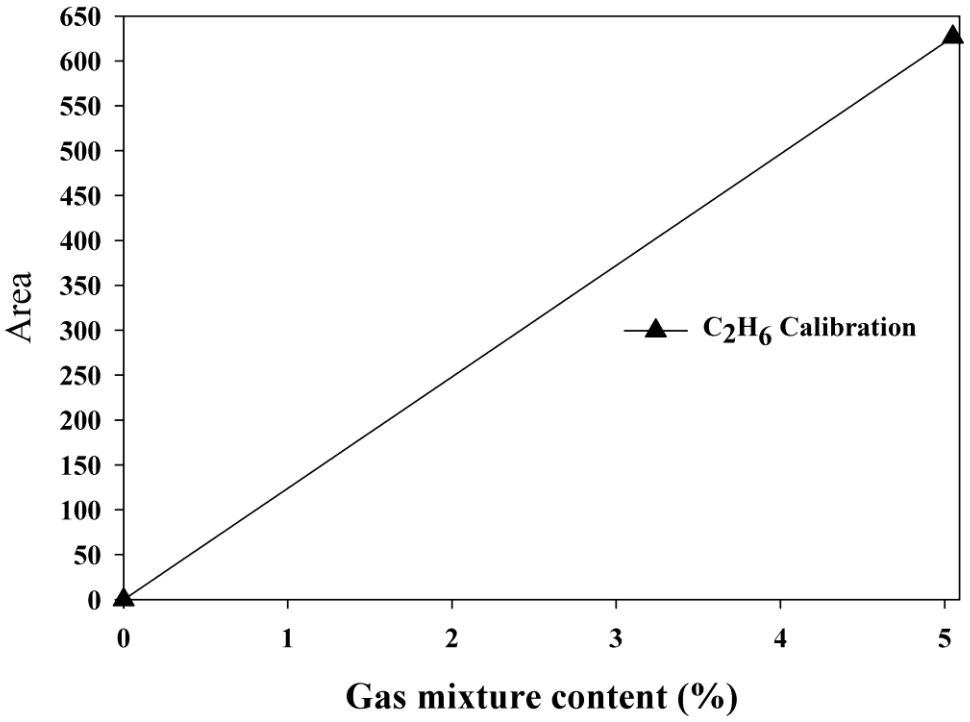

Figure 10.8: Channel 2, C_2H_6 calibration for the GC.

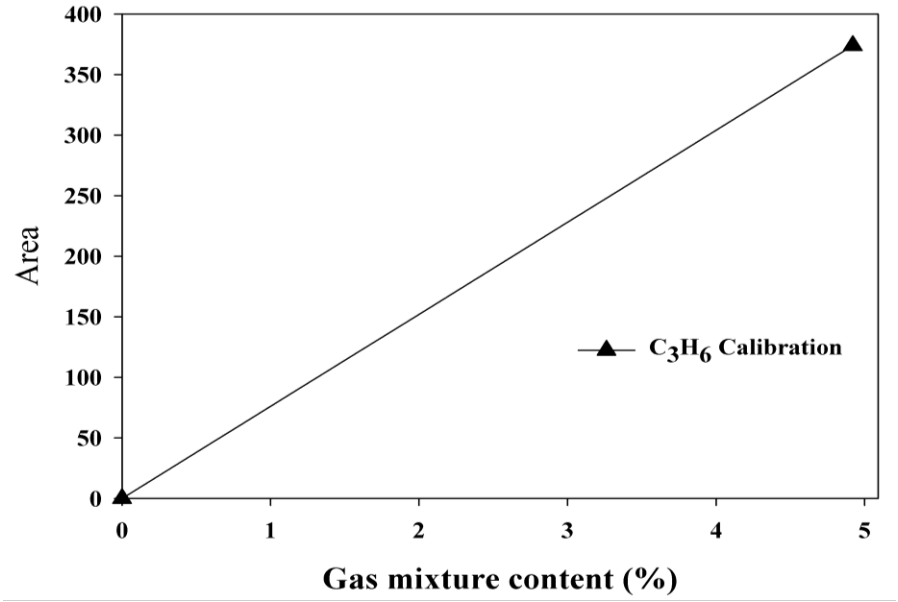

Figure 10.9: Channel 2, C_3H_6 calibration for the GC.

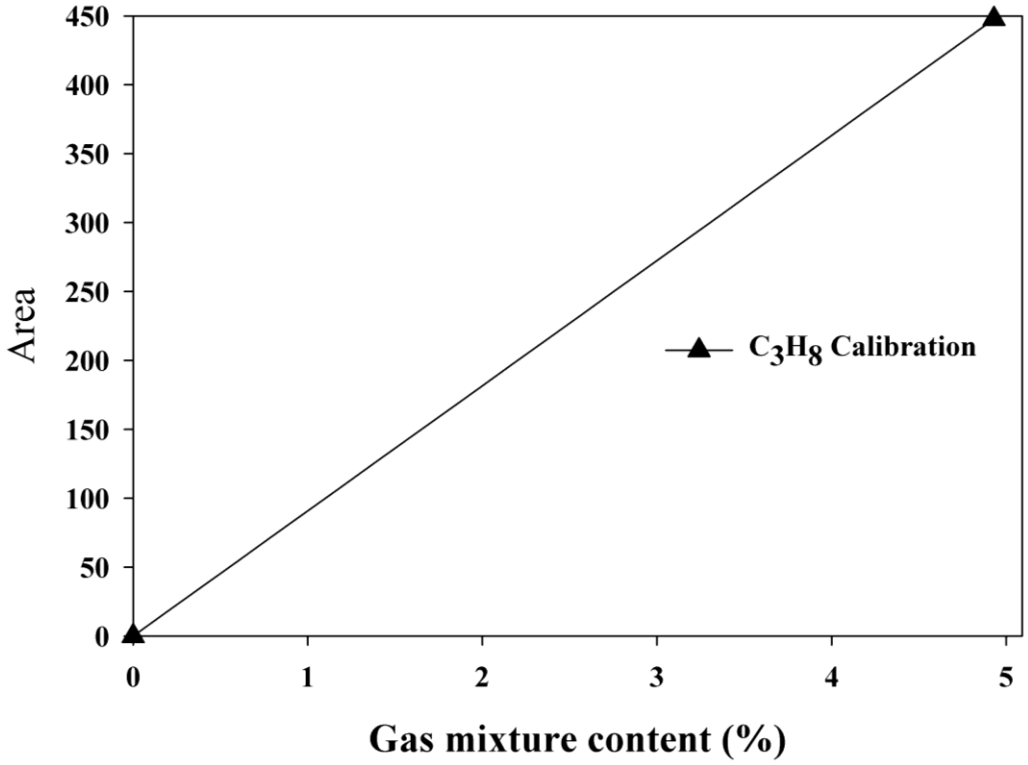

Figure 10.10: Channel 2, C_3H_8 calibration for the GC.

10.2. Appendix B: Equilibrium calculations

The input and output data of thermodynamic output is given below considering an example of SR of commercial biodiesel using S/C of 3 and WHSV of 3.18h^{-1}. The inlet biodiesel composition was used to calculate inlet mole fractions. Due to unavailability of the thermodynamic data of some of the methyl esters, the biodiesel composition obtained from gas chromatograph was regularised to 100% before calculating the mole fractions.

Table 10.1: Inlet molar composition used for equilibrium calculations for SR of commercial biodiesel at S/C of 3 and WHSV of 3.18 h^{-1}.

	Inlet
Compound	**mole fraction**
$C_{13}H_{26}O_2$	1.262865E-05
$C_{17}H_{32}O_2$	4.738665E-05
$C_{17}H_{34}O_2$	2.424214E-03
$C_{19}H_{38}O_2$	5.625648E-04
$C_{15}H_{30}O_2$	4.741212E-05
$C_{19}H_{36}O_2$	7.240017E-03
$C_{19}H_{34}O_2$	2.917506E-03
$C_{21}H_{42}O_2$	8.128071E-05
$C19H_{32}O_2$	2.251192E-04
H_2O	7.547660E-01
N_2	2.307359E-01
Ar	1.000000E-03

Table 10.2: Outlet molar composition used for equilibrium calculations for SR of commercial biodiesel at S/C of 3 and WHSV of 3.18 h^{-1}.

T	H_2	CO	CO_2	H2O	N_2	Ar	NH_3	CH4
200	5.38E-03	2.63E-06	6.55E-02	5.65E-01	2.08E-01	9.01E-04	1.15E-04	1.56E-01
250	1.52E-02	2.05E-05	6.76E-02	5.57E-01	2.07E-01	8.96E-04	1.62E-04	1.52E-01
300	3.54E-02	1.15E-04	7.20E-02	5.41E-01	2.05E-01	8.87E-04	2.07E-04	1.46E-01
350	7.00E-02	5.09E-04	7.92E-02	5.14E-01	2.01E-01	8.72E-04	2.40E-04	1.34E-01
400	1.21E-01	1.85E-03	8.92E-02	4.75E-01	1.96E-01	8.48E-04	2.53E-04	1.17E-01
450	1.85E-01	5.68E-03	1.00E-01	4.25E-01	1.88E-01	8.17E-04	2.46E-04	9.47E-02
500	2.56E-01	1.46E-02	1.09E-01	3.71E-01	1.80E-01	7.81E-04	2.21E-04	6.84E-02
550	3.23E-01	3.07E-02	1.11E-01	3.22E-01	1.71E-01	7.44E-04	1.84E-04	4.10E-02
600	3.72E-01	5.12E-02	1.05E-01	2.88E-01	1.64E-01	7.12E-04	1.42E-04	1.81E-02
650	3.94E-01	6.80E-02	9.69E-02	2.75E-01	1.60E-01	6.95E-04	1.01E-04	5.59E-03
700	3.95E-01	7.89E-02	8.87E-02	2.76E-01	1.59E-01	6.89E-04	7.05E-05	1.46E-03
750	3.91E-01	8.68E-02	8.15E-02	2.81E-01	1.59E-01	6.88E-04	4.96E-05	3.90E-04
800	3.85E-01	9.33E-02	7.52E-02	2.87E-01	1.59E-01	6.87E-04	3.58E-05	1.15E-04
850	3.80E-01	9.89E-02	6.97E-02	2.92E-01	1.59E-01	6.87E-04	2.66E-05	3.71E-05
900	3.75E-01	1.04E-01	6.47E-02	2.97E-01	1.59E-01	6.87E-04	2.02E-05	1.31E-05

Table 10.3: Equilibrium mass balance calculations of SR of commercial biodiesel at S/C 3 and WHSV of 3.18 h^{-1}.

Temp	Outlet moles	X_{H2O}	Y_{H2}	S_{H-H2}	S_{C-CO}	S_{C-CO2}	S_{C-CH4}
200	112.12391	16.41430	0.30691	3.27793	0.00120	29.89656	70.10224
250	112.67509	17.15141	0.87246	8.91584	0.00940	30.99280	68.99780
300	113.83002	18.68056	2.05229	19.23812	0.05326	33.25098	66.69576
350	115.89024	21.35138	4.13624	33.83797	0.23883	37.15232	62.60885
400	119.09834	25.37872	7.32996	50.21282	0.89228	42.84619	56.26153
450	123.57839	30.66658	11.66294	65.57913	2.83514	49.77632	47.38854
500	129.32900	36.67768	16.92468	78.43991	7.62519	56.36320	36.01161
550	135.97334	42.37626	22.52406	88.40622	16.88578	60.24829	22.86593
600	142.13034	46.32586	27.19984	95.17511	29.47420	59.85109	10.67471
650	145.79461	47.56141	29.55354	98.52479	40.27812	56.29619	3.42570
700	147.07290	46.94381	29.96988	99.61176	47.16576	51.92997	0.90427
750	147.41162	45.78648	29.69660	99.89460	51.95138	47.80605	0.24257
800	147.50296	44.60377	29.28724	99.96864	55.82201	44.10686	0.07112
850	147.52620	43.52197	28.88213	99.98972	59.15533	40.82168	0.02299
900	147.53865	42.55155	28.51329	99.99631	62.07979	37.91207	0.00814

Sample calculations performed at 650°C provides following results

Applying N_2 balance (6.18) outlet moles are calculated assuming 100 moles as basis.

Molar flowrate of gases leaving is

$$\text{Outlet moles} = \frac{(23.03)}{0.1582} = 145.75 \qquad (10.1)$$

Steam conversion calculated using Eq 6.13 is given below.

$$X_{H_2O} = \left(\frac{75.47 - 39.57}{75.47} \right) \times 100 = 47.56\ \% \quad (10.2)$$

The H_2 yield was caudated using Eq 6.22.

$$Y_{H_2}(wt\%) = \left(\frac{2.02 \times 0.396 \times 145.75}{394.93} \right) \times 100 = 29.55\% \quad (10.3)$$

The selectivities of H_2 and other carbon containing gases calculated using 6.23 and 6.25-26 is given below

$$S_{H-H_2} = \left(\frac{0.396}{0.396 + 0.005} \right) \times 100 = 98.52\ \% \quad (10.4)$$

$$S_{C\text{-}CO} = \left(\frac{0.069}{0.069 + 0.097 + 0.005} \right) \times 100 = 40.28\% \quad (10.5)$$

$$S_{C\text{-}CO_2} = \left(\frac{0.097}{0.069 + 0.097 + 0.005} \right) \times 100 = 56.29\% \quad (10.6)$$

$$S_{C\text{-}CH_4} = \left(\frac{0.005}{0.069 + 0.097 + 0.005} \right) \times 100 = 3.42\% \quad (10.7)$$

10.3. Appendix C: Carbon balance calculation

Carbon balance is shown below considering an e.g. Ni/Ce-Zr catalyst

Input molar flowrate of carbon 1.5×10^{-5} mol/s considering 7200 s experiment the inlet mole of carbon is calculated to 1.5×10^{-5} mol/s ×7200 s = 1.0798×10^{-1} mol. The biodiesel conversion was 96.09 hence C leaving the reactor with the gases is given by

$$\text{C leaving the reactor with gases} = 1.08\times10^{-1}\times0.9609 = 1.0376\times10^{-1}\text{mol} \quad (10.8)$$

The amount of C in the condensate was 781.34 mg/lit and the amount of condensate collected was 4 ml hence the amount of C in the condensate would be

$$\text{C in the condensate} = \left(\frac{781.35}{1000}\times\frac{4}{1000}\times\frac{1}{12}\right) = 2.6023\times10^{-4}\ \text{mol} \quad (10.9)$$

The amount of C deposited on the catalyst obtained from elemental analysis is 0.79 wt %

The total amount of C on the catalyst surface is

$$\text{C on catalyst surface} = \left(\frac{0.079}{1-0.079}\times\frac{2.0506}{12}\right) = 1.3596\times10^{-1}\text{mol} \quad (10.10)$$

$$\text{The total output C} = (\sum \text{C in gas} + \text{C on cat} + \text{C in condensate}) \quad (10.11)$$

$$\text{The total output C} = (1.0376\times10^{-1} + 1.3596\times10^{-3} + 2.6023\times10^{-4}) = 1.0538\times10^{-1}\text{mol} \quad (10.12)$$

$$\text{Unacounted C (\% feed)} = \left(\frac{1.0798\times10^{-1} - 1.0538\times10^{-1}}{1.0798\times10^{-1}}\right)\times100 = 2.40 \quad (10.13)$$

$$\text{C in gas (\%)} = \left(\frac{2.6023\times10^{-4}}{1.0538\times10^{-1}}\right)\times100 = 98.46 \quad (10.14)$$

$$\text{C on catalyst (\%)} = \left(\frac{1.3596\times10^{-1}}{1.0538\times10^{-1}}\right)\times100 = 1.29 \quad (10.15)$$

$$\text{C in condensate (\%)} = \left(\frac{2.6023 \times 10^{-4}}{1.0538 \times 10^{-1}} \right) \times 100 = 0.24 \qquad (10.16)$$

10.4. Appendix D: Vaporiser details

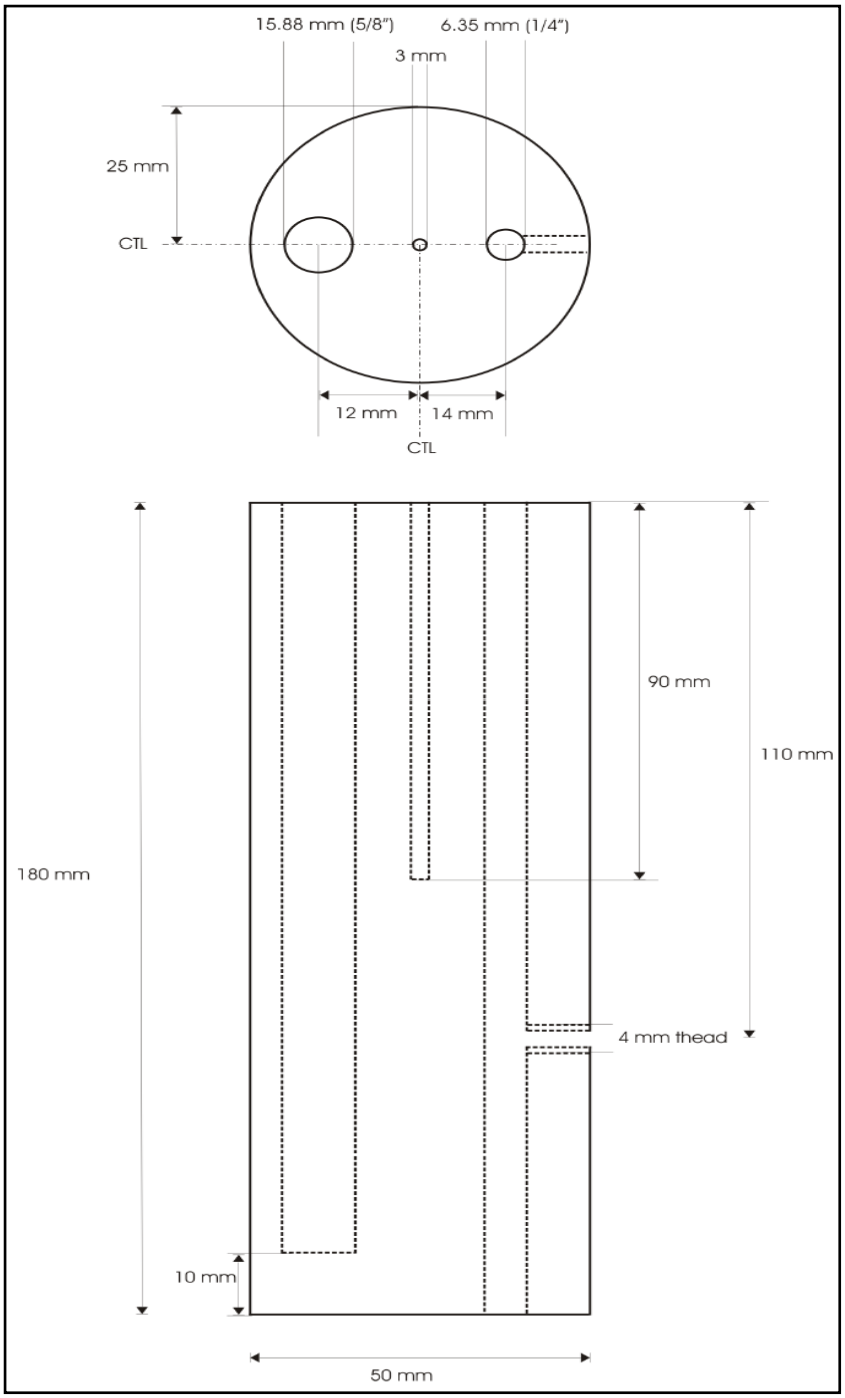

Figure 10.11: Engineering drawing of the vaporisers.

Table 10.4: Flowrates used for vaporizer design.

Mass flow of biod kg/h	Molar flow of biod kmol/h	Molar flow of water kmol/h[a]	Molar flow of N_2 kmol/h
5.4000E-03	1.82432E-05	1.0399E-03	1.22543E-05
6.0000E-03	2.02703E-05	1.1554E-03	1.22543E-05
1.2000E-02	4.05405E-05	2.3108E-03	1.22543E-05

a- Based on S/C of 3.

Energy required to heat water from 25 to 100°C.

$$Q_1 = \dot{n}_{H_2O} \int_{298}^{373} \Delta a + \Delta bT + \Delta cT^2 + \Delta dT^3 dT \tag{10.17}$$

Table 10.5: Specific heat constants for water and enthalpy calculation.

Δa	Δb	Δc	Δd	**Q_1 kJ/h**
9.1315E+01	-3.9399E-02	-2.0910E-04	5.2982E-07	7.2056E+00
9.1388E+01	-3.9454E-02	-2.0929E-04	5.3030E-07	8.0033E+00
9.1719E+01	-3.9701E-02	-2.1016E-04	5.3248E-07	1.5980E+01

Energy required to heat steam from 100 to 400°C.

$$Q_2 = \dot{n}_{H_2O} \int_{373}^{673} \Delta a + \Delta bT + \Delta cT^2 + \Delta dT^3 + \Delta eT^4 dT \tag{10.18}$$

Table 10.6: Specific heat constants for steam and enthalpy calculation.

Δa	Δb	Δc	Δd	Δe	**Q_2 kJ/h**
3.3872E+01	-8.2350E-03	2.9028E-05	-1.6262E-08	3.6486E-09	1.0900E+02
3.3878E+01	-8.2532E-03	2.9115E-05	-1.6416E-08	3.6530E-09	1.2138E+02
3.3905E+01	-8.3354E-03	2.9508E-05	-1.7117E-08	3.6729E-09	2.4520E+02

Energy required for phase change at 100°C

$Q_2 = n\lambda$ where λ is 39.5kJ/mol (10.19)

Table 10.7: Enthalpy calculation for phase change.

Molar flow of water kmol/h[a]	λ kJ/kmol	Q_3 kJ/h	$Q=Q_1+Q_2+Q_3$ kJ/h	Q W	Δ_{LMTD}	A m^2
1.0399E-03	39500	4.1075E+01	1.5728E+02	4.3688E+01	410	2.1269E-03
1.1554E-03	39500	4.5639E+01	1.7502E+02	4.8616E+01	410	2.3668E-03
2.3108E-03	39500	9.1277E+01	3.5246E+02	9.7905E+01	410	4.7663E-03

$$Q=UA\Delta_{LMTD} \tag{10.20}$$

$$A=n\times\pi\times do\times l \tag{10.21}$$

In the above equation U is assumed to be 50 W/m^2K. Assuming n=1 and do is ¼ inch which is 0.00635 m as result

Table 10.8: Area and length calculation for the vaporizer.

A m^2	l m	l cm
2.1269E-03	1.0660E-01	1.0660E+01
2.3668E-03	1.1863E-01	1.1863E+01
4.7663E-03	2.3889E-01	2.3889E+01

Based on fabrication limitations a vaporiser length of 180 mm was chosen with a vapourisation tube of ¼ ‘’ od. The vapouriser was designed taking into account high flowrates of biodiesel and steam, but easily could be used for smaller flowrates. Two vaporisers were fabricated using the same dimensions one was used for biodiesel and the other was used for steam.

10.5. Appendix E: Energy balance coefficients

Table 10.9: NASA coefficients for reactants used in energy balance calculations.

Compounds	a_1	a_2	a_3	a_4	a_5	a_6	a_7	b_1
$C_{13}H_{26}O_2$	0.000000E+00	0.000000E+00	-1.754888E+00	1.614386E-01	-1.075599E-04	3.704025E-08	-5.233795E-12	-8.301120E+04
$C_{15}H_{30}O_2$	0.000000E+00	0.000000E+00	-2.836721E+00	1.884326E-01	-1.267065E-04	4.390909E-08	-6.225764E-12	-8.569414E+04
$C_{17}H_{32}O_2$	0.000000E+00	0.000000E+00	-3.029283E+00	2.024666E-01	-1.342311E-04	4.588730E-08	-6.431215E-12	-7.628389E+04
$C_{17}H_{34}O_2$	0.000000E+00	0.000000E+00	-3.681177E+00	2.142768E-01	-1.452972E-04	5.090025E-08	-7.292151E-12	-9.167280E+04
$C_{19}H_{32}O_2$	0.000000E+00	0.000000E+00	-3.894658E+00	2.175327E-01	-1.500622E-04	5.380644E-08	-7.913133E-12	-5.035251E+04
$C_{19}H_{34}O_2$	0.000000E+00	0.000000E+00	-3.967656E+00	2.229967E-01	-1.511887E-04	5.303817E-08	-7.620720E-12	-6.591025E+04
$C_{19}H_{36}O_2$	0.000000E+00	0.000000E+00	-4.132870E+00	2.294491E-01	-1.556226E-04	5.511392E-08	-8.047574E-12	-8.176242E+04
$C_{19}H_{38}O_2$	0.000000E+00	0.000000E+00	-4.669568E+00	2.416043E-01	-1.660651E-04	5.919052E-08	-8.637092E-12	-9.720475E+04
$C_{21}H_{42}O_2$	0.000000E+00	0.000000E+00	-4.725162E+00	2.633073E-01	-1.772311E-04	6.128793E-08	-8.641197E-12	-1.027877E+05
H_2O	-3.947961E+04	5.755731E+02	9.317827E-01	7.222713E-03	-7.342557E-06	4.955043E-09	-1.336933E-12	-3.303974E+04
N_2	-3.425563E+04	4.847001E+02	1.119011E+00	4.293889E-03	-6.836301E-07	-2.023373E-09	1.039040E-12	-3.391455E+03
O_2	2.210371E+04	-3.818462E+02	6.082738E+00	-8.530914E-03	1.384646E-05	-9.625794E-09	2.519706E-12	7.108461E+02

Table 10.10: NASA coefficients for products used in energy balance calculations.

Compounds	a_1	a_2	a_3	a_4	a_5	a_6	a_7	b_1
H_2	4.078323E+04	-8.009186E+02	8.214702E+00	-1.269714E-02	1.753605E-05	-1.202860E-08	3.368093E-12	2.682485E+03
CO	1.489045E+04	-2.922286E+02	5.724527E+00	-8.176235E-03	1.456903E-05	-1.087746E-08	3.027942E-12	-1.303132E+04
CO_2	4.943651E+04	-6.264116E+02	5.301725E+00	2.503814E-03	-2.127309E-07	-7.689989E-10	2.849678E-13	-4.528198E+04
CH_4	-1.766851E+05	2.786181E+03	-1.202578E+01	3.917619E-02	-3.619054E-05	2.026853E-08	-4.976705E-12	-2.331314E+04
C	1.132857E+05	-1.980422E+03	1.365384E+01	-4.636096E-02	1.021333E-04	-1.082893E-07	4.472259E-11	8.943860E+03

10.6. Appendix F: Plug flow calculations

The schematic of the reactor used in the experiments is shown in the Figure 10.13.

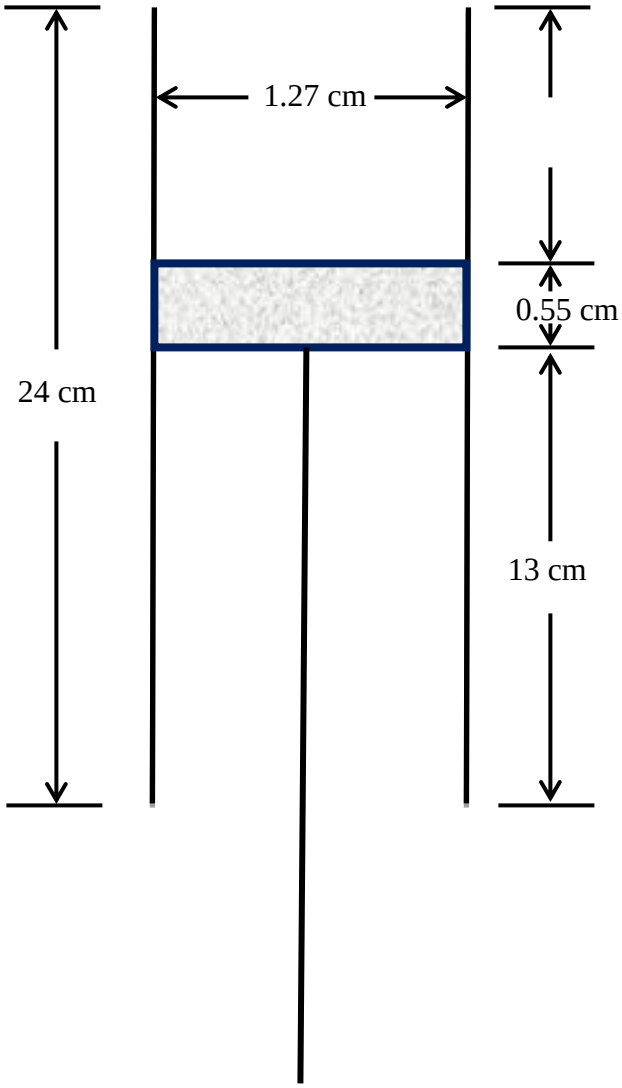

Figure 10.12: Schematic of the reactor used in the experiments.

The mass of the Ni/Ce-Zr catalyst used in an experiment is 2.0506 $\times 10^{-3}$ kg. The ρ_{cat} and ρ_{sand} are 5680 kg/m^3 and 2640 kg/m^3.

The density of ρ_{mix} is 4164 kg/m^3. The density of the bed is given by

$$\rho_b=\rho_m(1-\phi) \tag{10.22}$$

In the above equation ϕ is the void fraction and considered to be 0.3.

$$\rho_b=4164(1-0.3)=2914 \text{ kg/m}^3 \tag{10.23}$$

Diameter of the reactor (d) is 1.27×10^{-2} m and the d_p is 5×10^{-6} m. The ratio of d/dp is given by

$$\frac{d}{d_p}=\left(\frac{1.27\times10^{-2}}{5\times10^{-6}}\right)=2540 \tag{10.24}$$

$$\frac{d}{d_p}\geq 10 \text{ (plug flow)} \tag{10.25}$$

Similarly the volume of the bed used is

$$V_b=\left(\frac{m_b}{\rho_b}\right)=\left(\frac{2.0506\times10^{-3}}{2914}\right)=7.035\times10^{-7}m^3 \tag{10.26}$$

$$V_b=\frac{\pi}{4}\times {d_b}^2\times l_b \tag{10.27}$$

In the above equation l_b is the length of the bed and d_b is the diameter of the bed which is same as the diameter of the reactor.

$$l_b=\frac{(4\times V_b)}{\pi\times d^2}=\left(\frac{4\times7.035\times10^{-7}}{\pi\times(1.27\times10^{-2})^2}\right)=5.556\times10^{-3}m \tag{10.28}$$

$$\frac{l_b}{d_b}=\left(\frac{5.556\times10^{-3}}{5\times10^{-6}}\right)=1111.3 \tag{10.29}$$

$$\frac{l_b}{d_b}\geq 50 \text{ (plug flow)} \tag{10.30}$$